Transmission of the Magnetic Field to Nanoscale and Investigation of Its Spintronic Effects

Ageiskii Aleksandr

A thesis submitted to Queen Mary University of London in partial fulfillment of the requirements for the degree of

Doctor of Philosophy

School of Electronic Engineering and Computer Science,

Queen Mary University of London,

London E1 4NS, United Kingdom

July 2020

Statement of originality

I, Ageiskii Aleksandr, confirm that the research included within this thesis is my own work or that where it has been carried out in collaboration with, or supported by others, that this is duly acknowledged below, and my contribution indicated. Previously published material is also acknowledged below.

I attest that I have exercised reasonable care to ensure that the work is original and does not to the best of my knowledge break any UK law, infringe any third party's copyright or other Intellectual Property Right, or contain any confidential material.

I accept that the College has the right to use plagiarism detection software to check the electronic version of the thesis.

I confirm that this thesis has not been previously submitted for the award of a degree by this or any other university.

Signature:

Date: 04.07.2020

Details of collaboration

This work was supported by Marie Curie Initial Training Networks (ITN) FP7-PEOPLE-2012-ITN called Microwave Nanotechnology for Semiconductor and Life Sciences: "NANOMICROWAVE".

Abstract

While we are gradually approaching the fundamental limit of integrated circuits in classic electronics, smaller devices and new carriers for the information and signals are still in demand. There is also a problem of designing energy efficient electronics. One of the common issues in this area is how to manipulate microwave at very small scales, i.e., nanometers. Currently the fabrication of nanostructured materials either physically or in composition, and of nanoscale objects such as nanoparticles, nanotubes and nanowires is performed routinely in many research laboratories and private companies. In addition, the physical properties of these structures and objects (mechanical, electrical, magnetic etc.) are also relatively well understood in the two extreme frequency ranges corresponding to the low frequency range (up to 100 MHz) and to the optical frequency range (above THz). However, for the microwave frequency range 1 GHz-100 GHz most of these properties at the nanoscale are still to be investigated. The main reason for this situation has been the lack of enough development of theoretical and experimental techniques and tools to investigate this interaction at the nanoscale.

In this thesis, different approaches for characterization of nanostructures at microwave frequencies., namely, Atomic Force Microscope (AFM), the Electrostatic Force Microscope (EFM) and the Scanning Microwave Microscope (SMM) were performed. Before going deeply to the practice and simulation the basic principles of quantum mechanics were considered to understand the processes happening at the end of the tip, probe or any nanoscale source in free space. This theory is well-connected to the feeding device optimization study presented as it is shown Chapter 3 where the numerical simulation of the single electron wave function is shown. It has provided the first contribution of this thesis where the improvement of the AFM tip simulation is shown. The second objective of this thesis was to determine how the microwaves propagate, reflect or are transmitted from the nanoscale object. The optimization study results of the feeding device for a hall bar structure were presented in order to do that. The properties of this device were investigated theoretically and numerically. The optimized structure then will be prepared for the fabrication, i.e., the mask for electron-beam lightning will be presented.

Acknowledgements

This thesis was focused on research topics I have never encountered before. Therefore, completing this dissertation would not have been possible without the help and assistance of many people.

First, I would like to say many thanks to my primary supervisor Prof. Yang Hao for his constant encouragement and support, critics and recommendations to my ideas and initiatives, stimulating me to become an independent researcher. I'm sure it was not easy to work with me and it took a lot of patience and energy. I oversaw the very important and international Marie Curie project named Nanomicrowave. It would not be possible to complete it and go through it without Professor Hao's support and advice. I am very much appreciated.

I would also like to thank my second supervisor, Dr. Sayid-Khalid Rajab and Dr. Akram Alomainy for their useful and wise comments and suggestions during my study.

I'd like to say many thanks to Dr. Darryl Smith as he was not just my colleague but also my brother in spirit. He was giving me the advice in working hours about my study and job, we have discussed a lot of things together. He was my training partner in the gym and my provider to the UK culture. Without him my first time living abroad would not be so beautiful.

Many thanks to Dr. Oleksandr Sushko and Dr. Rostyslav Dubrovka for their support over the whole period of my study and for their advice in a field of microwave devices and characteristics. It is a hard period for our countries now and I was happy to have friends like them here in London. It helped me a lot.

I greatly appreciate the assistance of the EECS staff - Mellisa Yeo, Keith Bancroft, Sharon Cording, Hayley Cork, Mazharia Rahman and Alan Walker. I'd like to say many thanks to Jackie Stern and Julie Macdonald for their help and support as well.

I'd like to say thanks to Dr. Luigi La Spada for his support and help during the Nanomicrowave project as well as for his swimming lessons. I'd like to say thanks and show my respect to Dr. Max O. Munoz for his hospitality at the lab, for organizing

the soccer games and barbecue activities with my laboratory colleagues in the Antennas and Electromagnetics Laboratory (AEL). I'd like to say thanks to all those colleagues from AEL as the time I spent there with them was awesome.

I could not miss the team of the Nanomicrowave project here. It was an amazing journey to the world of the spintronics I have passed, and it was interesting and bright. Here they are: David Sarphie (BNC), Nanda Rahman (BNC), Dr. Gabriel Gomila (IBEC), Dr. Ferry Kienberger (Keysight), Dr. Romolo Marcelli (CNR-IMM), Ascanio Digiacomo (BNC), Maria Chiara Biagi (IBEC), Lazaro Fabregas (IBEC), Enrico Brinciotti (Keysight), Giorgio Badino (Keysight), Jorge Trasobares Sanchez (CNRS), Camilo Rojas (UNIGE), Joseph C Hardly (CNR-IMM), Loukas Michalas (CNR), Alexander Kolker (UCL), Silviu Sorin Tuca (JKU), Neil Curson (UCL) and many others who contributed to this huge international collaboration.

My warmest thanks and appreciation go to my wife, children and my mom for constantly supporting, inspiring and motivating me during my PhD studies.

Contents

List of Figures

List of Tables

List of abbreviations

2DEG 2-Dimensional Electron Gas

AFM Atomic Force Microscopy

AMR Anisotropic Magnetoresistance

CMOS Complementary Metal Oxide Semiconductor

CNR the Italian National Council of Research

CPS Coplanar Stripline

CPW Coplanar Waveguide

CSAFM Current-Sensing (or conductive) Atomic Force Microscopy

CST Computer Simulation Technology

DXF Drawing Exchange Format

EBL Electron-Beam Lithography

EFM Electrostatic force microscopy

EM Electromagnetic

EMR Extraordinary Magnetoresistance

EPR Electron Paramagnetic Resonance

ESR Electron Spin Resonance

FDTD Finite Difference Time Domain

GMR Giant Magnetoresistance

IBEC Institute for Bioengineering of Catalonia

IMM The Institute for Microelectronics and Microsystems

KE Kinetic Energy

KFM Kelvin Force Microscopy

LCN The London Centre for Nanotechnology

MEMS Microelectronic and Microelectromechanical Systems

MFM Magnetic Force Microscopy

MOCVD Metalorganic Chemical Vapor Deposition

NMR Nuclear Magnetic Resonance

PCB Printed Circuit Board

PE Potential Energy

PEC Perfect Electric Conductor

QMUL Queen Mary University of London

RCA Radio Corporation of America

SCM Scanning Capacitance Microscopy

SMM Scanning Microwave Microscopy

SPM Scanning Probe Microscope

SQUID Superconducting Quantum Interference Device

SSRM Scanning Spreading Resistance Microscopy

STM Scanning Tunneling Microscopy

UCL University College London

VNA Vector Network Analyzer

Chapter 1. Introduction

1.1 Background and motivation

Quantum mechanics emerged more than one hundred years ago as a new part of fundamental science. It was the time, when people realized the wave-particle duality of the light nature. Quantum mechanics provides a mathematical description of much of the dual particle-like and wave-like behavior and interactions of energy and matter. It is needed to point out also that it deals with physical phenomena at nano scales where the action is on the order of the Planck constant. Classical mechanics is very useful for description of macroscopic objects. But when we are dealing with objects like molecule, atom, electron and photon quantum mechanics come instead of classical one, exactly.

The first ideas of quantum theory were significantly reformulated in the mid-1920s by Werner Heisenberg, Max Born and Pascual Jordan (matrix mechanics); Louis de Broglie and Erwin Schrödinger (wave mechanics); and Wolfgang Pauli and Satyendra Nath Bose (statistics of subatomic particles). Basic equations and methods of the quantum mechanics appeared at this stage: Schrödinger equation, density matrix, Lindblad equation, Heisenberg picture, second quantization method and path integral formulation.

As electronic devices have been applied to many important subject areas for application, there are still rooms for studying fundamental science and technologies to advance them further. Thus, the understanding of the microwave devices and principles is necessary for us. At the same time, the design of electronics has moved towards the quantum level. Spintronic devices for micro-processing are a hot topic today, which has paved its way to the development of quantum computer. One of the phenomena widely used for these purposes is the Hall-effect. The latter is a change of electron distribution inside of a conductor at the presence of the external magnetic field. This effect was a target and a test of the magnetic field in several publications [1-4]. There is a rich amount of literature about qubits (theoretical [5, 6] and experimental [7-10]) and quantum gates [11] as well. In this area the entanglement time (the time during which the quantum object flips in between two states) is one of

the most valuable characteristics. It defines the ability of the device to be used for quantum processing. A lot of structures were made in last few years for the control of a single spin [12-15].

On the other hand, there are different ways to deliver the energy to this very localized and tiny areas where the quantum effect could be observed and investigated. With the invention of scanning tunneling microscopy (STM) and atomic force microscopy (AFM), several STM and AFM based techniques have been developed to probe materials properties. These include scanning near-field to scanning microwave microscopy (SMM), scanning capacitance microscopy (SCM), scanning spreading resistance microscopy (SSRM), electrostatic force microscopy (EFM), current-sensing (or conductive) AFM (CSAFM), and Kelvin force microscopy (KFM) [16]. While each method carries its own pros and cons, SMM and SCM have shown most promising potentials in this field for both industrial applications and scientific research. The scanning microscopy techniques will be considered in the upcoming chapters to investigate the spintronics in a better way and try to improve them

1.2 Challenges and Objectives

As a part of project collaboration in an EU funded research "Nanomicrowave", the new design for the feeding device for the structure performing the Hall effect was required. The Hall-bar structure is defined by our colleagues from London Centre for Nanotechnology, and it is a metallic conductor with one pair of electrodes for the electric current to be applied (see Fig.1). The others are for the purpose of measuring the Hall-effect. The device could be made generally in two ways. The first one is a classical metallic conductor that performs Hall effect when magnetic field is applied and the current flows through it. The second one is Delta-Doping is a technique [17], usually used in Metalorganic Chemical Vapor Deposition (MOCVD) growth, which can be used to get thin layers of high dopant concentration or, if combined with annealing, to get homogeneous doping with very high dopant concentration. Such layers could have very high conductivity.

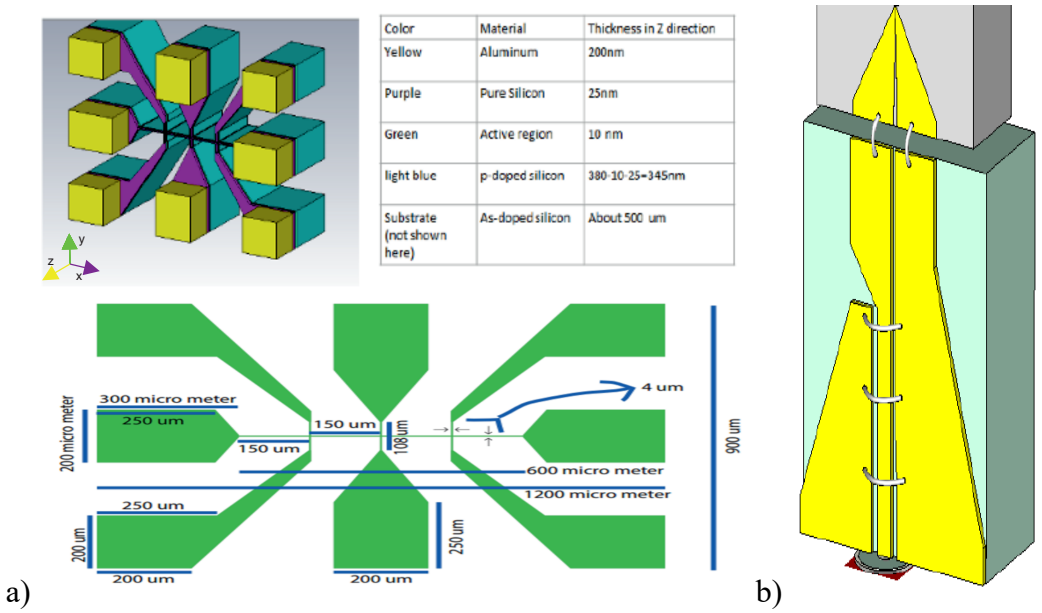

Figure 1 a) The hall bar structure to which the magnetic field need to be delivered is shown in detail on the left-hand side. b) The general view of the feeding device in charge of the magnetic field transfer is shown on the right.

The usual delta-doping procedure consists of multiple growth steps, where the host material and dopant sources are opened intermittently. Some people also leave the host material source open all the time and just open/close the dopant source. By this, relatively thick nominally undoped layers are interrupted by relatively thin layers with very high dopant concentration [17]. It is all about silicon devices (e.g., Silicon substrate, like a CMOS chip), in which some layer has very high dopant concentration. This could either be a p- or n- type dopant - which determines the element that one would dope with (e.g., Boron (B) for p-type Si, and Phosphorus (P) for n-type Si) [18].

Delta-doping is often used in Tunnel Junctions, for example in GaAs & InP-based photonic devices. GaAs can be delta-doped n-type with Silicon. The "delta" refers to a doping profile that looks like a delta function – i.e., a sharp spike in the amount of doping at a specific depth, and very little high doping in the adjacent layers [19].

One of the main objectives of my study is – to understand the microwave field to matter interaction in nanoscale. I have found that specific technique was developed in order to understand organic and inorganic radicals, transition metal complexes, and some biomolecules, electron paramagnetic resonance spectroscopy (EPR), also called electron spin resonance (ESR), has been developed to study chemical species with unpaired electrons. Specifically, every electron has a magnetic moment and spin

quantum number S=1/2, with magnetic components $m_s = \pm 1/2$. In the presence of an external magnetic field with strength B_0, the electron's magnetic moment aligns itself either antiparallel or parallel to the field, each alignment having a specific energy due to the Zeeman effect [20,21]:

$$E = m_s g_e \mu_B B_0 \quad (1),$$

where m_s spin quantum number, g_e the electron's so-called g-factor, μ_B is the Bohr magneton. Therefore, the separation between the lower and the upper state is ΔE for unpaired free electrons. This equation implies (since both g_e and μ_B are constant) that the splitting of the energy levels is directly proportional to the magnetic field's strength, as shown in the diagram below.

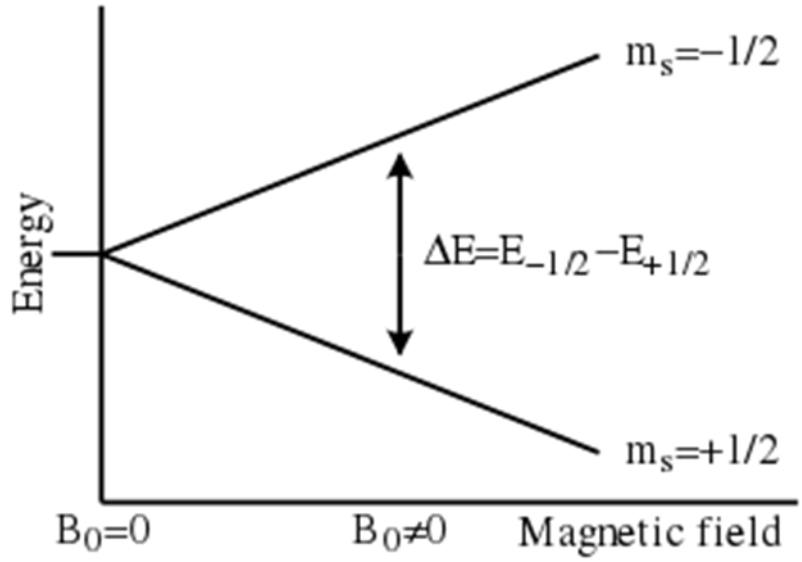

Figure 2 The typical Zeeman splitting of the single electron energy levels under the applied magnetic field Bo. Two energy states emerge $\mu_s = 1/2$ and $\mu_s = -1/2$, therefore [20]

An unpaired electron can move between the two energy levels by either absorbing or emitting a photon of energy. Experimentally, this condition permits a large combination of frequency and magnetic field values, but the great majority of EPR measurements are made with microwaves in the 9000–10000 MHz (9–10 GHz) region, with fields corresponding to about 3500 G (0.35 T) [21]. Furthermore, EPR spectra can be generated by either varying the photon frequency incident on a sample while holding the magnetic field constant or doing the reverse. In practice, it is usually the frequency that is kept fixed. A collection of paramagnetic centres, such as free

radicals, is exposed to microwaves at a fixed frequency. By increasing an external magnetic field, the gap between the $m_s = 1/2$ and $m_s = -1/2$ energy states are widened until it matches the energy of the microwaves, as represented by the double arrow in the diagram above [20]. At this point the unpaired electrons can move between their two spin states. Since there typically are more electrons in the lower state, due to the Maxwell–Boltzmann distribution, there is a net absorption of energy, and it is this absorption that is monitored and converted into a spectrum. The upper spectrum below is the simulated absorption for a system of free electrons in a varying magnetic field. The lower spectrum is the first derivative of the absorption spectrum. The latter is the most common way to record and publish continuous wave EPR spectra.

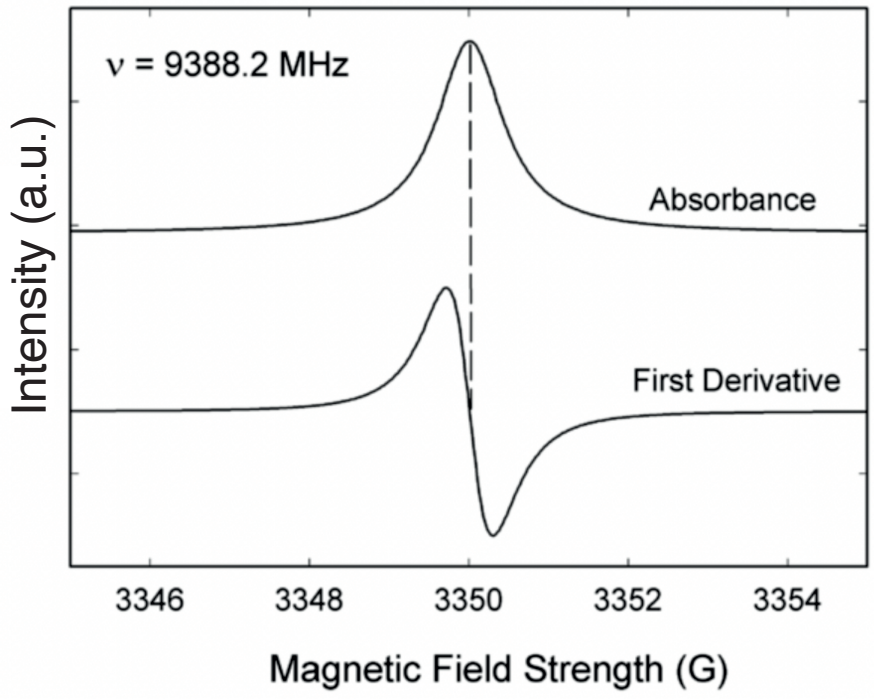

Figure 3 Simulated absorption for a system of free electrons in a varying magnetic field (upper spectrum) and the first derivative of the absorption spectrum (the lower one) [20].

For the microwave frequency of 9388.2 MHz, the predicted resonance occurs at a magnetic field of about B_o= 0.3350 T = 3350 G [20].

Because of electron-nuclear mass differences, the magnetic moment of an electron is substantially larger than the corresponding quantity for any nucleus, so that a much higher electromagnetic frequency is needed to bring about a spin resonance with an electron than with a nucleus, at identical magnetic field strengths. For

example, for the field of 3350 G shown above, spin resonance occurs near 9388.2 MHz for an electron compared to only about 14.3 MHz for 1H nuclei. This is what happening with free or unpaired electron under the applied magnetic field. There are unpaired electrons in the conducting layer when the current is flowing through.

In order to bring the H-field to the structure on Fig. 1, a planar transmission line was chosen. It has been widely described in the literature [22-25] that the Balun (for balanced to unbalanced structure conversion) is a crucial part of such transmission line as well as it is important to match the coaxial cable and the antenna impedances. In this work, the coaxial cable is an initial source of the field, and the antenna design is responsible for the concentration of the magnetic field in a very small area. The actual device should provide circumstances for the spin to flip in between the stages of up and down. Therefore, the signal with a wavelength of a few millimeters should be transmitted to the nanoscale object.

This process requires magnetic field to be applied perpendicular to the plane of the device. It is also needed to be so that the electric field should be as weak as possible. The results will be compared with the recent publication [26] and the general view of the structure is shown on Fig. 1. The aim of this research is therefore to manipulate magnetic fields at the microwave frequency within nanoscale objects and materials. It will effectively lead to an interdisciplinary research by linking microwave engineering with quantum mechanics and developing a better understanding of the field to matter interaction. In case of a nanoscale object, as its size is much smaller than the wavelength of the radiation, there have been significant challenges in retrieving experimental data through measurements [27].

As a part of this PhD study, a good number of secondment trainings were taken place and some basic principles of how they have worked will be reviewed in this thesis. This will lead to the proposals of studying, modelling and fabricating of nanoscale objects which interact with electric and magnetic fields at microwave frequencies.

High level objectives of this study can be found below:

- To investigate the microwave frequency range field to nanoscale objects interaction

- To study the state of art of design and modelling techniques in the area of microwave engineering and nanoscale objects.
- To design and evaluate the structure for magnetic field transmission to the nanoscale object to excite single electrons for measuring the Hall effect.
- To understand quantum mechanical processes and study the possibility of spin-effects.

1.3 Organization of the thesis

This work is organized as follows. I will start from the high-level introduction to the proposed research and describe challenges and objectives in Chapter 1. I will then go through some theoretical background of my work in Chapter 2. It will be focused on the introduction of spintronics and basic quantum-mechanic theory in relevant to the design of an electron spin (EPR). This chapter helps to understand the functionality of the feeding device which will be investigated in one of the later chapters. I will then present some introductions to a new characterization technique based on the use of Atomic Force Microscopy for microwave applications in Chapter 3. It is termed as the Scanning Microwave Microscopy (SMM). Some background information as well as the numerical simulation and experimental results for Electrostatic Force Microscopy (EFM) are shown. Numerical modelling of the SMM and its application for material sample characterization will be discussed in the Chapter 4 based on the use of COMSOL and CST Microwave Studio. Chapter 5 will be dedicated to the optimization study of the feeding device of EPR which is aimed to focus strong magnetic field to the nanoscale. Numerical simulation results will be presented together with a design optimization process and the mask fabrication. Finally, the conclusion and potential future work will be summarized in Chapter 6.

Chapter 2. Background and Literature Review

2.1 Introduction

The review of the theoretical background will be presented in this chapter. It is important to understand the basic things before going to details and this chapter has this aim as a target. The electron spin and Electron Paramagnetic Resonance (EPR) will be covered at fist. The EPR will be covered deeply from theoretical point of view to have a better view on the magnetic field applied function in this phenomenon. The typical experimental setup will be shown as well. Then, the quick overview of the spintronics will be given to feel their connection. Some of the relevant physical effects and their applications will be covered after. This will clearly give the picture of the area in which this investigation was made.

2.2 Electron spin

What is the first idea that comes to my mind when I hear the word "spin"? This is certainly the type of the movement taken by some object. It could be the head of any human, the tennis ball and the Earth daily circle. The latter was predicted by Ancient Greek philosophers and supported by the Galileo Galilei [28], Johannes Kepler [29] and Copernic at the time of the Renaissance [30].

This is quite common type of the action in nature, therefore. It is well-known from high school program that the electrons typically belong to atoms, and they are main the reason why the Periodical system created by Mendeleev in 1869 [31]. It is not common to use the quantum numbers at the school time, but the Pauli principle formulated in 1925 [32] is one of the fundamental things already. It is one of the main postulates of the theoretical physics which didn't arise from any law known at that time. It says that not more than two electrons could be on the same atomic orbital (in the same energy state) at the same time and their spins must be oppositely directed. The way the electrons are organized in all chemical elements is quite simple and the beginning of the Periodic table looks like as it is shown on the Fig. 4:

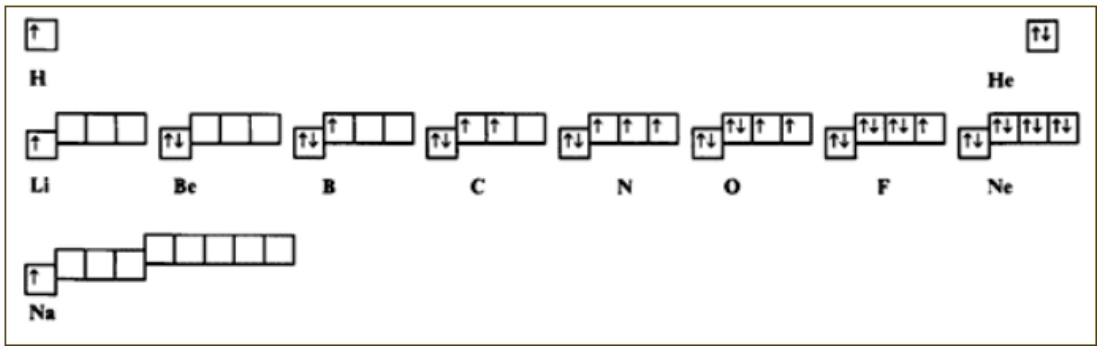

Figure 4 The electrons position structure within the atomic energy levels of chemical elements from the beginning of the Periodic table [33].

The atomic orbitals here presented as “boxes” which could be populated, and they show if there is a vacant place for the electrons as well. The shape and orientation of s-, p- and d-types of atomic orbitals are presented on the Fig. 5. There are much more types of them, but they are not used frequently as only the last atomic energy level is considered typically. Figure 5 shows the first 4 of them: their shape and orientation:

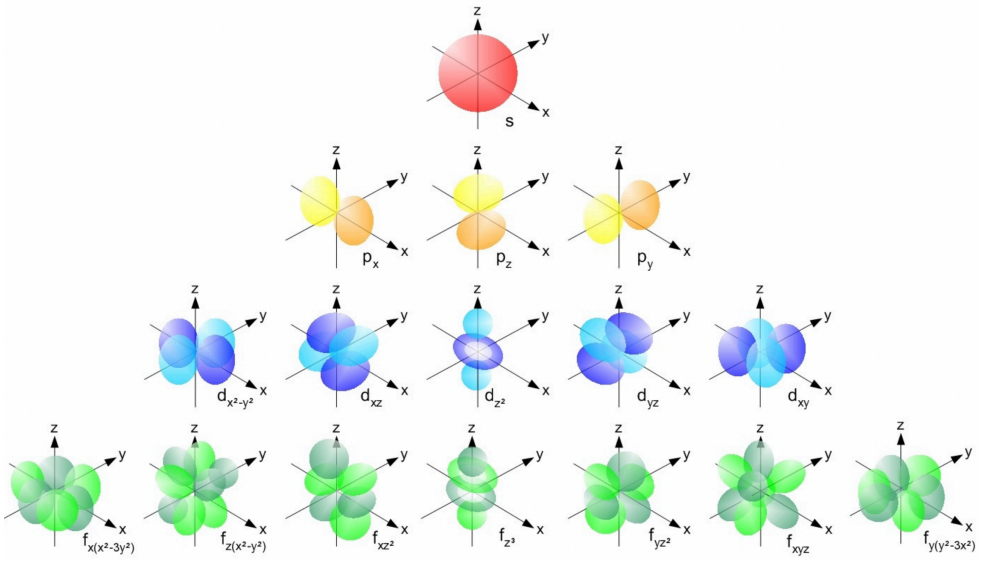

Figure 5 The typical shape and the orientation of atomic orbitals of s-, p-, d- and f- types [33]

The information presented on the figure above helps to understand the chemical and physical basement of chemical reactions and molecule’s structure. More complicated the shape of the orbital leads to more states the electron could take there. It shows the valent states in case if we talk about the last to energy levels of atom.

Thus, lots of effects could be achieved by applying the magnetic field due to the electron spin [34-36]. The electron spin and electron orbitals play the main role in very well-known type of the objects– NV (Nitrogen-vacancy) centres. This is a point defect in diamond most explored and useful property is photoluminescence, which can be easily detected from an individual N-V centre. Electron spins at N-V centres could be excited at room temperature by applying a magnetic field, electric field, microwave radiation or light, or a combination, resulting in sharp resonances in the intensity and wavelength of the photoluminescence. These resonances are widely used in electron spin related phenomena such as quantum entanglement and spin-orbit interaction. In two words, this defect generally consists of a nearest-neighbour pair of a nitrogen atom, which substitutes for a carbon atom, and a lattice vacancy. Two charge states of this defect, neutral N-V^0 and negative N-V^-, are known from spectroscopic studies using optical absorption [37-38], photoluminescence [39] and electron paramagnetic resonance (EPR) [40-42].

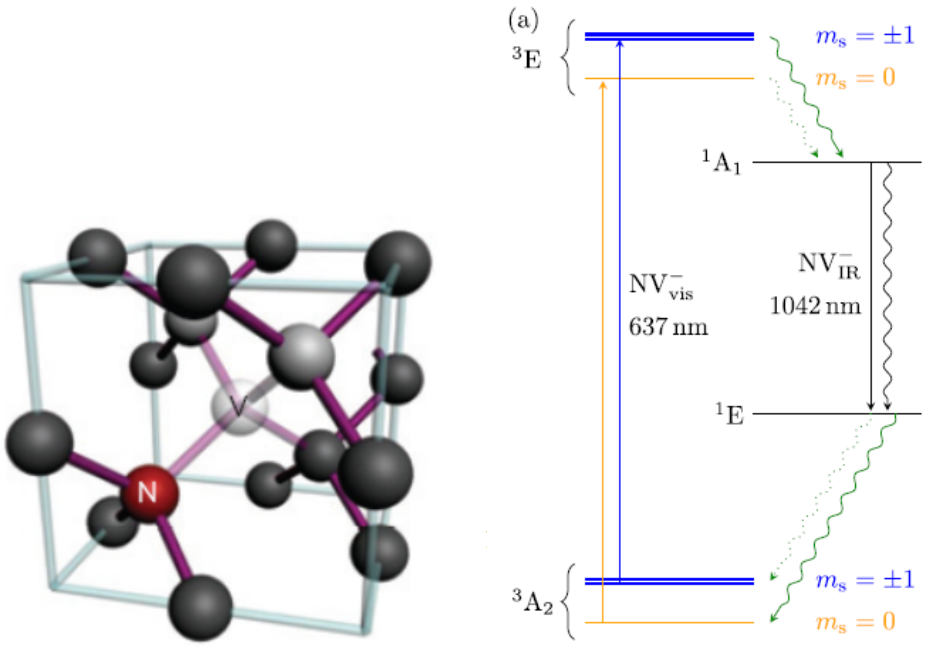

Figure 6 The schematic picture of NV defect in general case (left) and schematic energy level structure of the N-V− centre. Electron transitions between the ground 3A and excited 3E triplet states as well as two intermediate singlets as a way the decay goes gives a rise to spin polarisation from ±1 to 0 [38].

This is one another structure type where the EPR could be observed and where spin of electron is the key feature. This structure is much more complicated. The electron here is not isolated. A nitrogen atom has five valence electrons. Three of them

covalently bond to the carbon atoms and two remain non-bonded and are called a lone pair. The vacancy has three unpaired electrons. Two of them make a quasi-covalent bond and one remains unpaired. These unpaired vacancy electrons continuously exchanging their roles. How it could be affected by the external field? In the absence of an external magnetic field, the ground and excited states are split by the magnetic interaction between the two unpaired electrons at the N-V^- center: when two electrons have parallel spins (m_s=±1), their energy is higher than when spins are antiparallel (m_s=0). The farther apart the electrons are, the weaker their interaction energy D (roughly D is proportional to ~$1/r^3$) [41]. Thus, the smaller splitting in the excited state can be viewed in terms of larger electron-electron separation in the excited state. When an external magnetic field is applied to the N-V^- center, it does not affect the m_s=0 states nor the ^{1}A state (because it has S = 0), but it splits the $m_s = \pm 1$ level. If a magnetic field is oriented along the defect axis and reaches about 1027 G (or 508 G) then the $m_s = -1$ and $m_s = 0$ states in the ground (or excited) state become equal in energy; they strongly interact resulting in so-called spin polarization, which strongly affects the intensity of optical absorption and luminescence transitions involving those states [43]. There are lots of effects to investigate here. The Schrödinger Equation may become very complicated in that case as it could include the parts of close and far carbon atoms influence. Thus, it is not a place to start for me to analyze the quantum theory connection with the microwaves. Let's move to the simpler case of a single electron and its spin.

The spin as vector value was considered by scientists for the first time. Goudsmit and Uhlenbeck, in 1925 [44], recommended that an electron has an inherent angular momentum that is a magnetic moment which is recognized as a spin. In atomic physics, the inherent angular momentum of a certain particle is parametrized by spin quantum number. The spin quantum number is the fourth in between the quantum number's set. The rest three are a principal quantum number, azimuthal quantum number and magnetic quantum number. The spin quantum number explains the unique quantum state of an electron. This is nominated as m_s.

The Spins plays a noteworthy role in quantum mechanics in computing the characteristics of elementary units like electrons. The direction of spin of the particle regulates several things like spin quantum number, angular momentum, the degree of freedom etc. So, what it is the electron spin? The electron spin is one of the three

inherent properties of the electrons; the others are mass and charge of the electron. The electron spin is described as the spinning of the electron around its axis.

The electron spin theory describes the electron as a quantum particle instead of the simple sphere as in the classical theory. The theory says that the electron spin direction and its influence on the certain properties like magnetic properties of the atom. The electron can spin in two directions: spin up and spin down. The spin up and spin down directions are corresponding to the spinning in the opposite directions. These spins (spin up and spin down) are the particles which have spin m_s equal to 1/2, i.e., for electrons.

In the quantum theory, the electron is thought of as the minute magnetic bar and its spin points the north pole of the minute bar. If two proximate electrons have a similar spin direction, the magnetic field formed by them strengthens each other and therefore a strong magnetic field is gained. If the proximate electrons have an opposite spin direction, the magnetic field formed by them cancels each other and no magnetic field is existent. Let's go deeper in the terms we have mentioned above.

2.3 Electron paramagnetic resonance

2.3.1 Introduction

The electron paramagnetic resonance (EPR) experiments could be considered as the evolution of Stern-Gerlach experiment [45]. The latter was one of the most fundamental experimental investigations of the matter structure. They proved that the total electronic and magnetic momentum of the atom placed into the magnetic field could take discrete values. Uhlenbeck and Goldsmit have shown that the existence of the own magnetic moment of electron has a strong reason in the electron spin presence [44]. Apart from the huge experimental value this method helps a lot with understanding of basic theory and principles of quantum mechanics [45].

The most of information we have today about the molecules structure was accumulated by the molecular absorption curves Fig. 9-11. Those curves normally present a comparison of the transmitted and illuminated flow values as a function of wavelength or the frequency. The lines (wide or narrow) in those spectrums correspond to the transitions in between the energy levels within the molecule. So, they define the value of the energy gap in between those energy levels itself. Therefore, the molecule energy levels structure could be found from these curves. It is easy to conclude that not all the transitions could be performed from that picture. Thus, there is a special rule defining which one could be taken and which one could not.

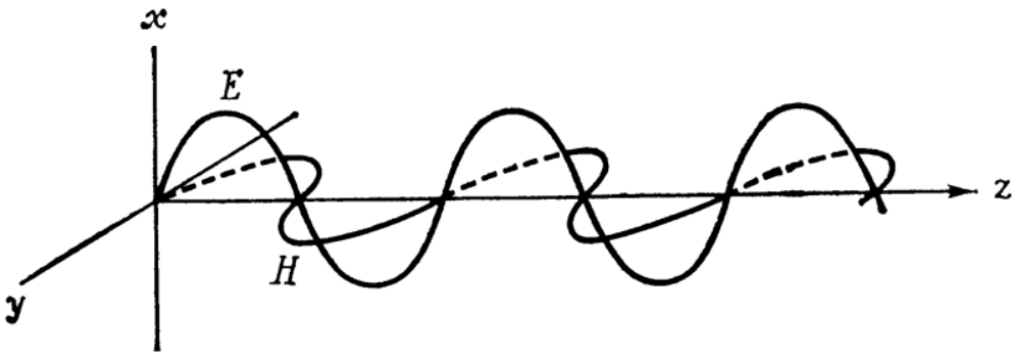

Figure 7 The electromagnetic field components (electric E and magnetic H) within the propagating electromagnetic wave.

Electromagnetic field could be considered as a pair of electric and magnetic components oscillating perpendicularly to each other and to the direction of the propagation (Fig. 7). It is the electric component that interacts with molecules in most of cases. There are two conditions that should be satisfied in order to perform the absorbance. First one is that the quant energy should be equal to the difference in between the molecule's energy levels. Second one is that the oscillating electric field should excite the oscillating electric dipole within the molecule. The microwave electromagnetic field interacts with molecules with a constant electric dipole (hydrogen chloride (HCl) molecule, for instance). The latter emerge due the circular molecule movement. Same as the IR- frequency range field interacts only with those oscillating degrees of freedom which changes the molecule's electric dipole moment.

It is easy to expect that the molecule with a constant magnetic dipole will interact with the magnetic component of the field. It is hard to have visible observance when illumination of the molecules in a wide frequency range considered. On the other hand, it is possible to have it at one or several characteristic frequencies due to the change of a magnetic dipole moment when putting the sample under the static magnetic field [45].

EPR spectrometer is a device for magnetic dipoles transitions detection. The one of the first and possible schemas of such a device is shown on the Fig. 8-b. The typical schema of optical spectrometers is represented on the Fig. 8-a, for comparison. It is clear these devices have something in common. The sample is illuminated by the monochromatic electromagnetic field and the researcher is fixing the changes in the transmitted field intensity from a suitable detector in both cases. The absorbance will take place when the illuminated quant energy will be equal to the distance in between the energy levels. The static field is a characteristic property of dipole transitions. The static magnetic field could be intrinsic as well as corresponding to the intrinsic magnetic moments of the atomic nuclei within the molecule. The energy levels of the magnetic dipole are equal when no field applied to them. The constant magnetic moments could be related to electrons or to the nuclei. Their presence is highly connected to the electron and nuclei mechanical moments respectively. It is a fundamental property of the angular momentum that it is quantized.

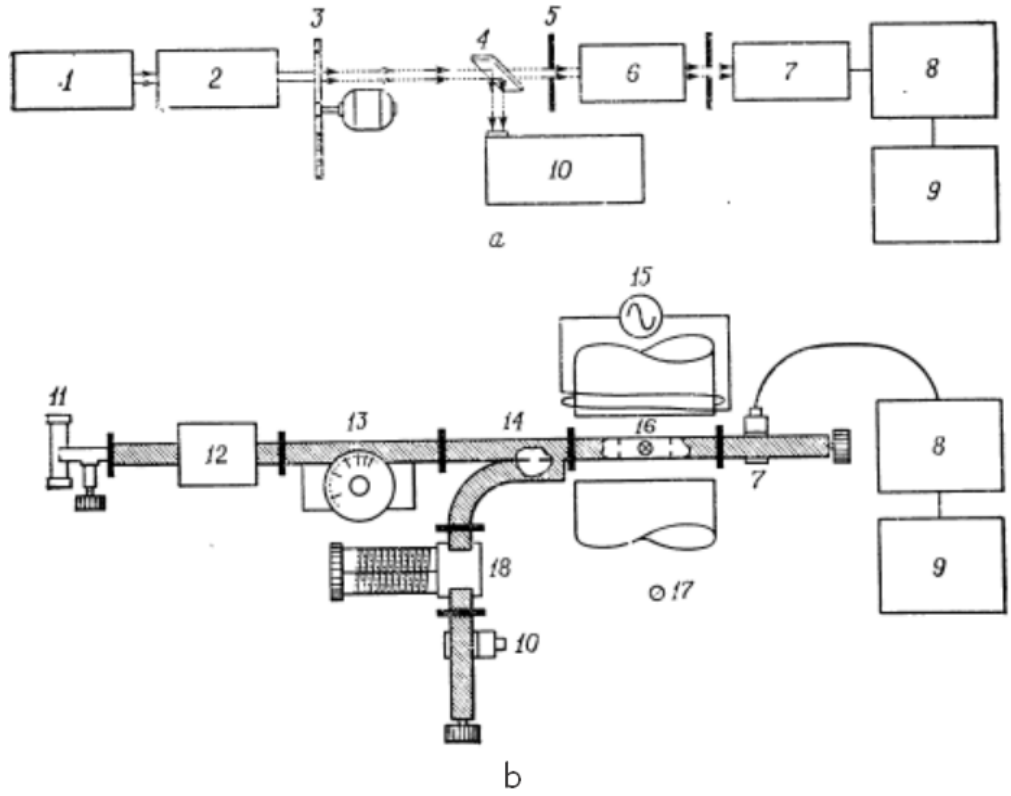

Figure 8 The principal schemas of optical – a – and EPR spectrometers – b. 1 – the source, 2 – monochromator, 3 – the turning sector, 4 – the semi-transparent mirror, 5 – the connection hole, 6 – the sample holder, 7 – the detector, 8 – the amplifier, 9 – the self-writer, 10 –the fixing detector, 11 – the klystron, 12 - the isolator, 13 – the attenuator, 14 – the separator, 15 – the field modulator, 16 – the resonator, 17 – the sample, 18 – the wave-fixer [45].

The magnetic moments of electrons exist due to the uncompensated spin or orbital angular momentums or due to their combination. The orbital angular momentum has a tiny influence on the magnetic momentum value. In 99 percent of cases, it is the spin angular momentum that matters the most. The resonance absorption of such systems under the static magnetic field called “paramagnetic resonance”, “electron paramagnetic resonance” or “electron spin resonance”. The term “resonance” means the exact match to the condition of equality in between the energy levels gap and the portion of the electromagnetic energy taken, the similar process of energy absorption and transfers in between the nuclei energy levels called the nuclei paramagnetic resonance. Spin resonance is a more precise term as this method is based on the electron spin moment theory. Even when the orbital momentum taking part in the effect it is the spin part of the Hamiltonian that is used to describe the energy changes and it is the effective spin which is considered which involves both orbital and spin moment’s parts.

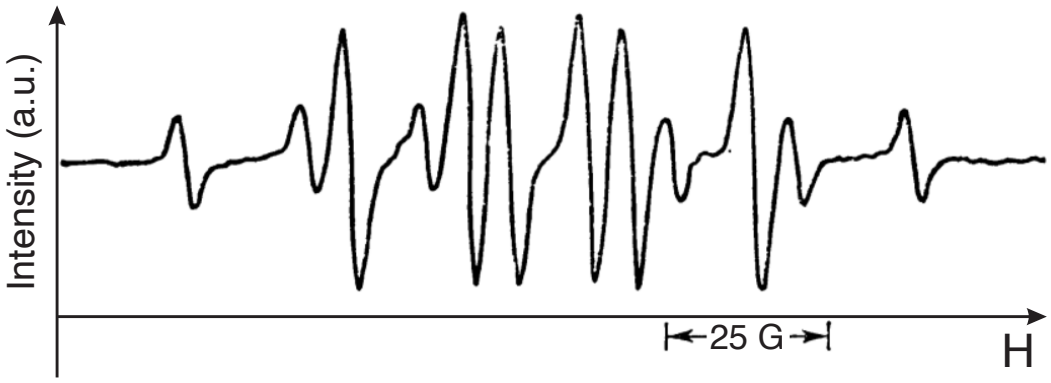

Figure 9 The example of EPR spectrum (the first derivative of absorption) of NH3+ radical ion within the bulk NH4ClO4 monocrystal [45].

The EPR spectrum is like a passport for any material under investigation. It clearly gives the information about all the possible transitions and the energy levels structures. It makes this method widely applicable for the materials characterization as well as very important. The spectrum presented above is the one derived by applying the γ-radiation towards the NH4ClO4 molecule. The number of the lines, their intensities (one to each other as well) and the distances in between them give the certain information to us. The characteristic lines performed on the graph (Fig. 9) [45].

There are some other examples which could give a picture of the possible electron spin paramagnetic resonance images obtained from the experimental data.

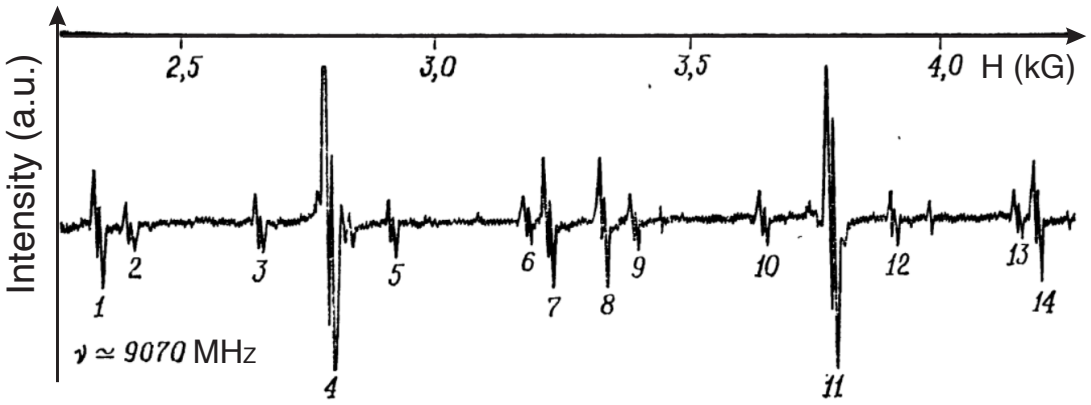

Figure 10 The first derivative of absorption (EPR spectrum) of the XeF molecule within the XeF4 monocrystal [45]

The characteristic spectrum xenon tetrafluoride is shown on the Fig. 10. The number of high peaks is determining the number of atoms within the molecule. There are two of them in that case again – the xenon atom and the fluorine one.

The other good example is the CH3CHOH molecule EPR spectrum for detection of the free radical intermediates in chemical reactions (Fig. 11).

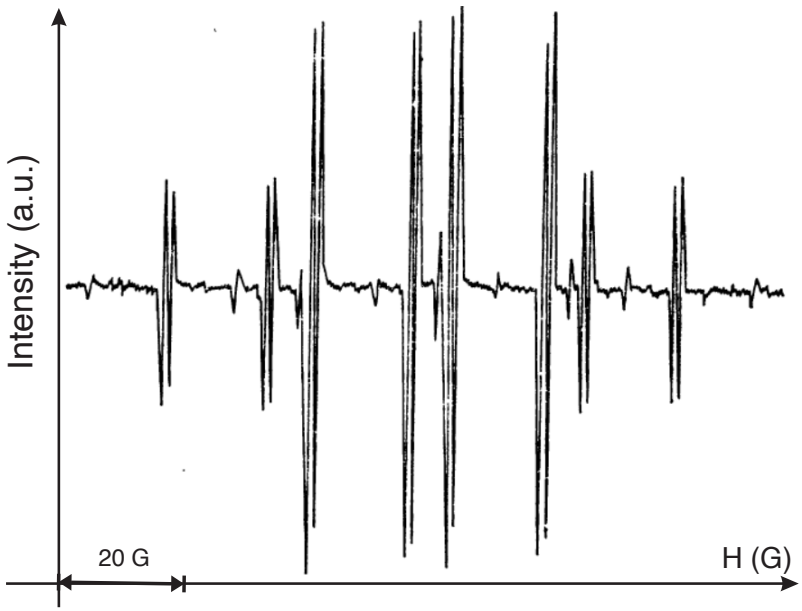

Figure 11 The EPR spectrum of CH3CHOH radical. The horizontal axe is for the H filed and the shown dimension corresponds to 20 G [45].

It is not always easy to analyze the EPR spectrum, but therefore they have attracted many researchers to study a versatile technique to characterize the particle and its surrounding. The EPR spectroscopy method could be applied to the systems with nonzero total spin momentum only. There are quite a few types of the systems which satisfies this condition:

1. Free radicals in a solid, liquid and vaporous states. The free radical represents itself the molecule with unpaired electron.
2. Local defects within the crystalline lattice.
3. Bi radicals. This is the systems which have two unpaired electrons, but these electrons are so far from each other that their interaction is too weak. Such molecules perform like two radicals which have very weak interaction.

4. The systems in a triplet state (two unpaired electrons). Some of such systems are in a ground state, others are in an excited one. They could be passed to the excited one by illuminating the optical signal or by the thermal excitation.
5. Systems with 3 or more unpaired electrons.
6. Ions of rare-earth metals.

In order to analyze the EPR spectrum important to know and to understand the laws of quantum mechanics as well as angle momentum rules. It is better to split the EPR spectrum by several parameters which are obtained when the system considered from the quantum mechanical point of view. It is vital to know the following points:

1. The angular momentum, which is defined by the quantum numbers and related to the magnetic momentum.
2. The main characteristics of EPR spectrometers.
3. Solutions to the Schrodinger equation solutions for simple systems with a few energy levels. The main principles of quantum mechanics like operators and matrix operations are crucial at this point.

The properties of many systems are not a function of the magnetic field orientation. It means that they are isotropic, and they are not sensitive to the changes of the applied field's direction. Of course, there are anisotropic systems as well. 3x3 tensors are used to describe them. For instance, the wire medium metamaterial is very well-known for the permittivity tensor [46]. It is anisotropic:

$$\varepsilon = (\varepsilon_{xx}(\omega, k)\hat{x}\hat{x} + \hat{y}\hat{y} + \hat{z}\hat{z}) \quad (2),$$

The unique properties of this metamaterial go along the X axis as it is clear from the equation above. Basically, it is quite common and typical to describe the anisotropic media in this way. Magnetic permeability and permittivity tensors are used to describe the media with anisotropic or even more complicated properties.

2.3.2 The energy of magnetic dipole placed in a magnetic field.

It is always important to start from something simple. The system of isolated magnetic dipoles in a static magnetic field is exactly what we need. Magnetic dipole moment μ in that case will be described by the following equation:

$$W = -\mu \cdot H = -\mu H \cos(\mu, H) \qquad (3)$$

where W is an energy of magnetic dipole moment μ in the magnetic field H, and θ=(μ, H) is the angle in between the vectors μ and H.

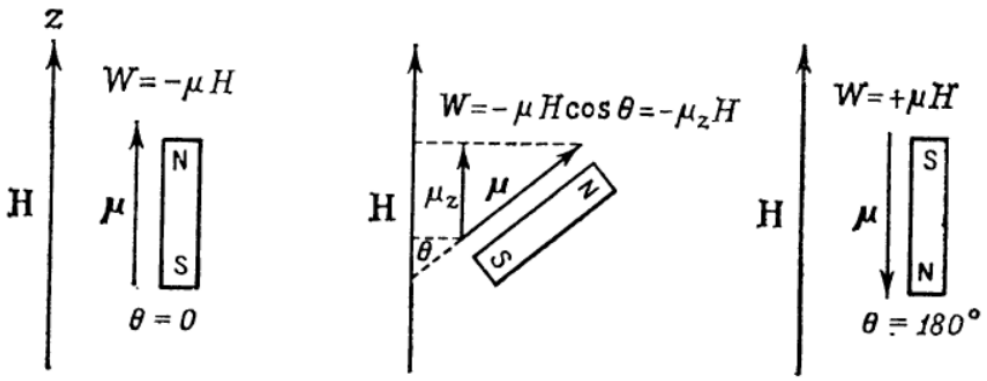

Figure 12 The energy of a classic magnetic dipole in a magnetic field as a function of an angle in between the direction of the field and the dipole axis (θ). The maximum energy corresponds to the angle equal to 180 degree and the minimum to the 0 [45].

When the μ is positive the energy takes the minimal possible value when the angle in between the μ and the H is equal to zero. The maximum of the energy $W_{max} = \mu H$ is reached when the H is defined, and the dipole takes anti-parallel position towards the field (Fig. 12). Almost all the dipoles in a system will be oriented parallel to the field H in the case of the minimum energy. The total magnetic moment M emerges in that case. It's called the magnetization also. The value of the latter is close to the N multiplied by μ where N is the number of dipoles in a volume single cell. The M value is proportional to the applied filed by the coefficient called magnetic susceptibility

$$\chi = \frac{M}{H} = \frac{N\mu^2}{3kT} \qquad (4)$$

The value of magnetic susceptibility is normally defined experimentally from the $N\mu^2$ value. The EPR lets the scientist to obtain the values of μ and N independently. This is very important and interesting point about this method.

2.3.3 Quantization of angular momentum.

The angle in between the μ and the H could take any possible value generally. But the electrons and nuclei follow the quantum mechanics rules. The circle movement of a particle with a mass equal to m [47] is a good analogy which could be considered here for better understanding. The moment of such particle will be determined by equation p=m*v, where v is a speed of a particle. The quantum mechanical particle is determined by the de Broglie wavelength. The de Broglie wavelength is the wavelength, λ, associated with a massive particle and is related to its momentum, p, through the Planck constant, h: λ=h/p.

The idea that the matter behaves like a wave was proposed by Louis de Broglie in 1924. It is also referred to as the de Broglie hypothesis [48]. Matter waves are referred to as de Broglie waves. Wave-like behavior of matter was first experimentally demonstrated by George Paget Thomson's thin metal diffraction experiment [49], and independently in the Davisson–Germer experiment both using electrons, and it has also been confirmed for other elementary particles, neutral atoms and even molecules. Recently, it was also found that investigating the elementary process of diffusion gives the theoretical evidence of the relation of matter wave, regardless of the photon energy [50].

The square of de Broglie wave amplitude at any point on a circle will show the probability to find the particle at this point. The wave function should have one single value in order to make the probability time independent. The wave should not decay due to the interference process when move along the circle. Therefore, it is length should be equal to the integer number M of de Broglie wavelength:

$$2\pi r = M\lambda = M\frac{h}{p} \qquad (5)$$

Therefore

$$pr = p_\varphi = M\frac{h}{2\pi} \quad (6)$$

The value p_φ is the particle's angular momentum and it should be equal the integer number of h/2π and M=0,1,2,3...The p_φ is referred to some axis normally and it's specified like p_{φ_z} regarding the z axis. This is a trivial model that could be applied to describe the angular momentum of electron and nuclei referred to the axis of the molecule consist of two atoms. The orbital where the electrons located is called σ-orbital in a case of M=0. When the M=1 then the orbital is called π-orbital. The unpaired electron is located on π-orbital in most of cases. Obviously, the angular momentum is quantized here, however this model works if the potential energy is constant and the direction of p_φ is not clear.

Obviously, the electron movement is not limited by the plane within the atom. It is better to consider the sphere, therefore. Such a model [51,52] gives an understanding that not only the full moment but also any projection of it to any direction is quantized. The orbital momentum values are determined by the equation $h\sqrt{l(l+1)}$, where l=0,1,2,3... The l is an orbital quantum number which state the orbital name s, p, d, f, ...The projections of this moment to any direction will take the values –l, -l+1, ..., l-1, l. Thus, it has (2l+1) different values of quantum number Ml.

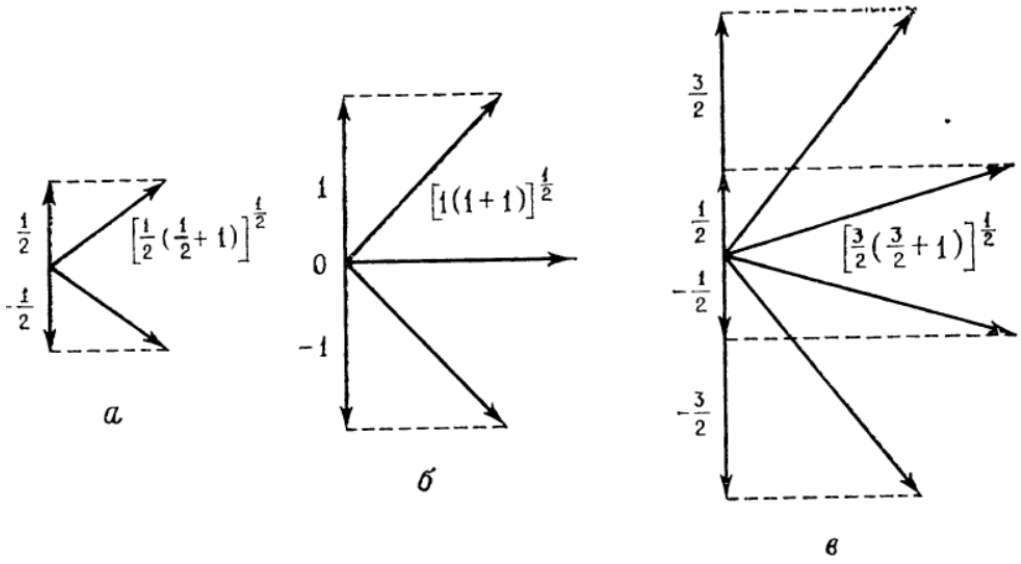

Figure 13 The possible values of a full spin momentum √(S(S+1)) and its projection Ms to the fixed direction for S=1/2, S=1, S=3/2 from left to the right respectively [45].

The spin angular momentum could be considered as a movement of a spin around a specific point smaller than the orbital sphere. Therefore, it takes $h\sqrt{S(S+1)}$ values, where S is a spin quantum number.

The S vector components projected to the specific direction takes the values M_{sh}. M_s could take the values in between the –S and S (the total number is 2S+1 with a step equal to 1). The spin momentums and their projections represented on a Fig. 13. The nuclei spins are quantized as well. They could take integer and semi-integer values.

The spin and the orbital momentums could be considered independently in theory. They interact, and this interaction should be considered when we are talking about the spin value. It is called spin-orbital interaction.

2.3.4 Magnetic angular momentum

The angular moments are proportional to each other, the same as those in classical mechanics. Magnetic dipole moments could be taken into account once we consider the particle with a mass m and the q charge. This particle goes circular with a speed of v over the round trajectory with a radius r. There is a current "i" as the particle has a charge and a correspondent magnetic field of cause. Such a dipole has a component of magnetic moment μ=i*A which is perpendicular to the circle it moves around [45]. $A = \pi r^2$ and the $i = \frac{q}{c} * \frac{v}{2\pi r}$. Thus, one can obtain the value of magnetic moment (with a current divided by c):

$$\mu_z = \frac{qv\pi r^2}{2\pi rc} = \frac{q}{2mc} m_v r = \gamma p_{v_z} = \gamma M_l h \qquad (7)$$

The constant value $\gamma = \frac{q}{2mc}$ called giromagnetic ratio. It transforms the angular momentum to the magnetic one by multiplying by the classical term $\frac{e}{2mc}$ in case of electron. It should be taken in a form of $\gamma = -\frac{ge}{2mc}$ in general case, where "g" is a coefficient that should be there in all the cases except the one where the truly orbital momentum is considered. The magnetic orbital moment $\frac{eh}{4\pi mc}$ corresponds to every value of the orbital moment which is proportional to the even number of h. The sign β

is normally used for this value when the electron is the particle under consideration, and it is called Bohr magneton (it is the magnitude of the magnetic dipole moment of an orbiting electron with an orbital angular momentum of h. According to the Bohr model, this is the ground state, i.e., the state of lowest possible energy.) and the exact value is 9.2741×10^{-21}erg·G^{-1}(CGS) and 9.2741×10^{-24}J·T^{-1}(SI). Although the spin angular momentum of an electron is 1/2h, the intrinsic magnetic moment of the electron caused by its spin is still approximately one Bohr magneton. The electron spin g-factor is approximately two (g_e=2.00232 for free electron). The component of the electron spin magnetic moment μ_z along the magnetic field H direction is:

$$\mu_z = \gamma M_s h = -g\beta M_s \tag{8}$$

The negative sign emerges here due to the negative charge of the electron.

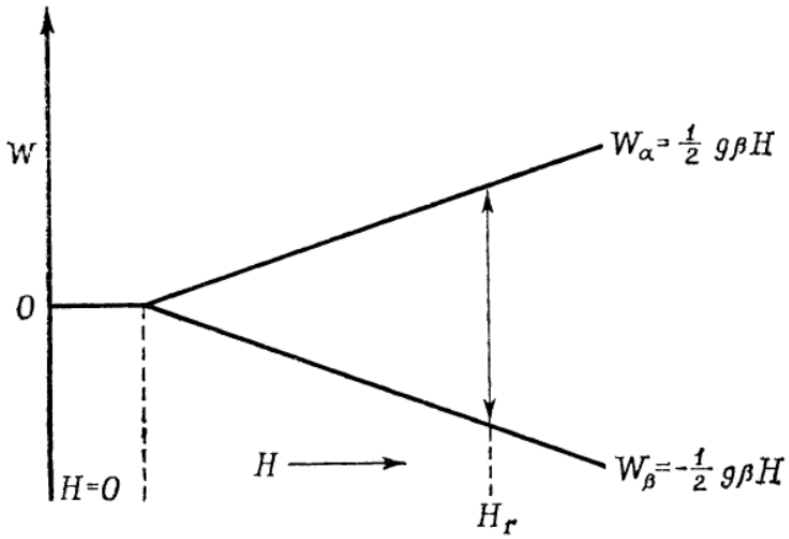

Figure 14 The energy levels of a simplest system where the EPR absorption could be observed. W_α and W_β are the energy values for the M_S=+1/2 and M_S =-1/2 respectively.

Quantization of the spin moments along the certain direction in space leads to the energy levels quantization of the magnetics moments system within the magnetic field. The equation $W = -\mu_z H$ leads to the "purely spin" system and the (8) is giving the following resulting expression for the energy levels:

$$W = g\beta H M_s \tag{9}$$

M_s may take the +1/2 and -1/2 values only. Therefore, energy W takes two values as well $W = \pm 1/2\, g\beta H$. These two energy levels we have already mentioned

previously. They called the Zeeman levels. And the gap in between them $g\beta H$ is proportional to the magnetic field as it shown here again but with direction of the filed applied.

2.3.5 The magnetic dipole in electromagnetic field. (Part 1).

The flips in between the Zeeman's levels could be induced by the electro-magnetic field at the certain frequency. The energy "distance" ΔW in between those levels should be equal to the photon energy hν. Therefore,

$$\Delta W = h\nu = g\beta H_r \qquad (10),$$

where ν is the frequency (Hz) and the H_r is the magnetic field value corresponding to the condition (10) being satisfied. It is assumed to be so that M_s from the equation (9) is increased by the value of 1 when the flip electron transition happens, or $\Delta M_s=1$ in other words. Thus, the transitions up and down correspond to the values $\Delta M_s=+1$ and $\Delta M_s=-1$ respectively.

The true proportion of the resonance frequency and the value of the field applied works for the frequencies from 10^{th} of G to 10^{th} of kG. The resonance field is equal to 10.7 G at the 10 MHz frequency as g=2.0032 for the case when the free electron is considered. At ν=30 GHz (1 GHz is equal to 10^9 Hz) the resonance field will be 10700 G. Most of the free radicals and ions of metals have g≈2. There are systems where this value is different of course.

The first experiment took place in 1944 when Russian physicist Zavoyskiy [53] had discovered the maximum of paramagnetic absorption of the $CuCl_2*2H_2O$ molecule. The resonance field value was equal to 47.6 Gs at frequency of 133 MHz and g≈2.

It will be quite useful to obtain the (10) equation for the system which the spin is S=1/2 through the operator's technique. It is a good point to talk about them here a bit.

2.3.6 Quantum mechanics of the angular momentum

2.3.6.1 Introduction

The properties that remain unchanged within the isolated system (like the full energy and angular momentum) called "constants of the movement". Those values and their properties are quite important in quantum mechanics. This is a moment when it's time to talk about Hamiltonian from the operator's point of view. Hamiltonian is the full energy operator H. Therefore, it brings the eigenfunction $\psi_n(x,y,z)$ to the expression:

$$H\psi_n(x,y,z) = W_n\psi_n(x,y,z) \qquad (11)$$

Where W_n is an energy value of the system's n-state and the (11) is Schrodinger equation. The exact values of W_n are called the eigen values. Let's consider λ_n as another movement constant with an operator A corresponding to that. The fundamental result of quantum mechanics is that eigen functions $\boldsymbol{\psi}_n(x,y,z)$ of H operator could be taken so that they would be the eigen functions for the A operator as well. The angular momentum is a movement constant of an isolated system. Thus, the total momentum operator (or the moment of the square of the total momentum) applied to the chosen functions $\boldsymbol{\psi}_n(x,y,z)$ in a certain manner is giving the certain values. Let's name this operator as J^2 and

$$J^2\psi_n(x,y,z) = \lambda_j\psi_n(x,y,z) \qquad (12),$$

where λ_j is an eigen value of J^2, which could be taken in accordance with $\left(\frac{h}{2\pi}\right)^2 = \hbar^2$. The function $\boldsymbol{\psi}_n(x,y,z)$ could be the eigen one for any of J components, e.g., J_x, J_y or J_z with the coordinate system taken in a right way. Therefore, this function will be the eigen function both for J^2 and H. At the same time $\boldsymbol{\psi}_n(x,y,z)$ could not be the eigen function for two or more components of J^2 at the same time. If $\boldsymbol{\psi}_n(x,y,z)$ will be the eigen function for the group of operators each of those corresponds to the certain moving constant then all these operators must be commuting. For instance, if $\boldsymbol{\psi}_n(x,y,z)$ is the eigen function for H, J^2 and J_z the following expressions taking the place:

$$(HJ^2 - J^2H)\psi_n(x,y,z) = 0$$

$$(HJ_z - J_zH)\psi_n(x,y,z) = 0$$

$$(J^2J_z - J_zJ^2)\psi_n(x,y,z) = 0 \qquad (13),$$

λ_j is an eigen value of J2 and has one very important property – its value is a function of the $\boldsymbol{\psi}_n$ symmetry only. Thus, λ_j will be the same for all wave functions with the same symmetry, whereas W_n is changing depending on the certain wave function. E.g., $\lambda_j = 0$ for all spherically symmetrical wave functions, Thus, if we have managed to solve the equation (12) then the eigen functions we have found could be applied to all the wave functions with the same kind of symmetry.

The $\boldsymbol{\psi}_n(x,y,z)$ was considered as three-dimensional wave function. It was shown that λ_j is a function of the j quantum number, which takes integer values only. For example, j could be the quantum number of the electron orbital momentum l or the rotational quantum number for the J molecule. The electrons and nuclei possess their own mechanical moment at the same time which called the spin moment. The latter could not be described by the spatial wave functions $\boldsymbol{\psi}_n(x,y,z)$. We must include the specific "spin coordinate" into the wave function. It was shown that the quantum number j could take semi-integer values (like 0, ½, 1, 1.5, ...). This spin moment doesn't have the classical analogy. It was described through the angular momentum term within the quantum mechanics.

2.3.6.2 Angular momentum operators

It is important to consider the classical expressions for angular momentum p_φ for the particle that moves from zero point in order to get the quantum mechanical operators of the same value:

$$p_\varphi = r \times p \qquad (14),$$

where vector r is specifying the particle exact location, and p is an impulse vector (the movement value). There is a vector multiplication in (14). Thus, it could be represented as the vector components in another way:

$$p_{\varphi x} = yp_z - zp_y$$

$$p_{\varphi y} = zp_x - xp_z$$

$$p_{\varphi z} = xp_y - yp_x \quad (15)$$

The r operator is equal to the simple r value in quantum mechanics. But p should be changed by $-i\hbar\boldsymbol{\nabla}$, where $\boldsymbol{\nabla} = \boldsymbol{i}\,\boldsymbol{\partial}/\boldsymbol{\partial x} + \boldsymbol{j}\,\boldsymbol{\partial}/\boldsymbol{\partial y} + \boldsymbol{k}\,\boldsymbol{\partial}/\boldsymbol{\partial z}$. Therefore, the components of vector p_φ looks like:

$$p_{\varphi x} = -i\hbar(y\,\boldsymbol{\partial}/\boldsymbol{\partial z} - z\,\boldsymbol{\partial}/\boldsymbol{\partial y})$$

$$p_{\varphi y} = -i\hbar(z\,\boldsymbol{\partial}/\boldsymbol{\partial x} - x\,\boldsymbol{\partial}/\boldsymbol{\partial z})$$

$$p_{\varphi z} = -i\hbar(x\,\boldsymbol{\partial}/\boldsymbol{\partial y} - y\,\boldsymbol{\partial}/\boldsymbol{\partial x}) \quad (16)$$

It is simpler to consider the angular momentum operator through the other one – J. The latter if proportional to ħ value, or in other words $p_\varphi = J\hbar$. It let us to update the (16) to the other form:

$$J_x = -i(y\,\boldsymbol{\partial}/\boldsymbol{\partial z} - z\,\boldsymbol{\partial}/\boldsymbol{\partial y})$$

$$J_y = -i(z\,\boldsymbol{\partial}/\boldsymbol{\partial x} - x\,\boldsymbol{\partial}/\boldsymbol{\partial z})$$

$$J_z = -i(x\,\boldsymbol{\partial}/\boldsymbol{\partial y} - y\,\boldsymbol{\partial}/\boldsymbol{\partial x}) \quad (17)$$

The quarter of the vector operator is equal to the sum of components quarters same as in classical mechanics. Thus, we have:

$$J^2 = J_x^2 + J_y^2 + J_z^2 \quad (18)$$

The exact value and the direction of the angular momentum could be found in classical mechanics. We could find the total momentum value and only one of its components in quantum mechanics. Two values could be found at the same time if only their operators commutate (as it stated in the previous subchapter).

We will see that J^2 commutates with J_z. But the latter doesn't commutate with J_x and J_y.

2.3.6.3 Commutative expressions for angular momentum operators

Let's prove the statement at the end of the previous chapter. In other words, we need to know if J^2 commutates with J_z, J_y, J_x. Mathematically it means that:

$$[J^2, J_x] = [J^2, J_y] = [J^2, J_z] = 0 \qquad (19)$$

Here $[J^2, J_x] = [J^2 J_x - J_x J^2]$, etc. But the operators of any two components do not commutate. For instance:

$$J_x J_y = -(y\,\boldsymbol{\partial/\partial z} - z\,\boldsymbol{\partial/\partial y})(x\,\boldsymbol{\partial/\partial z} - z\,\boldsymbol{\partial/\partial x}) =$$

$$= -[y\,\boldsymbol{\partial/\partial z} + yz\,\boldsymbol{\partial^2/\partial z \partial x} - xy\,\boldsymbol{\partial^2/\partial z^2} - z^2\,\boldsymbol{\partial^2/\partial y \partial x} + xz\,\boldsymbol{\partial^2/\partial z \partial y}] \qquad (20)$$

$$J_y J_x = -(z\,\boldsymbol{\partial/\partial x} - x\,\boldsymbol{\partial/\partial z})(y\,\boldsymbol{\partial/\partial z} - z\,\boldsymbol{\partial/\partial y}) =$$

$$= -[x\,\boldsymbol{\partial/\partial y} + yz\,\boldsymbol{\partial^2/\partial z \partial x} - xy\,\boldsymbol{\partial^2/\partial z^2} - z^2\,\boldsymbol{\partial^2/\partial y \partial x} + xz\,\boldsymbol{\partial^2/\partial z \partial y}] \qquad (21)$$

$$[J_x, J_y] = J_x J_y - J_y J_x = (x\,\boldsymbol{\partial/\partial y} - y\,\boldsymbol{\partial/\partial x}) = iJ_z \qquad (22).$$

The same expressions are valid for the other components of the vector. Thus, we could not get all three or even two components of angular momentum at the same time. But we may get the square if J and one of its components. J_z for instance. Here are the commutative expressions for all components:

$$[J_x, J_y] = iJ_z$$

$$[J_y, J_z] = iJ_x$$

$$[J_z, J_x] = iJ_y \qquad (23),$$

And really, as it is stated in (19)

$$[J^2, J_x] = [J^2, J_y] = [J^2, J_z] = 0$$

The total angular momentum which includes the spin value is determined like any value that satisfies the commutative relations (18) and (22). It useful to replace:

$$J_+ = J_x + iJ_y$$

$$J_- = J_x - iJ_y \quad (24)$$

for further expressions simplification. The "+" operator called the increasing one and the "-" one – decreasing respectively. Therefore, we have:

$$[J^2, J_+] = [J^2, J_-] = 0,$$

$$[J^2, J_-] = -J_-, [J^2, J_+] = J_+ \text{ and}$$

$$[J_+, J_-] = 2J_z \quad (25)$$

2.3.6.4 Eigen values of J^2 and J_z

Let's consider the eigen values of J^2 and J_z as λ_j and λ_m respectively. The eigen values of the angular momentum depend on the j and m quantum numbers only. J characterize the total momentum and m- it's z component only. Thus, the eigen values will be the functions of only j and m while we consider the properties which determined by the angular momentum.

In terms of quantum mechanics, the wave functions could be presented as |j,m>, as properties of those functions are in dependence from j and m only. Thus, the following expressions could be written for the eigen values if J^2 and J_z:

$$J^2|j,m\rangle = \lambda_j|j,m\rangle \quad (26)$$

$$J_z|j,m\rangle = \lambda_m|j,m\rangle \quad (27),$$

where λ_m and λ_j are the eigen values of J_z and J^2 accordingly. It is needed to point out that functions $|j,m\rangle$ are orthonormal, i.e.

$$\langle j', m'|j,m\rangle = 1, when\ j' = j\ and\ m' = m,$$

$$\langle j', m'|j,m\rangle = 0, when\ j' \neq j\ and\ m' \neq m. \quad (28)$$

J^2 operator could be presented in the form of $J^2 = J_x^2 + J_y^2 + J_z^2$ as we remember from (17). Therefore, $J_x^2 + J_y^2$ has its own eigen values of a discreet type:

$$(J_x^2 + J_y^2)|j,m\rangle = \left(J^2 - J_y^2\right)|j,m\rangle = (\lambda_j - \lambda_m^2)|j,m\rangle \quad (29)$$

When operators J_x^2 and J_y^2 act on the |j,m> they are corresponded to the observed values (which means they are Hermitian), their action should resolve into to the real values. Thus, the eigen values of $(J_x^2 + J_y^2)$ should be real and positive, i.e.

$$\lambda_j - \lambda_m^2 \geq 0 \quad (30).$$

It is good to look at the commutator's $[J_z, J_+] = J_+$ matrix element from the equation (25) in order to get the exact form λ_m eigen values:

$$\langle j, m' \mid J_z J_+ - J_+ J_z | j,m\rangle = \langle j, m' \mid J_+ | j,m\rangle \quad (31)$$

The left part of the equation above shows the way operator J_+ act on the wave functions |j,m>. The matrix element of the left part could be substituted by two as follows:

$$\langle j, m' \mid J_z J_+ | j,m\rangle - \langle j, m' \mid J_+ J_z | j,m\rangle. \quad (32)$$

The second one could be updated by using the (27)

$$\langle j, m' \mid J_+ J_z | j,m\rangle = \lambda_m \langle j, m' \mid J_+ | j,m\rangle \quad (33)$$

The first one could be substituted following the Dirac formulas which were proposed long time ago [54].

In a few words, the wave function ψ_n is substituted by the $|n\rangle$, where n is a symbol which provides function identity. This is a quantum number in most of a case. The $|n\rangle$ called the "ket" function. The simple equation determining the eigen function itself

$$\Lambda\psi_n = \lambda_n \psi_n \quad (34),$$

where λ_n is a constant value, could be rewritten by using "ket" terminology in the following form:

$$\Lambda|n\rangle = \lambda_n |n\rangle \quad (35).$$

It is obvious that λ_n is in dependence from n. Therefore, the $|n\rangle$ function could be described by the quantum number n. The spin functions corresponding to the M_s=+1/2 and M_s=-1/2 are taken as $|\alpha\rangle$ and $|\beta\rangle$. Each "ket" function has a corresponding "bra"

function taken as $\langle n|$. The "bra" function is only valuable with "ket" one. The expression $\langle n|m\rangle$ means the integration over the whole area of the variables where they change:

$$\langle n|m\rangle = \int_{\tau} \psi_m^* \psi_n \, d\tau \qquad (36).$$

The wave functions called orthogonal in case of m≠n and $\langle n|m\rangle = 0$. In the other case, when $\langle n|m\rangle = 1$ and m=n, the wave functions are called normalised. It is common and very useful to take the wave functions of the angular momentum in the way when they are both orthogonal and normalised, or orthonormalized. It is quite common in quantum mechanics to have the matrix element in a form of $\int \psi_n^* B \psi_m \, d\tau$ which could be simplified following the "bra-ket" terminology:

$$\int \psi_n^* B \psi_m \, d\tau = \langle n|B|m\rangle \qquad (37).$$

The $\langle n|B|m\rangle$ expression is called "the matrix element". It is the diagonal matrix element when m=n, and its non-diagonal matrix element when the m≠n. The average (highly anticipated) value $\langle b\rangle$ of any observed value b described by the orthonormalized wave function ψ_n is determined by the following expression:

$$\langle b\rangle = \int \psi_n^* B \psi_n \, d\tau = \langle n|B|n\rangle \qquad (38),$$

where B is an operator corresponding to the observed value b.

The functions "bra" and "ket" has a very important property:

$$\langle n|m\rangle = [\langle m|n\rangle]^* \qquad (39).$$

It is normally so that matrix operator B within the matrix element $\langle n|B|m\rangle$ is acting "from the right side" on the "ket" function $|m\rangle$. We need to take the element of the adjugated matrix in accordance with (39) in order to act on "bra" function "from the left":

$$\xrightarrow{\langle n|B|m\rangle} = \left[\xleftarrow{\langle n|B|m\rangle}\right]^t = \left[\xrightarrow{\langle m|B|n\rangle}\right]^* = \chi_n^* [\langle m|n'\rangle]^* = \chi_n^* \langle n'|m\rangle \qquad (40).$$

χ_n^* here could be a complex value. If B is non-Hermitian (uplift and downshift operators for instance) then the action of this operator is equal to the change of the wavefunction ($|n\rangle$ -> $|n'\rangle$), and the multiplication with the constant value χ_n. In

another case, when B operator corresponds to any observed value and is Hermitian, therefore. Thus, χ_n should be the real value and n=n'. Thus, it doesn't matter if B acts from the right or from the left.

Thus, going back to our matrix element the first one will take a form of

$$\langle j,m' \mid J_z J_+ | j,m\rangle = \lambda^*_{m'} \langle j,m' \mid J_+ | j,m\rangle \quad (41)$$

The J_z is Hermitian operator. This is the reason why the λ_m values must be real, and the following condition must be satisfied as well $\lambda^*_{m'} = \lambda_{m'}$. Therefore, the (31) equation is taking the form of

$$(\lambda_{m'} - \lambda_m)\langle j,m' \mid J_+ | j,m\rangle = \langle j,m' \mid J_+ | j,m\rangle \quad (42)$$

This equation has one consequence that comes straight forward. The (42) means that nonzero matrix elements of J_+ will be those which left brackets part will satisfy the condition $\lambda_{m'} - \lambda_m = 1$. Therefore,

$$J_+ | j,m\rangle = \chi_m | j, m+1\rangle \quad (43).$$

This result is based on obvious reason. When $\lambda_{m'} - \lambda_m \neq 1$, the (42) equation is true if only $\langle j,m' \mid J_+ | j,m\rangle = 0$. The same logic is used to consider the matrix elements of J_-. It shows that nonzero elements of J_- will be only those which satisfies $\lambda_{m'} - \lambda_m = 1$. In other words

$$J_- | j,m\rangle = y_m | j, m-1\rangle \quad (44).$$

y_m and χ_m from equations (43) and (44) could be the complex values. Therefore, they could be presented in the form which includes $e^{i\varphi}$, where ϕ is a phase angle. The (43) and (44) equations show clearly why J_- and J_+ called the step down and the step-up operators respectively.

Analysis shows that for current λ_j value we could get the set of $|j,m\rangle$ states with eigen values

$$\ldots \lambda_{m-2}, \lambda_{m-1}, \lambda_m, \lambda_{m+1}, \lambda_{m+2} \ldots$$

This set must have a limit on the right side and on the left side as well, because $\lambda_m^2 \leq \lambda_j$ in accordance with (30) equation. The values of λ_m have an integer

difference, and for the m quantum number for the current j value it increases by exactly the same value. Thus, we could take m and λ_m to be equal.

Let's take the lowest eigen state of J_z as $\underline{m}$, and the top one as $\overline{m}$. In that case the following two expressions taking the place

$$J_+|j,\overline{m}\rangle = 0 \tag{45}$$

$$J_-|j,\underline{m}\rangle = 0 \tag{46}$$

There will be $\overline{m}$ value bigger than $\lambda_j^{1/2}$, and $\underline{m}$ value smaller than $-\lambda_j^{1/2}$. These two conditions together could not satisfy (30) condition. Thus the (45) and (46) are correct.

Let's take J_- operator and apply it to the function (45). The J_+J_- will be equal to

$$J_+J_- = (J_x - iJ_y)(J_x + iJ_y) = J_x^2 + J_y^2 + i[J_x, J_y] = J^2 - J_z^2 - J_z \tag{47}$$

Thus, by applying this expression to (45):

$$J_-J_+|j,\overline{m}\rangle = (\lambda_j - \overline{m}^2 - \overline{m})|j,\overline{m}\rangle = 0 \tag{48}$$

$$\lambda_j = \overline{m}(\overline{m}+1) \tag{49}$$

By acting in the same way on (45) by J_+ operator we will get the pretty close expression for the lowest eigen state

$$\lambda_j = \underline{m}(\underline{m}-1) \tag{50}$$

(50) and (49) could be taken together only when $\overline{m} = -\underline{m}$.

The values m takes has a gap equal to 1. Thus $(\overline{m} - \underline{m})$ should be a positive number, which could be equal to 2j. Therefore, j could take one of the following values:

$$j = 0, \frac{1}{2}, 1, \frac{3}{2}, \ldots$$

Going further, we take $\overline{m} - \underline{m} = 2j$ and $\overline{m} = -\underline{m}$. Thus, we get the exact expressions for both of m states:

$$\overline{m} = j \; and \; \underline{m} = -j \tag{51}$$

Therefore, m=j, j-1, …, -j+1, -j and there is 2j+1 of m values for each j value. (48) and (49) are giving us one more expression:

$$\lambda_j = \overline{m}(\overline{m} + 1) = j(J + 1) \tag{52}$$

Finally, the eigen values of J_z and J^2 will be

$$J^2|j,m\rangle = j(j + 1)|j,m\rangle \tag{53}$$

and

$$J_z|j,m\rangle = m|j,m\rangle^* \tag{54}$$

Now we could go back to the magnetic field influence on the magnetic dipole.

2.3.7 The magnetic dipole in electromagnetic field. Part 2.

We could always write down the eigen values equation for the systems which has discrete energy level value described by the certain values of quantum numbers. For the $\lambda_i$as an eigen value of the state and the $\psi_i$as a wave (eigen) function of the same state such an equation will look like

$$\hat{\Lambda}\psi_i = \lambda_i\psi_i \tag{55}$$

Here we use operator $\hat{\Lambda}$ as the one which corresponds to the property of the system we are investigating. The most interesting thing will be the quantization of the spin angular momentum. Therefore, we need to find the spin operator which acts on the function describing the spin state. This operator should act in a manner which equal to the integer number being multiplied by the function. This number should be characteristic for this state. For the systems with S=1/2 two states are characterized by the quantum numbers M_s=±1/2. The latter are characteristic for the components of the

angular momentum $M_s\hbar$ along the direction of the magnetic field applied. Let's take this direction as z and the angular momentum operator as $\widehat{S_\hbar}$. In that case

$$\widehat{S_z}\psi_i = M_s\psi_i \quad (56)$$

Or we could consider this expression in another way using the exact values for quantum number of M_s:

$$\widehat{S_z}\psi(M_s = 1/2) = 1/2\,\psi(M_s = 1/2)$$

and

$$\widehat{S_z}\psi(M_s = -1/2) = -1/2\,\psi(M_s = -1/2) \quad (57)$$

The way we put the eigen functions here could be simplified. The functions have a difference in quantum numbers only so we could include the latter to the function syntax. Paul Dirac proposed to use $|n\rangle$ as we saw above ("ket"-function). It allows us to rewrite the equations (57) in the following way:

$$\widehat{S_z}|1/2\rangle = 1/2\,|1/2\rangle$$

and

$$\widehat{S_z}|-1/2\rangle = -1/2\,|-1/2\rangle \quad (58)$$

The states $M_s = -1/2$ and $M_s = +1/2$ are substituted by the β and α respectively sometimes. In that case the wave functions will look like:

$$|+1/2\rangle = |\alpha\rangle = \psi_\alpha$$

$$|-1/2\rangle = |\beta\rangle = \psi_\beta \quad (59).$$

Now we could move to the energy value. This value could be taken from the following equation for the systems which M_s is the exact value of the spin angular momentum:

$$\widehat{H}\psi_i = W_i\psi_i \quad (60),$$

where H is the energy operator called spin-Hamiltonian. (56) and (60) are very important because the same function ψ_i is the eigen function of the z component of spin angular momentum and the energy. Therefore,

$$\widehat{H}|\alpha\rangle = W_\alpha|\alpha\rangle$$

$$\widehat{H}|\beta\rangle = W_\beta|\beta\rangle \quad (61)$$

The energy is determined by the expression $W = -\mu H = -\mu_z H$. We need one more equation for magnetic momentum and spin angular momentum. We already know from (8) that $\mu_z = -\gamma M_s \hbar$. Therefore, we could expect that magnetic momentum operator $\widehat{\mu_z}$ will be proportional to the spin operator $\widehat{S_z}$. Thus, we see that

$$\widehat{\mu_z} = -\gamma \widehat{S_z} \hbar = -g\beta \widehat{S_z} \quad (62).$$

Thus, (3) and (62) taken together are providing the expression for spin-Hamiltonian as the system in the following form:

$$\widehat{H} = g\beta H \widehat{S_z} \quad (63)$$

Going further to the up and down states we see the further update.

$$\widehat{H}|\alpha\rangle = g\beta H \widehat{S_z}|\alpha\rangle = \frac{g\beta H}{2}|\alpha\rangle \quad (64)$$

and the down state has the same expression as well, obviously

$$\widehat{H}|\beta\rangle = -\frac{g\beta H}{2}|\beta\rangle \quad (65)$$

The last two expressions clearly show the expressions for the energy of up and down states:

$$W_\alpha = \frac{g\beta H}{2} \quad (66)$$

and

$$W_\beta = -\frac{g\beta H}{2} \quad (67)$$

Obviously, we can see that in order to flip in between the $|\alpha\rangle$ and $|\beta\rangle$ the electron must have the energy $\Delta W = W_\alpha - W_\beta = g\beta H_r = h\nu$ as it was already shown in (10). There is a wider case for the energy from (66) and (67). In that case both sides of the (60) are multiplied by ψ_i^*

$$\psi_i^* \widehat{H} \psi_i = \psi_i^* W_i \psi_i = W_i \psi_i^* \psi_i \quad (68)$$

We can move the W_i as it is a constant value. Then it goes further to the integral form. Both sides are multiplied by $d\tau$, where τ is one or a few variables to which the integral is taken. The integration over the whole τ area taken from both sides of the equation above gives us the following:

$$\int_\tau \ \psi_i^* \hat{H} \psi_i \, d\tau = W_i \int_\tau \ \psi_i^* \psi_i \, d\tau \tag{69}$$

One could easily find the expression for the energy

$$W_i = \frac{\int_\tau \ \psi_i^* \hat{H} \psi_i \, d\tau}{\int_\tau \ \psi_i^* \psi_i d\tau} \tag{70}$$

If the functions ψ_i are normalized, their integration is following their main property and could be substituted

$$\int_\tau \ \psi_i^* \psi_i \, d\tau = 1 \tag{71}$$

Therefore, the (70) could be updated

$$W_i = \int_\tau \ \psi_i^* \hat{H} \psi_i \, d\tau \tag{72}$$

The last few equations could be rewritten with Paul Dirac technique of "bra-ket" we've mentioned and used above. The symbol for the case when we are multiplying the current expression from the left side by the ψ_i^* is equal to the "bra" kind of a function in term of Dirac syntaxy's $\langle \psi_i^* |$. When "bra" $\langle \psi_i^* |$ goes together with "ket" $|\psi_i^* \rangle$ it means that the integration will be taken over the whole range of possible values of the variable. Thus, $\langle \psi_i^* | \psi_i^* \rangle$ is going together as "bra[c]ket" as we've mentioned above, and it is used to most of quantum mechanical expressions. The (42) looks different now in "bracket" terminology and takes the form of:

$$\langle \psi_i^* | \ \hat{H} | \psi_i^* \rangle = W_i \langle \psi_i^* | \psi_i^* \rangle \tag{73}$$

The functions ψ_i^* could be the normalized one of cause, therefore

$\langle \psi_i^* | \psi_i^* \rangle \ = 1,$

and

$$W_i = \langle \psi_i^* | \, \hat{H} | \psi_i^* \rangle \tag{74}$$

Going back to our simple case we consider two states $|\alpha\rangle$ and $|\beta\rangle$ only the (74) will take a form of:

$$W_\alpha = \langle \alpha | \, \hat{H} | \alpha \rangle = \frac{1}{2} g\beta H \tag{75}$$

and

$$W_\beta = \langle \beta | \, \hat{H} | \beta \rangle = -\frac{1}{2} g\beta H \tag{76}$$

This is important from the theoretical point of view to have the same equation obtained by the different approaches, The equations (75) and (76) are proving this here and the whole derivation is helping to understand the theory in a better way. Here it is important to say a few words about the general case when the particle is going circular and determined via the angular momentum operator as well as via energy operator.

We may say a few words about the general operator's properties. The $\hat{A}$ operator is generally the sign of those predefined mathematical actions which will be taken under the function to which operator is applied and which is written under this sign. The simplest operator is the one which is equal to the integer number multiplication:

$$\hat{k}\alpha = k\alpha$$

The operator $\hat{\Omega}$ is called linear one if this action on the sum of the function is equal to the sum of this operator applied to each of the functions. Therefore, if we know that

$$\hat{\Omega}\alpha = \beta \, ,$$

Then we may say that

$$\hat{\Omega}(\alpha_1 + \alpha_2) = \hat{\Omega}\alpha_1 + \hat{\Omega}\alpha_2 = \beta_1 + \beta_2 \tag{77}$$

At the same time, it is obvious that if we have c as a constant value within the function under operator, we could say that

$$\hat{\Omega}(c\alpha) = c\hat{\Omega}\alpha \ = c\beta \tag{78}$$

If $\alpha_i = f(q_1)$, then $\partial/\partial\, q_1$ is a linear operator. On the other hand, the $\sqrt{q}_1$ will be non-linear one. There are some operators very well-known. For instance, the one which means the sum of all the variables under him:

$$\sum_{i=1}^{n} \alpha_i = \ \alpha_1 + \alpha_2 + \alpha_3 + \cdots + \alpha_n \tag{79}$$

This operator is very useful for series formulas. The huge sums of variables and constant values multiplied

$$\psi_1 = c_{11}\phi_1 + c_{12}\phi_2 + c_{13}\phi_3 + \cdots + c_{1n}\phi_n$$

$$\psi_2 = c_{21}\phi_1 + c_{22}\phi_2 + c_{23}\phi_3 + \cdots + c_{2n}\phi_n$$

$$\psi_3 = c_{31}\phi_1 + c_{32}\phi_2 + c_{33}\phi_3 + \cdots + c_{3n}\phi_n \tag{80}.$$

The double sum operator applied could significantly simplify the formula above into the very short and very informative expression

$$\sum_j \psi_j = \sum_j \sum_h c_{jh}\phi_h \tag{81}$$

The (81) is an example of two operators applied together. In general, it will look like $\hat{A}\hat{B}$. It is assumed to be so that we take $\hat{B}$ at first and then we act by the $\hat{A}$ operator on the result. The order is crucial. Sometimes it may dramatically change the result. Let's consider the linear operator we've already mentioned above:

$$\hat{x}\frac{\widehat{d}}{dx}(x^2) = 2x^2$$

and

$$\frac{\widehat{d}}{dx}\hat{x}(x^2) = 3x^2.$$

If $\hat{A}\hat{B} = \hat{B}\hat{A}$, then $\hat{A}$ and $\hat{B}$ called commutative operators and the expression $\hat{A}\hat{B} - \hat{B}\hat{A}$ called the commutator of $\hat{A}$ and $\hat{B}$ and it has a special expression for it $\left[\hat{A}, \hat{B}\right] = \left(\hat{A}\hat{B} - \hat{B}\hat{A}\right)$. The commutator is a very important term in quantum

mechanics, and it possess very deep physical meaning for angular momentum, for instance.

The $\hat{\Omega}$ operator called Hermitian if it satisfies the following equation:

$$\int \psi_j^* \hat{\Omega} \psi_i \, d\tau = \int \hat{\Omega}(\psi_j^*) \, \psi_i \, d\tau \qquad (82)$$

If the Hermitian operator stands in between two functions as it is in (82), then we could carefully take it to act from the left side ("back" action). Important property of Hermitian operators is the one that stands for the point that if the result of operator action to the function is this function itself multiplied by the constant value, then this value is the real one. Some of the valuable quantum mechanical operators are related to the observable properties of the physical system, more precisely with their dynamic variables. There are a few important linear operators described in the following table. Some of those operators are equal to the variables, some has differentials within (Table 1.). The eigen functions and eigen values need to be described in general here as well to make everything clear. If the result of operator $\hat{\Lambda}$ action on the function ψ_n is equal to the following expression we've seen before.

$$\hat{\Lambda} \, \psi_n = \lambda_n \psi_n \qquad (83),$$

where λ_n is a constant value, then ψ_n called the eigen function of $\hat{\Lambda}$ operator with the eigen value equal to λ_n(if there are several ψ_n functions they called "the basis set"). In particular, spin-functions ψ_α and ψ_β, proposed above, are the proper example of the eigen functions. They are the eigen functions of the $\widehat{S_z}$ operator

$$\widehat{S_z}\psi_\alpha = +\frac{1}{2}\psi_\alpha \qquad (84)$$

$$\widehat{S_z}\psi_\beta = -\frac{1}{2}\psi_\beta \qquad (85)$$

Functions ψ_n from the set of some functions could be the eigen functions for several operators at the same time. On the other hand, operators with equal set of eigen functions have one very important property which has so many applications – they commutate.

Dynamic variables	Classical value	Quantum mechanical operator//
Coordinate	Q	Q
Time	T	T
Impulse	$p_q = m\frac{dq}{dt}$	$\widehat{p_q} = -i\hbar\frac{d}{dq}$
Angular momentum	$p_\varphi = r \times p$ $p_{\varphi_z} = (xp_y - yp_x)$	$\widehat{p_\varphi} = r \times \hat{p}$ $\widehat{p_{\varphi_z}} = -i\hbar\left(x\frac{d}{dy} - y\frac{d}{dx}\right) = -i\hbar\frac{d}{d\varphi}$
Kinetic energy as a function of coordinate	$T = \frac{p_q^2}{2m}$	$\hat{H} = \frac{\widehat{p_q^2}}{2m} = -\frac{\widehat{\hbar^2}}{2m}\frac{d^2}{dq^2}$
Potential energy	V(q)	V(q)

Table. 1 Classical and quantum mechanical dynamic variables.

In case when we have a particle going over the circular path the wave functions ψ are the eigen functions of the angular momentum operator $\widehat{p_\varphi}$ and Hamiltonian $\hat{H}$ at the same time. The equations for the eigen values will look like

$$\widehat{p_\varphi}\psi = p_\varphi\psi \tag{86}$$

and

$$\hat{H}\psi = W\psi \tag{87}$$

The latter is exactly the Schrodinger equation. It is pointed out in the Table.1 that $\widehat{p_\varphi} = -i\hbar\frac{d}{d\varphi}$, where φ is the angular coordinate of the particle under investigation. The Kinetic energy of the classical particle with the angular momentum p_φ and with the inertia momentum I, is equal to

$$W = \frac{{p_\varphi}^2}{2I} \tag{88}$$

If V is taking the 0 value, the quantum mechanical operator is taking the form of the following expression

$$\widehat{H} = \frac{\widehat{{p_\varphi}^2}}{2I} = \frac{(-i\hbar)^2}{2I}\frac{d^2}{d\varphi^2} = -\frac{\hbar^2}{2I}\frac{d^2}{d\varphi^2} \tag{89}$$

Now we are ready to put the expression (89) into the Schrodinger equation (87) and get the further update

$$-\frac{\hbar^2}{2I}\frac{d^2\psi}{d\varphi^2} = W\psi \tag{90}$$

or in other words

$$\frac{d^2\psi}{d\varphi^2} = -\frac{2I}{\hbar^2}W\psi = -M^2\psi \tag{91}$$

Here we took the constant value $\frac{2I}{\hbar^2}W$ as M^2. The equation (91) has two solutions:

$$\psi_1 = Ae^{+iM\varphi} \tag{92}$$

and

$$\psi_2 = Ae^{-iM\varphi} \tag{93}$$

It's quite easy to check by simple plugging in. On the other hand, we have the normalization condition for the functions like those two

$$\int_0^{2\pi}\psi^*\psi d\varphi = 1 \tag{94}$$

From this condition we could easily find the $A = (2\pi)^{-1/2}$. Therefore, we may update the (90) and (91) expressions

$$\psi_1 = (2\pi)^{-1/2} e^{+iM\varphi} \tag{95}$$

and

$$\psi_2 = A = (2\pi)^{-1/2} e^{-iM\varphi} \tag{96}.$$

Thus, we may update the Schrodinger with the (95) and (96)

$$\frac{-\hbar^2}{2I}\frac{d^2}{d\varphi^2}\left(\frac{1}{\sqrt{2\pi}}e^{iM\varphi}\right) = \frac{M^2\hbar^2}{2I}\left(\frac{1}{\sqrt{2\pi}}e^{iM\varphi}\right) \tag{97}$$

It is clear, therefore, that the eigen value of the W as an operator of the $\widehat{H}$, corresponding to the eigen function ψ_1, is equal to $\frac{M^2\hbar^2}{2I}$. We will get the same expression for the energy if we take the ψ_2.

The operator $\widehat{p_\varphi}$ applied to the ψ_1 and $\psi_2$leads to the following equations

$$-i\hbar\frac{d}{d\varphi}\left(\frac{1}{\sqrt{2\pi}}e^{iM\varphi}\right) = M\hbar\left(\frac{1}{\sqrt{2\pi}}e^{iM\varphi}\right) \tag{98}$$

$$-i\hbar\frac{d}{d\varphi}\left(\frac{1}{\sqrt{2\pi}}e^{-iM\varphi}\right) = -M\hbar\left(\frac{1}{\sqrt{2\pi}}e^{-iM\varphi}\right) \tag{99}$$

Therefore, the eigen values of the $\widehat{p_\varphi}$ for the eigen functions ψ_1 and ψ_2 are equal to $M\hbar$ and $-M\hbar$ respectively.

We may exclude the eigen functions from equations (97), (98) and (99) by multiplying by the ψ^* from the left side and integration. In that case we will get the expressions in exact form for the angular momentum and the energy of the particle which goes circularly.

Going back to the energy expressions, we must stress that the flips between the Zeeman's energy levels lead to the changes in electron's magnetic momentum orientation. Therefore, these flips are only possible on the condition that this orientation change is provided by the electromagnetic radiation. We may take this radiation to be polarised so that oscillating magnetic field is parallel to the static one. It will lead to the oscillating energy changes of the Zeeman's levels in accordance with (9). There won't be any change of electron's magnetic momentum orientation change at the same time. The transitions are impossible in that case. The oscillations of the

magnetic field must have the component perpendicular to the static magnetic field in order to make them possible to happen. This condition is easily affordable in microwave frequency range.

We may understand from equation (10) that there are two possible techniques to investigate the resonance absorption of the paramagnetic sample. In the first case, the distance in between the Zeeman's levels is fixed by the constant value of the magnetic field. The microwave frequency is changing at the same time till the moment the resonance absorption will be observed. In the second one, we could fix the electromagnetic radiation frequency and change the value of the constant magnetic field applied. Technically it is more convenient to use the second way. That is why it was more popular at the beginning of the time. This is the characteristic point of EPR spectroscopy when the distance in between the energy levels is varied by the magnetic field variation. The energy levels are fixed in the other areas of molecular spectroscopy and the frequency is the thing which is changing.

Everything above was about the spins of electrons. It could be applied to the spins of the nuclei as well. It is interesting that six years before the first electron paramagnetic resonance was observer in the experiment with condensed gases [55], the transitions in between the nucleus spin levels in molecular and atomic groups with radio frequency radiation applied [55]. Soon enough, it was shown [56] that the same technique could be used to provoke the transitions in between the spin energy levels in general. Nucleus Zeeman's levels could be described by the equation close to the equations (64) and (65):

$$W = -g_N \beta_N H M_I \tag{100}$$

Here g_N is a nucleus g-factor,

$$\beta_N = \frac{eh}{4\pi m_N c} \tag{101},$$

where m_N is a proton mass, M_I is a component of the nucleus spin momentum vector along the z-direction. The transitions are permitted for $\Delta M_I = \pm 1$ only by analogy to the electron spin. Therefore, we may state for the energy gap that

$$\Delta W = h\nu = g_N \beta_N H_r \tag{102}.$$

The resonance absorption is called the Nucleus Magnetic Resonance in that case. We may say a few words about the g-factor.

2.3.8 Properties of the g-factor

The g-factor in the simple resonance equation could be taken as

$$g = \frac{h\nu}{\beta_N H_r} \qquad (103),$$

and there is no dependence from the applied field direction but for isotropic systems only. For instance, the electron in F-center (negative ion vacant position) in the halogenic of any alkali metal crystal is in the centre of the regular octahedron formed by the positive ions. The g-factor is an isotropic value, same as other properties, for such kind of a system with local octahedron symmetry.

The g-factor is a characteristic value for a wide range of the systems. Paramagnetic particles could be identified through it. Let us consider the EPR spectrum of the MgO crystal under the X-radiation. The resonance frequency is ν=9.41756 GHz.

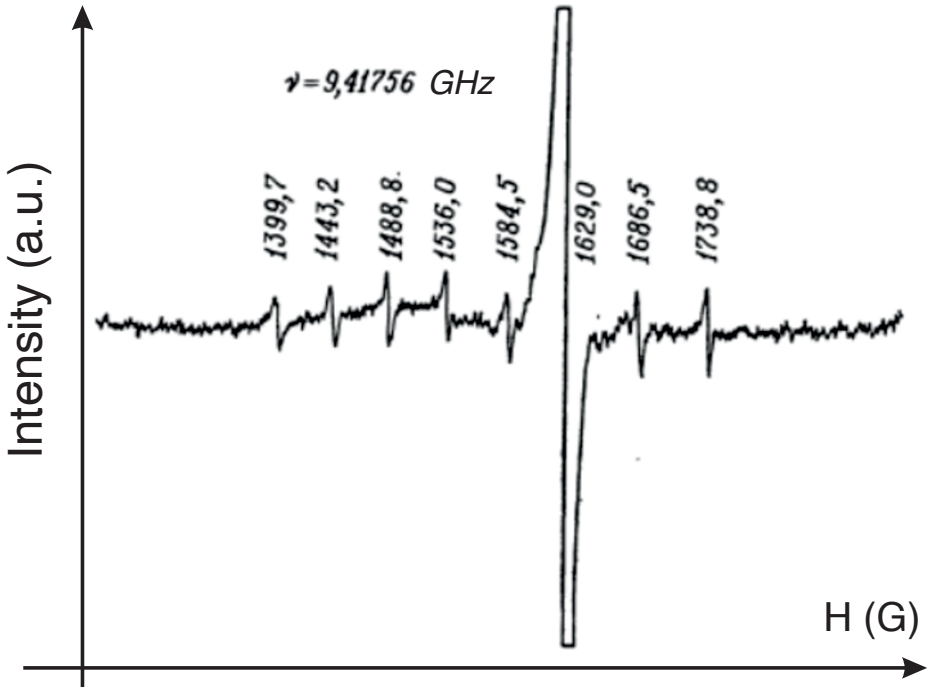

Figure 15. The EPR spectrum of Fe+ and Co^{2+} ions within the MgO at the 4.2 K. The Fe^{+} spectrum consists of one line only, the Co^{2+} one has eight lines with hyperfine structure of these spectral lines based on the ^{59}Co isotope $I = 7/2$ [45]

It is interesting to understand the nature of the high intense line within this spectrum which "hides" the 6th line in between the octet of the $^{59}Co^{2+}$ ions. The g is equal to 4,2785 for this ion. If we insert the value of the magnetic field of 1629.06 G correspondent to the line center to the (102) we get:

$$g = \frac{h\nu}{\beta_N H_r} = \frac{(6{,}62620 * 10^{-27} erg * s)(9.41756 * 10^9\ Hz)}{(9{,}27410 * 10^{-21} erg/G)(1629.06\ \mathrm{G})} = 4.1304$$

Such a value of the g-factor is not a trivial one and gives us a key to the ion nature. This ion is a source of this line within the spectrum. Iso-electron ions (the ions with the same electron configuration) with the same symmetry have the same g-factors normally. The Fe^{+} ion is an iso-electron one for the Co^{2+} one with $3d^7$ configuration. The Fe has more than 97.7% of the isotopes with a zero spin values by nature. Therefore, the Fe^{+} ion should have a single line in the spectrum (except those cases when the line is a narrow type since nucleus momentum of the ^{37}Fe is one of the smallest in between the isotopes with $I = 1/2$). Because both g-factors are very different from electron's one (4.279 and 4.1304 compare to the 2.0023) we may consider them like two very close values and their ions to be considered as isoelectronic [57]. Therefore, the intensive line could be considered related to the Fe^{+}

ion. This like disappears if we heat up the crystal to 400 K. This happens in accordance with the point that this valent state is not the stable one. We could observe the lines of electron paramagnetic resonance for Fe^{2+} and for Fe^{3+} within the same crystals. It is quite common for isoelectronic ions to perform the EPR signals in similar experimental setup and with the same symmetry around. We could not observe the EPR signal for Co^{2+} neither for Fe^{+} at the temperature of 77 K. But when the latter is going below the 20 K and lower both ions perform strong resonance absorption. This property let us to identify the Fe^{+} completely. We may add here that the resonance lines could not be observed at the room temperature or even at 77 K due to the strong line broadening. The latter happens because of the very short relaxation times.

Diluted liquid solutions with low viscosity could be considered as magneto-isotropic systems. The resonance behaviour occurs due to the quick random rotational motion of the dissolved matter molecules. We could lower the temperature or even freeze them. Electron Paramagnetic Spectrum could be observed in these conditions. The resonant line within this spectrum is wide and not structured. The asymmetry of the EPR lines shows that the molecules which have the effect on the signal have magnetic anisotropy as a property. There are other matter properties which could be anisotropic. Obviously, one of those is magnetic permeability of the anisotropic crystal. This property is in the strong dependence from the crystal to magnetic field orientation. The simplest tensor of the anisotropic permeability μ has nonzero diagonal elements μ_{xx}, $\mu_{yy} = \mu_{zz}$ and others are equal to zero. Thus, the object reacts to the magnetic field applied depending on the angle in between the crystal axis and the direction of the magnetic field applied. The term “magnetic anisotropy” is not a primary unit, although magnetic anisotropy is of utmost importance for soft and especially hard magnetic materials. Since the magnetic anisotropy is linked to coercivity, usually the magnetic anisotropy of any origin is minimized in soft magnetic materials. Medium-soft magnetic materials, especially magnetic recording materials, rely on a sufficiently large (because of long-term stability) but sufficiently small (because of the necessity of frequent re-magnetization) coercivity, and is usually in the range of 104–105 Am^{-1} (ca. 100–1000 Oe). For such applications materials with shape anisotropy (e.g., Fe_2O_3 needles), surface anisotropy (thin films), or magneto-crystalline anisotropy are needed. A clear-cut distinction of the nature of magnetic anisotropy is rarely possible [58]. For instance, the absolute value of the permeability

of the graphite is twice bigger if we have the magnetic field applied perpendicular to its layer surface compare to the case when the same field applied parallel to it. At the same time, the number of the parameters we need to describe the permeability is finite. There are three directions (main axes) that perpendicular to each other for any anisotropic system (independently from how complicated this system is and from how low the level of this system symmetry is) which has the values of this permeability measured along them (main values). This values totally determine the permeability of the system. The same thing is valid for the optical properties of the crystals like absorption or permittivity. For instance, it is very popular to use the permittivity anisotropic properties in metamaterials these days because you could control the light propagation with it. For instance, the wire medium metamaterial properties are unique [59,60], and they are based on the permittivity tensor, which could be shown slightly deeper here compare to (2):

$$\varepsilon = \begin{pmatrix} 1 - \frac{k_p^2}{k^2 - k_x^2} & 0 & 0 \\ 0 & 1 & 0 \\ 0 & 0 & 1 \end{pmatrix} \quad (104),$$

where k_p^2 is a plasmonic frequency, existing due to the specific properties of noble metals within the optical frequency range, and it is equal to

$$k_p^2 = \frac{2\pi/a^2}{\ln\frac{a}{2\pi r} + 0.5275} \quad (105).$$

Here we need to say that wire medium is a metamaterial formed by the metallic wires. Those wires are grouped as an array with a period “a”. The incident light located in the XY plane. “r” is a radius of the wires. The Fig. 16 presented below shows 2 configurations under study from the [61]

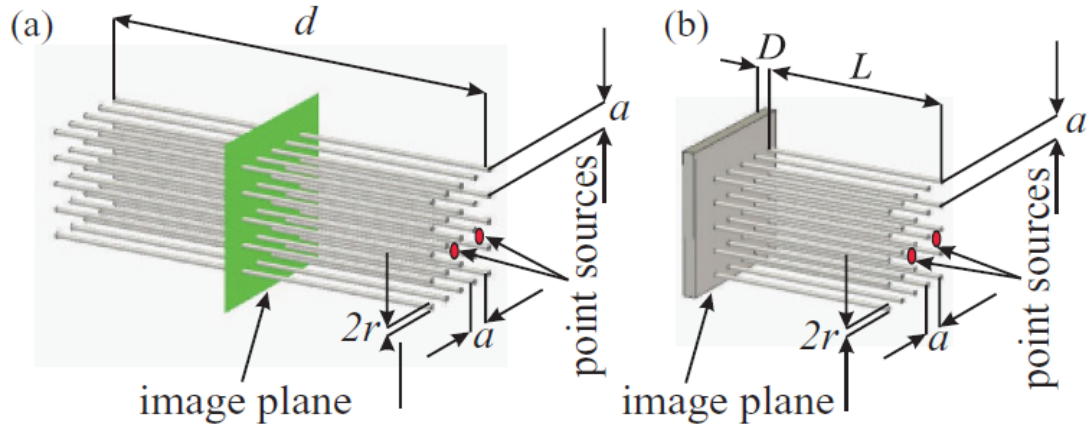

Figure 16 Internal imaging in an array of metallic nanorods with the length (a) d = λ/2 and (b) L = λ/4. Here, r is the nanorod radius, and a is the lattice period. In (a) the image plane (the green shaded rectangle) is located at the middle of the structure. In the case of panel (b) the nanorods are attached to a metallic screen with thickness D which is much larger than the metal skin depth, and the image plane is located near the screen. The image is encoded in the distribution of the nanorod currents

The electromagnetic wave will pass through this metamaterial in two different ways as it has two different axes. It comes straight away from the Maxwell equations [62]. In the wire medium the angle of incidence of the electromagnetic wave is a variable from which all the functions are in dependence from [63-65].

The resonance properties of the anisotropic system could be described in the same way. The resonance value of the magnetic field is in dependence from the field orientation and crystallographic (molecular) axis. This angular dependence is given to the g-factor. The g factor gets the indexes towards the orientation variations. If we take main axis of the molecule as X, Y and Z then we should take g_{xx} as $\frac{h\nu}{\beta_N H_r}$. This is the g-factor value when the magnetic field H is parallel to the X axe if the molecule. The system gets the "isotropic" name in case when $g_{xx} = g_{yy} = g_{zz}$ only. The g-factor should be considered as an effective value (the result of averaging out by all possible orientations) for paramagnetic samples within the low-viscosity fluid.

Some systems could provide the symmetry axes of the third, fourth or even sixth orders. Those systems which possess the symmetry of an order greater than 3 are named as "axially symmetrical". The X and Y are absolutely the same for those systems. Z is a direction without equivalent for most of cases and the g-factor for the case when H$\|$Z is taken as $g_{\|}$. On the other hand, the g-factor value is constant and named $g_{\perp}$when the H is within the XY plane and H is perpendicular to Z.

2.3.9 Typical Experimental Setup

The first techniques to measure the resonance absorption within the systems with unpaired electrons were known in 70's. We need to have a spectrometer with constant magnetic field for it. EPR spectrometers have the source of the radiation and some device to measure the absorption within the sample.

There is a difference in between the EPR spectrometers and the optical one. Firstly, the source (klystron) produces the monochromatic waves. Thus, we do not need any prism or the diffraction grating to correct the signal. Secondly, the EPR spectrometer works on the certain frequency of operation, and the EPR spectrum is scanned by the linearly changing magnetic field. This method is possible because the distance in between the energy levels is in determined by the magnetic field. This is a great, as it is not easy to have highly sensitive measurements when the frequency is from the microwave range as the frequency characteristics of the microwave resonators are fixed.

The absorption curves will be observed when the gap in between the energy levels will be equivalent to the energy hν of the photons which are illuminating the sample. The absorption is highlighted by the change of the current from detectors. The direct detection of the absorption signal is possible for the samples with high unpaired electrons concentration. There is a lot of noise within the signal when we are doing the measurement in a wide frequency range, and it is not easy to detect the clear signal. The signal to noise ratio on optical spectrometers could be improved by the light pulse modulation at the certain frequency. Therefore, we could use the very narrow band detector for the detection. Thus, the noise components will be bounded by the narrow frequency band with a centre at the modulation frequency.

The light modulator replaced by the magnetic field modulator in the magnetic resonance spectrometers. Those devices allow to put the varied component of the magnetic field alongside with the static magnetic field H_0. Thus, the total magnetic field comes over the resonance value H_r periodically. The true signal in the detector will be the variable potential with a frequency equal to the frequency of modulation. This signal could be enhanced by the narrowband amplifier. This signal could be shown on the oscillograph synchronised with the modulation as it shown on the Fig.

17. The modulation amplitude should be a few times wider than the width of the line observed with this observation technique.

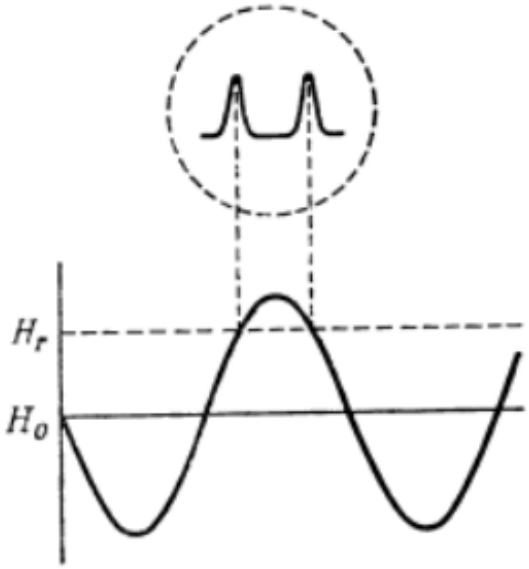

Figure 17 The detection of the EPR absorption with high amplitude of the modulation field. The paramagnetic system goes through the resonance conditions $2 * \nu_m$ times per second when $H_0 \approx H_r$ if the modulation frequency ν_m amplitude is big enough. The top part of the image shows the oscillograph image that could be observed in that case.

The resonance condition $h\nu = g\beta H_r$ is valid for any frequency, in general. The EPR absorption is a typical thing at the values of the magnetic field from several Gauss (ν~3 MHz) to 20000 G roughly (ν~60 GHz). For instance, geologists use very sensitive magnetometer in order to measure the magnetic field from our planet (~0.5 G) which based on the EPR effect. In fact, the choice of the frequency of operation is very limited by the range of factors. First, the detector should be very sensitive. Therefore, the frequency should not be as high as possible as the sensitivity of the EPR spectrometer is growing proportionally to the ν^2. There are three more factors which limit the possible range of frequencies from above. The first one is the actual size of the sample. The microwave resonator size would be a few millimetres in case if we choose the frequency from 30 to 40 GHz. In that case, the size of the sample should be around 0.02 cm^3 apart from the point that volume sensitivity is very high. Secondly, we should have strong and stable magnetic field covering the sample. It is not easy to get this condition satisfied with common magnets and with a value of the field over 25000 G (2.5 T). The superconductive magnets can generate up to 10 T. Finally, the sensitivity is going down at high frequencies due to the dielectric loses for the liquid

samples. That's why most of spectrometers operate at 9.5 GHz. The waveguides transmit the waves with low loses at frequencies from 8.2 to 12.4 GHz called 3 cm frequency band or X-band. The operation frequency could go up. We could use the frequency of 35 GHz in case if we investigate monocrystals and the samples with low dielectric loses. This frequency is taken from the 33-50 GHz frequency band which is called the Q-band. Thus, the frequency range could be quite different depending on the sample. Further we consider the typical spectrometer parts.

The spectrometer typically consists of the "source part" (all the devices for frequency and intensity of the microwave signal control), the "resonator system" (it is where the sample is placed as well as the devices for the direct and control of the microwave signal), the "detector and modulation" (for signal receiving, enhancing and registration) and, finally, the "magnet"(providing the stable and linearly changing magnetic field of random intensity).

The "resonator system" is a true heart of any spectrometer. Here is a place where the sample under investigation is located. Acoustic resonance is a well-known thing. For instance, this phenomenon could be observed within the pipes of the organ. The properties of the resonators were studied and described by the Helmholtz [66]. The reflection of the acoustic waves from the walls of resonator leads to the damping of the waves due to the interference but only those which half wavelengths is not proportional to any characteristic resonator dimensions. Those, which half wavelength is equal to one of the resonator dimensions, called the main resonance frequency. This frequency is getting smaller if we make the resonator larger. The 3D resonator could be excited in the specific way so there will be standing waves of a few types (modes). The frequency of the cylindrical resonator could be changed if we place the displaceable piston. This methodology is used for the wavelength measurements.

The energy density of the propagating wave is not so high, normally. But the significant volume of the energy could be concentrated within the standing acoustic waves. The acoustic resonance is easy to observe, as acoustic waves have the wavelengths from centimetres to a few meters. The waves from the microwave frequency band possess the wavelengths for about a few centimetres, obviously. Therefore, the microwave resonators should have the comfortable dimensions. The shape of the resonator could be random, same as for the acoustic frequencies. On the

other hand, we must consider the presence of both the magnetic and the electric fields (H_1 and E_1). The maximum position of the E_1 is not the same as for the H_1, their relative locality is in dependence from the oscillations type (from the type of the resonator mode). We should take the modes which will allow us to concentrate significant density of the energy as well as they should provide the possibility to place the sample into the oscillation loops of the H_1. At the same time the H_1 must be perpendicular to the static field H. The most popular resonators for EPR spectrometers are shown on the Fig. 18 and Fig. 19. The modes are named towards the magnetic component of the field (H). The indices show the number of the half wavelengths in proportion to the characteristic dimensions of the resonators. For instance, the H_{102} means that along with A and C directions could be placed one and two of the half wavelengths respectively and there is no change of the field along the B direction. The spatial distribution of the magnetic and the electric fields for this type of the resonator represented on the right part of the Fig. 19. This type of the resonators could be used for large scale samples with low value of the dielectric constant without significant decrease of the energy density. Moreover, this type is very useful for the liquid samples if they could be placed inside and take all the available space inside.

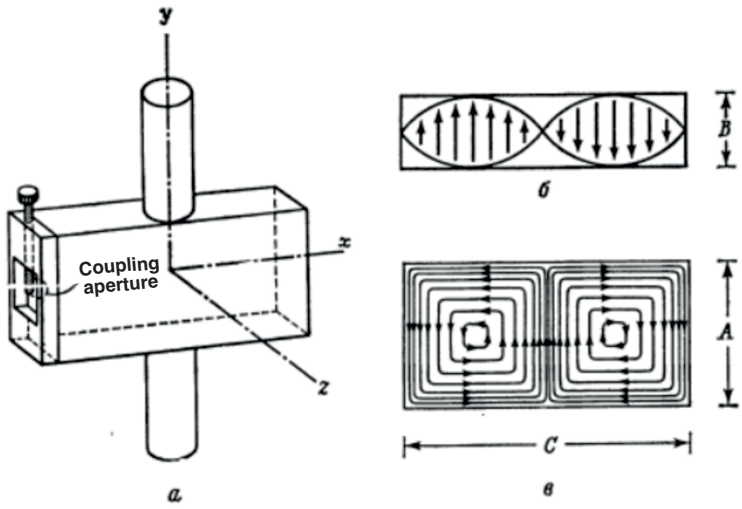

Figure 18 Rectangular resonator of the H_{102} type. Cylindrical parts above and below the resonator protect it from the signal leakage and act as a guiding line when the sample is placed onto the resonator. The microwave signal comes to it though the square window which could be reduced in the size (picture on the left). The top right part represents the electrical field in the XZ plane. The half of the wavelength along the X direction is equal to the shortest distance in between the points with the same filed intensity but with the opposite phase. The lower right image shows the magnetic field flow in XY plane. The A value is roughly equal to the half wavelength and C is twice bigger. The dimension B is not so crucial, but it should not be less than the half wavelength as well.

Significant value of the energy density could be achieved within the cylindrical resonator shown on the Fig. 19 if we will take the H_{011} mode as the operating one. The energy density is at least three times higher for this mode compare to the H_{102} in rectangular resonator with all the other conditions being the same. This type is very useful for observation of the electron transitions within the vapor samples as the pipe diameter could be increased to the value of the 25 mm. We will see these resonator types in use in Chapter 4 when we will be discussing the feeding device through the references.

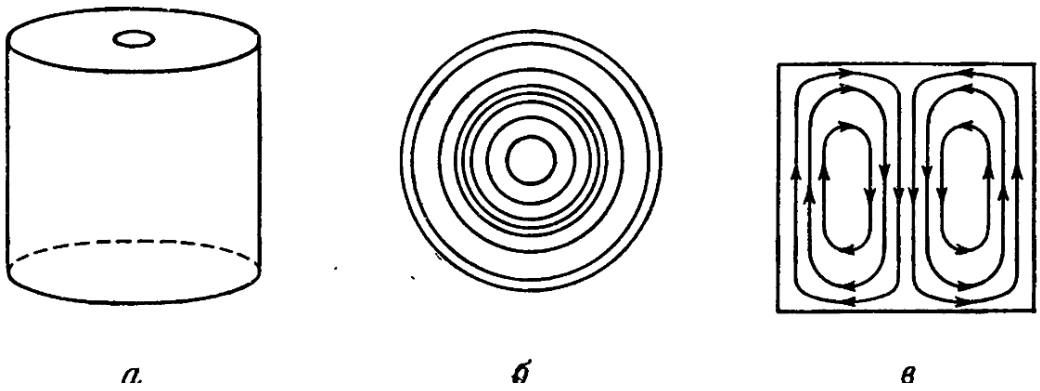

Figure 19 Cylindric resonator of the H_{011} type. The left image has the resonance frequency determined by the height and the diameter of the cylinder. The middle image shows the electric field contour, the right one is for the magnetic one.

The speed of response of any resonance system is scaled by the Q-value. There is a typical image of the electrical oscillating circuit response close to the resonance frequency on the Fig. 20.

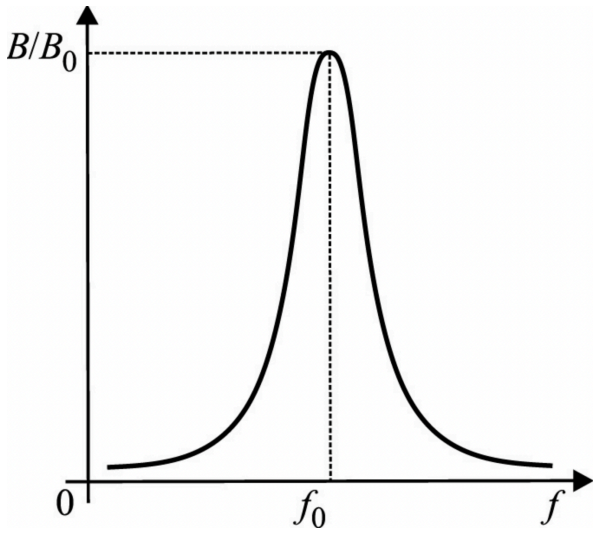

Figure 20 The typical response curve of the LC resonance contour in dependence from the external magnetic field applied [45].

The impedance over the LC contour goes to its maximum close to the resonance frequency ν_r. determined by the expression $1/\left(2\pi\sqrt{LC}\right)$ (this is f_0 on the Fig. 20). The frequencies corresponding to the half of the power applied could determine the $\Delta\nu$ and let us calculate the Q

$$Q = \frac{\nu_r}{\Delta\nu} \tag{106}$$

The same way we could apply to describe the response of the resonator towards the frequency of the microwave radiation illuminating it close to the resonance frequency. Therefore, the reflected power is minimal when $\nu = \nu_r$. The other way to determine the Q value (equivalent to the previous one) is

$$Q = \frac{2\pi(maximum\ energy\ within\ the\ resonator)}{(energy\ losses\ per\ one\ cicle)} \tag{107}$$

We could easily figure out from that formula that the energy value at the current frequency (as well as Q) is growing towards the grow of the resonator volume. Also, we could improve the Q if the losses will be lower within the resonator borders and within the sample (there are currents there). The resonator walls could be covered by the thick layer of the silver and the thin golden layer to save the silver shell from destruction. The Q value will decrease if we take the sample with high permittivity value and put it to the area with a strong electrical field at the microwave frequencies.

The microwave energy is delivered and going out of the resonator through the square window (Fig. 18). This window has the same purpose as the transformer, which match the impedances within the electric circuit. We need to decrease the part if the power we are losing due to the reflection from the resonator. Obviously, this could be made by the impedance matching as any line could be optimised from that point if it is loaded with a certain impedance. Impedance matching to minimize reflections is achieved by making the load impedance equal to the source impedance. If the source impedance, load impedance and transmission line characteristic impedance are purely resistive, then reflection-less matching is the same as maximum power transfer matching [67]. Thus, if the load is good enough the power transfer will be as good as possible. This is very important moment for our case as well. There could be an adjustable screw tuning applied (the screw position is shown on the Fig. 18) to adjust the impedance to the optimum value. The screw position is determined by the size and the type of the sample placed to the resonator.

The breaks within the waveguides or the defects at the places where the microwave devices are connected to each other leads to the losses. This is very important for us as well as this is the main difference of our design compare to the one presented in [12] as the transmission line presented there has a gap on the substrate as well as within the conducting layer and the parts connected by the bonding wires (Fig. 1). This is the same as those designs from my colleague Abiola from University College London (UCL). The part of the energy that comes from the source and reflecting is hence increased. It is not only determined by the reflections within the resonator, but also the reflections from the other parts decreasing the device sensitivity as well. Specifically. a device called the balance to unbalance «matcher» (Balun), helps to convert an unbalanced signal to a balanced one or vice versa, so that both reflection and transmission losses can be reduced due to the connection from a small sensing electrode being placed within or alongside with a resonator. There is one more device which is used within the resonator part called “circulator”. It performs differently with the waves passing through it in the forward and backward directions. It let the waves passing forward to go with very low losses and opposite to those waves which are going in a backward direction. It is mainly for directing the microwave power to the resonator and the reflected signal to the detector.

The magnet is another very important part of any system like that. This is the device responsible for the static magnetic field. The latter must be homogeneous and stable within the sample volume. The changes of the field should not go out of the 10 mG (10^{-6} T) range in case the sample is liquid and there are organic free radicals within. This range is wider in case of the most non-organic samples and equal to 1 G (10^{-4} T). The stability of the magnetic field is provided by the very sensitive source. The sensors based on the Hall effect could be not the sample but the controlling and testing device in the modern magnets. The scanning system connected to the source let us to change the magnetic field linearly over the time. The changes of the field should be linear and repeatable in order to simplify the spectre analysis. The Nuclear Magnetic Resonance (NMR) sensor could be placed close or even within the resonator to measure the magnetic field. The NMR signal detection and the measurement of the corresponding resonance frequency let us understand the H with up to 10^{-5} precision.

2.4 Basic Concepts, Structures and Applications of the Spintronics

2.4.1 History

An electric current was a giant step up in a technological progress of humanity in nineteenth century. Today many people believe that the progress has stopped in these years. It could be so due several important inventions which we are still using everyday had been invented in these years: the telegraph (1832) and the telephone (1876), the radio (1895), the electric lamp (1860), etc. Theoretical basement for modern physics was made in these years as well. Maxwell equations are still one of the most useful tools in analytical research area.

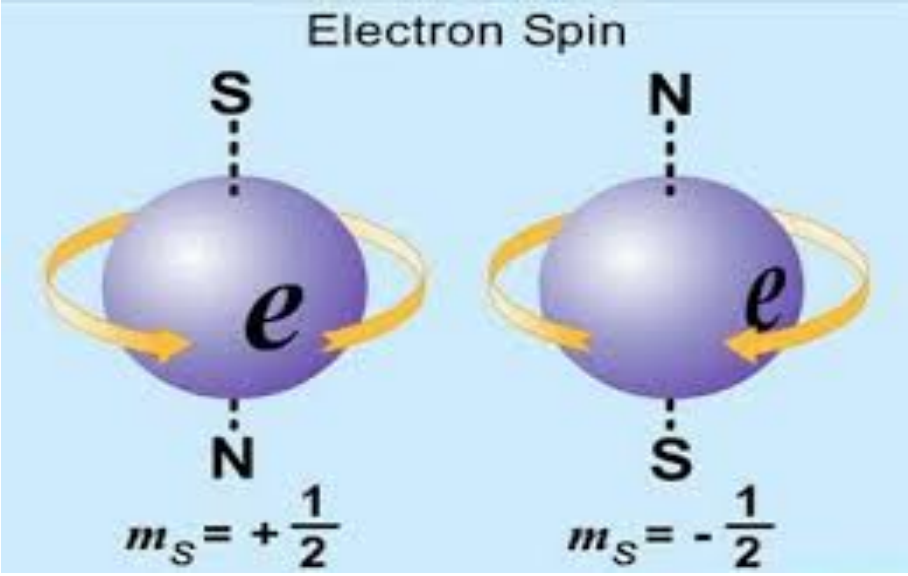

Figure 21 The classical electron spin model. Two potential states presented with a spin value $1/2$ and $-1/2$.

On the other side from those who are not so positive about the evolution of the humanity there are others who noticed that on the border of two centuries another highly important area of physics was developed very intensively. It was quantum mechanics. All the basic laws of this area were stated at the beginning of the 20th century. It was a giant step forward in understanding of the nature and processes around us. As it happens quite frequently in technological area when technology is not as quick as it needed. Thus, it was basically just fundamental investigations and publications.

2.4.2 Magnetoresistance and related physical effects

Spintronics is quite young area of physics. It stays on the border between solid state physics, quantum mechanics and electronics which cover a huge number of applications and problems. In 1990's scientists used this term to describe the devices which employ the property of the electron to be in only two states: spin-up and spin down. The discovery of the Giant Magnetoresistance (GMR) phenomenon was one of the first and most important steps towards the future. Proving the importance of this discovery to the modern physics the Nobel Prize in Physics in 2007 was given to Albert Fert and Peter Grunberg in 2007. It is a more specific, quantum-mechanical case of the magnetoresistance first discovered by the William Thomson in 1856 [68]. It is mainly the change of material's electrical resistance due to the magnetic field applied to it externally. Thomson noticed that the resistance of a sample (pieces of iron) increases when the current and the external magnetic force are codirectional. A few types of materials perform the magnetoresistance. It could be performed in non-magnetic materials and semiconductors as a geometrical case of effect, as the Shubnikov–de Haas effect or as a positive magnetoresistance in metals, as anisotropic magnetoresistance (AMR) in ferromagnets also called negative magnetoresistance. The multilayered structures perform giant magnetoresistance (GMR), Tunnel Magnetoresistance and Extraordinary magnetoresistance (EMR).

The first one could be described for the case of the Corbino disc with a battery connected to it [69]. The disc consists of PEC rims and conducting annulus. If applied B-field is equal to zero the lines of a current are simply radial, but in the presence of an axial magnetic field they lengthen by spiraling. This latter occurs because of the disk geometry is such that the Lorentz force acting on the charge carriers is not counterbalanced by a Hall-effect electric field. The resistance of the disk increases as the field increases, largely as a result of the geometrical magnetoresistance effect associated with the lengthening of the current path.

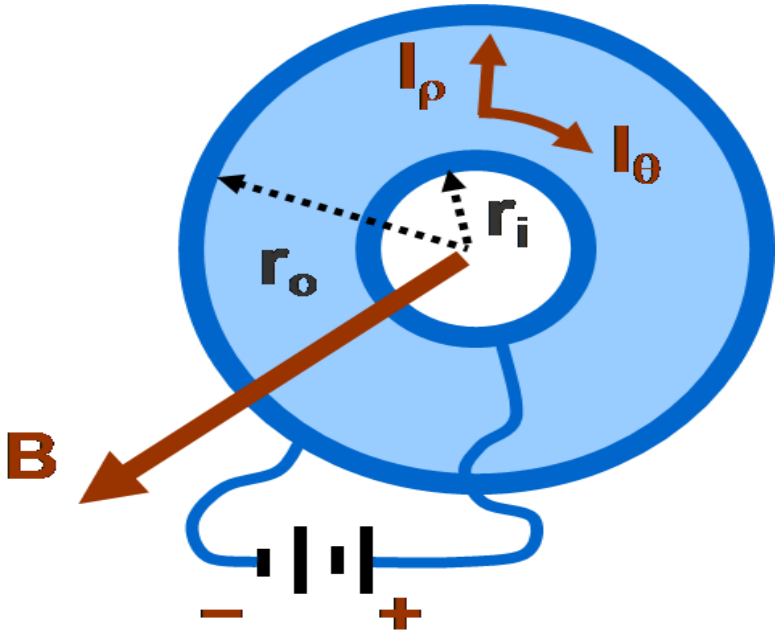

Figure 22 The Corbino disc as a typical model of geometrical magnetoresistance. With a magnetic field being turned on, the Lorentz force impact on the circular component of the current and the resistance between the outer and inner rims is increasing. Thus, it changes due to the magnetic field presence.

The second one, the Shubnikov–de Haas effect [70-72]. The Shubnikov-de Haas oscillations are oscillations of the resistivity parallel to the current flow in the edge states of a 2DEG (2-dimensional electron gas) in an applied magnetic field. Therefore, they are related to the Quantum-Hall effect. The Shubnikov-de Haas oscillations have a 1/B-periodicity.

Fig. 23 shows the results of the measurements of the Quantum-Hall-resistivity and of the Shubnikov-de Haas oscillations. You can see that the peaks in the Shubnikov-de Haas oscillations occur at the same magnetic fields as the changes in the Quantum-Hall-resistivity. Applied to a 2DEG (two-dimensional electron gas), the magnetic field provokes the electrons in the bulk regions perform circular motions. In the border regions of the sample, the electrons cannot perform full circular motions, because they get scattered back from the interface. These scattering events give these electrons a higher energy. Those scattered electrons are forced by the magnetic field to move in forward direction so that the current flows without resistivity in the edge channels. The energy-eigenvalues of the circular motion are the same as for the harmonic oscillator with the eigenfrequency w_c, where w_c is the cyclotron frequency:

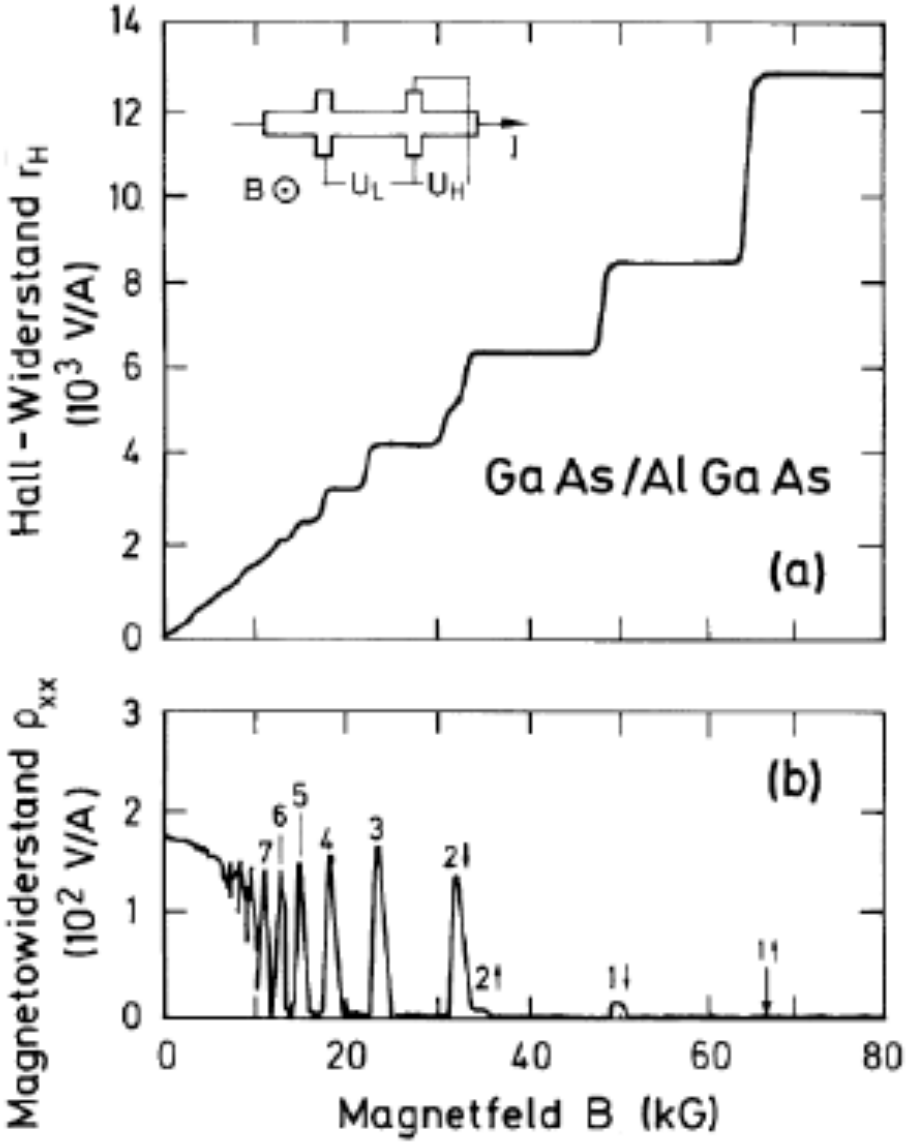

Figure 23 Results of the measurements of the Quantum-Hall-resistivity (a) and the Shubnikov-de Haas-oscillations (b). The peeks in the Shubnikov-de Haas oscillations occur at the same magnetic fields as the changes in the Quantum-Hall-resistivity [72].

$$w_c = -\frac{e*B}{m^*_{\parallel}} \qquad (108),$$

where $m^*_{\parallel}$ is the effective mass of the electrons parallel to the circular movement.

The cyclotron frequency or gyrofrequency is the frequency of a charged particle moving perpendicular to the direction of a uniform magnetic field B (constant magnitude and direction). It is notable that the cyclotron frequency is independent of

the radius and velocity and therefore independent of the particle's kinetic energy - all particles with the same charge-to-mass ratio rotate around magnetic field lines with the same frequency. Thus, the magnetic field causes a further quantization of the energy bands. The resulting energy bands are called Landau-levels. The energy-eigenvalues of the Landau-levels from the Schrodinger equation for free electrons in a magnetic field are:

$$E_{k_z,\nu} = \frac{\hbar^2 * k_z^2}{2 * m^*} + \hbar * w_c * (\nu + 1/2) \qquad (109)$$

In this equation ν indicates the number of the Landau-level. The energy gap between two Landau-levels is $\hbar * w_c$. Therefore, the gap between the Landau-levels gets bigger when the magnetic field is increased. Figure 24 shows the Landau levels (a). If the highest Landau-level is far away from the Fermi-energy, then there are no states available for scattering (see Fig. 24 b)) and the Quantum-Hall resistivity remains constant and the Shubnikov-de Haas-resistivity goes to zero. In that case the electron transport in the edge states is ballistic. When you increase the magnetic field, the highest Landau-level gets near the Fermi-energy (see Fig. 24 c)). In that case there are states available for scattering in the bulk regime. This scattering causes the peeks in the Shubnikov-de Haas oscillations and the growth of the Quantum-Hall resistivity.

When a Landau-level crosses the Fermi-energy as a result of an increasing magnetic field it gets de-occupied. It means that the electrons jump into the lower lying Landau-levels. As soon as the highest Landau-level is completely de-occupied the Fermi-energy is in the next highest Landau-Level. This level has a lower energy than the now unoccupied level and therefore the Fermi-energy is lower than before [73]. This effect is related to the other one- de Haas–van Alphen effect. The signature of the latter is a periodic waveform when plotted as a function of inverse magnetic field (1/H). The "frequency" of the magnetoresistance oscillations (in inverse field space) indicates area of the extreme Fermi surface.

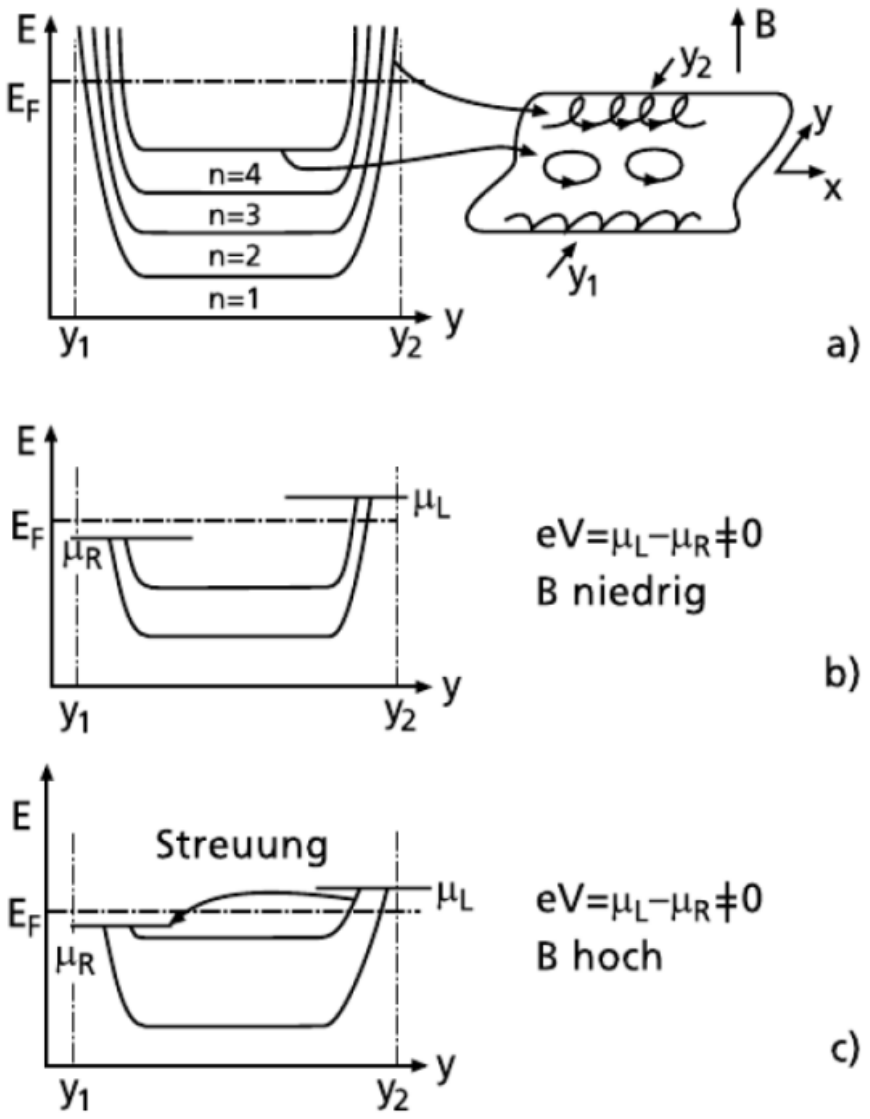

Figure 24 a) The resulting Landau-levels after applying a magnetic field, b) highest Landau-level is far away from Fermi-energy - no scattering happening, c) highest Landau-level is near the Fermi-energy - scattering is possible [73].

The next type is positive magnetoresistance [74]. It is known that the electrical resistance of a metal is usually changed when a magnetic field is applied to it. Every metal behaves differently, and the effect is highly dependent on the direction of the field relative to the crystal axes.

The Anisotropic Magnetoresistance (AMR) [75] is a property of a material in which the electrical resistance is in dependence from the angle between electric current and magnetization. It happens due to simultaneous action of magnetization and spin-orbit interaction. It was noticed that the electrical resistance experiences up to 50%

increase for some materials [76] in case of the direction of current is parallel to the applied magnetic field. The is a picture of this effect on the Fig. 25. The section b) of this figure shows exactly the resistance dependence of the Permalloy films from the angle of external field applied. The Permalloy was one of the materials we have studied during our practice with the scanning microwave microscopy (SMM) setup (will be discussed in more details later below).

Here is a need to say a few words about the spin-orbit interaction which is basically the behavior of particle's spin with the particle's motion. The best example is an interaction of electron's spin with magnetic field around the nucleus. It could be considered as a Zeeman effect (typical picture shown on Fig. 26 a)). The latter is spectral line splitting under due to static magnetic field presence. It is like the Stark effect. The difference is that the electric field causing the splitting in this case. It results from the interaction of an emitter with an electric field, causing a shift in energy that is linear in the field strength [77]. Spin noise spectroscopy is an optical technique which can probe spin resonances non-perturbatively (Fig. 26 b)). First applied to atomic vapors, it revealed detailed information about nuclear magnetism and the hyperfine interaction. In solids, this approach has been limited to carriers in semiconductor heterostructures.

Here we show that atomic-like spin fluctuations of Mn ions diluted in CdTe (bulk and quantum wells) can be detected through the Kerr rotation associated to excitonic transitions. Zeeman transitions within and between hyperfine multiplets are clearly observed in zero and small magnetic fields and reveal the local symmetry because of crystal field and strain. The linewidths of these resonances are close to the dipolar limit. The sensitivity is high enough to open the way towards the detection of a few spins in systems where the decoherence due to nuclear spins can be suppressed by isotopic enrichment, and towards spin resonance microscopy with important applications in biology and materials science.

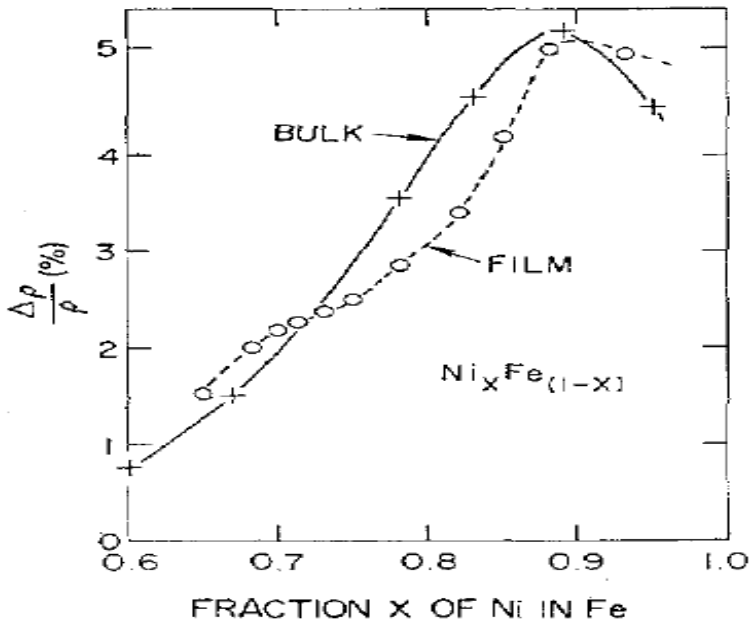

a)

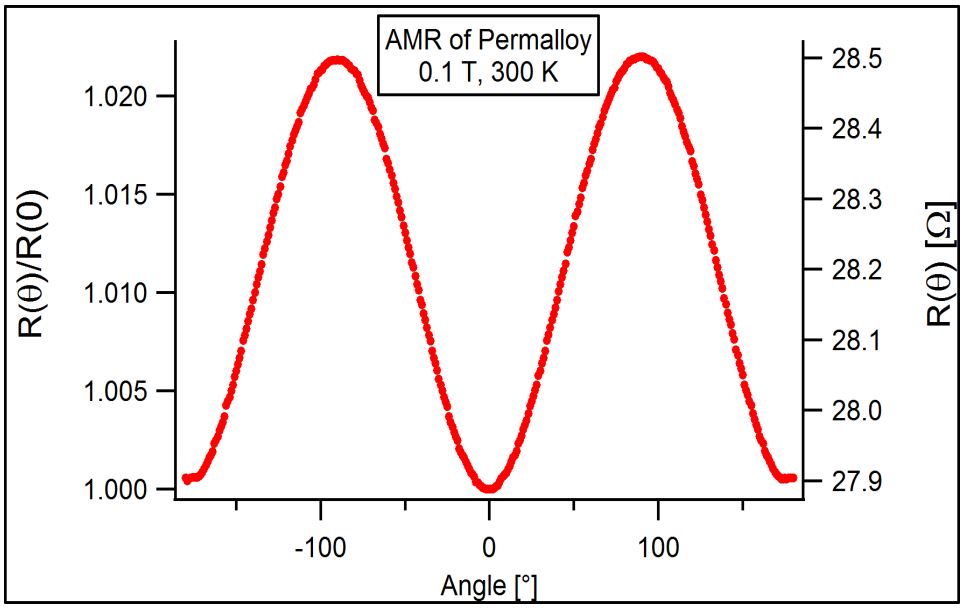

b)

Figure 25 a) Comparison of the anisotropic magneto-resistivity ratio of thin films and bulk alloys of NixFe (l-x) as a function of composition. b) The resistance of a thin Permalloy film is shown here as a function of the angle of an applied external field [76].

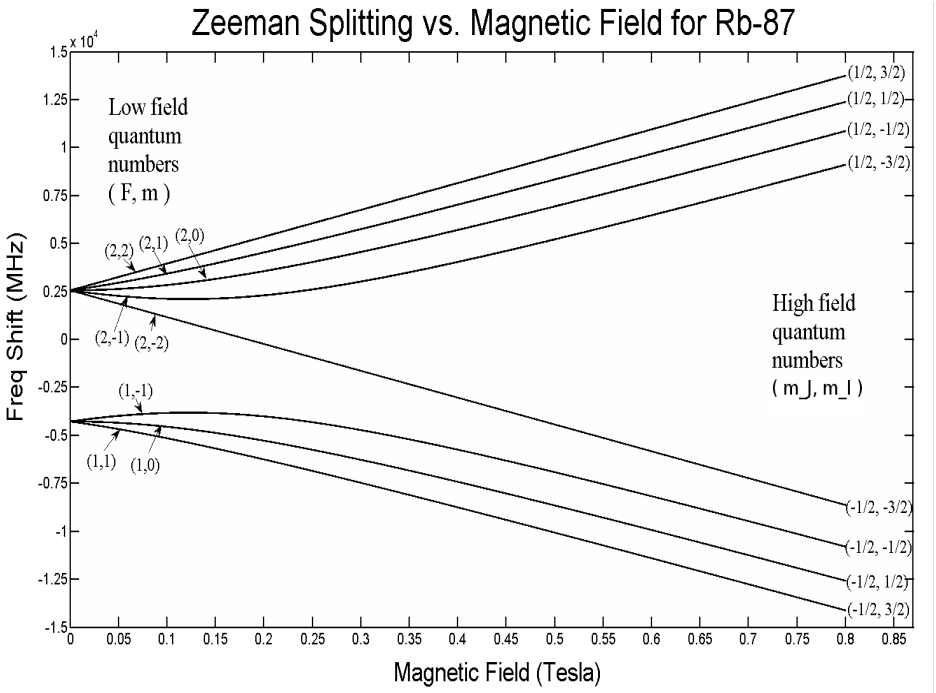

a)

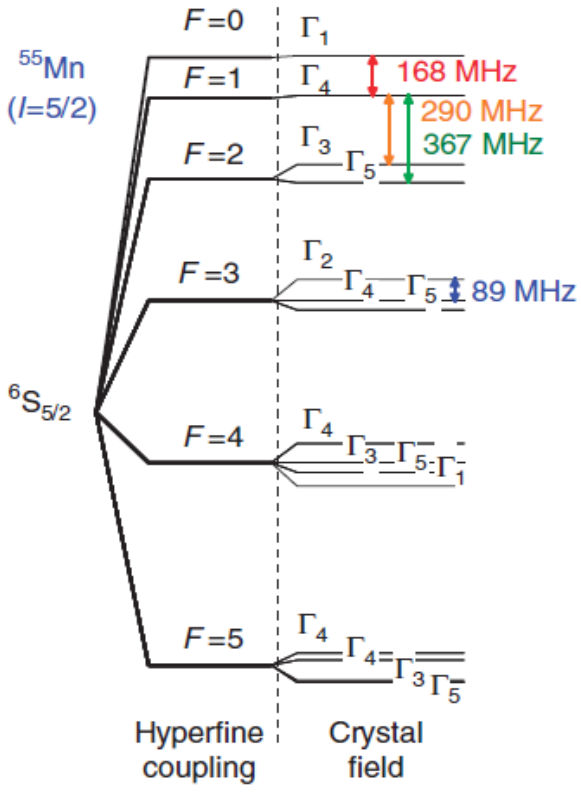

b)

Figure 26 a) The Zeeman splitting of the 5s level of Rb-87, including fine structure and hyperfine structure splitting. b) The picture of the spin-noise reason. There are more than just one available energy levels [77].

The AMR effect is used in a wide array of sensors for measurement of Earth's magnetic field (electronic compass), for electric current measuring (by measuring the

magnetic field created around the conductor), for traffic detection and for linear position and angle sensing.

After that it was discovered that the electron current becomes spin polarized on the way through the magnetic and non-magnetic layers. And moreover, this polarization can be controlled by the magnetic field applied to the device [78-80]. The effect of magnetoresistance in thin-film multilayered structures was named GMR (Giant Magnetoresistance). In spin valve GMR (Fig. 27), two magnetic layers are separated by a thin (~3 nm) non-magnetic (insulating) layer. It is possible to measure and adjust the strength of magnetism between these layers. Materials used in spin valves are copper and an alloy of nickel and iron. The study of the effects of the interfacial conductivity and spin asymmetry at the boundaries between the ferromagnetic (FM) and nonmagnetic layers (NM) of a current perpendicular-to-plane spin-valve trilayer, based on the semi-classical drift-diffusion model was presented to show this effect. Spin valve GMR is the most useful sort for hard drives and is tested carefully to meet industry standards

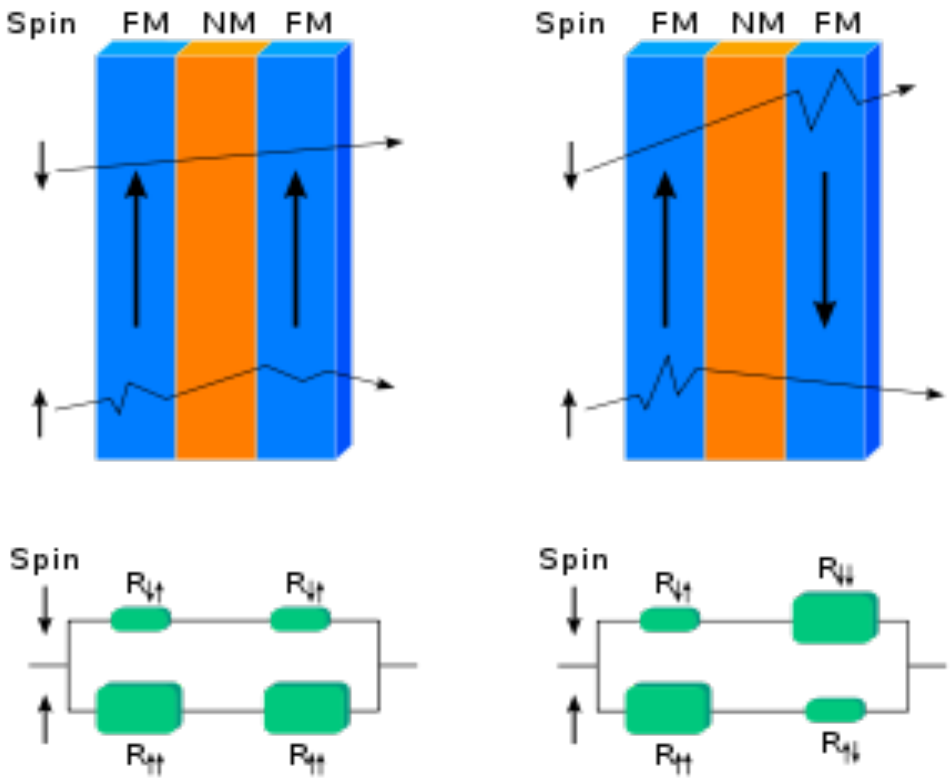

Figure 27 The non-magnetic layer of material between two magnetic layers (GMR case). Electrical current became “spin-polarized” [79].

The main application of GMR is magnetic field sensors, which are used to read data in hard disk drives, biosensors, microelectromechanical systems (MEMS) and other devices. GMR multilayer structures are also used in magneto resistive random-access memory (MRAM) as cells that store one bit of information.

Thus, the spintronics started to take the leading position in the modern electronics (if this name is still applicable). Following the technological progress, the spin started to play the role of electron, there are more and more investigations and experiments in this filed, the proposed setups are very promising in terms of the performance improvement of the current electronic devices as well as significant decrease of their size. Therefore, the better understanding of small, quantum size effects and properties should be understudied as the size of the sample is decreasing.

2.4.3 Topological insulators

There are a lot of areas which are united by spintronics which emerged at the end of 1980's as a part of magneto electronics as it was already mentioned above. One of the first things that were discovered was the spin-dependent electron transport. New possibilities in the field of material construction provide future investigations in this area. And the new kind of the materials - topological insulators - is one of the hot topics today. Few papers were published in the last years [81-91].

Topological insulators are materials with a bulk band gap (Fig. 28) and protected conducting states which exist due to spin-orbit interaction and time-reversal symmetry (theoretical symmetry of physical laws under the transformation of time reversal). This kind of a structure supports spin-polarized propagation because of fermions on its edge.

A wire medium is a well-known metamaterial suitable for the far and near field imaging. The general view of the wire medium metamaterial is shown on Fig. 29. Transmission properties of this material were deeply studied. Recently, it was found that such a structure can be considered as a topological insulator [81, 82]. The main idea is to put together two wire arrays connected to metallic planes from the opposite sides. The structure represents itself a two-dimensional bi-anisotropic meta-

waveguide (Fig.28), mimicking the spin-orbital interaction in topological insulators and opening a photonic topological band gap.

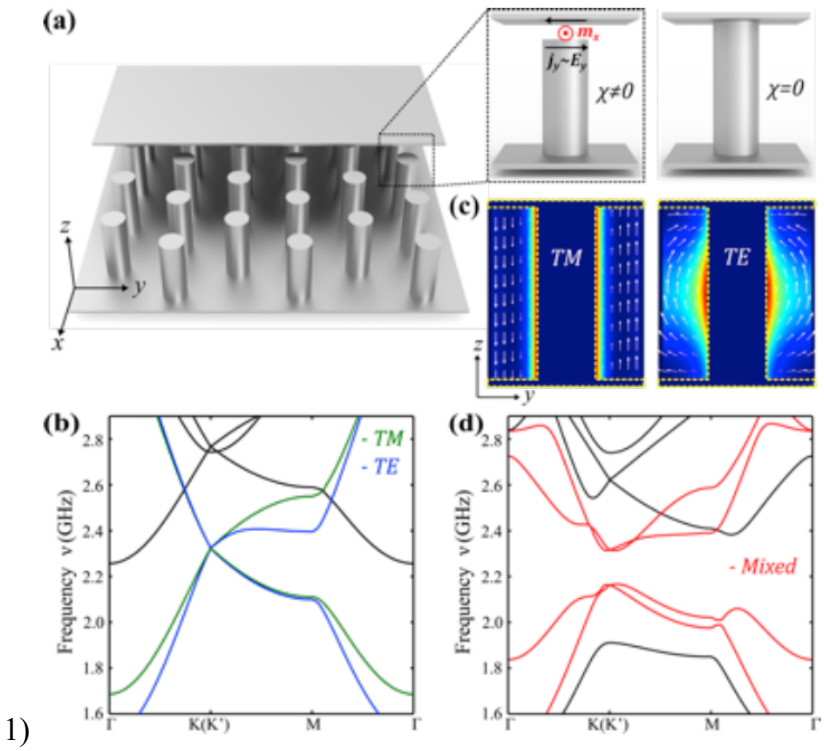

1)

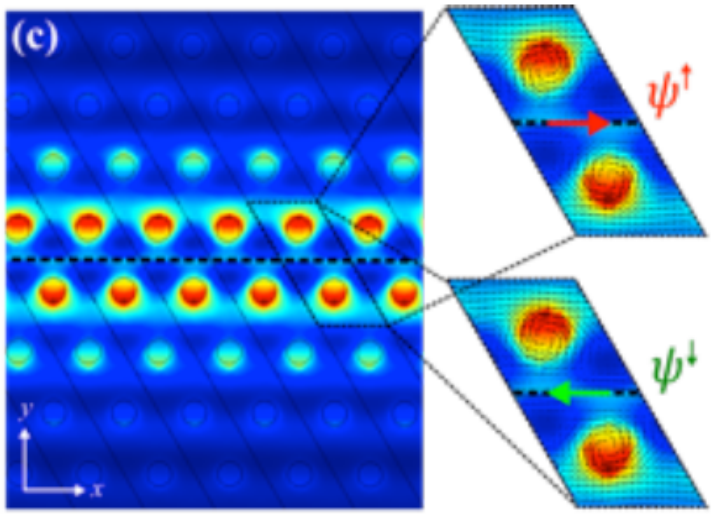

2)

Figure 28 1) a) The "fakir's bed of nails" metamaterial formed by the metallic wires short-circuited to the metallic plate and b) the field distribution along the metallic wires in it. b), d) Band gap structure of the present metamaterial. 2) Spin-polarized transport of photonic edge states provided by the band gap structure of the metamaterial. This is the unique feature of this structure which makes it part of the spintronics [82].

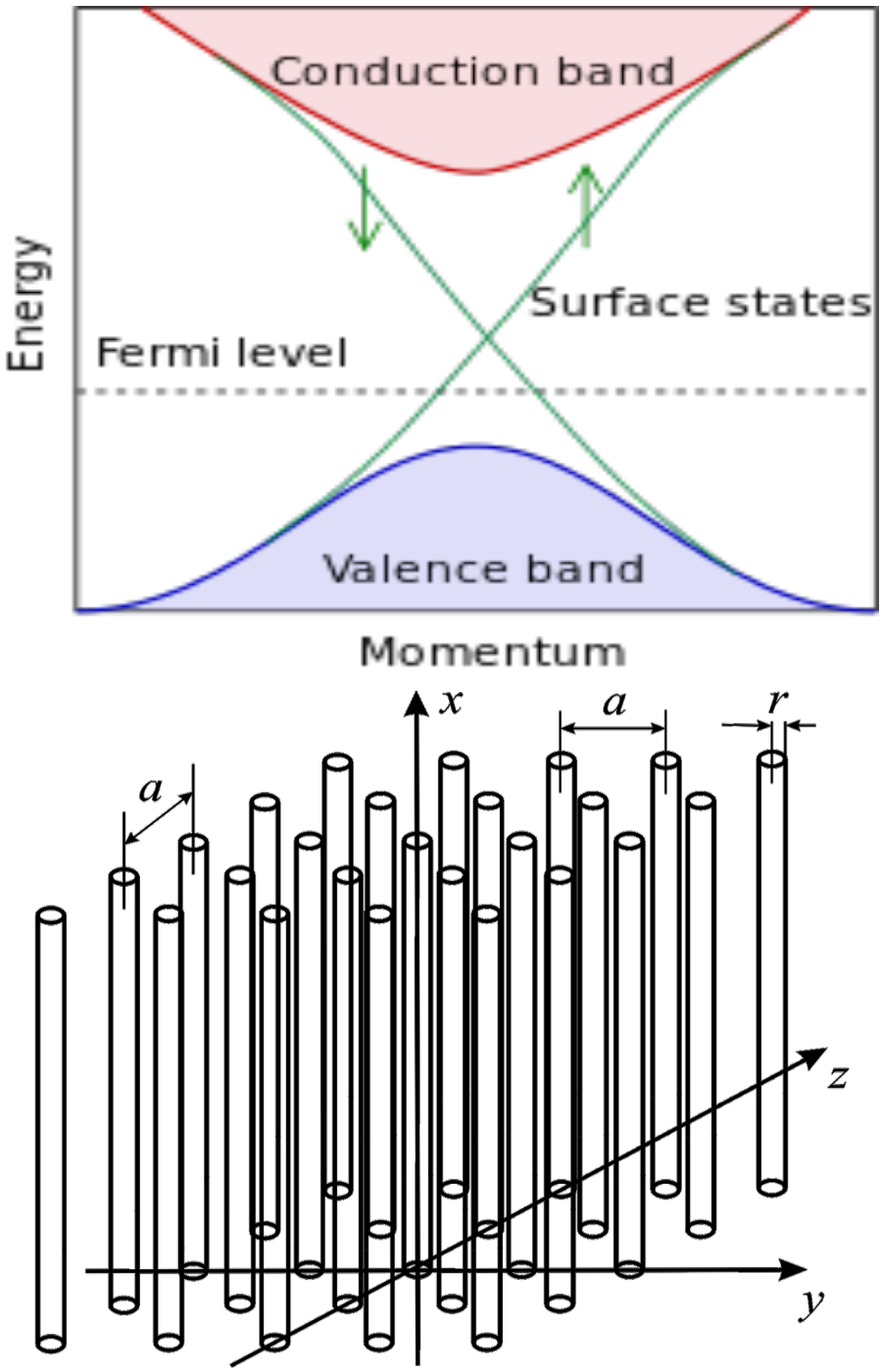

Figure 29 An idealized band structure for a topological insulator [81] and a general view of the wire medium.

Apart from that the wire medium is a well-known metamaterial for imaging purposes [92-94]. The last research activities with it are related to the power transfer and radiation enhancement [95-97]. Recently it was found that the wire medium with thick wires (the wire diameter is larger than the half of the array period value) has a magnetic permeability not equal to one [98]. In addition, the influence of the host matrix was recently performed [99]. Therefore, it could be a good idea is to analyze

the properties of the meta-waveguide described above with the magnetic response and host media constant of the material considered.

2.5 Conclusion

Thus, many theoretical and practical models which are parts of the very promising area of spintronics were considered. The theoretical basement of this area which answers the question on how the electron spin reacts to the applied magnetic field shown. It helped to understand the physics of the Electron Paramagnetic Resonance phenomena as well as the properties of the materials which are important in spintronics in a netter way. The magnetic field strength is nothing but the function, which defines the EPR effect. The observed materials and effects clearly show that the spintronic properties are very widely presented across the different setups.

The device for the transfer of the magnetic field from coaxial source cable to the Hall-bar structure will be investigated numerically in the further chapters. A few scanning techniques based on Atomic Force Microscopy setup will be studied theoretically, numerically and experimentally as well. The microwave field to nanoscale objects interaction is a common point for all these models. The unique and interesting features and applications of these devices will be covered.

Chapter 3. Spintronic modifications of the Atomic Force Microscopy

3.1 Scanning Microwave Microscopy (SMM)

3.1.1 Atomic Force Microscopy Basics

Mapping physical properties of materials, such as impedance, capacitance, dielectric constants, dopant density, etc., at the nanoscale is of great interest to both materials and semiconductor industries [100]. Such mapping, however, usually is not as straightforward as topography imaging because, in many cases, these properties are related to structures not directly shown on the surface but buried inside of a sample. It takes innovative approaches to "see through" and meanwhile achieve sufficient sensitivity and resolution.

Using microwave frequency as the medium, Scanning Microwave Microscopy (SMM) measures electromagnetic interactions of the microwave signal from a sharp probe or aperture with the sample under test on a scale that is significantly less than the wavelength of the radiation [101]. STM or SMM typically uses a metal or metal-coated probe in-line with a coaxial resonator. Materials properties were obtained from the frequency shift and/or change of quality factor of the resonance.

AFM based scanning capacitance microscopy firstly has been applied to semiconductors, measuring two-dimensional dopant density [102]. Operating at 915 MHz, commonly used SCM employs a Radio Corporation of America (RCA) capacitance sensor that detects the capacitance-induced frequency shift. In fact, SCM measures changes of capacitance, rather than capacitance, caused by depletion of doped carriers with a change of applied voltage, known as $\frac{dC}{dV}$, which correlates to the dopant density under certain conditions. This technique, however, is widely used in a qualitative manner for the lack of quantification process [100].

The scanning microwave microscope consists of an AFM [103] interfaced with a vector network analyzer [104], as shown in Fig. 30. With appropriate calibration standards, the system is capable to perform quantitative measurements on capacitance and dopant density.

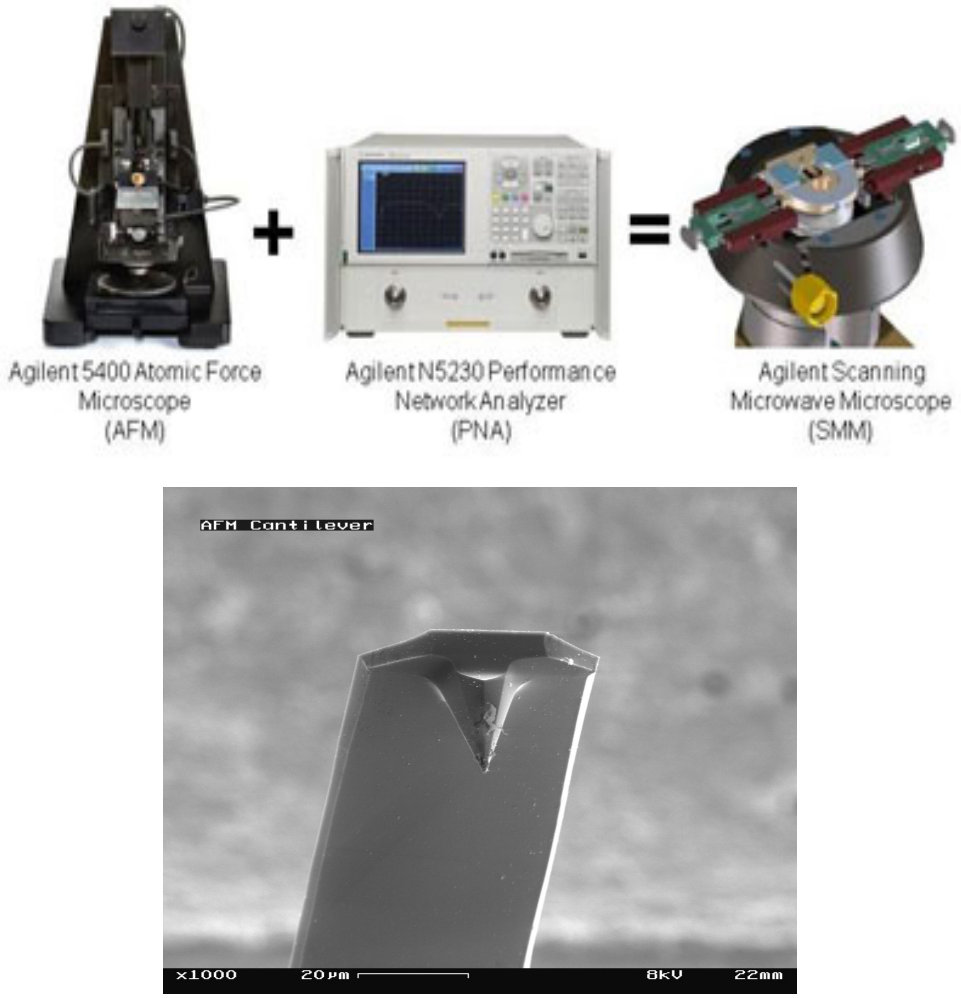

Figure 30 SMM Mode consists of an AFM interfaced with a vector network analyser (top image). A microwave signal is transmitted from the network analyser through a matched resonant circuit to a conductive cantilever – the very sensitive part which interacts with a sample (bottom) [100].

Detailed theory of scanning microwave microscopy should consider both the electromagnetic interaction of the probe and the sample at the contact point and the transmission line theory for microwave network analysis. A simplified picture can be understood using an optical analogy.

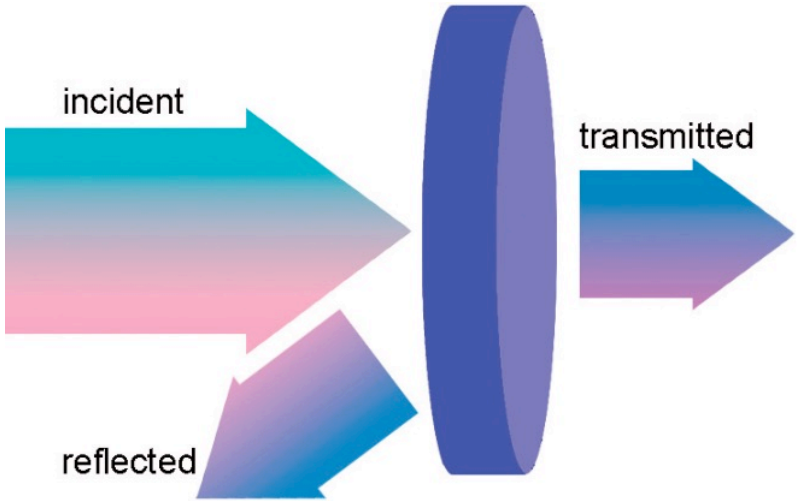

Figure 31 An optical analogy of microwave network analysis. The object illuminated by the incident wave [100].

As shown in Fig. 31, when light strikes an object, some of the light is reflected from the object, and some passes through. By measuring the amount of light reflected and/or transmitted, optical properties of the object can be calculated. Applying the same principle for microwave frequency of a few GHz, measurements of the incident and reflected, and/or transmitted waves can provide detailed information about the properties of the material under test. The two-port vector network analyzer can provide both reflection and transmission measurements. In the reflection mode (S11 measurement), the measured complex reflection coefficient Γ of the microwave signal from the contact point can be written as [100]:

$$\Gamma = \frac{V_{reflected}}{V_{incident}} = \frac{Z_L - Z_0}{Z_L + Z_0} \quad (110),$$

where $V_{incident}$ and $V_{reflected}$ are the incident and reflected waves respectively, and Z_L and Z_0 are the impedance of the sample under test and the characteristic impedance of the transmission line respectively. The maximum sensitivity is obtained at the resonance where the impedance of the sample under test matches the characteristic impedance, typically 50 Ω. Near the resonance, the measured complex reflection coefficient directly correlates to the impedance of the sample at the contact point. Small changes in the slightly mismatched impedance signal can be separated from the big background, resulting in a very high sensitivity. Under negligible variation of the resistance, the measured impedance signal then reflects changes of the capacitance of the sample at the contact point with appropriate phase offset. After calibration, the capacitance can be then obtained along with the surface topography.

3.1.2 Obtained experimental results

A few representative samples have been examined to test the capabilities of the SMM mode in a group of Ferry Kienberger in Linz (Keysight, Austria). These samples were provided by our colleagues from CNR (Rome) and BNC (London). It wasn't a typical measurement for these guys, but we were curious to find any interesting facts and artifacts within these samples.

Firstly, the magnetic domains in Permalloy sample were investigated. The latter is a well-known kind of nickel–iron magnetic alloy as it was invented by Gustav Elmen at Bell Telephone Laboratories in 1914 [105]. This kind consists of about 80% of nickel and 20% of iron. It possesses very high magnetic permeability, which makes it useful as a magnetic core material in electrical and electronic equipment, as well as in the magnetic shielding to block magnetic fields. Commercial Permalloy alloys typically have relative permeability of around 100,000 compared to several thousand values for ordinary steel [106] which is impressive. Later, in 1923, it was found that its permeability could be greatly enhanced by heat treatment [107].

In addition to high permeability, its other magnetic properties are low coercivity (a measure of the ability of a ferromagnetic material steadiness against an external magnetic field without becoming demagnetized), near zero magnetostriction (property of ferromagnetic materials that causes them to change their shape or dimensions during the process of magnetization), and significant anisotropic magnetoresistance.

The frequency was taken to be 19 GHz. The idea was to show that in contrast to the classical atomic force microscopy images (AFM, Fig.33 a)-b)) where you see quite good picture of the sample's surface you could also get an information about the magnetic properties of the material (Fig.33 c)-d)). It shows the deflection and the phase of the tip, and you could easily notice the magnetic artifact in the middle of the bottom part of the investigated area (it is a black ovel curve on Fig. 34 c) and the white one in the middle bottom on Fig. 34 d)). There is no sign of it on the AFM images (Fig. 33) where only the surface of the sample is obtained.

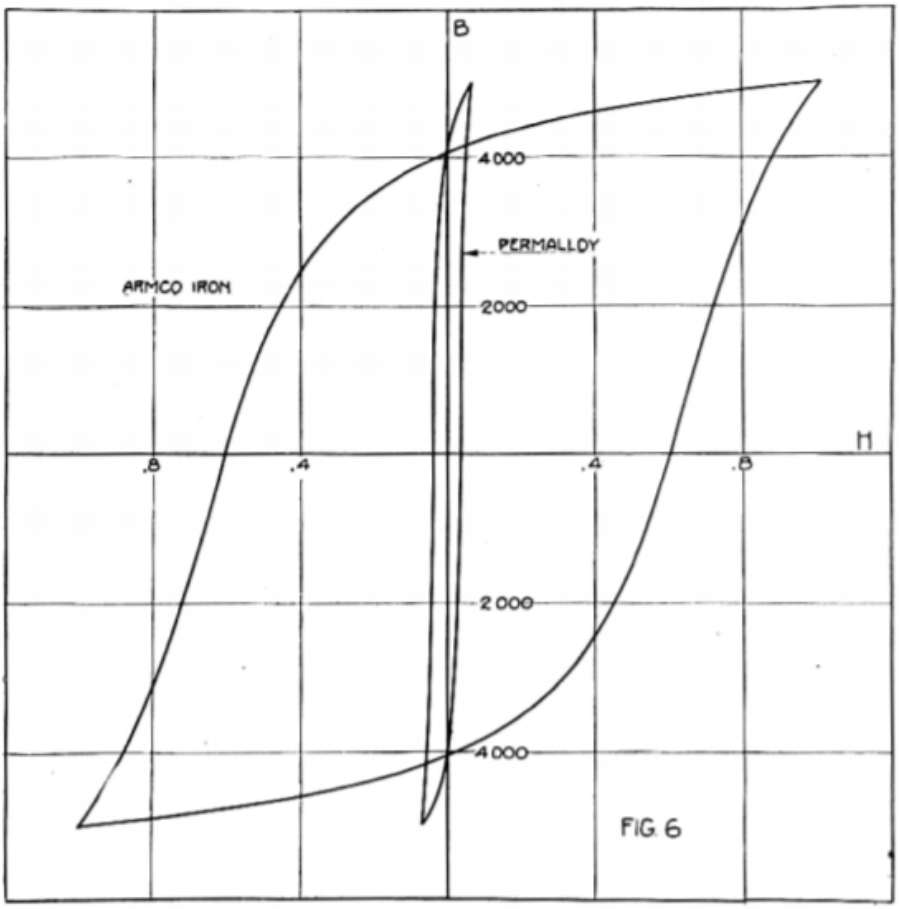

Figure 32 The hysteresis loop for Armco iron compare to Permalloy, carried to a maximum induction of 5000 Maxwell's. The area of the Permalloy loop is only one sixteenth of the loop for soft iron [106].

It is needed to be pointed out that before the measurement there is a crucial part of any AFM, SMM or EFM (Electrostatic Force Microscopy, will be described below) investigation - it is a calibration of the experimental setup. Without it nobody could distinguish the experimental data from the noises and the setup measurement uncertainties.

a)

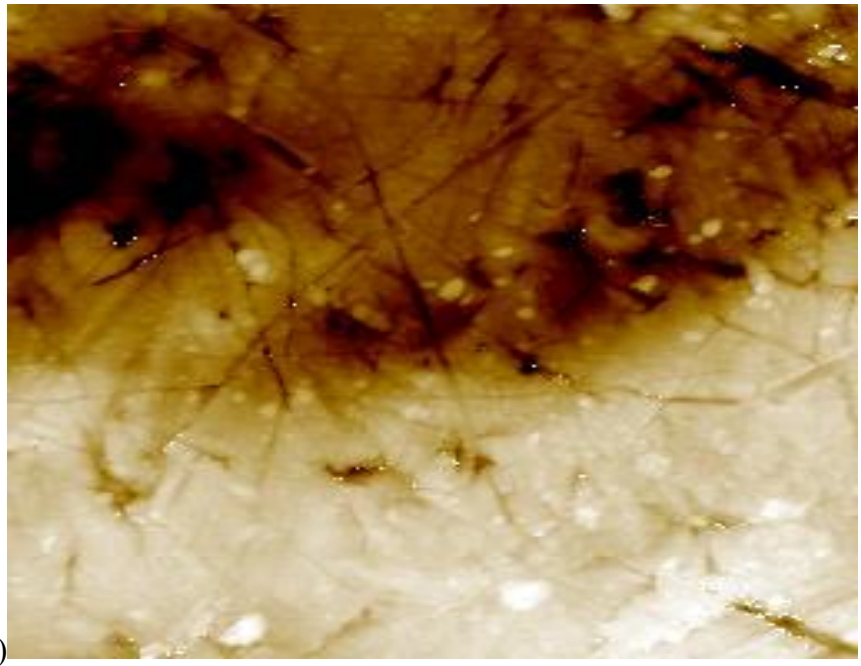

b)

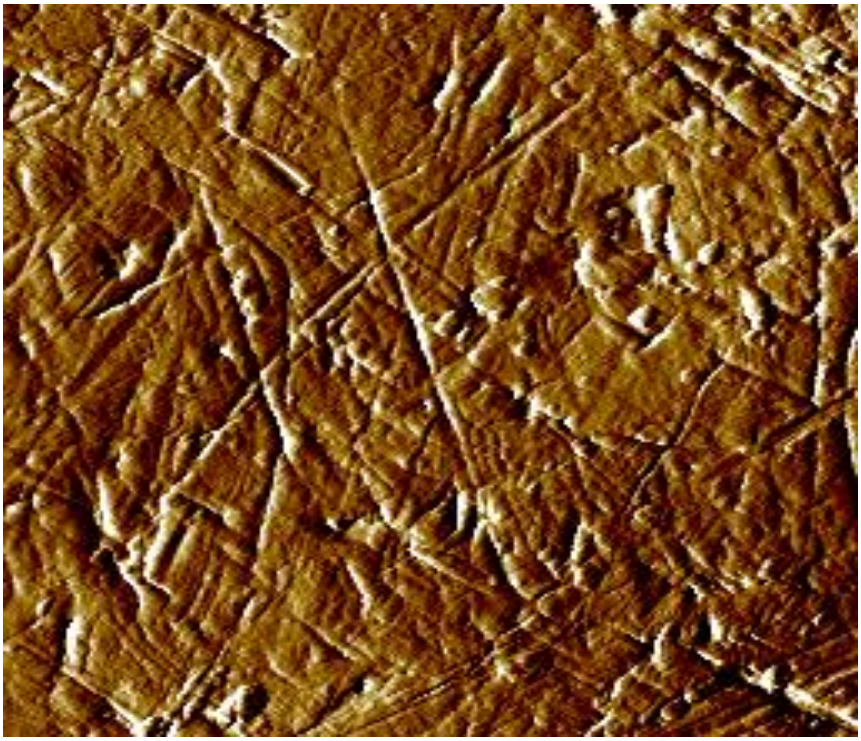

Figure 33 The classic pack of experimentally obtained SMM images. Two of them (a-b) are typical atomic force microscopy (AFM) pictures obtained for the Permalloy sample. Those pictures are normally taken for comparison.

a)

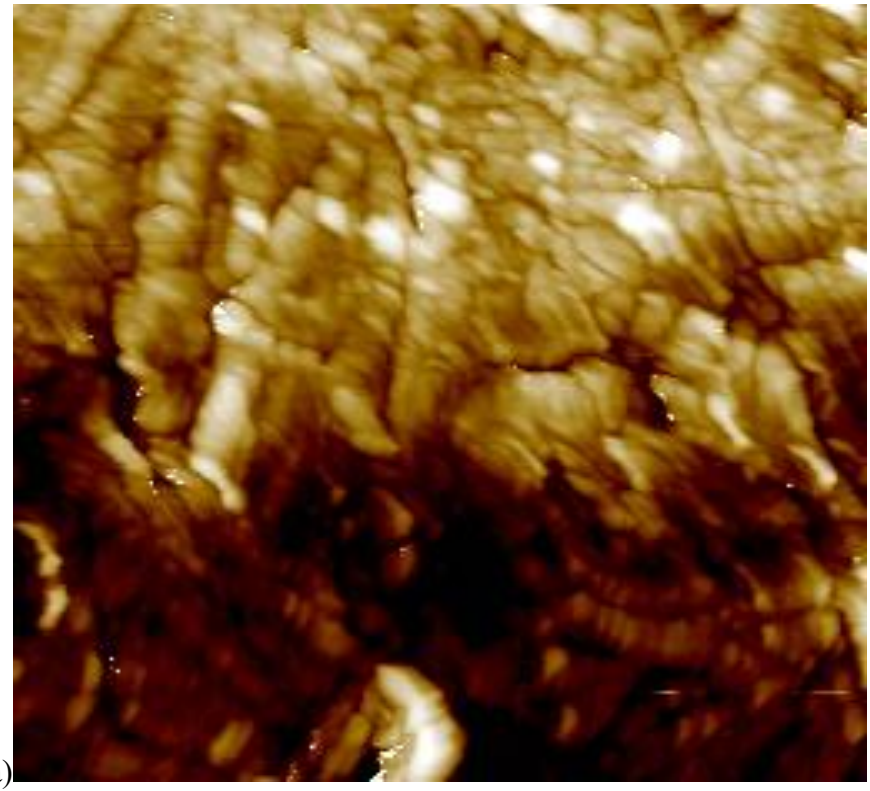

b)

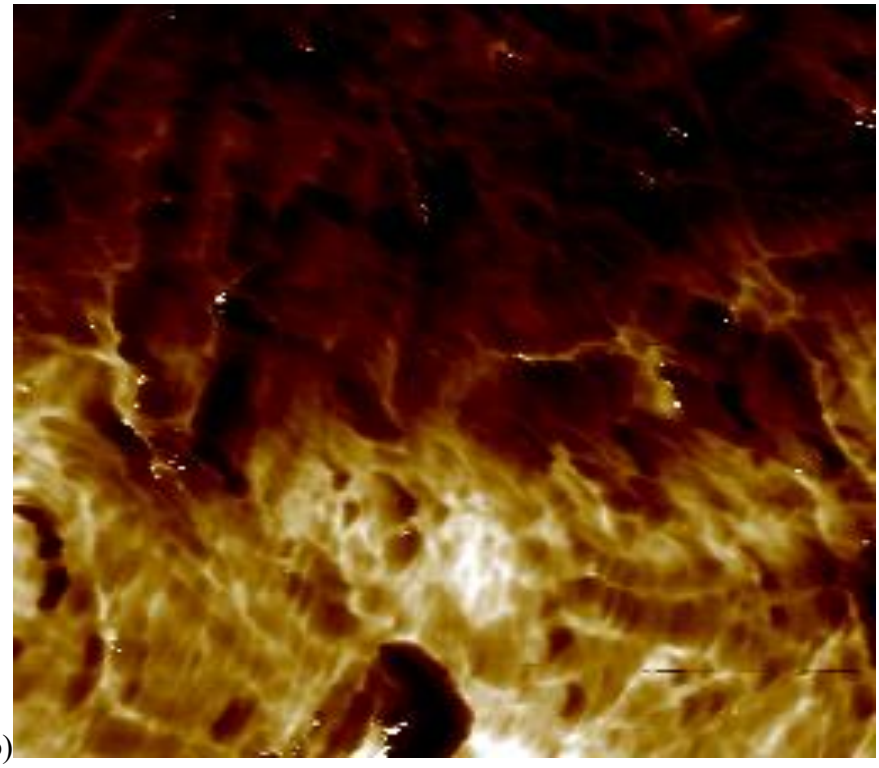

Figure 34 The classic pack of experimentally obtained SMM images. Pictures (a-b) showing the data distinguished by the SMM for the same Permalloy sample. The artefact was found at the bottom part of the SMM images, and the sample was further investigated by CNR in Rome.

Normally a few approach curves (the S11 signal curves) performed on test sample before the main sample measurement in order to calibrate the setup. It takes time and patience, but it is necessary point for correct measurements.

The further experimental was taken from the sample with a different dopant concentration. It is quite popular kind of materials these days as highly doped silicone performs almost as metal, and it brings more challenges into modern physics research activities [108-109]. Thus, the setup was calibrated exactly as it was done in [110], where the Si sample with a SiO2 was investigated as well (Fig. 35).

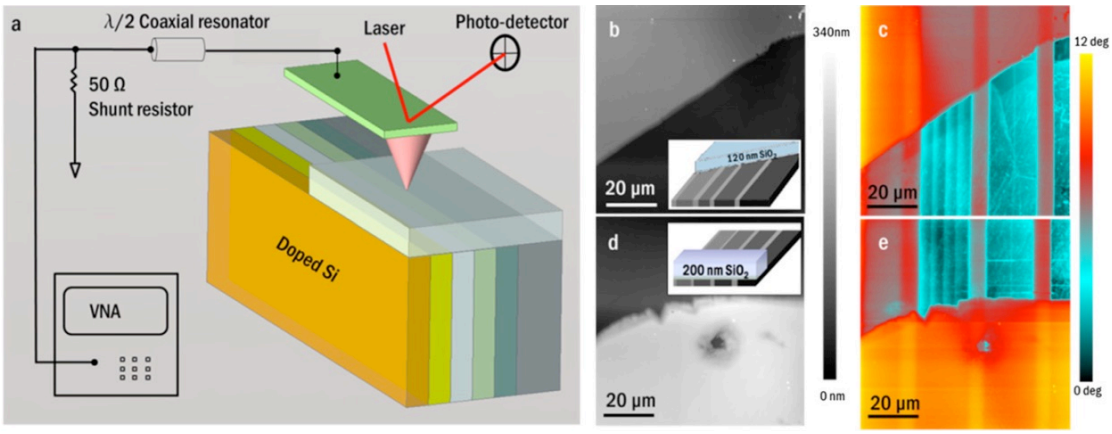

Figure 35 (a) The scanning microwave microscope (SMM) consists of a vector network analyzer (VNA) and an atomic force microscope (AFM). In reflection mode a GHz microwave signal is sent through a conductive platinum cantilever to electrically characterize the sample under investigation. One port of the VNA is used to measure the reflection coefficient S11. (b), (d) SMM images of a doped Si substrate partly covered with 120 nm and 200 nm. Panels (b), (d) show the topography images with a sketch of the sample (inset) and panels (c), (e) show the reflection S11 phase images with the subsurface dopant features [110].

The measurements were taken to be equal to the one performed in [111] where the ability of SMM to simultaneously probe topography, capacitance, and resistance of semiconductor samples was performed. Additionally, a method was presented to calculate resistivity and doping concentration from SMM resistance that could be applied to any semiconductor sample. The method has been validated on two doping profiling silicon samples, one measured in cross-section and the other one in standard top-down approach. The SMM capacitance and resistance values were characterized at 18 GHz with a noise level of 1 aF for capacitance.

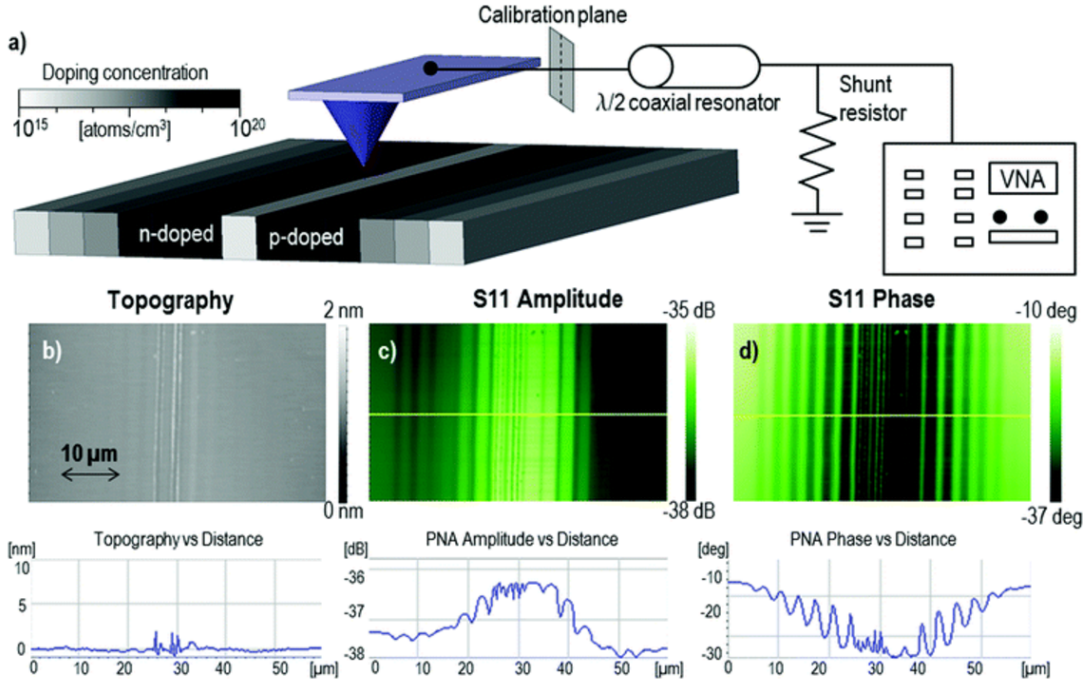

Figure 36 (a) Sketch of the SMM experimental setup and of the doped Si sample with flat topography. The sample consists of 10 different n-implant areas (left region) and 10 different p-implant areas (right region), each area with a width of 2 µm, with doping concentrations ranging from 4 × 1015 to 1 × 1020 atoms per cm^3. The SMM raw images of this sample are shown including flat topography (b), S11 amplitude (c) and S11 phase (d). The horizontal cross-sections are given below the images [111].

The SMM was at the stage of calibration and further development in Keysight at that moment. The secondment in Linz was taken to get e better understanding and get an experience in SMM usage. This has led to further investigations presented in the Chapter 3.4. The same experiment setup and sample as in [111] was taken for further calibration understanding and proof of the results. It could be easily seen that we have got even better images of the same sample (Fig. 37). The contrast of the obtained images is way better and the different in between the areas with a different doping level is very clear (compare to the bottom right images on Fig. 36). This sample has helped us to see how to investigate the sample without contact which looks plain and solid from the side but has a complicated layered dopped structure within. The SiO2 sample with Au particles on top were also investigated (Fig. 38) to test the SMM capabilities and limitations. The measurements of a classic magnetic hard disc were performed as well. It was noticed above that the new kind of a memory performance was one of the main outputs from the spintronics (GMR). Thus, it was very interesting to test the sample with an information decoded in a magnetic way.

a)

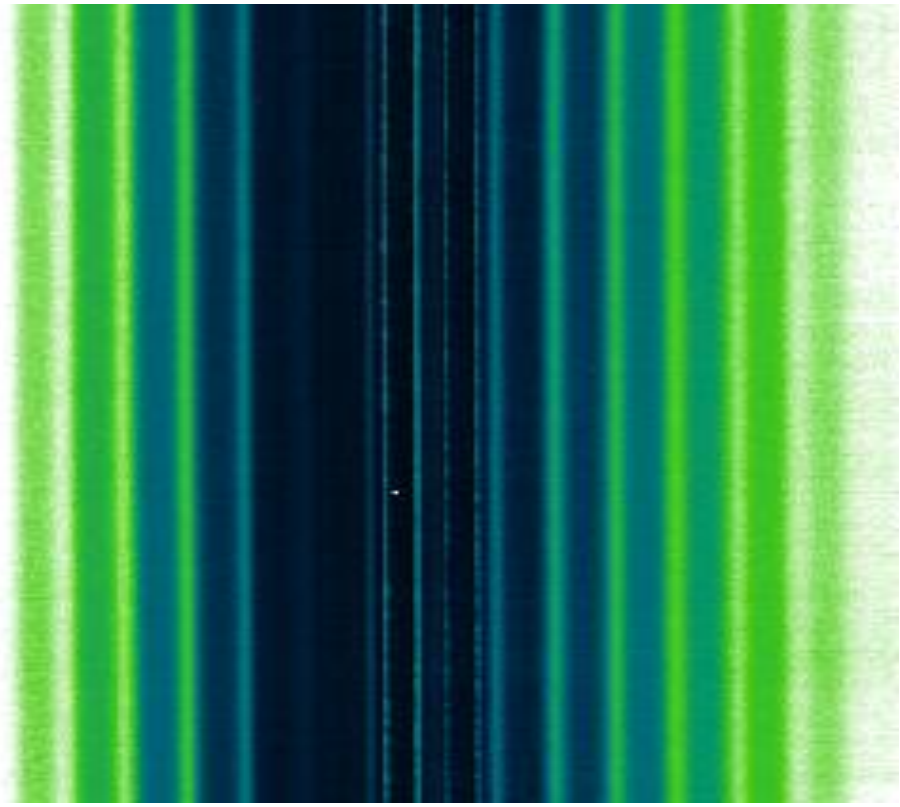

b)

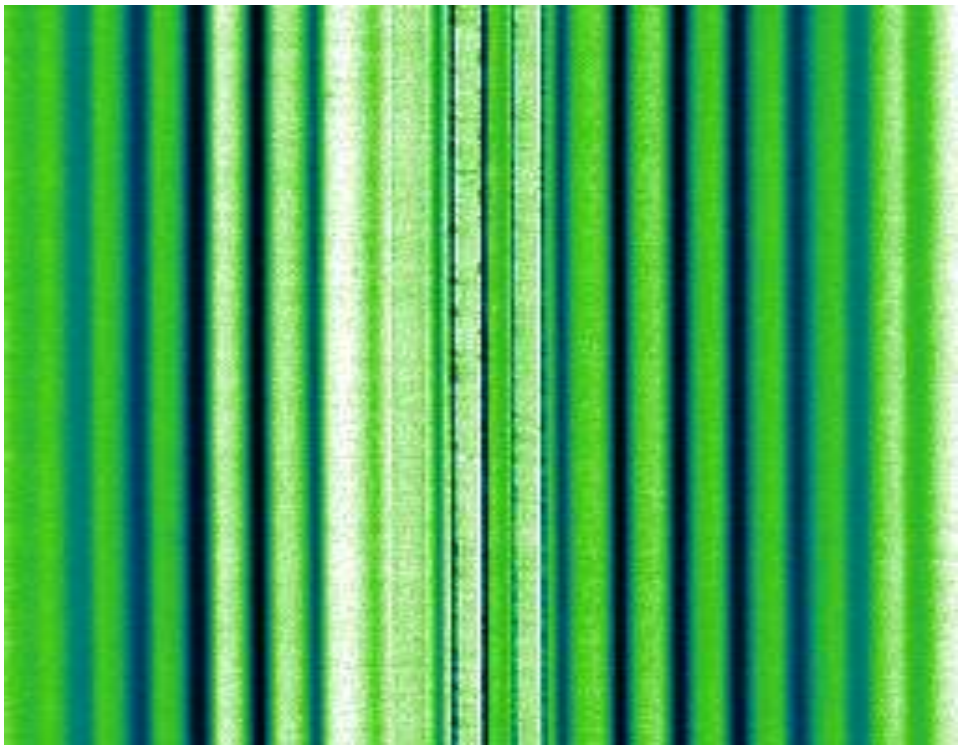

Figure 37 (a-b) S11 amplitude and phase of the doped Si sample obtained with SMM setup. The borders in between the layers with a different doping level are very clear.

a)

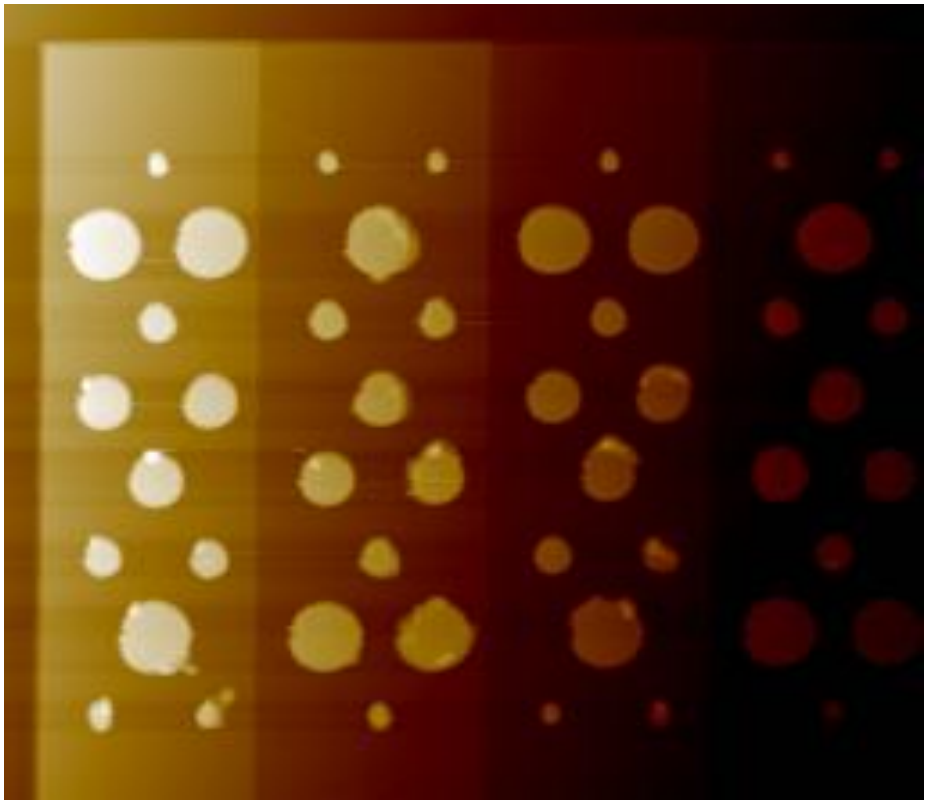

b)

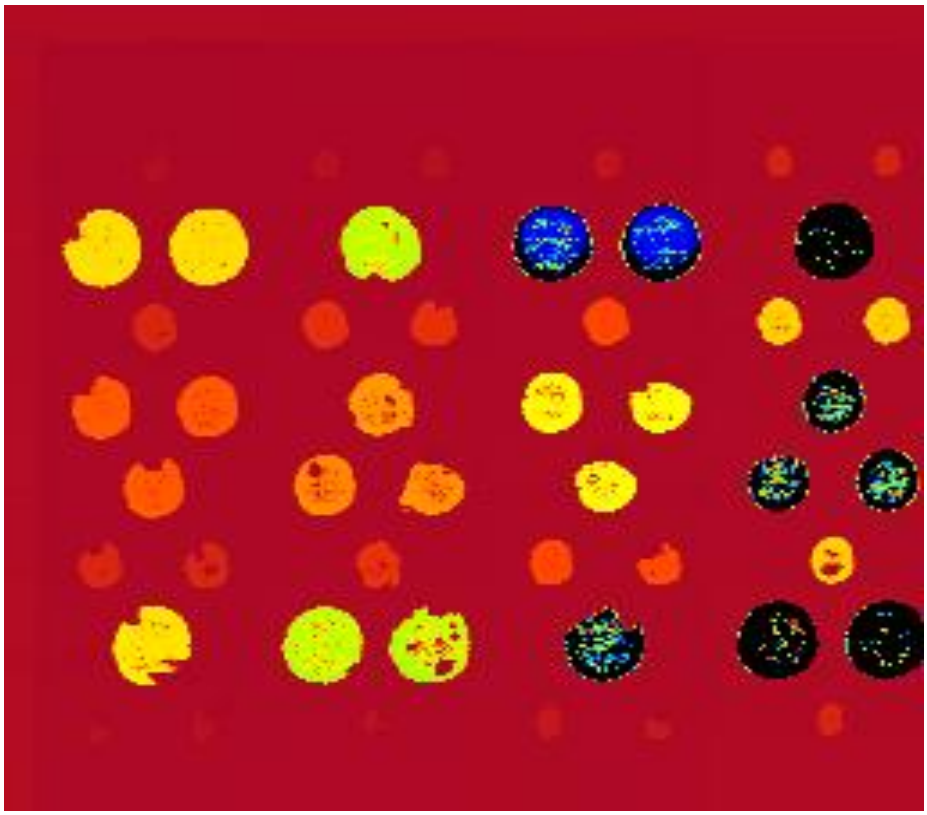

Figure 38 (a-b) S11 amplitude and phase for the sample with golden particles placed on top of the SiO2 obtained with SMM setup.

There was no image from the classic SMM tip. So, the special kind of measurement using a tip with a magnetic coating called magnetic force microscopy (MFM) was made. MFM is a family of techniques used to measure magnetic fields using an AFM.

In fact, there are a huge number of different techniques used to measure magnetic properties, but in general, they all use the AFM to measure the oscillation of a magnetically sensitive probe when it is far (5-100 nm) from the sample surface. MFM probes are usually made by coating normal silicon probes with a thin magnetic coating. The magnetic coating means that the oscillation of the probe will change when in a magnetic field. However, when the probe is touching the sample, the short-range tip-sample forces will obscure the magnetic forces (which are much weaker).

Fortunately, since magnetic forces can be measured at a distance, it is possible to remove the probe from the surface, and still measure magnetic forces, while removing these short-range forces. In order to make accurate measurements, the probe should be at the same distance from the sample throughout the image. There are several techniques to do this, which are reviewed in [112], but in most commercial implementations, the so-called "Lifting" method first used by Bard [113] is used. This method is illustrated schematically below.

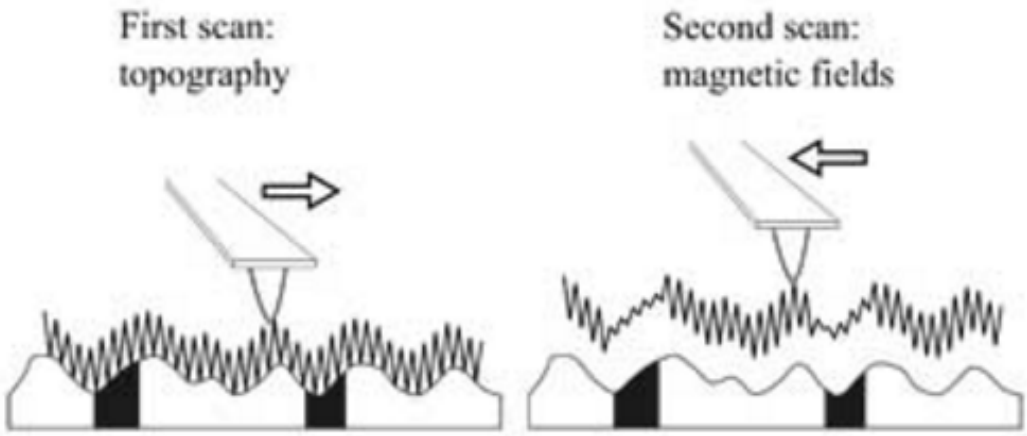

Figure 39 The way the MFM lifting modes work.

In order to make MFM measurements with this lifting mode, an oscillating mode is used, typically intermittent contact mode AFM. For each line of the image, two scans are made. In the first line, the topography is measured as usual (see Fig. 39). The probe is then lifted a user-defined distance above the surface (typically in the

range 5 to 50 nm). The second line will then be measured, but the topography measured in the first line is added to the height of the probe as it scans along the line.

a) 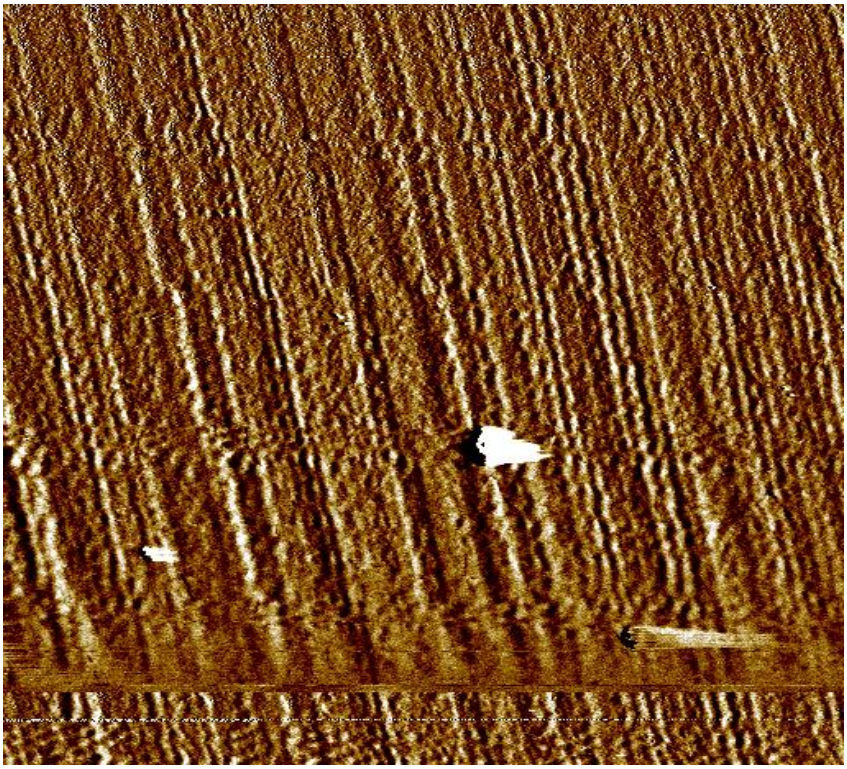

b) 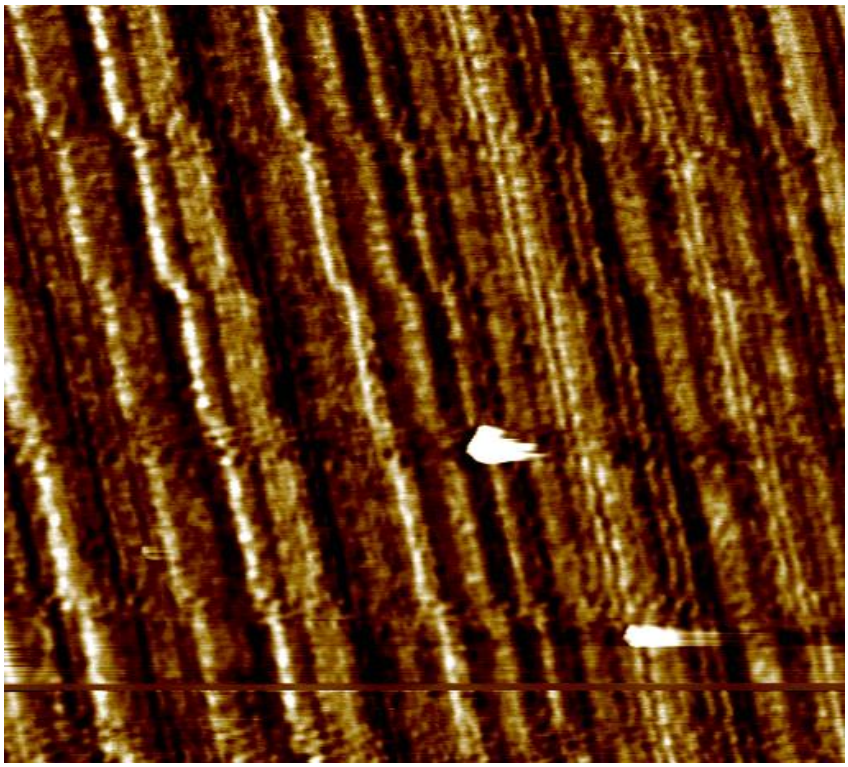

c) 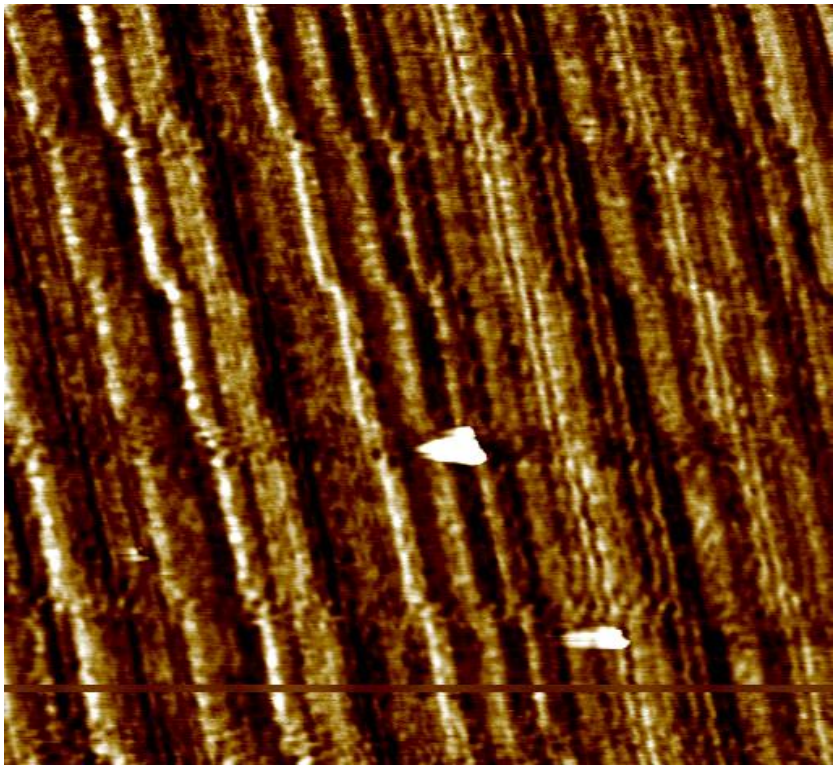

Figure 40 The MFM images of the old hard disc sample (the zoom capability tests from 10 to up to x200).

In this way, the instrument attempts to keep the probe at the same distance from the sample surface at each point in the MFM image. MFM is widely used to generate images of magnetic fields associated with small domains and is particularly of use in the development of magnetic recording technology. By applying the special kind of the tip, the images of the hard disc sample were observed (see Fig. 40).

The bacteria sample was also investigated. There is no need to go deep inside of the biological part of this measurement, but it is important to stress that the SMM could be used for biological samples measurements as well. This is a very important application for the scanning microscope these days. There are a lot of investigations with different types of bacteria. As part of the "Nanomicrowave" project the lecture about the current state of art and the popular topics for investigations in the aria of medical drugs investigations. It has become obvious that there are a lot of measurements happening every day in the laboratories with those bacteria, mice, blood and so on.

a)

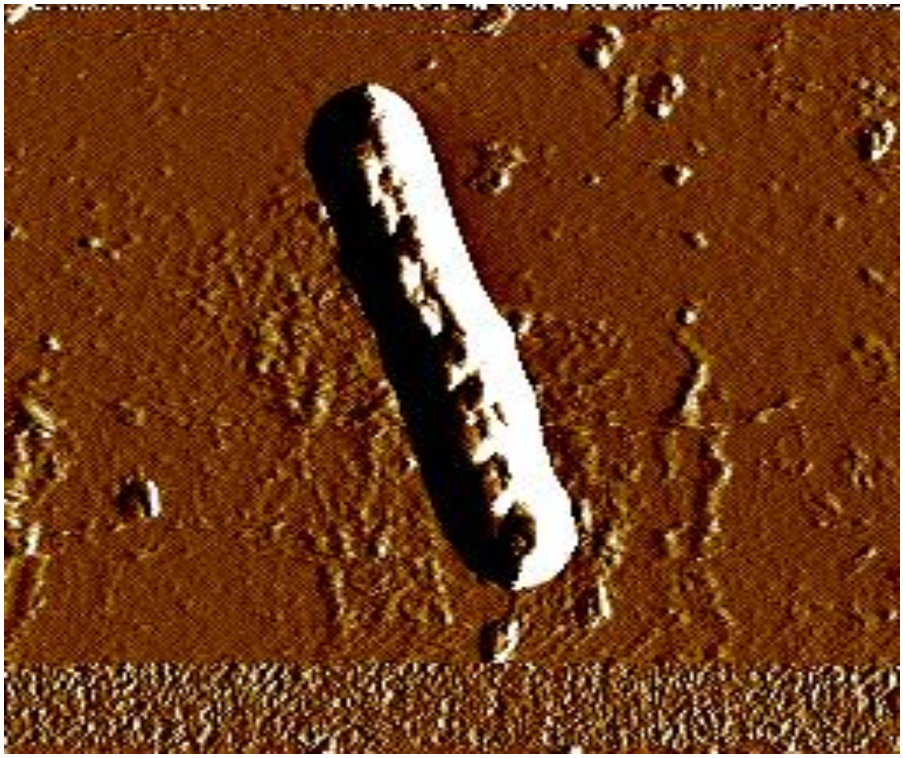

b)

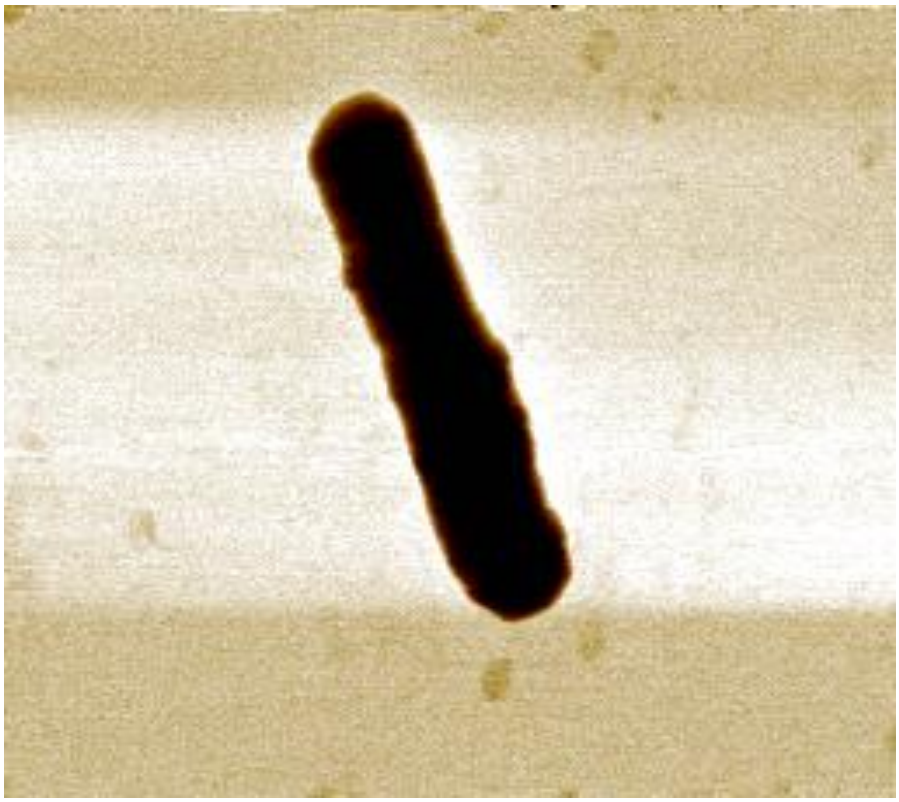

Figure 41 The topography (a-b) of the bacteria sample obtained with SMM setup.

a)

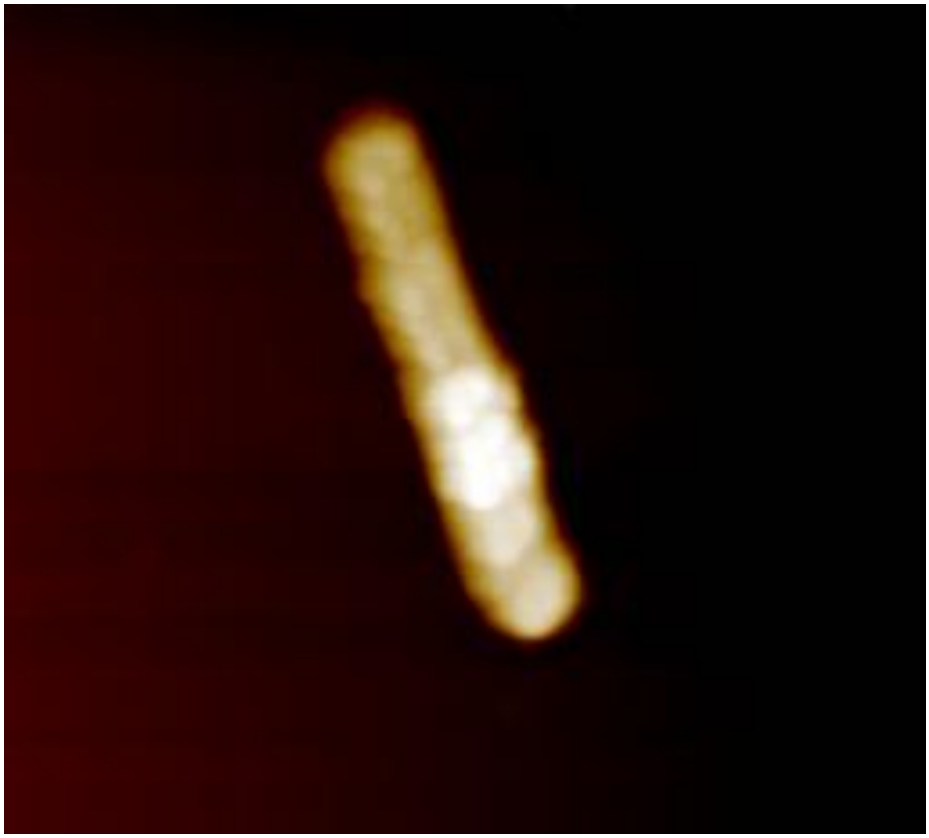

b)

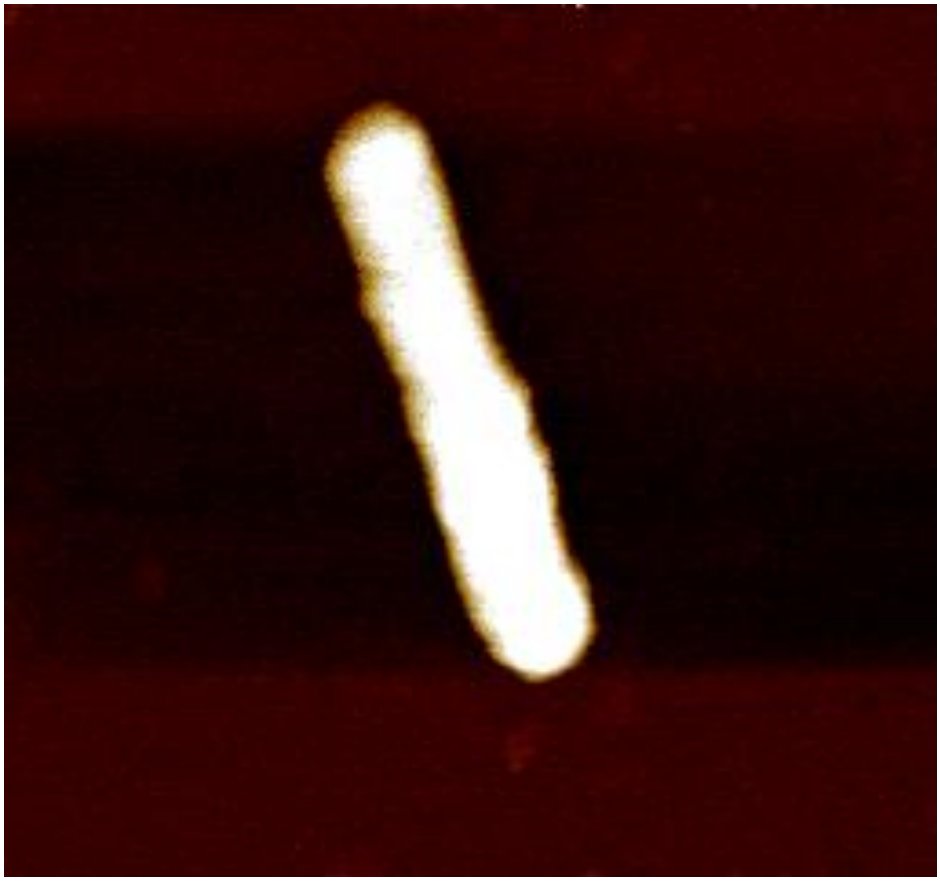

Figure 42 (a-b) S11 images of the bacteria sample obtained with SMM setup.

There is a common issue with bacteria and any other living being under investigation these days – sometimes we could not touch the sample of this kind, but we need to investigate its properties. Therefore, any technique or method with an ability to provide the precise image of the properties we need in that case is very useful and has lots of applications. From the images that was taken (Fig. 41-42) the protein concentration profile inside of the bacteria could be achieved. Those images and lots of others we've made in Liz with my colleague Ascanio (Imperial College of London) were used for his PhD thesis. It is time-consuming (as many samples need to be investigated in the same way to proof the theory behind) but very useful technique to study the biological samples.

The SMM was not the only scanning technique tested and investigated. The other approach to modify classical AFM setup was studied and the details are given in the next Chapter 3.2. Not only the experiment setup was tested but the theory and numerical calculations for better understanding as well.

3.2 Electrostatic Force Microscopy (EFM)

3.2.1 Introduction

As it was mentioned above the SMM is not the only one variation of the typical atomic force microscopy (AFM). There is another one called Electrostatic Force Microscopy (EFM).

Based on AFM equipment, the EFM is now an experimentally established method for local observations and measurements on semiconductors. In addition to morphology, three other classes of data related to electrical characterization can be obtained: nano-Kelvin operation gives the work function which can be correlated with surface to bulk capacitances; the spatial extent of constant voltages, force or capacitance, particularly for any low-dimensional semiconductor structure; the local voltage behavior on an operating structure, or noncontact nano potentiometry. All these data are important for technological process control and failure analysis. Improvements in spatial resolution, as recently shown in electrostatic force gradient microscopy, make EFM of even greater interest in connection with other electrical methods such as scanning capacitance or spreading resistance. Finally, concerning more fundamental studies, the capability for nano connection with AFM-like methods could offer soon the ability to explore the electrical or optical behavior of individual nanostructures [115].

3.2.2 Key Principles

It is needed to go a little bit into the theory here. Since EFM is mainly devoted to voltage detection and can lead to measurements of the local dc voltage, we shall essentially concentrate on this point. When a voltage V occurs between a sample and the EFM sensor maintained at close proximity, the electrostatic force F can be written as:

$$F = \frac{1}{2} dC/dz\, V^2 \qquad (111),$$

where C is the tip to sample capacitance. We assume that the voltage V is composed of the contact potential V_{cp} plus applied dc and sinusoidal voltages, V_{dc} and V_{ac} respectively, with, in addition, an externally induced surface voltage $V_{induced}$ related to the extra dc voltages on an operating device, for example $V = (V_{cp} + V_{dc} + V_{induced}) + V_{ac} \sin \Omega t$ Then, referring to the frequency, i.e. dc, or 2, the force can be decomposed into three terms. Firstly,

$$F_{dc} = \frac{1}{2} dC/dz \left[(V_{cp} + V_{dc} + V_{induced})^2 + \frac{1}{2} V_{ac}^2 \right] \quad (112)$$

which bends the cantilever continuously, but which is difficult to detect. Secondly

$$F_{\Omega} = dC/dz \left(V_{dc} + V_{cp} + V_{induced} \right) V_{ac} \sin \Omega t \quad (113)$$

This term has a simple linear dependence on the capacitive coupling dC/dz and the sample voltages V_{cp} and $V_{induced}$. So capacitive coupling and voltage contrasts are expected to be seen on the force signal F_{Ω}. Using signal processing it can easily be extracted from noise and imaged when scanning the sample at a constant tip–sample distance.

If, in addition, a closed loop injects a voltage V_{dc} such as $F_{\Omega} = 0$, i.e. $V_{dc} = -(V_{cp} + V_{induced})$, surface voltage variations related either to V_{cp} or to $V_{induced}$ can be measured and imaged; this is called nano-Kelvin operation. The third term

$$F_{2\Omega} = -\frac{1}{4} dC/dz \, V_{ac}^2 \cos 2\Omega t \quad (114)$$

depends on local capacitive coupling. If only ac signals are involved, with different frequencies on the tip and the sample, their behavior is mixed, giving rise to bending of the cantilever at both the sum and the difference of frequencies. So, even in the gigahertz range the presence of a voltage on the sample can be analyzed [115, 116] if the frequency difference is in the kilohertz range. If charges are involved instead of voltages, the F_{Ω} signal is also observed [117, 118]. It is generally assumed that an insulator, bringing charges to its surface at a distance z from the tip, is sandwiched between a conducting plane and the EFM sensor, and that voltages are applied similarly to the case we examined first. Then a supplementary Coulomb force

arises between the static charge Q_s of the sample and the ac charge induced on the tip, i.e., CV_{ac}. Then F_Ω can be written as

$$F_\Omega = \left[dC\ /\mathrm{dz}\left(V_{cp} + V_{dc}\right) - Q_s C\ /(4\pi\varepsilon_0 z^2)\right] V_{ac} \sin \Omega t \qquad (115)$$

So, the sign and position of charges Q_s can be obtained, but their measurement strongly depends on the particular tip to sample configuration and is not as simple as for voltages. Thus, by using the EFM non-contact method physical data such as surface to bulk sample capacitance and DC surface voltages can be measured. The localization of DC charges and high-frequency voltages has been reported. However, the scale of performance must be precise in terms of voltage resolution but also in terms of spatial resolution if application to the analysis of low-dimensional semiconductor devices is to happen.

3.2.3 Experiment and Post-processing

In order to get the skills in an EFM measurements and post-processing under this data the training was passed in the Institute for Bioengineering of Catalonia (IBEC, Barcelona) in a Nanoscale bioelectrical characterization research group of Gabriel Gomila Lluch.

Firstly, a few experimental curves were taken on 26 nm thick SiO2 layer on a highly doped silicon substrate under a few assumptions. In the thin film limit, the simplified dependence of the polarization force on only the nanometric probe geometry allows us to derive an analytical expression for the electrostatic force. We start by remembering that, in general, there are three contributions to the electrostatic force signal, coming from the apex, cone, and cantilever, respectively. Thus, the capacitance gradient detected in EFM includes only contributions from these components, that is,

$$C'_{TEFM}(z, \varepsilon_r) = C'_{apex} + C'_{cone} + C'_{contilever} \qquad (116)$$

The variation of the cantilever contribution for nanometric displacements of the tip can be shown to be negligible, as compared to the cone and the apex contributions [119]. However, this is not the case for the bottom part of the cone. In

particular, the cone contribution plays an important role in the case of tips with a relatively small radius (R < 50 nm) and small/intermediate tip-sample distances (z < 100 nm). Therefore, for accurate interpretation of EFM data, the model in terms of capacitance gradient variations must include both the apex and cone contribution

$$\Delta C'_{TEFM}(z,\varepsilon_r) = \Delta C'_{apex}(z,\varepsilon_r) + \Delta C'_{cone}(z,\varepsilon_r) \tag{117}$$

The capacitance curves can then be theoretically interpreted in two different ways: (i) by assuming that the capacitance variation has two contributions as in [120], namely, the apex contribution and a linear stray contribution, which includes the cone, cantilever, and chip [120]

$$\Delta C'_{T}(z,\varepsilon_r) = \Delta C'_{apex}(z,\varepsilon_r) + k_{stray,T}(z_0 - z) \tag{118}$$

or (ii) by assuming that the capacitance variation has three contributions, namely, the apex contribution, the cone contribution, and a stray linear contribution, which includes only the cantilever and the chip contributions here,

$$\Delta C'_{T}(z,\varepsilon_r) = \Delta C'_{apex}(z,\varepsilon_r) + \Delta C'_{cone}(z,\varepsilon_r) + k_{stray,T}(z_0 - z) \tag{119}$$

and where

$$\Delta C'_{cone}(z,\varepsilon_r) = C'_{cone}(z,\varepsilon_r) - C'_{cone}(z_0,\varepsilon_r) \tag{120}$$

is obtained from the integration between z and z_0, i.e.,

$$C'_{cone}(z,\varepsilon_r) = \frac{-2\pi\varepsilon_0}{\ln[\tan(\theta/2)]^2} * \left[\left(z + \frac{h}{\varepsilon_r} + R(1-\sin\theta)\right)\ln\left(\frac{H}{z+\frac{h}{\varepsilon_r}+R(1-\sin\theta)}\right) + R(1-\sin\theta) + \frac{R\cos\theta^2}{\sin\theta}\ln\left[z + \frac{h}{\varepsilon_r} + R(1-\sin\theta)\right]\right] + C_1 \tag{121}$$

where c_1 is an irrelevant constant independent from z, the detailed description could be found in [121].

So, basically, there is a special way to implement the curve data and get the permittivity value by using the equations shown above. In order to do that several steps though writing the MATLAB code were passed and a bunch of numerical simulations was made. The approximation utilizing the approach stated above is shown on Fig. 43.

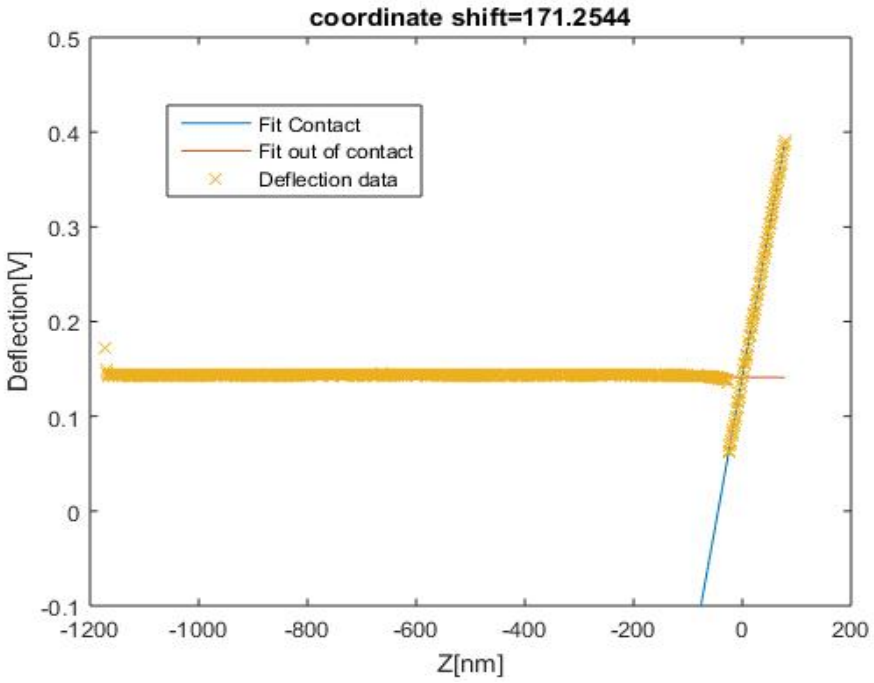

Figure 43 The EFM approximation of the curve data by splitting it into two parts.

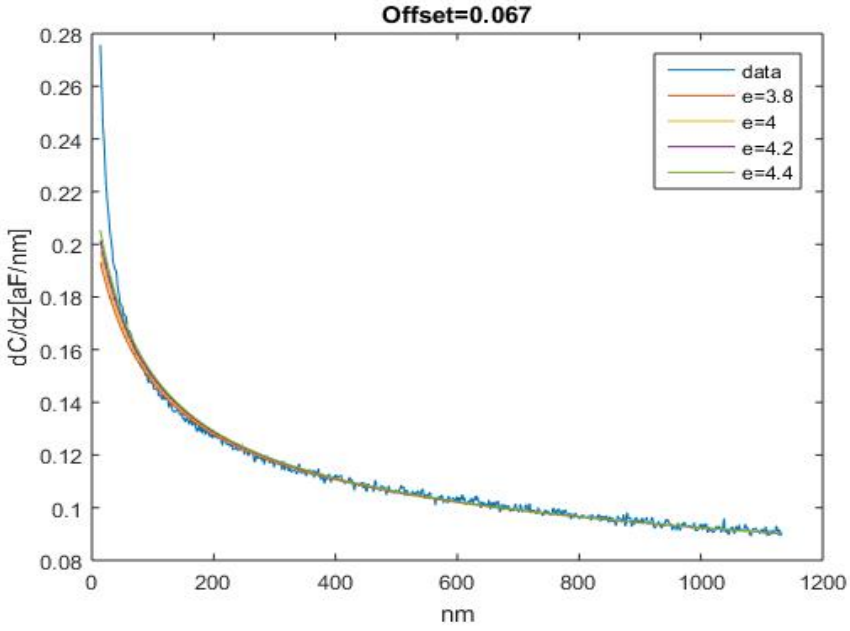

a)

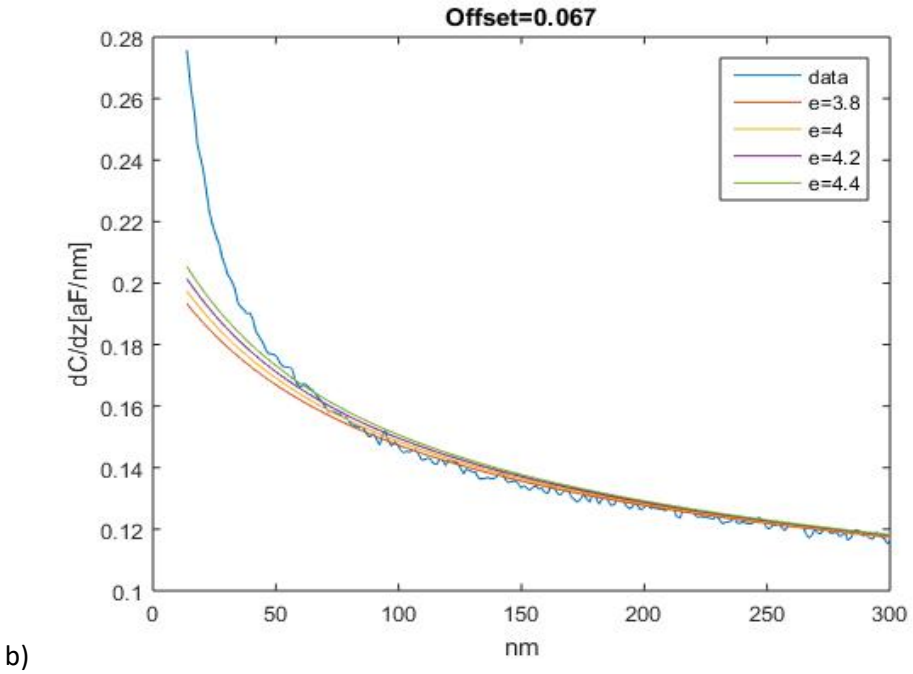

b)

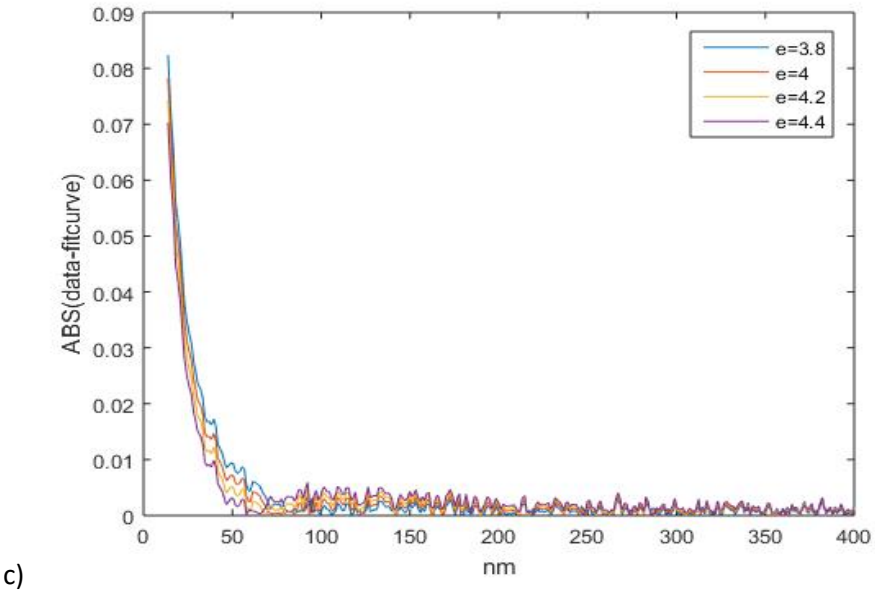

c)

Figure 44 The EFM fitting procedure for permittivity constant derivation. b) image is the enlarged copy of the a) one. It is necessary in order to pick the closest value and obtain the dielectric constant value.

Firstly, the curve was taken on a metal part without the SiO2. The original graph was approximated for contact and out of contact part equations. It is a typical calibration procedure. And, again as it was stated in Chapter 3.1, it is a necessary action which must be taken before any further measurements of the sample happened.

It has provided the first constant which was applied to the next MATLAB code for the curve on SiO2.

The next part was associated with a manual play in order to fit the final curve to the original experimental data. By doing this the permittivity constant could be distinguished. Thus, the post-processing was made, and it was the time to probate the skills on practice. A few EFM images were taken (Fig. 45 and Fig. 47), and the permittivity constants were derived from them (Fig. 46 and Fig. 48 respectively). The measuring area was tested to be as small as it possible for good results also. So, the single pillar images were taken (images b), d), f) on Fig. 45 and Fig. 47).

To sum up, the SMM and EFM measurements of a few samples was performed to test and prove the ability of the scanning microwave microscopy and electrostatic force microscopy to go deeper inside of a sample and tell the researches more than classic atomic force microscopy does. The biggest problem here was to be very focused during the calibration process as any tiny mistake could lead to the incorrect images at the end of a process. The EFM is very time-consuming process as every image is made step-by-step, point-by-point absolutely the same as SMM. These techniques are the very powerful tools as they provide the ability to study the properties of the samples which could not be investigated in the direct way. The experiments have provided to us a better understanding of a big area of experimental physics, the setup, the materials which used in the setup, and which could be investigated. We have found the gap in the setup simulations studies and tried to fill this “gap” in the next part of this work.

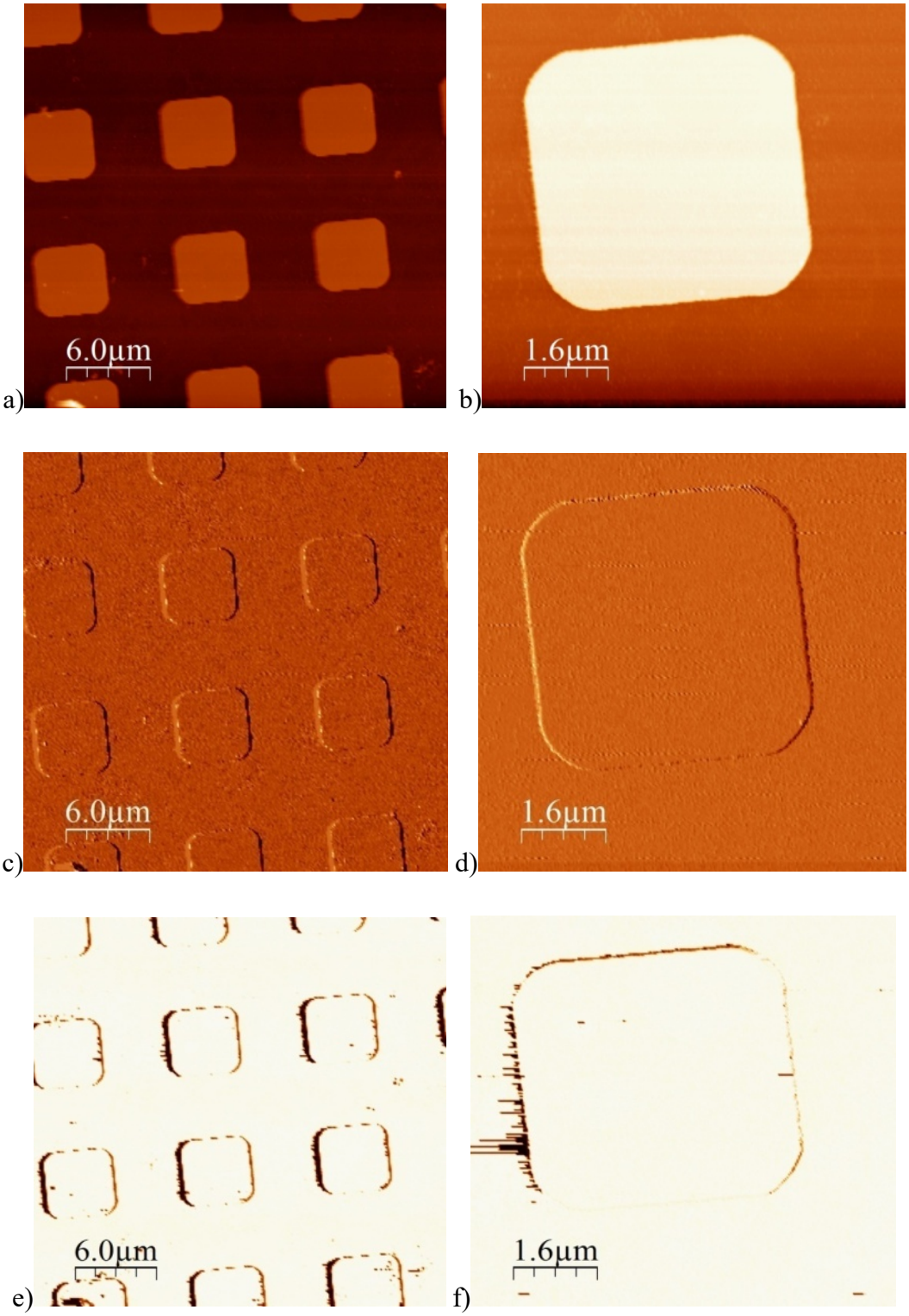

Figure 45 The Topology and EFM Images of the SiO2 pillars on top of the metal: larger(a),c),e)) and smaller area(b),d),f)).

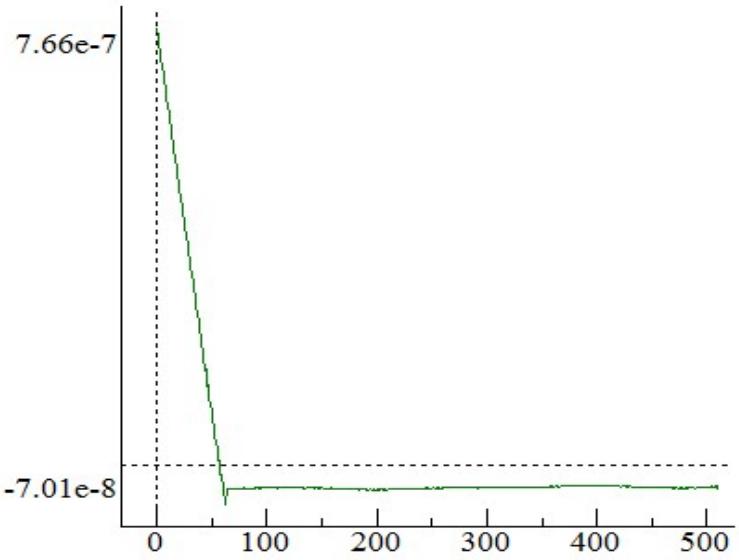

a)

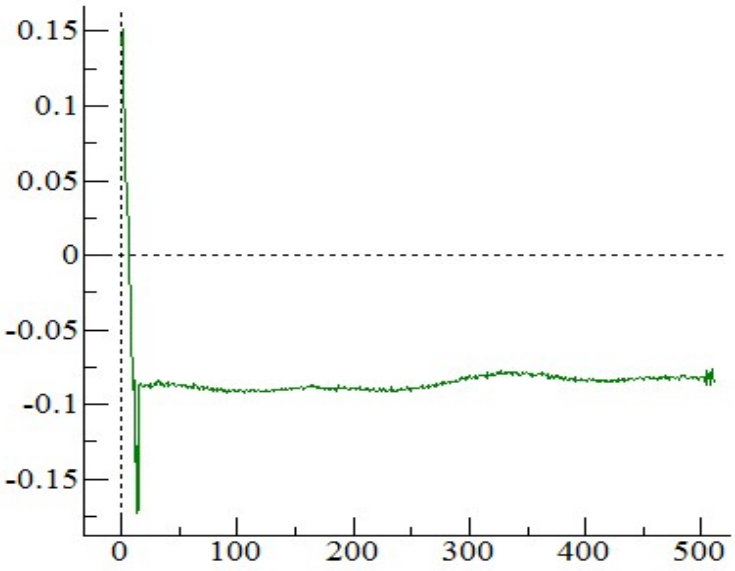

b)

Figure 46 The EFM approach curves on metal a) and on Sio2 b).

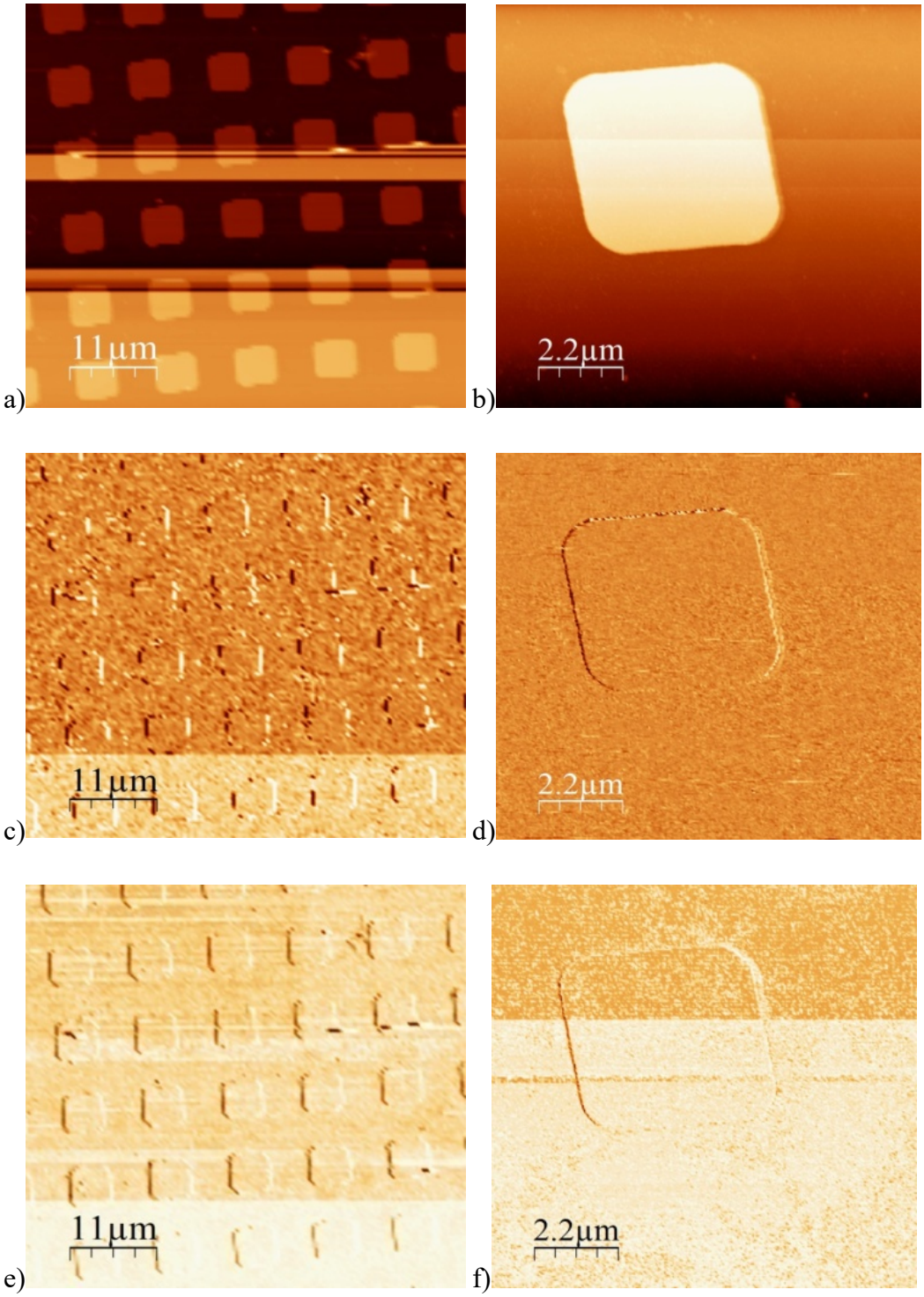

Figure 47 Different area of the sample. The Topology and EFM Images of the SiO2 pillars on top of the metal with 11-micron scale(a),c),e)) and 2.2-micron scale (b),d),f)).

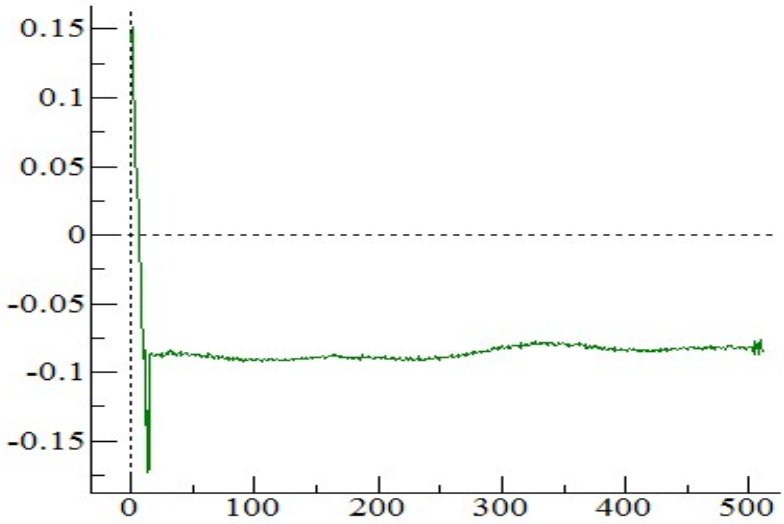

a)

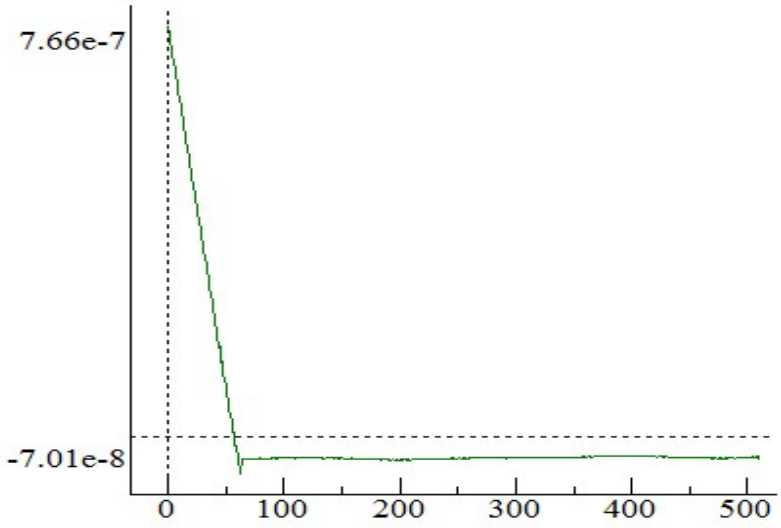

b)

Figure 48 The EFM approach curves on metal a) and on Sio2 pillar b).

3.4 Modelling of Atomic Force Microscopy Tip

3.4.1 Introduction

The study of numerical techniques, undertaken at the Institute for Bioengineering of Catalonia (IBEC) where both the experimental setup of the Electrostatic Force Microscopy (EFM) and modeling in MATLAB were completed presented above. It was important to understand both the theory and the experiment to find the gap in simulations approach. This time it was about the modelling in COMSOL simulations package. The aim was to obtain the knowledge and skills about this popular simulation tool and try to go deeper in the understanding of the physical processes which lays behind the three letters "EFM".

A few geometries were tested to see the way the COMSOL works and which of them are affordable. Finally, we've moved to the tip modeling. Here is a need to say a few words about the background of this task.

3.4.2 AFM tip simulation models comparison

Electrical scanning probe microscopy (SPM) techniques, such as EFM, nanoscale impedance microscopy or scanning near field microwave microscopy, are a relatively new branch of microscopy techniques that can generate images of the nanoscale electrical properties of samples (conductivity, permittivity, charge, etc.). These techniques scan the surface of a sample (bacteria, cells, polymer nanocomposites, nanomaterials, etc.) with an electric potential applied between tip and sample and provide electrical images with nanoscale spatial resolution. The established types of SPM have been proposed as a novel family of non-invasive techniques for medical diagnosis as well as non-destructive methods of quality controls for the MEMS and nanotechnology industries.

There are several theoretical models that mimic the SPM setup and its exploration techniques. These models solve the Maxwell's equations under the assumption of steady-state conditions in either conductive or insulating media (i.e.,

Poisson's or Laplace equations). However, very few of them have solved the full electromagnetic system and setting out the validity of the quasi-statics approximation.

Our goal is to quantify verify whether the above approximation holds valid for the case of the SMM, in which electromagnetic fields at GHz frequencies are used.

To achieve it we will first, solve the steady-state electric field for a SPM setup and determine the measurable quantities (e.g., tip-sample capacitance). Second for the same geometry of SPM setup used to the previous case, we will solve the full set of Maxwell equations, making special attention to the near field region which is the relevant one for the case of an SPM set up.

We will use a three-dimensional model in COMSOL Multiphysics. The SPM tip is modeling as a spherically blunted cone of semi-angle θ and height H, ending with a semi-sphere of radius R and capped with a disc of radius L + H tan(θ) and thickness W. The AC/DC electrostatic module will be used to solve the quasistatic solutions as well as the Radio Frequency module will be used for the full set of Maxwell equations.

We modeled the SPM setup at a known frequency ω, where both the electric fields and the magnetic fields are significant, or an induced current is present. We used the Frequency Domain interface on the Radio Frequency (RF) module of COMSOL. Consider the frequency-domain form of Maxwell's equations:

$$\nabla \times (\mu_r^{-1} \nabla \times E) - \omega^2 \varepsilon_0 \mu_0 \left(\varepsilon_r - \frac{i\sigma}{\omega \varepsilon_0}\right) E = 0 \qquad (122)$$

This equation solves for the electric field, E, at the operating (angular) frequency $\omega = 2\pi f$. The other inputs are the material properties: μ_r is the relative permeability, ε_r is the relative permittivity, and σ is the electrical conductivity. The boundary conditions on the metallic tip surface

$$n \times E = 0$$

$$n \times E = J_s \qquad (123)$$

with absorbing boundary conditions at the

$$\mathrm{n} \times (\nabla \times E) - jk_0 \mathrm{n} \times (\mathrm{E} \times n) = 0 \qquad (124)$$

The impedance of the antenna is

$$Z = R + jX \tag{125}$$

where R is the radiation resistance which is that part of an antenna's feed point resistance that is caused by the radiation of electromagnetic waves from the antenna, as opposed to loss resistance (also called ohmic resistance) which is caused by ordinary electrical resistance in the antenna, or energy lost to nearby objects, such as the earth, which dissipate RF energy as heat

$$R = \frac{P_{rad}}{0.5*|I_0|^2} \tag{126}$$

I_0 is current flow over the antenna load, P_{rad} is radiation power of the antenna, and it can be obtained by a surface integral over the outflow Poynting vector. While X is the reactance resistance by

$$X = \frac{P_{rea}}{|I_0|^2} \tag{127}$$

The reactive power describes the electrical or magnetic energy stored near zone of the antenna

$$P_{rea} = \mu \int V(|H|^2 - \varepsilon|E|^2)\, dv \tag{128}$$

when it's positive it means predominantly magnetic energy is stored (and the reactive resistance is inductive), otherwise electrical energy is predominantly store (and the reactive resistance is capacitive).

The reactance resistance of a small antenna (h << λ) is largely due to its capacitance,

$$X_{Tip} = \omega L - \frac{1}{\omega C} \approx -\frac{1}{\omega C} \tag{129}$$

Thus, the capacitance is

$$\mathrm{C} = -\frac{1}{\omega X_{Tip}} \tag{130}$$

A three-dimensional modeling of the electric SPM using the finite element method was made after that (Fig. 49). The contributions of the probe are laying down in capacitance and capacitance gradient. The tip of probe was modeled by a truncated

cone ending with a hemispherical apex. The simulations highlight the effect of considering a quasi-static model or a model in which electromagnetic field at GHz frequencies play an important role.

The cone was separated into several parts in order to have a better mesh and include the model of the coaxial cable transmission line at the top of the cone to simulate the source (Fig. 50).

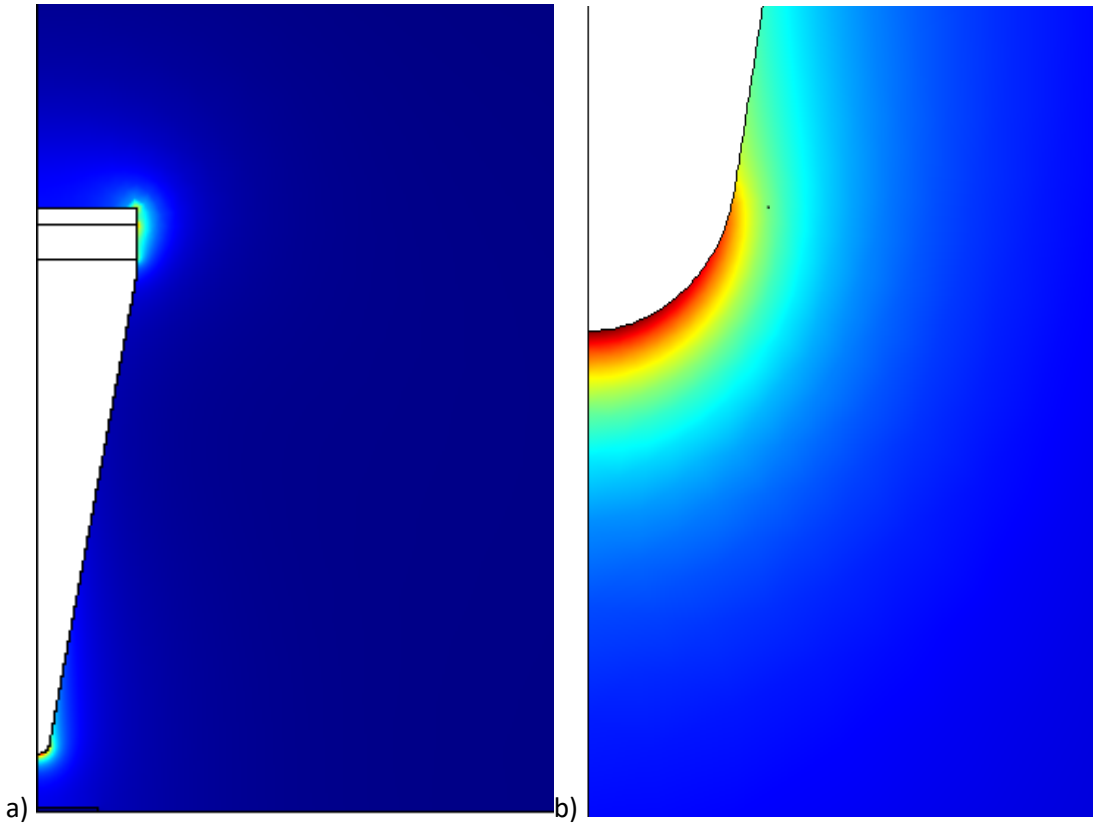

Figure 49 a) The modelling of the AFM tip cone in COMSOL. b) The field concentration at the end of the tip is shown.

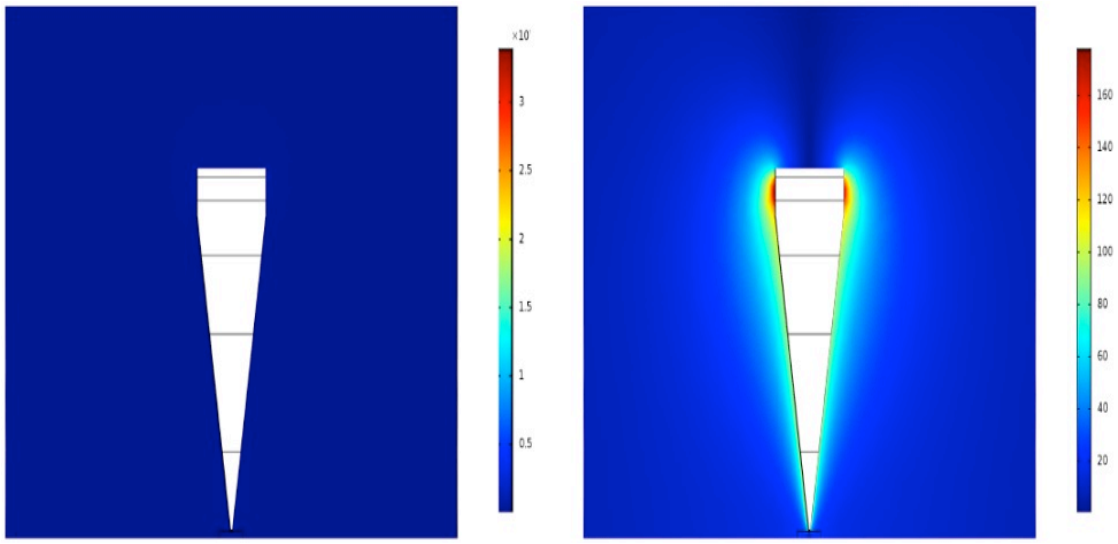

Figure 50 The modelling of the AFM tip in COMSOL separated into several parts in order to have a better mesh. The fields plot.

These simulations have provided a better understanding of the SPM setup and its characteristics. The scanning probe was considered in the detailed way. The analytical equations were combined to perform a better precision in the numerical simulations. Obviously, the importance of the correct simulation model and accurate calibration of the setup in case of the real measurements are vital things.

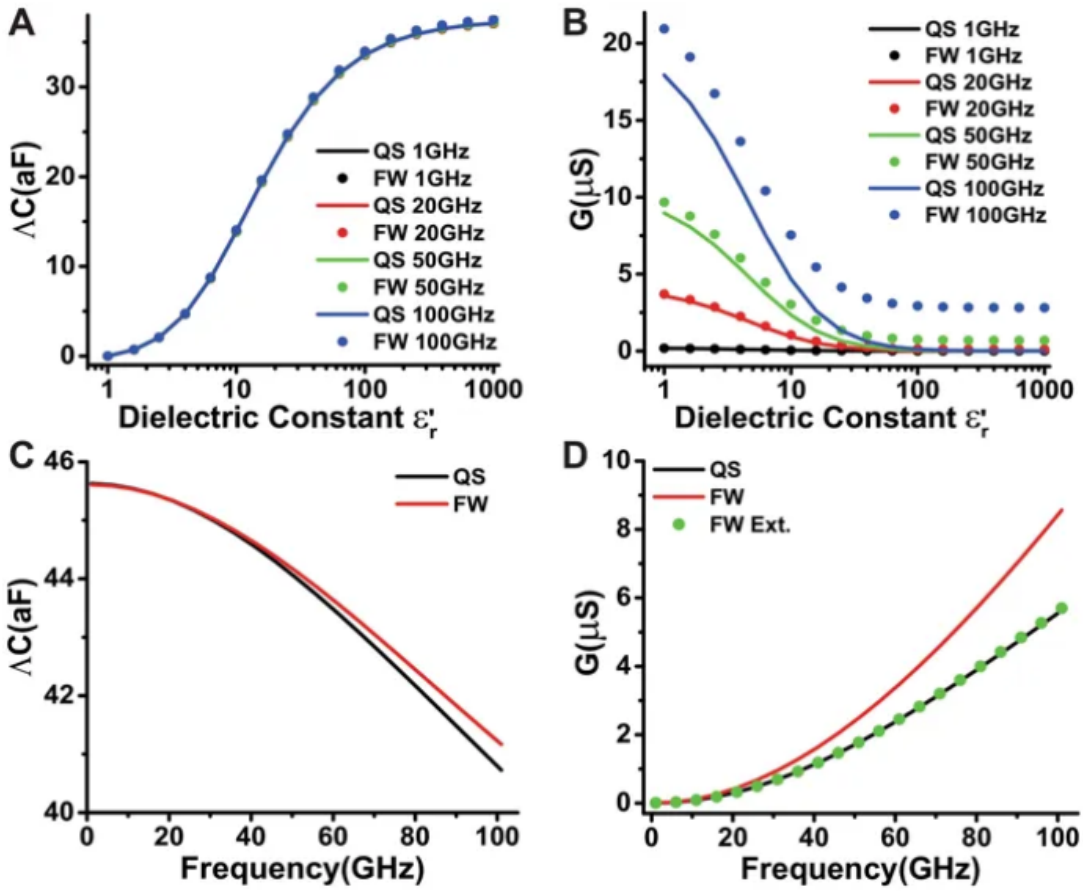

Figure 51 Contribution of a sample with hemi ellipsoidal geometry that mimics a droplet of water by using the quasi-static model and full-wave method at different frequencies. Dimensions of the droplet of water: D_w=1.0 μm and C_w=0.6 μm; relative permittivity of sample is $\varepsilon_{Sample}=\varepsilon_r' - j\varepsilon_r''$. (A, B) Intrinsic capacitance and total conductance as function of ε_r' for fixed ε_r'' =5.0. (C, D) Intrinsic capacitance and conductance as a function of frequency for a dispersive sample [122].

The simulations were taken together with my colleagues Bivi Wu (QMUL) and Rene Fabregas (IBEC) as the focus of the investigation was shifted towards the simulations shown in the last chapter. My colleagues have presented the rigorous modeling of nanosized SMM probes and their electrodynamic interaction with material samples at microwave frequencies [122].

We've started by setting out the full-wave model derived from the Maxwell's equations for the SMM setup and then considering the regularization of low-frequency breakdown problem in the numerical implementation. The accuracy of the models in a few examples by using the scanning techniques of approach curves and constant height was demonstrated. First, the point that the quasi-static model provides a quite

good accuracy for the calculation of capacitance at low frequencies was presented. While this model is less accurate for the dissipation loss for the higher frequencies as it is clearly seen from the Figure 51, B. This is one of the main contributions of this thesis. It was pointed also out that the quasi-static model and the PEC boundary are good approximations for the theoretical calculation of capacitance. Here, the simulations show that the SMMs operating at higher frequency provide greater sensitivity on the evaluation of dielectric loss (Fig. 51). It was stressed that for accurate analysis the field radiation and skin effect need to be taken into consideration.

The numerical modeling presented there for the full wave model to mimics the SMM setup can be extended in several ways. First, the model can be used for the development of broadband near field microwave scanning spectroscopy with high imaging precision by taking into consideration the propagation and evanescent wave components. Another extension is to use the model to determine local properties of materials by applying the evanescent-scattering field to propagating field conversion. This will enable to study new frontiers of SMM research at higher frequencies up to THz. A third extension is to embed the model in realistic physiological conditions (liquid media). This extension will enable the quantification of biological samples (bacteria, cells) in a realistic media [122].

3.5 Conclusion

Thus, different (bacterial and semiconductor) samples with different modifications of classical Atomic Force Microscopy were investigated. The SMM and EFM studies have provided a wider understanding of current and future scanning microscopy capabilities. It has provided the better understanding of theoretical basement of the way the AFM interacts with the sample. The theoretical and numerical improvements of the current state of art in AFM tip simulations were presented as one of the main contributions of the thesis.

Chapter 4. Feeding device characterization

4.1 Introduction

Various EPR structures was considered in literature but none of them performs the magnetic field perpendicular and stable to the area of the conductor. Magnetic resonance has been an essential tool for studying the physical and chemical properties of matter for over 60 years. For most of its history it has been a 'bulk' technique, where a large ensemble of spins is excited by means of radiofrequency and microwave excitations delivered by a cm-size resonant structure, designed according to microwave engineering guidelines. The scope of applications of magnetic resonance has evolved radically since the realization that both electron and nuclear spins in the solid state can be used as qubits for quantum information processing. For this purpose, the focus must shift towards the control and detection of individual spins at the nanometre scale. This new and exciting line of research has driven the fusion of two traditionally separate disciplines: magnetic resonance and nanotechnology. Applying high frequency oscillating magnetic fields to a single spin is not any harder than to a large ensemble. The difficulty arises in integrating the microwave excitation with the ultra-sensitive detection techniques that must be employed to observe the signal of a single spin [26].

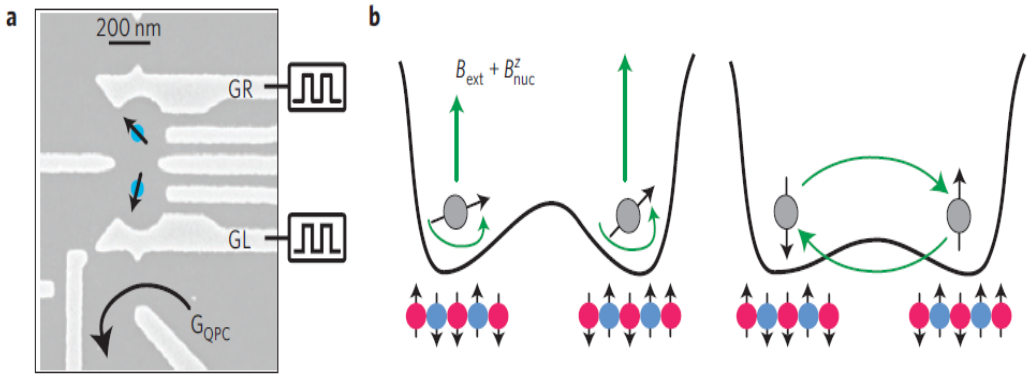

Figure 52 The picture of the controlling device a) and the spin flips in a presence of the magnetic field b).

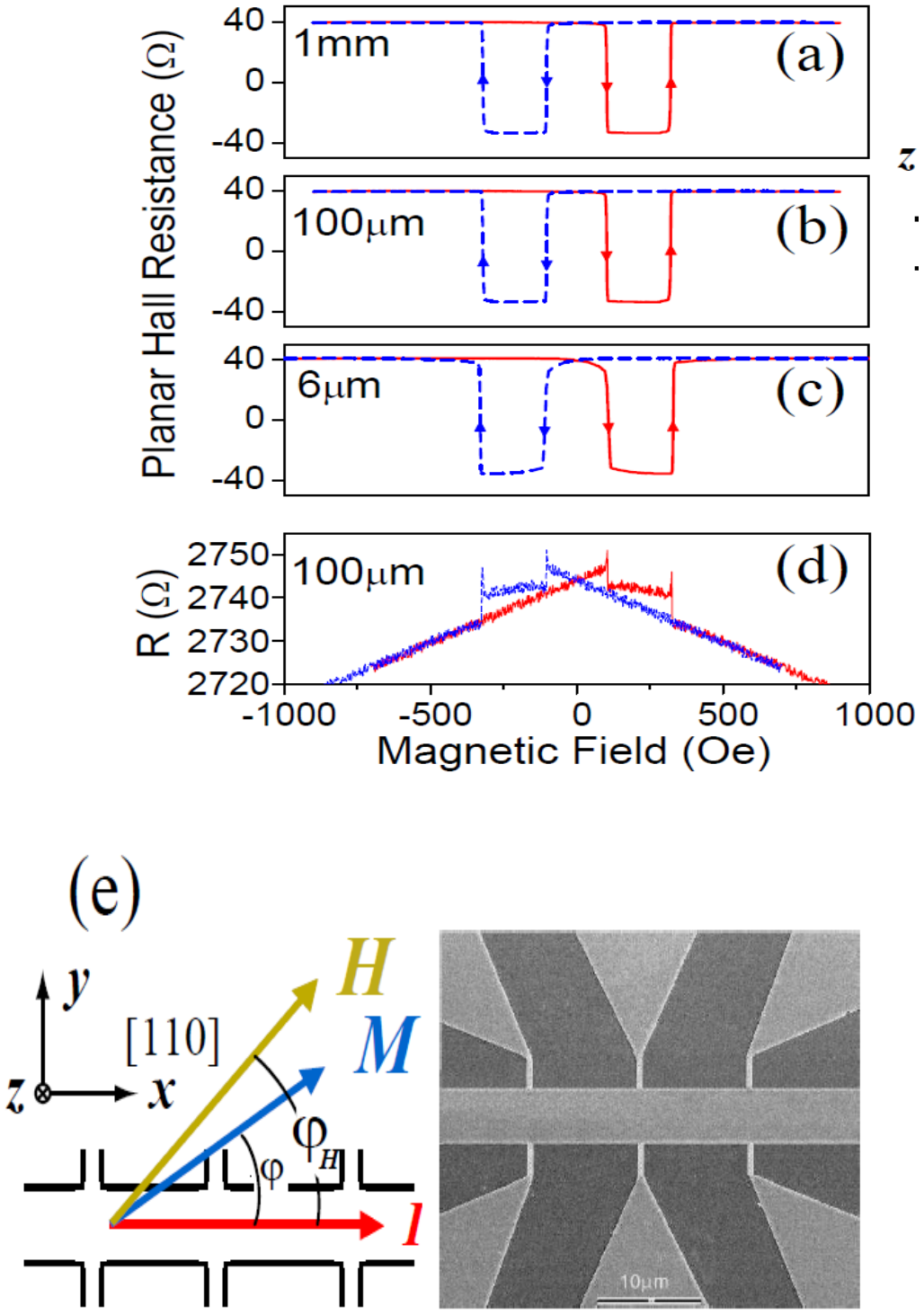

Figure 53 (a)–(c) Planar Hall resistance for Hall bars (1 mm, 100 μm, 6-μm-wide) at 4.2 K as a function of in-plane magnetic field (at fixed orientation φ_H=20). (d) Field dependent sheet resistance of a 100-μm-wide Hall bar. (e) Sketch of the relative orientations of sensing current I, external field H, and magnetization M.

The Hall Effect is one of the effects which are very important in our case. A typical image was already considered for Shubnikov-de Haas Effect above-it is about the certain levels that the voltage could take in presence of the magnetic field applied to the conductor. The Giant Planar Hall Effect (not the quantum one, but the classic one) could be considered in a simple conducting structure as well [1].

Transport properties of conducting and semiconducting films, in particular, Hall-effect and magnetoresistance, are important for material characterization. The Hall-effect could be also measured by the Polarization-sensitive scanning microwave microscope measurements. The microscope operates at 26 GHz in the reflection mode and has a subwavelength spatial resolution. It allows contactless mapping of the conductivity tensor, including magnetic-field-induced terms such as the Hall effect. The local contactless measurement of the ordinary Hall effect in semiconducting wafers and of the extraordinary Hall-effect in thin ferromagnetic Ni films were demonstrated (Fig. 54). The latter yields out-of-plane magnetization. The microwave measurements are in good agreement with the dc Hall-effect measurements [4].

Various EPR structures was considered in literature but none of them performs the magnetic field perpendicular and stable to the area of the conductor. They are not stable or brings too much of the electric field to the same area which has no need to be there in our case (Fig. 55-56). The E- and H-field simulations shown on the Fig.55 to show the strength and the presence of each around the resonators. Thus, there is a certain need of such structure in between the scientific community these days as the spin control is in high demand. The less electric field we have the better performance of the Hall-bar structure we will have [123-124].

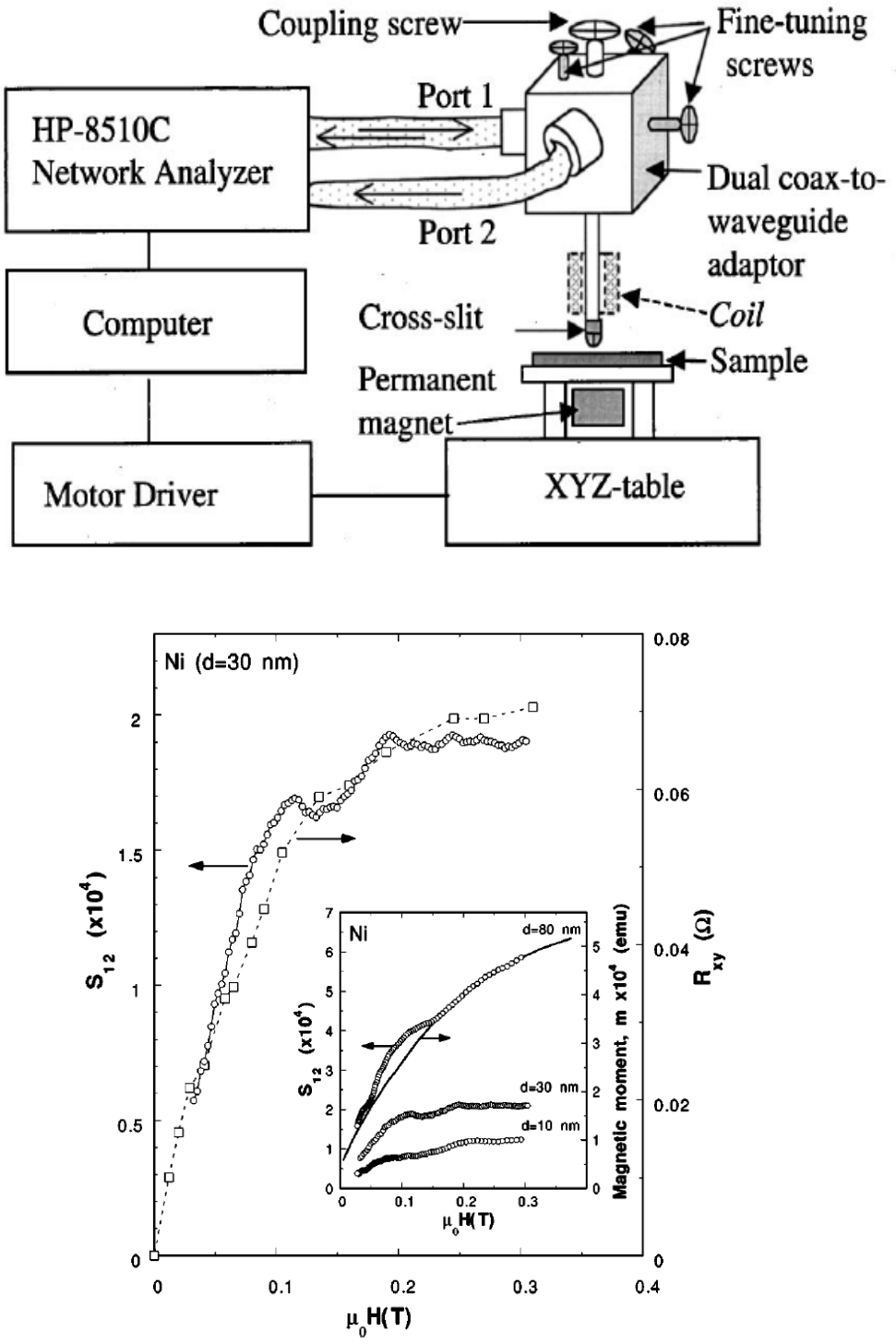

Figure 54 The set up (top) and microwave Hall resistance in thin Ni films on glass (open circles) and four-point dc measurements (filled circles). Note the nonlinear field dependence of S_{12} followed by saturation, as expected for the extraordinary Hall effect. The inset shows that the microwave Hall effect increases with increasing film thickness. The continuous line (inset) shows the magnetization of a small piece of the same film (3x3 mm^2) as measured by superconducting quantum interference device (SQUID) magnetometry [4].

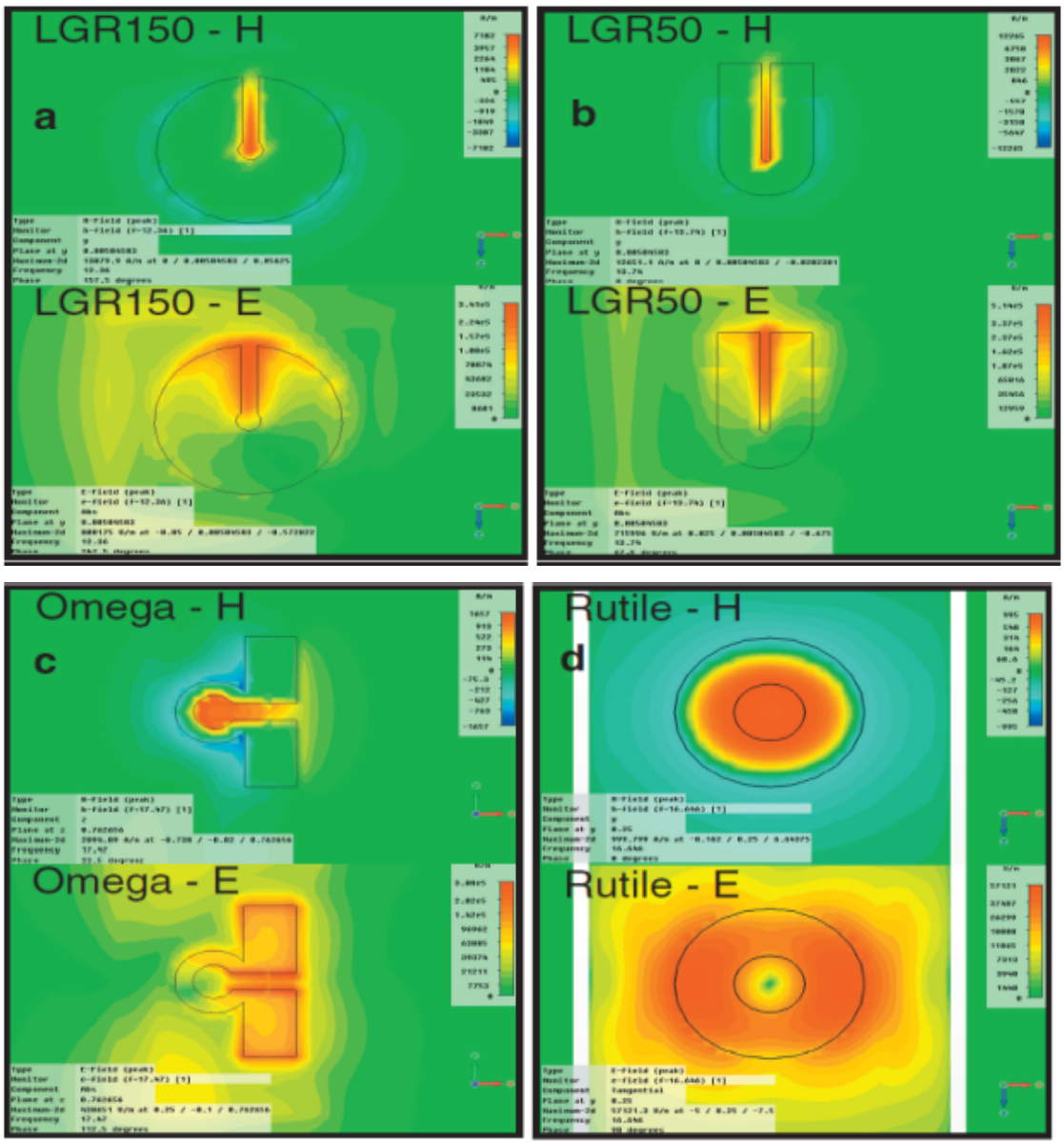

Figure 55 The feeding device variations. The numerical simulations of the magnetic and electric field strength inside and outside of resonators [123].

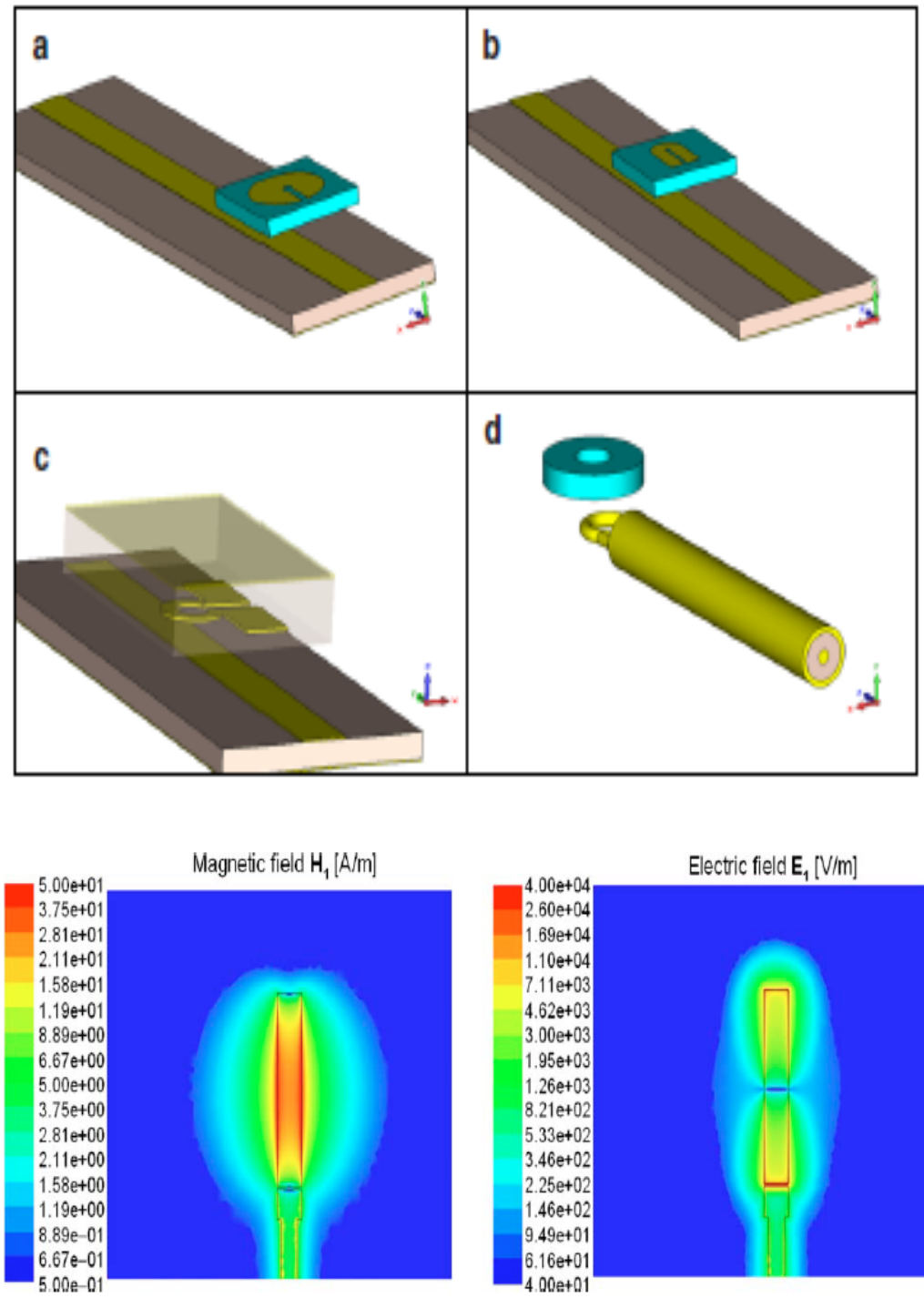

Figure 56 The feeding device variations. Top a),b),c),d) images shows options for the position of the transmission line behind the resonators. The bottom pare of graphs shows the magnetic and electric field strength within [124].

4.2 Analysis

At first, the structure was analyzed from very basic point in order to understand better all the details and principles and to be critical to all the results available for the moment. The feeding device was "divided" into four parts: coplanar waveguide transmission line (CPW, directly connected to the coaxial cable), Balun, CPS and the loop. Further the optimal parameters were investigated. The CPW line was tested as a first part of the device separately. This part is assumed to be connected to the coaxial cable. It is known that the impedance of the coaxial cable is equal to 50 Ohms. Thus, the impedance of the line should be matched to this value in order to avoid losses. Signal line width, gap width, thickness and dielectric permittivity of the substrate, conductor thickness of the CPW are responsible of the impedance value. The structure used, provided by the London Centre for Nanotechnology (LCN) has a substrate thickness of 500 micrometers, and it's made of silicone. Also, according to the thickness of the layers on a hall bar structure the conductor thickness ideally should be 270 nanometers (these two parameters were fixed to be constant). The impedance was calculated in CST (by using macros tool) and in MATLAB (by using in-house packages written for the transmission lines analysis). These two techniques helped us to find correct values of the other transmission line parameters listed above.

4.2.1 Balun structure analysis and single electron wave function simulation

Further, the Balun analysis will be performed. In accordance with an article, we've found out that a back-to-back configuration was used to test this part of the line [24]. In this case the length of the parts (Fig. 57) responsible for the minimization of the radiation losses at the border between the coplanar waveguide and the coplanar strip line will be defined and optimized. Each "W" on the Fig. 57 stans for the "width", capital "G" and "s" are for "ground" and "signal" parts.

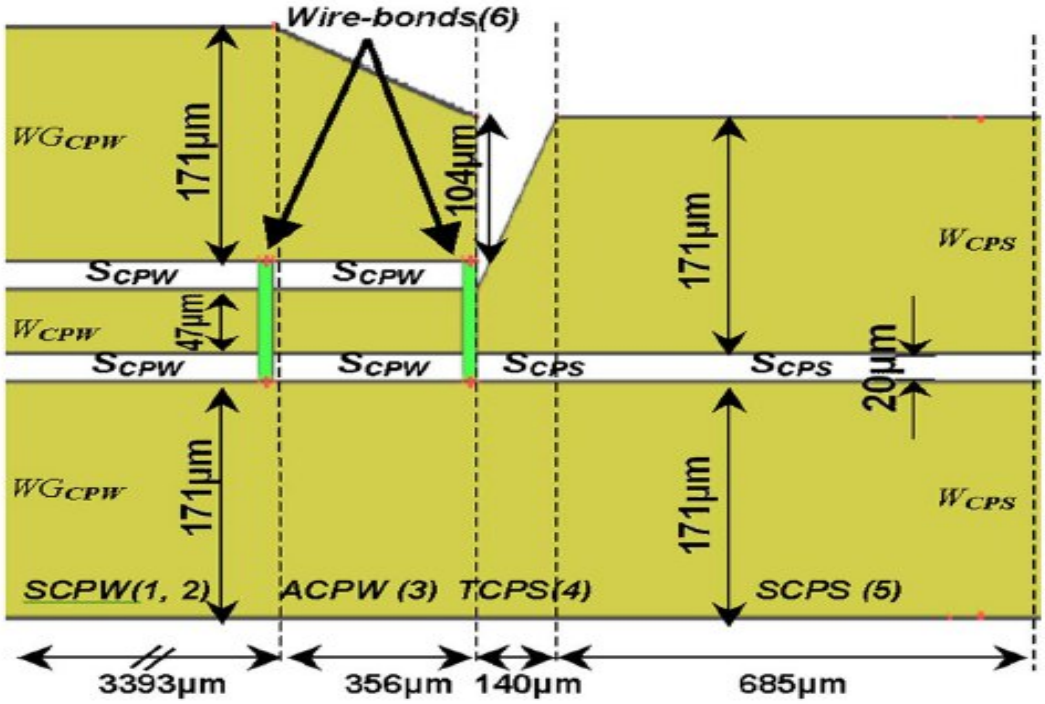

Figure 57 The Balun structure. The clear split of the transmission lime to parts for further analysis and simulations, bonding wires position and dimensions [24].

The number of the bonding wires required for this Balun structure is also defined. It was shown in [24] that the certain bonding wire is needed before each asymmetric section discontinuity to suppress any non-CPW mode and retain the balance on the transmission line. In order to reduce the number of these discontinuities the slot width of both parts of the device was taken to be the same. It must be pointed out that the existence of the bonding wires is the very important part of the Balun, otherwise we lose almost half of the signal on the way. The conductor width of the part which doesn't change the design of itself was also taken to be constant. The coplanar stripline (CPS) is a symmetric device; therefore, the width of the signal part was changed to be equal to the width of the ground plane. In order to proof the numerical results, an analytical modeling will be used. A well-known technique [125-128] called "Equivalent Circuit Model" will be applied. In order to do that the line was again considered to be consists of several parts as it shown at the Fig. 58.

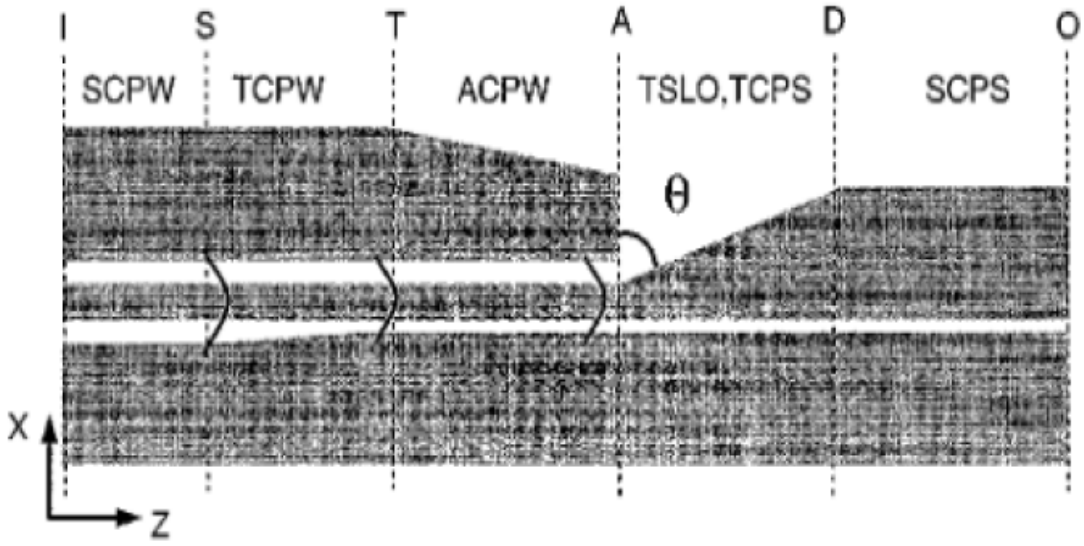

Figure 58 The general way to divide the Balun into sections for equivalent model characterization [25]. For theoretical modelling, this transition structure is decomposed into six parts, i.e., the symmetric coplanar waveguide (SCPW), the asymmetric coplanar waveguide tapered linearly in the lower slot (TCPW),the asymmetric coplanar waveguide tapered linearly in the upper ground plane (ACPW), the unterminated slotline open(TSLO), the asymmetric coplanar stripline tapered linearly in the upper strip (TCPS), and the symmetric coplanar stripline (SCPS).

ABCD-matrices of the Balun are combined from the same equations for each section. The general form of the equations [25] is presented right here below.

$$A_i = \frac{\pi k}{2m_i}[J_1(u_1)Y_0(u_2) - J_0(u_2)Y_1(u_1)]$$

$$B_i = -j\frac{\pi k}{2m_i}Z_i(1 + m_i L_i)[J_1(u_2)Y_1(u_1) - J_1(u_1)Y_1(u_2)]$$

$$C_i = j\frac{\pi k}{2m_i Z_i}[J_0(u_1)Y_0(u_2) - J_0(u_2)Y_0(u_1)]$$

$$D_i = -\frac{\pi k}{2m_i}(1 + m_i L_i)[J_0(u_1)Y_1(u_2) - J_1(u_2)Y_0(u_1)] \qquad (131).$$

Here is a need to say that the ABCD matrices are a common way to describe the RF circuit (Fig. 59). It is also called the equivalent circuit model. The theoretical foundations of linear circuit theory rest on Maxwell's theory of electromagnetism. In its more applied form, circuit theory rests on the key concepts of Kirchhoff's Laws, impedance, Ohm's Law (in its most general sense by encompassing impedances), and

the Principle of Superposition. From this foundation, any linear circuit can be solved: Given a specification of all sources in the circuit, a set of linear equations can be found and solved to yield any voltage and current in the circuit. One of the most surprising concepts to arise from linear circuit theory is the equivalent circuit: No matter how complex the circuit, from the viewpoint of any pair of terminals, the circuit behaves as if it consisted only of a source and an impedance. From a narrow view, the equivalent circuit concept simplifies calculations in circuit theory, and brings to fore the ideas of input and output impedances. More broadly, the equivalent circuit notion means that a simpler but functionally equivalent form for complicated systems might exist [128, 129].

This theory was tested to see the resulting impedance and s-parameters of a simple coplanar waveguide kind transmission line. In order to get them the code in a MATLAB simulation package was written and the result was considered for the starting parameters of transmission line device simulation in CST microwave studio as it provided the general information for the impedance matching in between the starting point of the feeding device and the coaxial cable connected to it (the waveguide port in CST).

Figure 59 The general view of two-ported system with ABSD parameters defined(here they are a_1, b_1, a_2 and b_2).

The idea is to apply this method for the whole line including the loop at the end and then to characterize the flips of the single electron or nuclear spin through the Hamiltonian, as the magnetic field is taking a part in the equation for the latter,

$$H = AI * S + g\mu_B B * S + \frac{a}{6}\left[S_x^4 + S_y^4 + S_z^4 - \frac{1}{5}S(S+1)(3S^2 + 3S - 1)\right] \quad (132),$$

where I and S are nuclear and electronic spins, μ is Bohr magnetron, B is magnetic field. The first two are Zeeman terms (in Eq.132) very in line with what was investigated about the Zeeman effect in Chapter 2, and the terms is brackets are for cubic crystal field coupling. This is Hamiltonian equation for more specific case when the nuclear and electronic spins are considered.

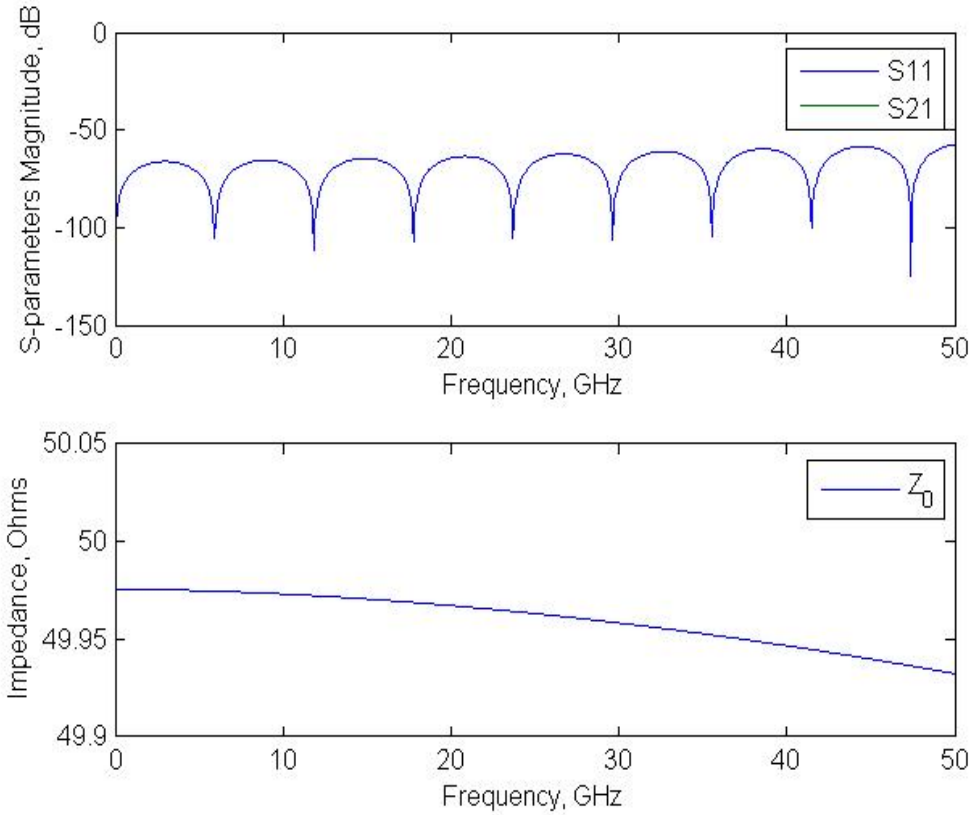

Figure 60 MATLAB simulation results. The s-parameters and the Impedance in the frequency band from 1 to 50 GHz. This code in MATLAB use ABCD-matrices method to calculate all the characteristics of the CPW transmission line.

Obviously, it's easier to start from the case when the nuclear spin is not considered. We will try to understand the less complicated case when only the electron spin is considered.

The quantum mechanics is described by the time-dependent Schrodinger equation:

$$\frac{i\hbar\,\partial\psi}{\partial t} = -\frac{\hbar^2}{2m}\nabla^2\psi(x,t) + V(x)\psi(x,t) \tag{133}$$

It's an equation related to the energy, the left part of the equation stands for the total energy, the two terms at the right side stands for the kinetic energy and potential energy correspondingly. In the FDTD framework, we use the following method to calculate the kinetic energy (KE) and potential energy (PE) using the value of $\psi(x,t)$:

$$KE = \frac{p^2}{2m_e} = \frac{1}{(2m_e)}\left(\frac{\hbar}{i}\frac{\partial}{\partial x}\right)^2 \tag{134}$$

The aim of this part is to investigate the B field effect on the single electron for further potential research topics. Together with the numerical simulation of the feeding device it could help to build up the universal numerical tool to simulate different options of the feeding device and more complicated molecules at the end. Here the Laplacian operator is calculated using $\psi(k+1) - 2\psi(k) + \psi(k-1)$ schema

And finally:

$$KE = -\frac{\hbar^2}{2m_e\Delta x^2}\sum_{k=1}^{NN}\psi^*(k)(\,\psi(k+1) - 2\psi(k) + \psi(k-1)) \tag{135}$$

In a similar way we can get

$$PE = \sum_{n=1}^{NN}\left(\psi_{real}^2(n) + \psi_{imag}^2(n)\right) * V(n) \tag{136}$$

To do the simulation we only need to input the wavelength of the particle, set potential function to the whole area and input the total number of time steps. The wavelength of the particle and potential function must be properly chosen.

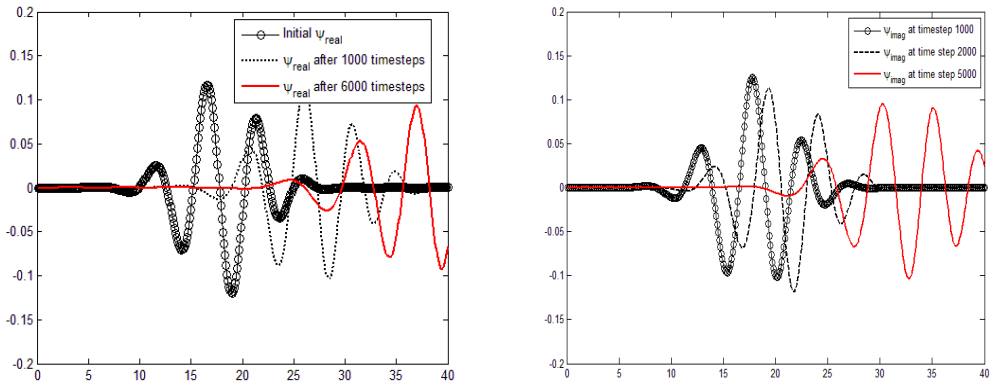

Figure 61 The real and the imaginary parts of the wave function time evolution. This is the connection point of the feeding device we consider and simulate with further applications.

The particle movement inside the simulation domain is characterized by the time domain wave function ψ, which will be separated into real part $\psi_{\mathrm{real}}$and imaginary part ψ_{imag}. Since these wave function stands for the possibility of finding a particle in a certain position. Its value could not exceed 1.0 (as this is the highest probability), so every time we launch a wave function, we need to normalize the wave function. On the other hand, the energy in the simulation area should be conserved, we need to compute the KE and potential energy PE to check for the conservation.

The simulation results are illustrated in the Figure 61. There is the value of ψ_{real} at different time step on the top image. The bottom part of the Fig. 68 shows the value of ψ_{imag} at different time steps. If sufficient large simulation time steps are given in the program, after the simulation finished, both values should be zero, because the particle has left the simulation region. Therefore, it is nothing else but the one more step to understand the spin evolution is taken. The spin normally is represented as a wave-function, so the simulation results presented above is a straight way to perform the single electron or nuclear spin evolution in presence of the magnetic field applied.

By doing this simple simulation we also took a slight view on the future work we could do with our device. The simulation tool with different feeding device designs and different particles could be created. The evolution of the wave functions could be visualized for any case in this way. This is the point where we have a strong connection with Chapter 2 where the theoretical equations were considered very deeply.

4.2.2 The numerical modeling

In order to get the magnetic field strength at the end of the feeding device the numerical simulation in CST Microwave studio was performed. The complexity of the feeding device parts simulated was growing step-by-step. At first, the CPW line connected to the coaxial cable source was considered. Secondly, the back-to-back structure with Balun. Then the loop at the end was added. All the parts were optimized.

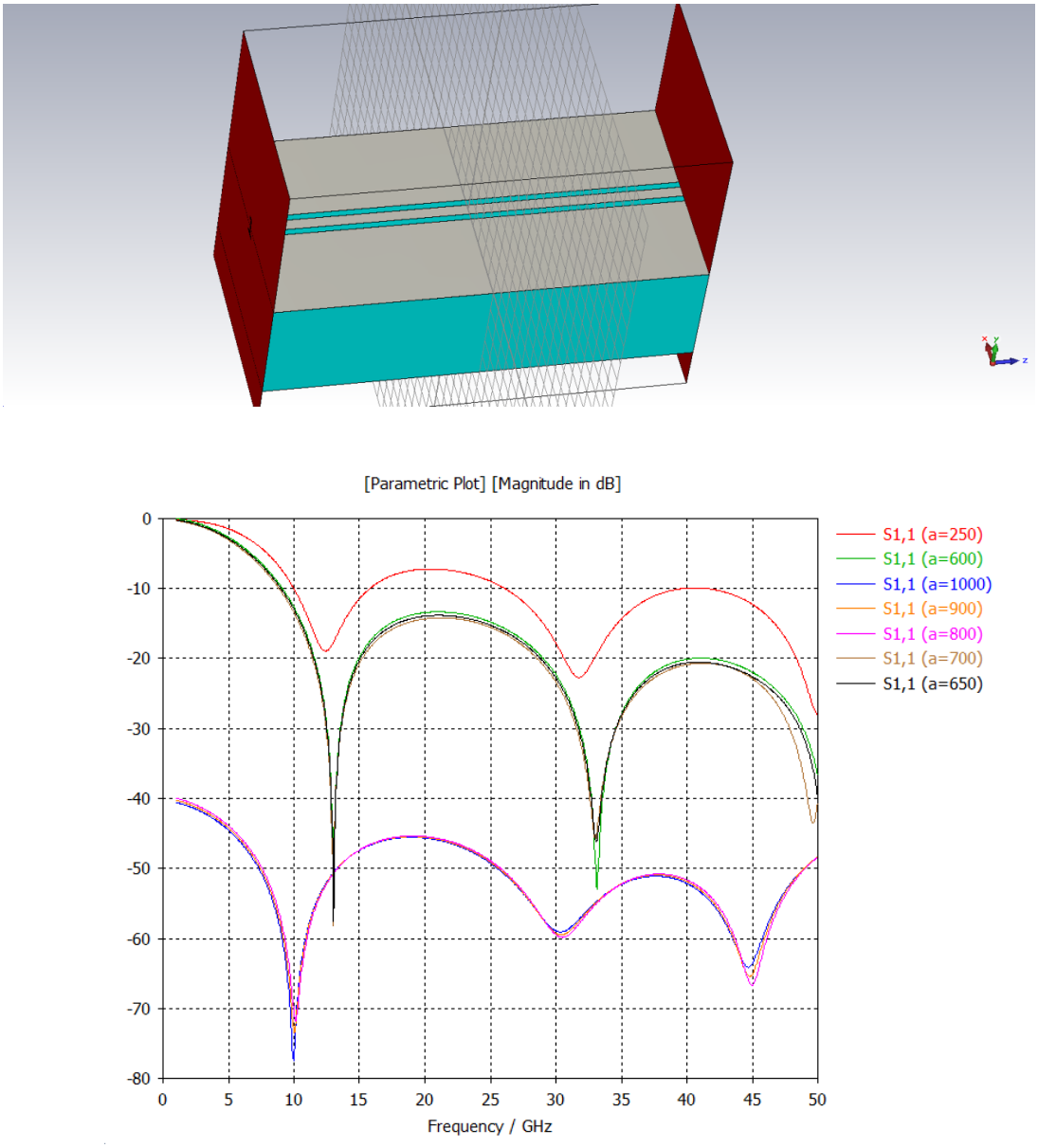

Figure 62 Picture of the coplanar waveguide and port-to-port CST simulation results ('a' is a length of the coplanar waveguide).

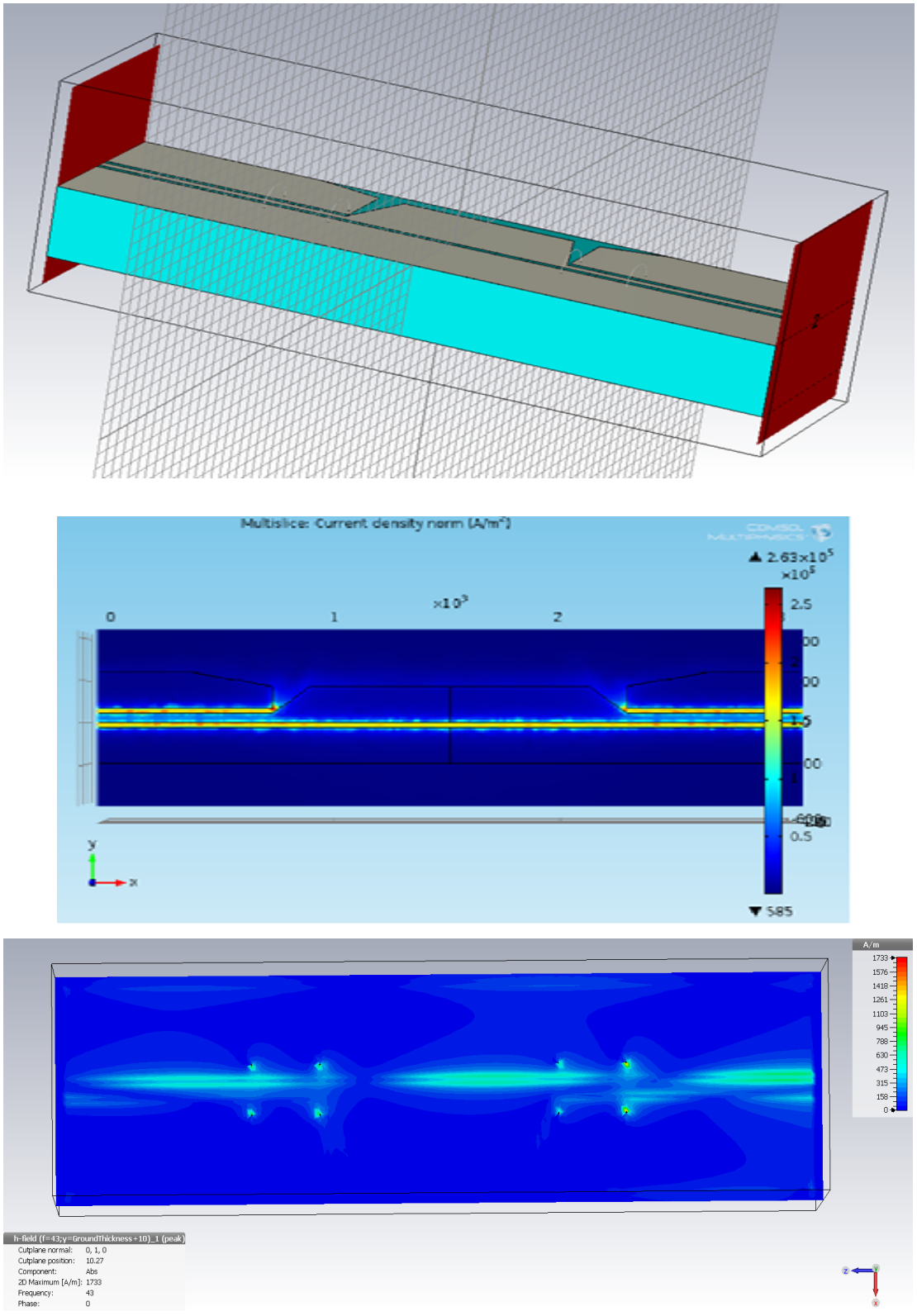

Figure 63 Back-to-back Balun structure formed by the CPS and CPW transmission line parts, the current density plot and the magnetic field view proving the correct dimensions

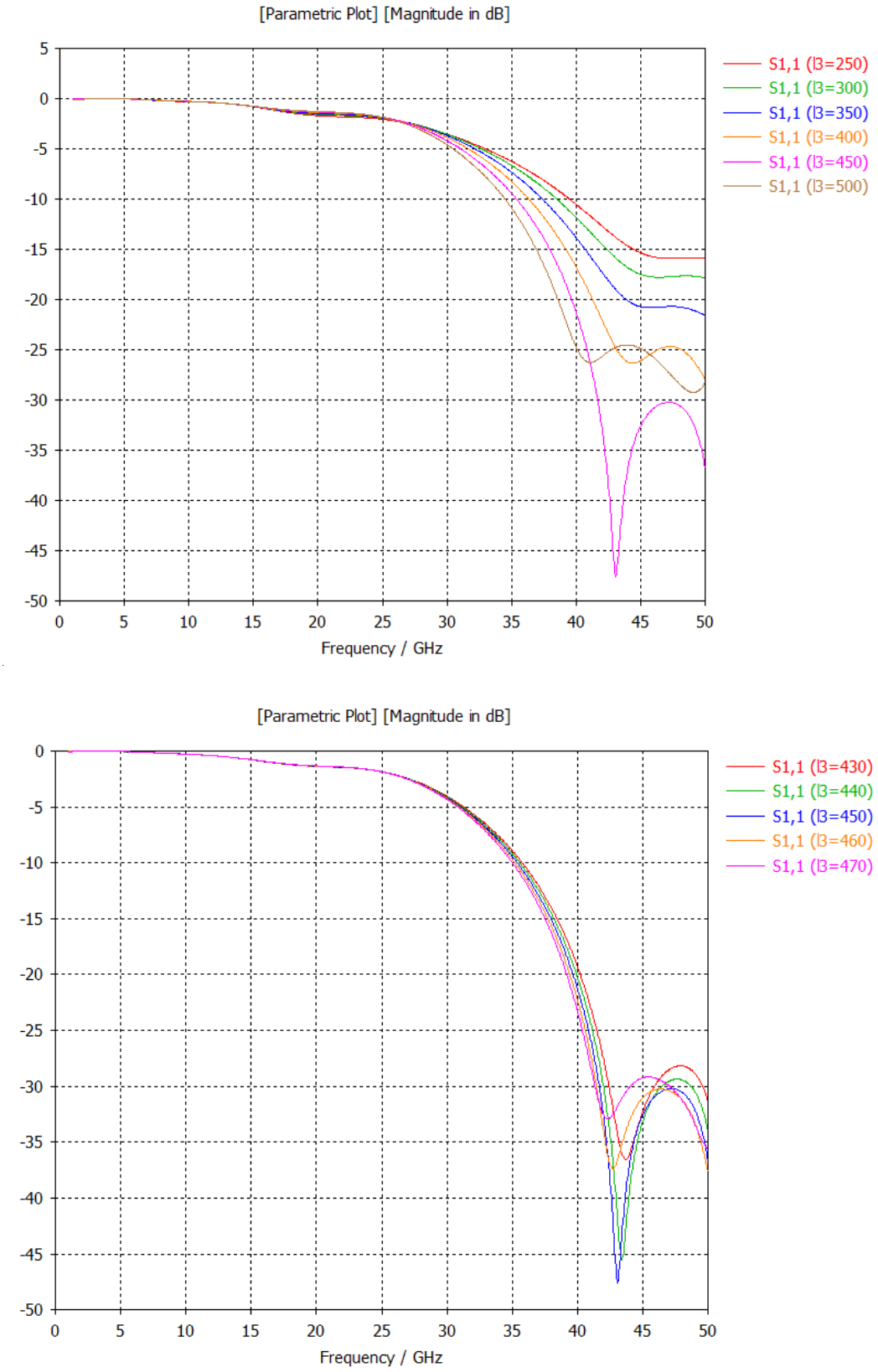

Figure 64 The S-parameters of the back-to back configuration from CST simulations. L3 is the length of the coplanar strip line part in microns. The operation frequency has shifted to the higher frequency region.

We've started from the zero point - the CPW study. The length of the transmission part of the line was a target of the parametric sweep and the resulting reflection parameters were obtained. There is a need to say that the operating frequency range was taken to be from 1 to 50 GHz. The pretty good reflection was obtained so the next step was taken (Fig. 62).

The Balun was considered further. It is needed to be placed there in order to connect the balanced coplanar waveguide transmission line (CPW) and unbalanced coplanar strip line (CPS) as it mentioned above. This is crucial as this part helps to avoid losses. The back-to-back configuration was considered in the simulation (Fig. 63).

As it clearly seen from the plots on Fig. 64 the operating frequency has shifted significantly to the higher frequency region but good in terms of the dB level.

The loop should be added at the end of our transmission line structure in order to have the magnetic field with a high strength which will decay very fast as we go out of the end of the conducting layer. It is logical that the strength of the magnetic field will be higher if we will make the loop as small as it possible. There is one more limitation to our design. The structure with Hall-effect we need to feed has such configuration that the end of our device should be perpendicular to the longer part of itself. Thus, the end of our line will be parallel to the part of the Hall bar structure we should deliver the H-field to. Therefore, the field would be uniform at the very small area and very localized as the scale will be very small.

4.2.3 The Loop Analysis and the total line

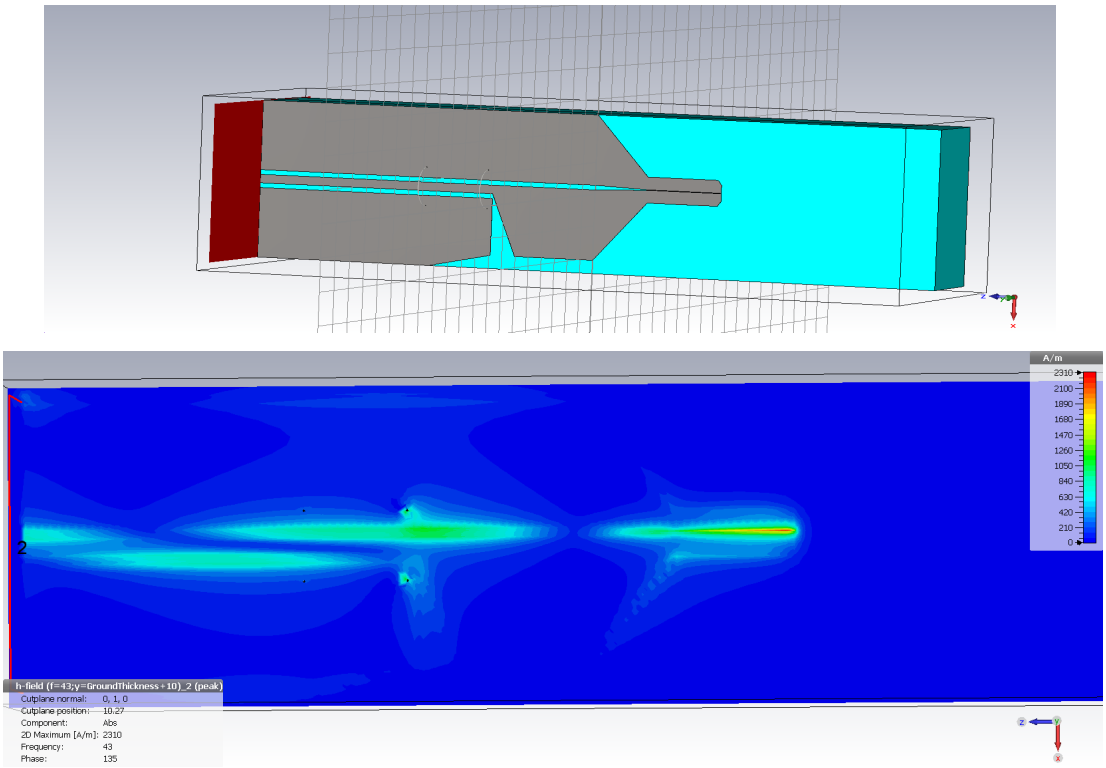

Figure 65 The magnetic field top view over the first iteration of the feeding device structure simulation.

The study of the feeding device for the q-bit structure has taken the next step and we've moved further from the analysis of the Balun (Fig. 63-64) to the study of the loop at the end of the structure (Fig. 65-66).

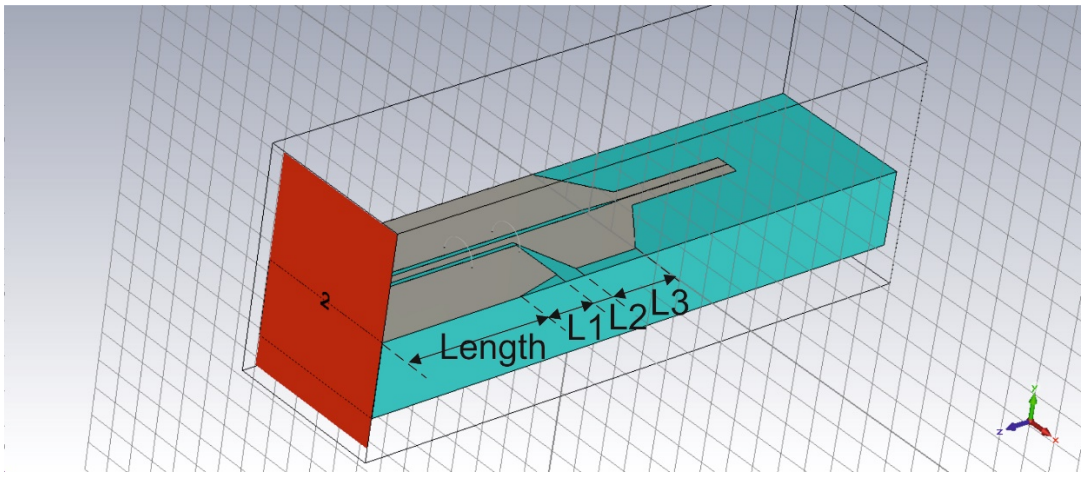

Figure 66 The feeding structure view including the parameters used for the optimisation study.

The purpose of this part is to bring the magnetic field to the q-bit area at the end of it perpendicular to the surface of the substrate at the distance of 20 nm according to the requirements of the LCN colleagues.

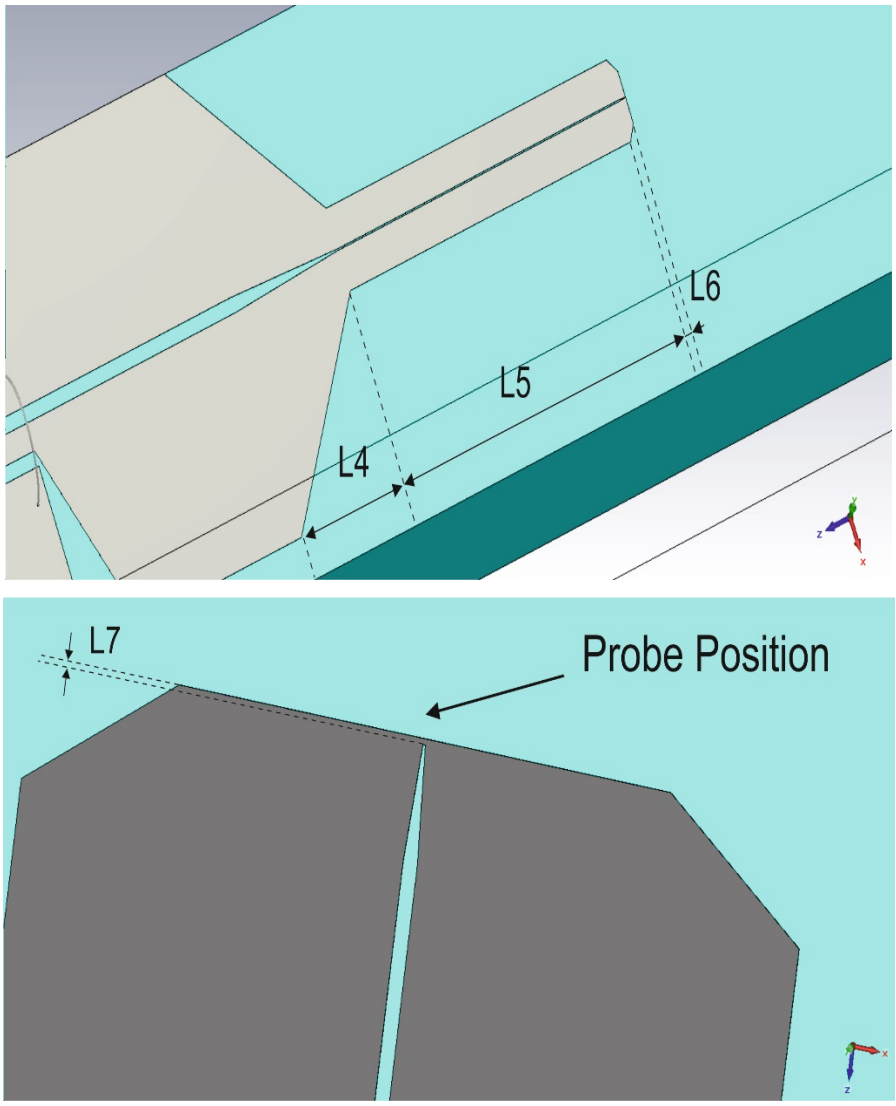

Figure 67 The loop parameters of the feeding device under study as well as the main probe position.

As we've noticed from the Balun study the length of each segment could make the impact on S-parameters of the structure. This idea was taken into account, and we've investigated the influence of the dimension's changes on the resulting transmittance properties. The sweeps were made in CST Microwave Studio and the results are presented below.

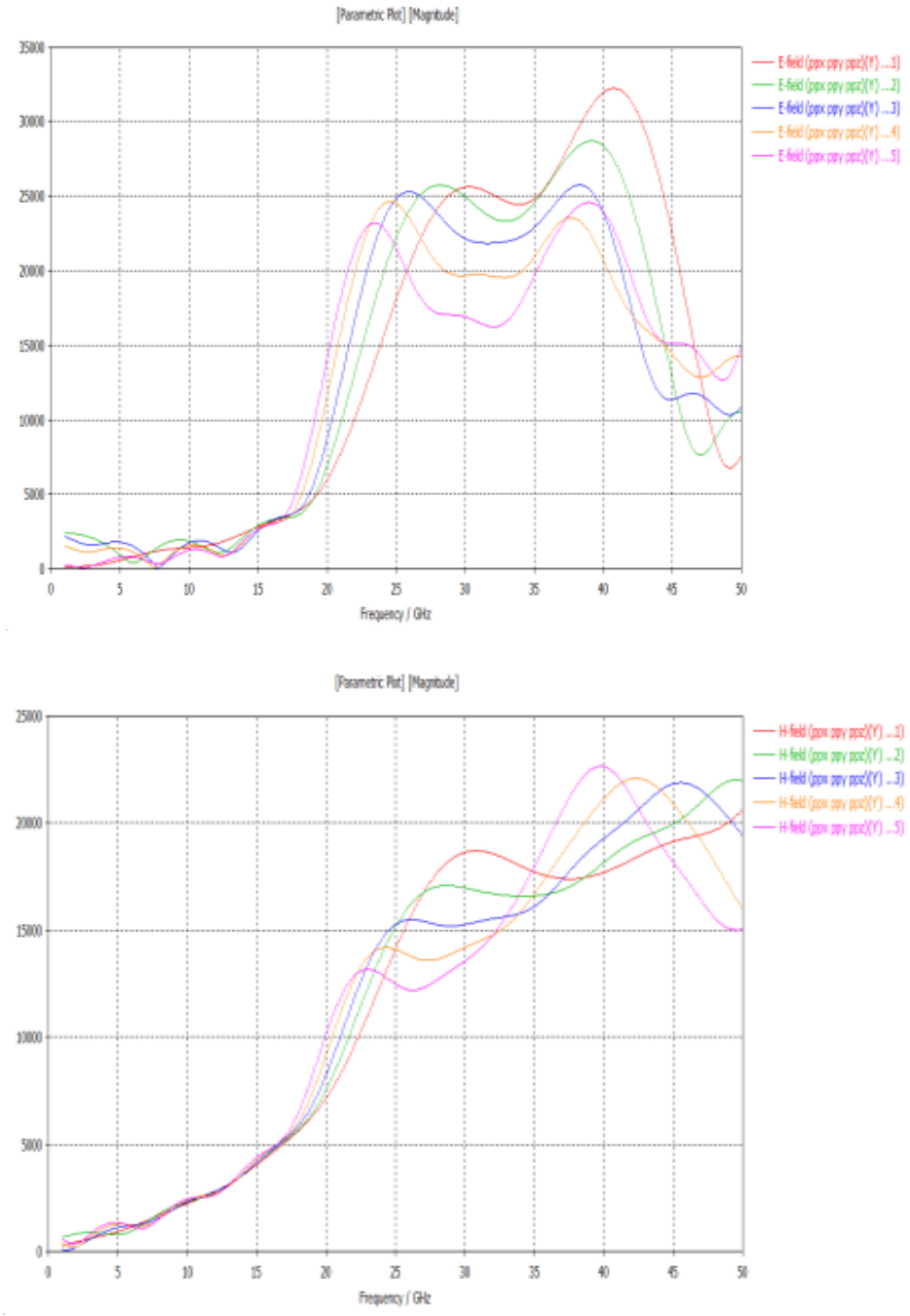

Figure 68 The sweep of the L4 parameter from Figure 67 from 200 to 1000 µm. Electric and magnetic field components.

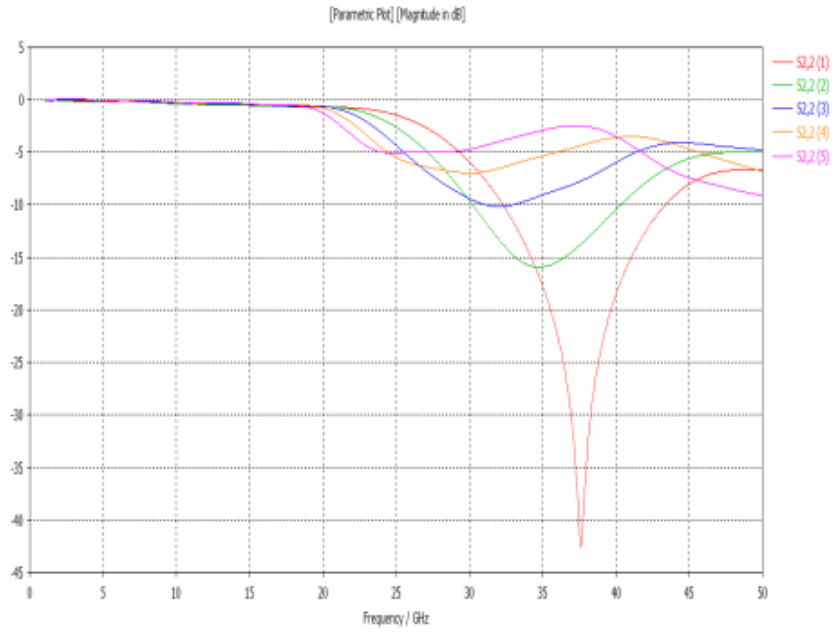

Figure 69 The sweep of the L4 parameter from Figure 67 from 200 to 1000 µm. S-parameters.

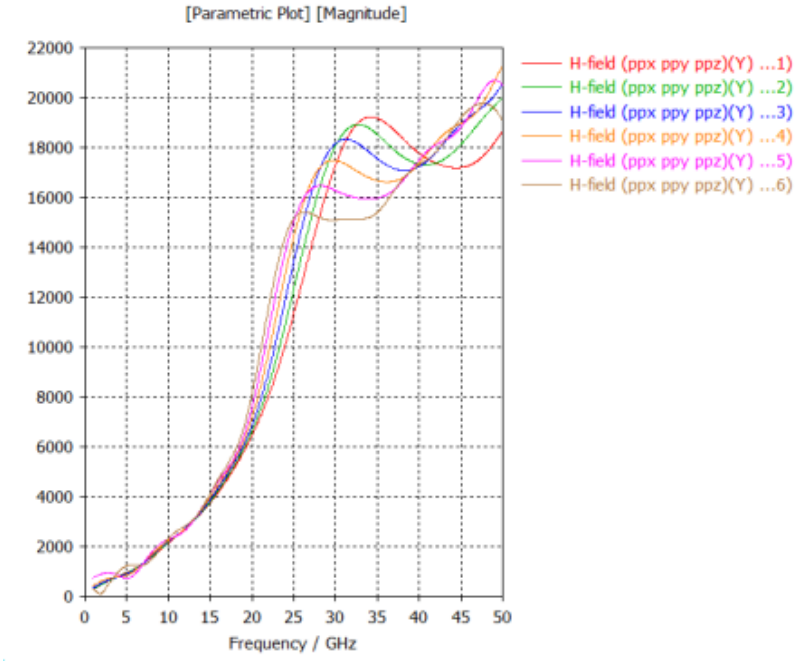

Figure 70 The sweep of the L4 parameter from Figure 67 from 500 to 1000 µm. Magnetic field.

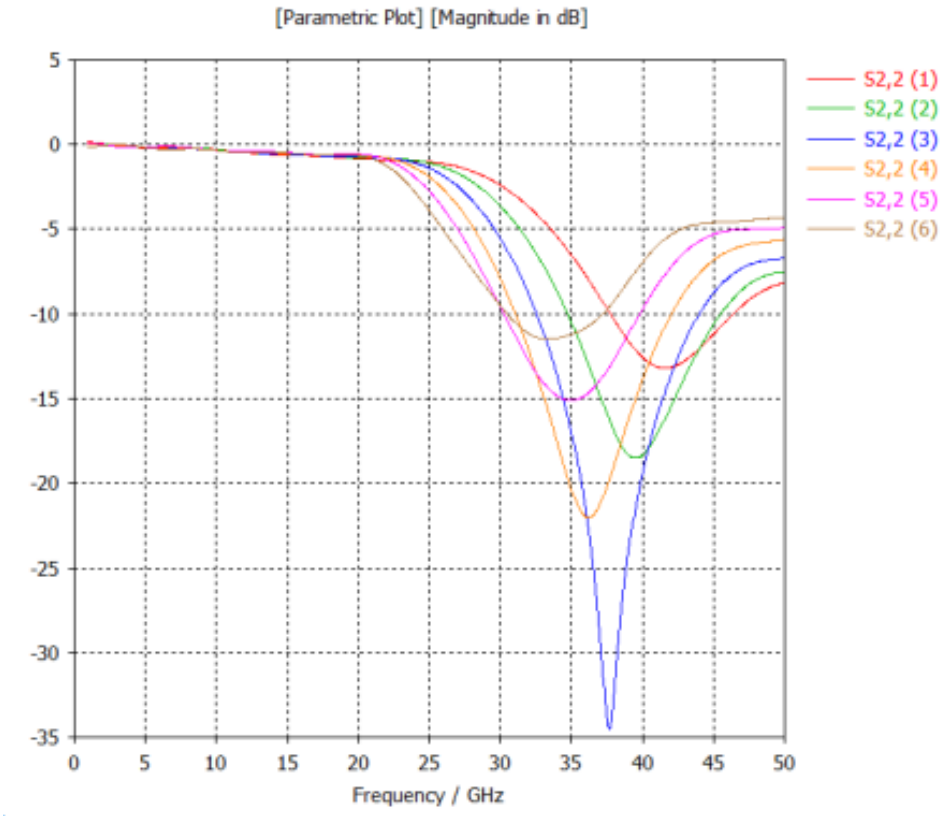

Figure 71 The sweep of the L5 parameter from Figure 67 from 500 to 1000 µm. S-parameters.

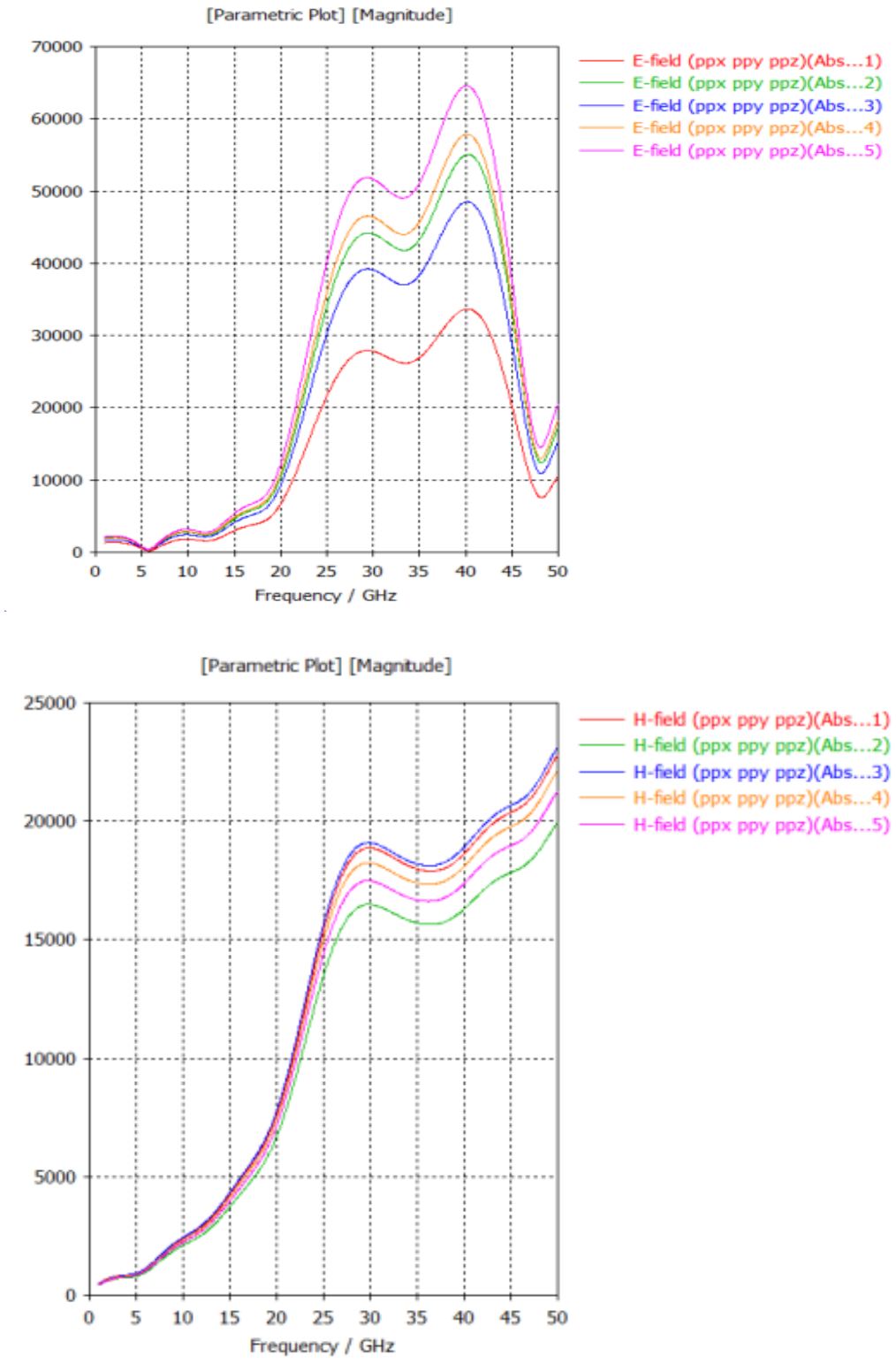

Figure 72 The sweep of L6 parameter from Figure 67 from 4 to 20 µm. Absolute value of E and H fields.

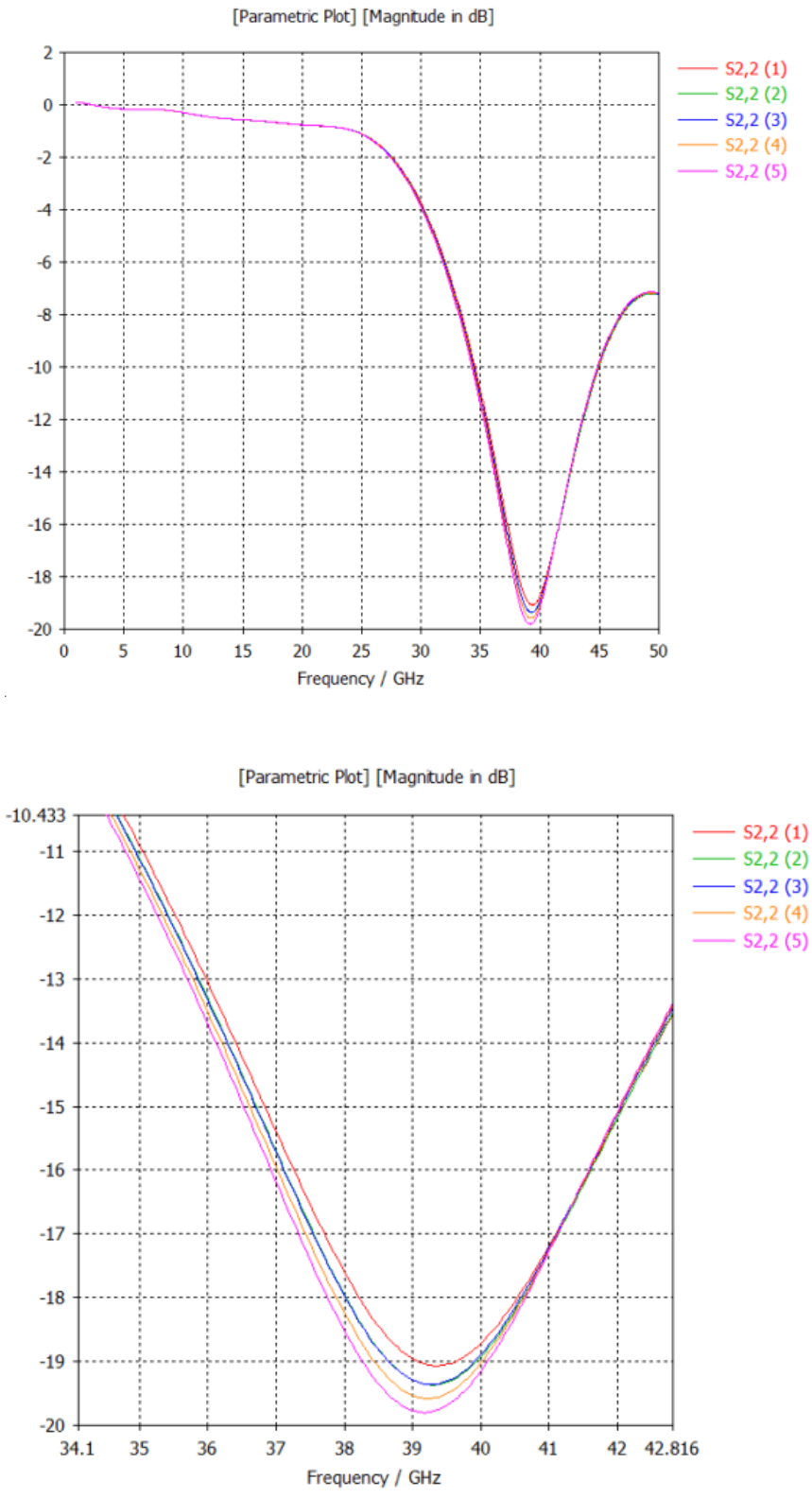

Figure 73 The sweep of L6 parameter from Figure 67 from 4 to 20 µm. S22 parameter.

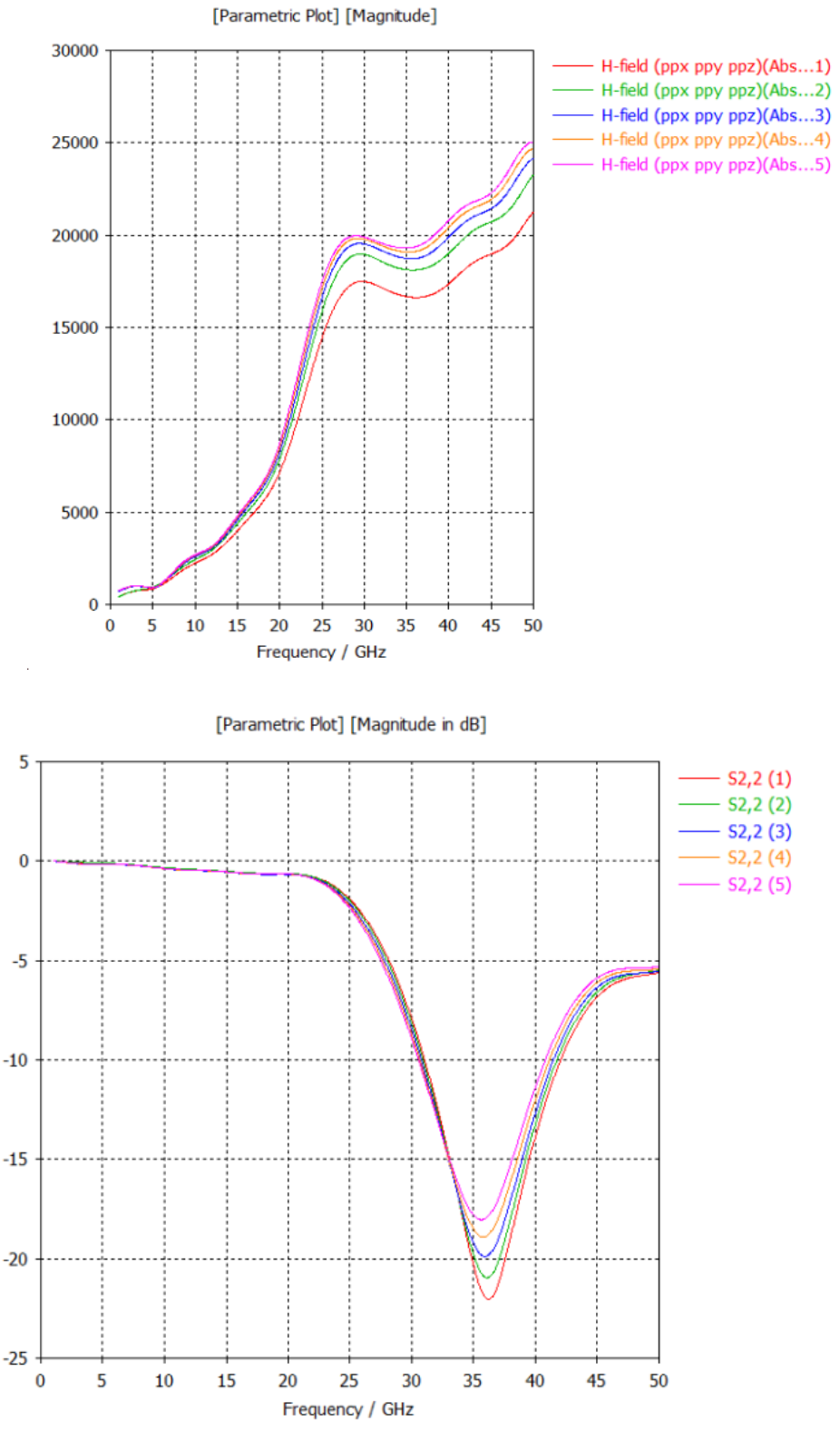

Figure 74 The sweep of L6 parameter from Figure 67 from 20 to 100 µm. Absolute H field value and S22.

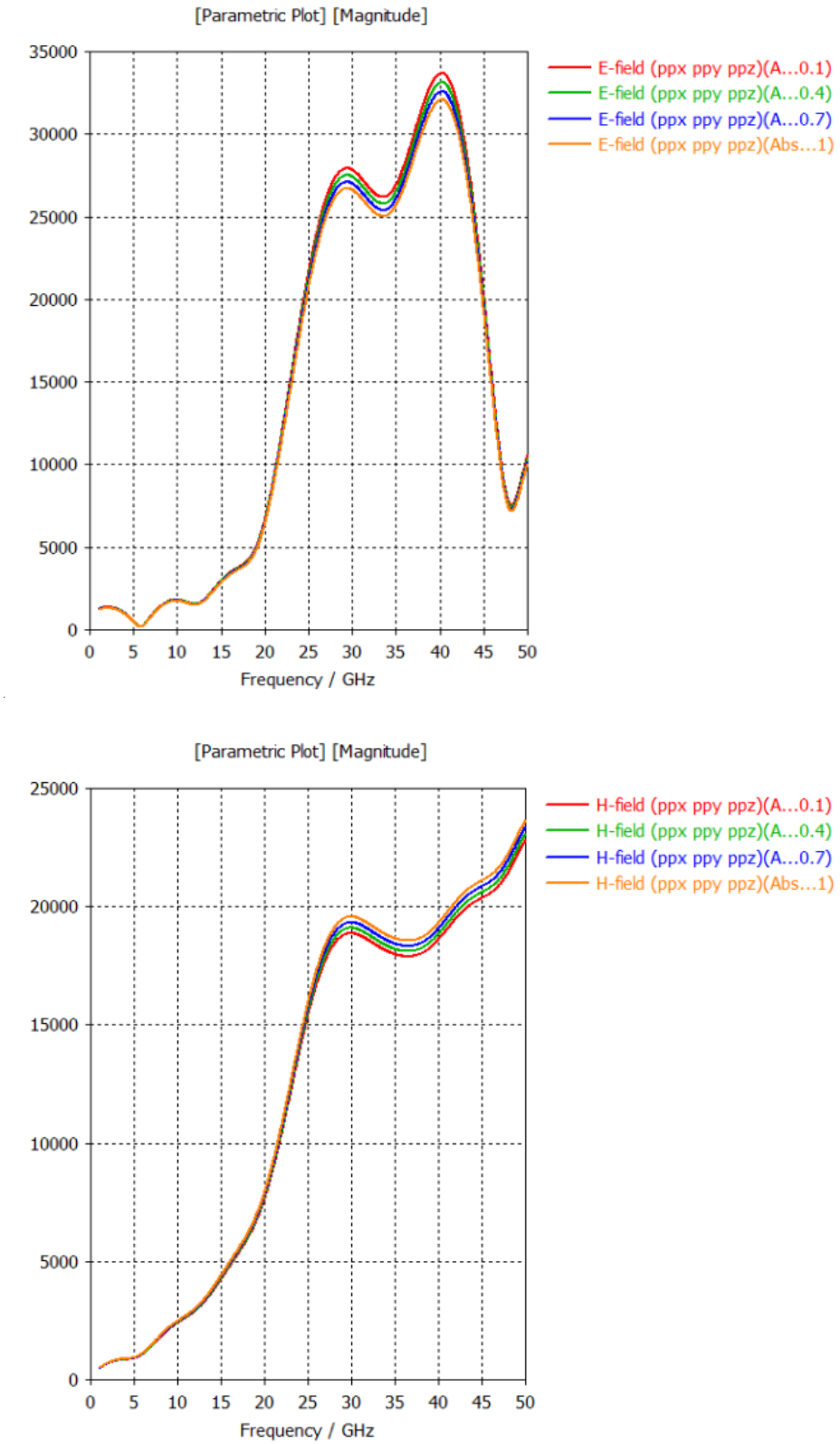

Figure 75 The sweep of L7 parameter from Figure 67 from 0.1 to 1 μm. Absolute E and H field values.

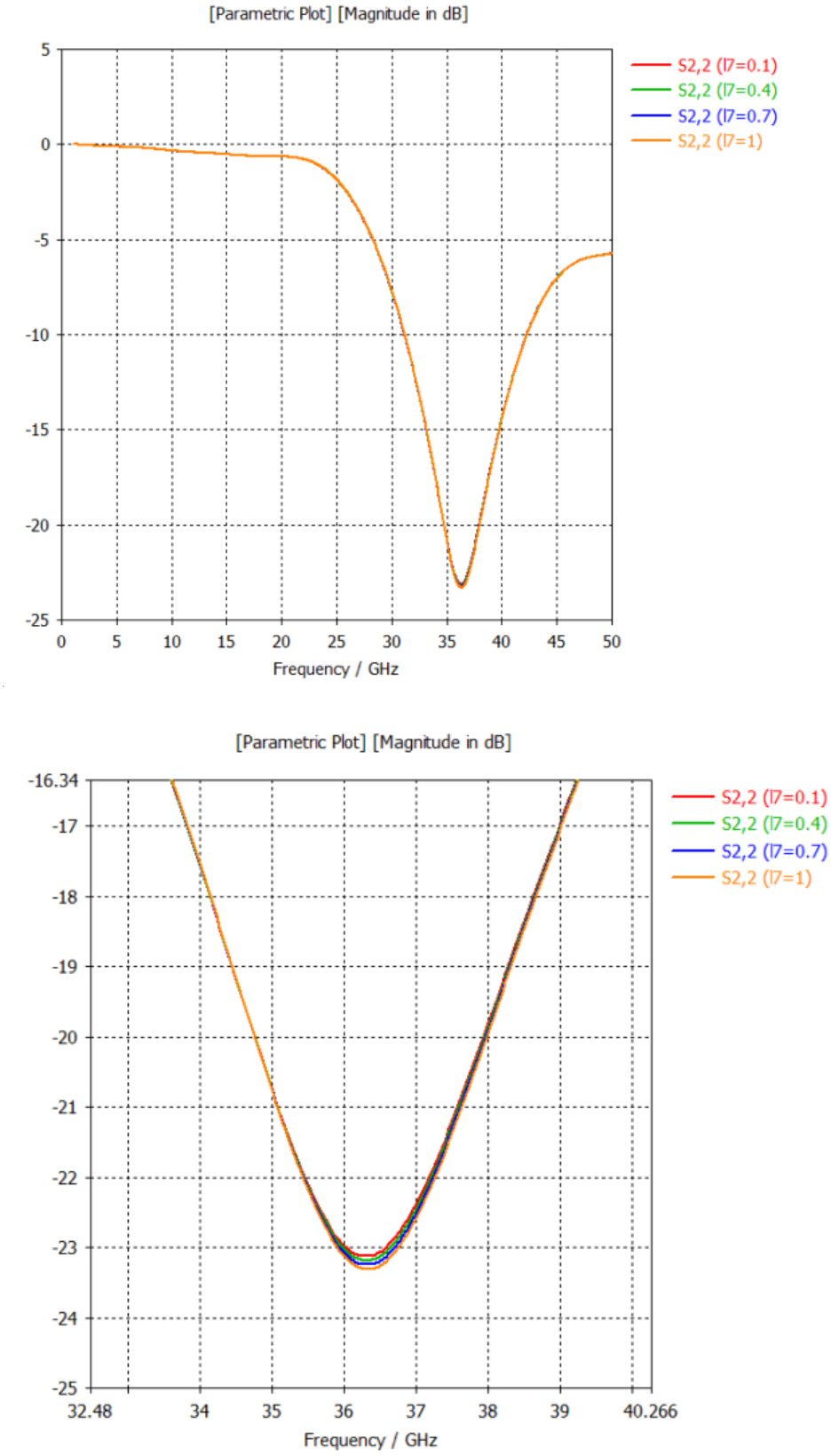

Figure 76 The sweep of L7 parameter from Figure 67 from 0.1 to 1 µm. S22. The difference is very tiny, so zoomed version is provided to pick the best option.

As it comes from these sweeps the optimum parameters of the structure should be chosen like this:

L4=200 µm, L5=700 µm, L6=12 µm, L7=0.1 µm.

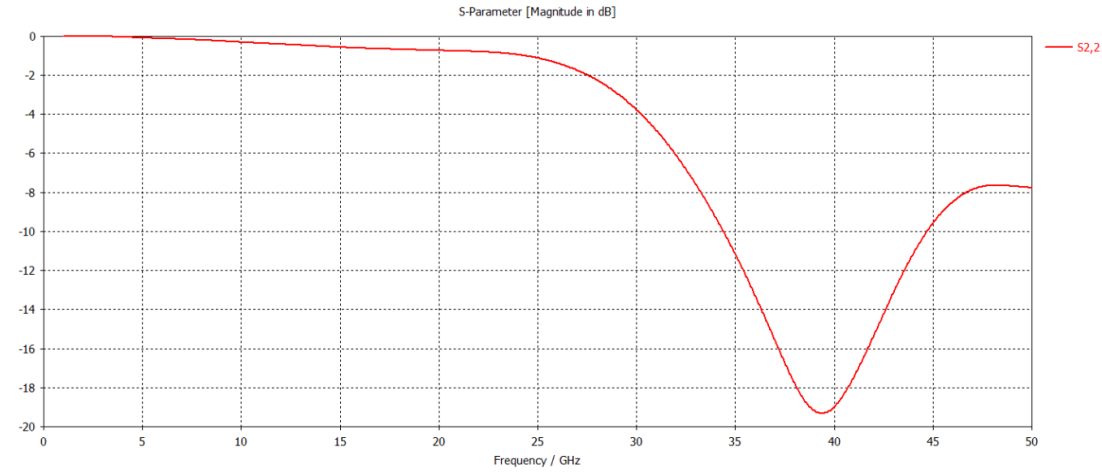

Figure 77 S22 of the feeding device with obtained parameters from Figure 67 i.e., L4=200 µm, L5=700 µm, L6=12 µm, L7=0.1 µm.

The initial design of the structure we need to feed could be seen on the Fig. 1. According to it the design and the dimensions of the loop at the end of the feeding device were taken accordingly. Finally, it became clear that the geometry of the electrodes position should be changed. In a current position it was not possible to bring the end of the loop close to the conducting middle part of the Hall-bar device.

It is needed to be so due to the fact the generally the magnetic field goes around the conductor of the feeding device. The end of this device should be parallel and close to the middle conductor of the structure for the Hall effect detection.

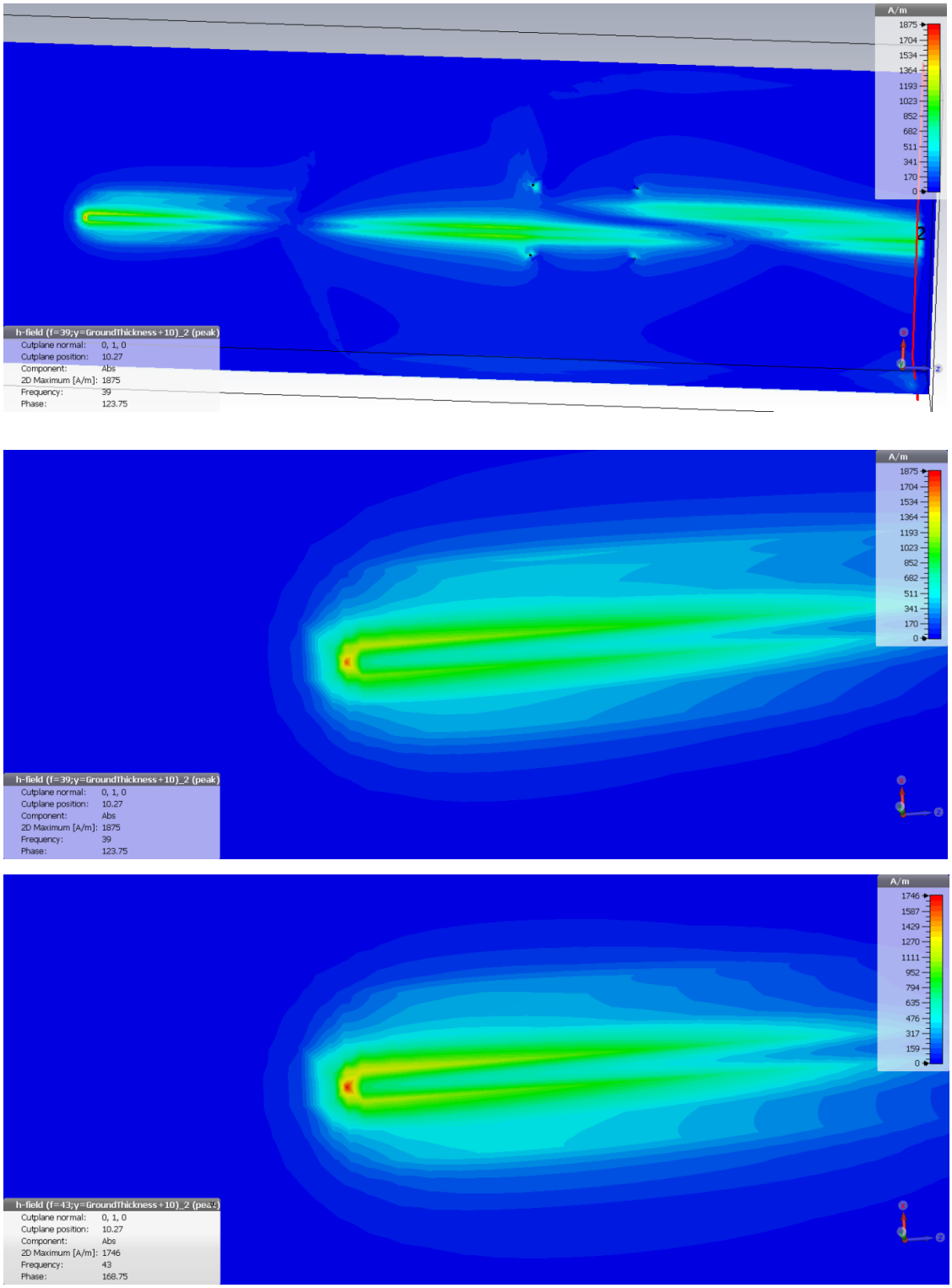

Figure 78 The H field 10 µm above the metallic part of the feeding device and zoomed view of the H field at the end of the device where the loop is taking place at 39 and 43 GHz for clear picture of the field concentration and the quick decay of it when going out from the conducting part

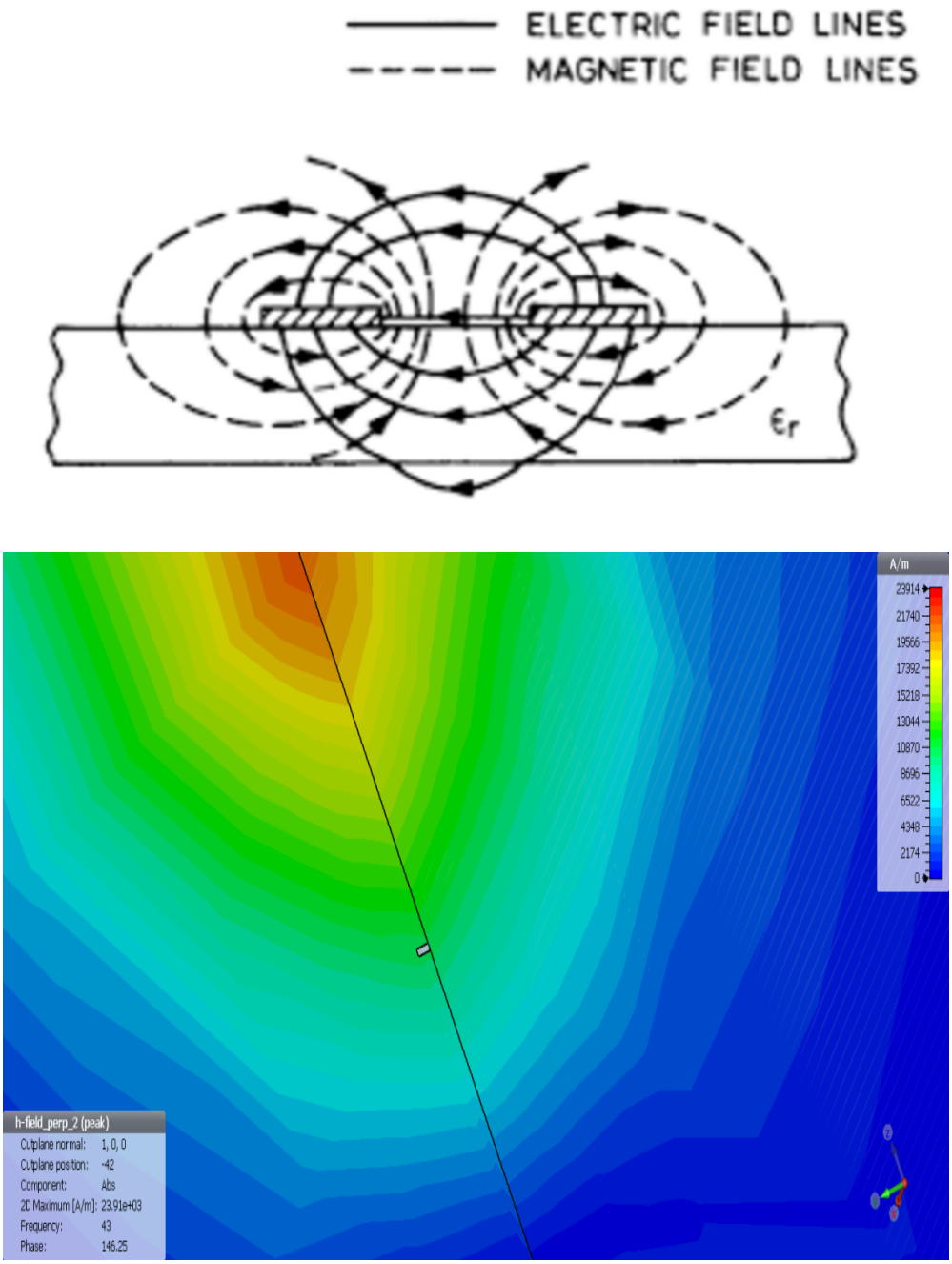

Figure 79 The typical plot of the fields around the CPS line (top image) and the "speed of decay" of our magnetic field at the end of the loop (the bottom one). The small rectangular box in the central part of the image is a conducting part of the transmission line and the black line is the substrate border (the image plane is perpendicular to the substrate therefore)

Thus, the final Hall-bar geometry was adjusted for these purposes. The middle electrodes position was changed in order to bring the possibility to put the parallel conducting feeding structure close to it. The symmetry of the structure was saved in order not to bring any distortion to its performance. Therefore, the new design was finally look like Fig. 80.

The possibility to fabricate the structure was noticed. The final simulations of the loop were awaited.

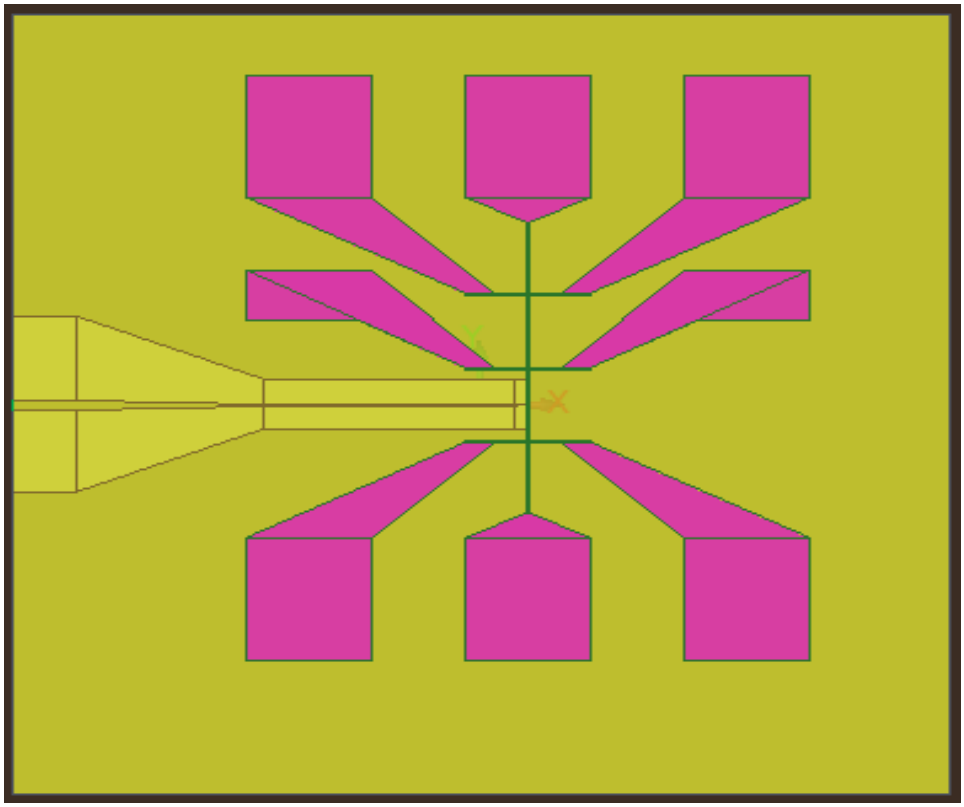

Figure 80 The final design of the Hall-bar structure updated compare to initial one to let the transmission line go closer to the conducting part of the Hall-bar device

The design and the dimensions of the feeding device were in need to be reconsidered and adjusted to the new geometry. The final dimensions of the Hall-bar structure were provided by our colleagues, so we've moved to the final stage of the simulation process.

There were a few points to be proved. The first one was to show how fast the field decays as we go away from the end of the loop. The second was to prove that exactly the middle of the loop end perform the higher magnetic field than the side parts of it. Thus, we've put a few field probes around the loop end. The loop end geometry was also changed to be not so wide to fit the width of the gap in between the electrode's wires. Firstly, we've analyzed the tapered variation compare to the square one.

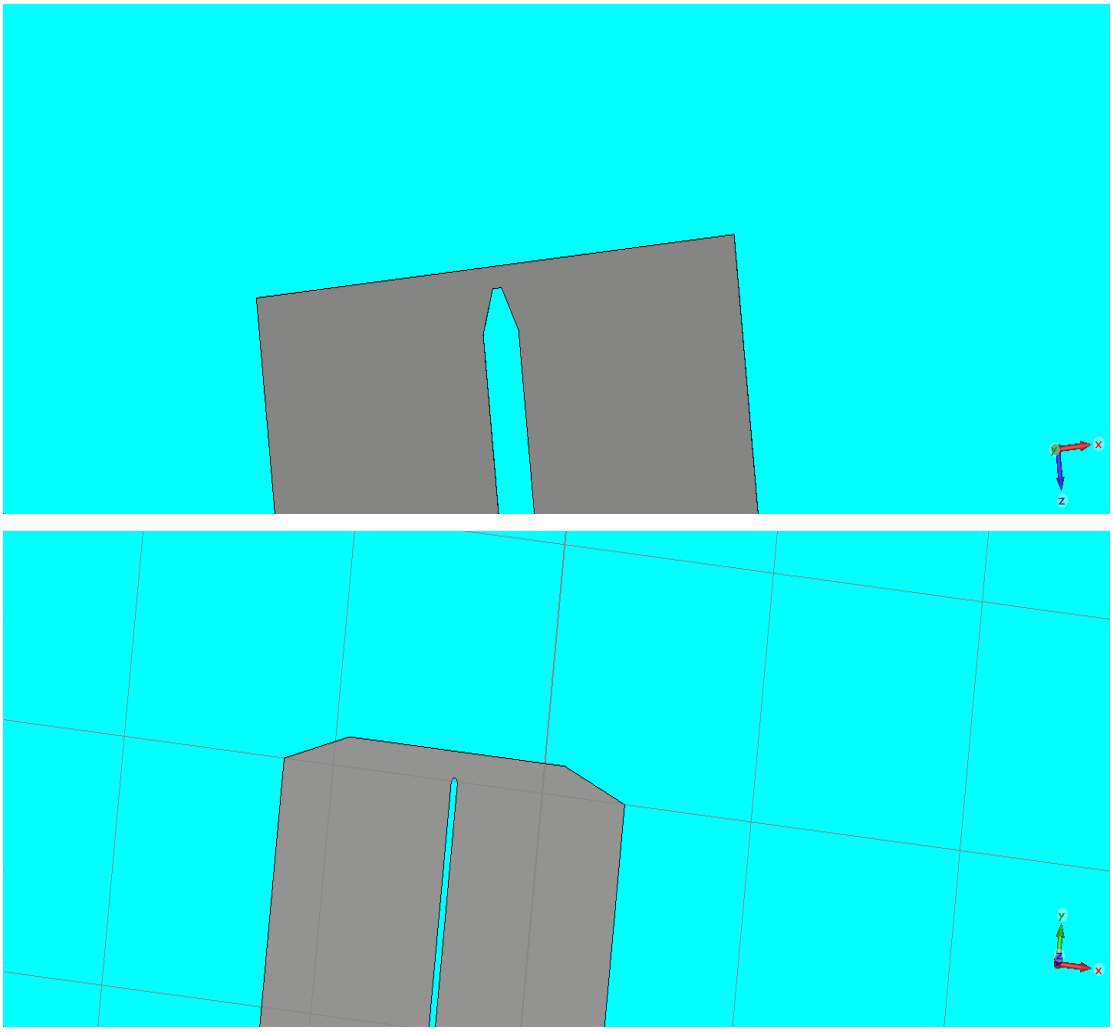

Figure 81 Variations of the loop ending geometry (one of the last sweeps in this investigation). The tapered and the square geometries.

The square variant without tapering has won, and it was chosen to be the final variant. The s-parameters, the H-field strength and the field probes data presented on the plots below at the Fig. 82. In order to have the best performance the sweeps of the CPS width and the size of the “bridge” in between the conducting parts were made. The same characteristics were plotted to see the best option. Thus, the concentration of the field in the middle of the loop was proved as well as the fact that the decay of the field at the position away from the loop end exist. The latter was well predictable according to the classical image of the field lines picture presented at the Fig. 79.

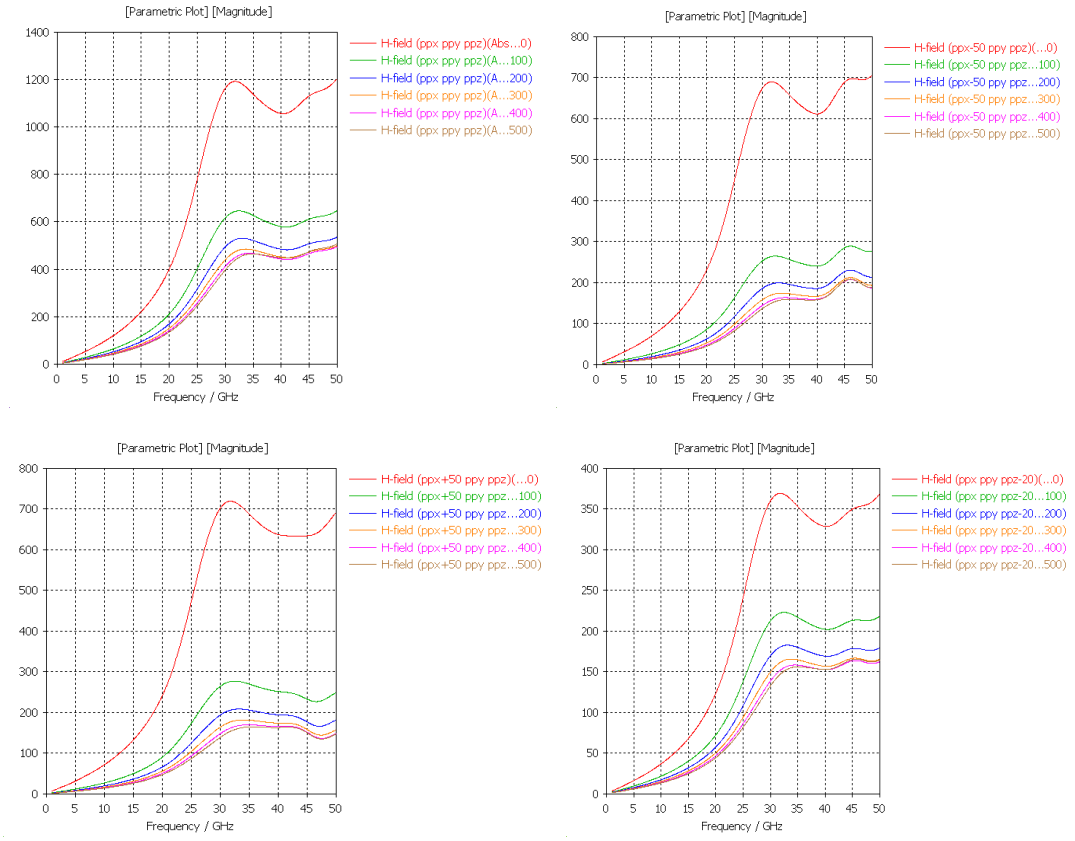

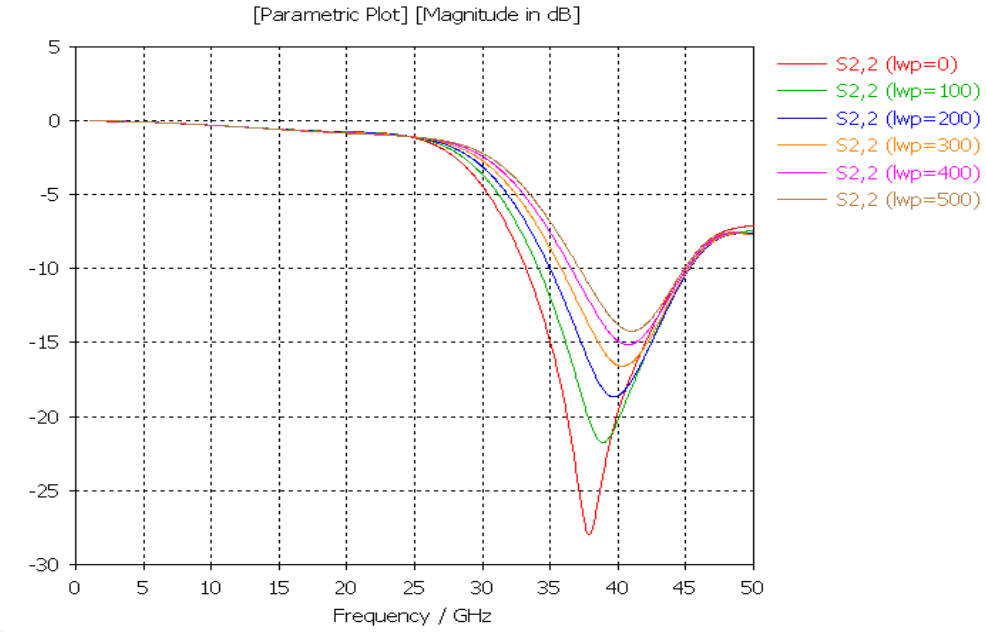

Figure 82 The S-parameters, and the H-field strength 20 nm away from the middle and side parts of the loop, 50 nm away from the middle part of the loop. 4 H field plots from each probe on the Figures 82-84 showing the difference in between them (the order of the lines is the same across the first 4 plots, thus it's easy to compare them with the winning one highlighted on the first plot, (which is for the Probe 1)). Then the S22 in dB shown for the Probe 1 position as well for clarification and for double-check. The sweeps of tapering degree performed

Further the sweeps of the CPS width were taken for further optimization.

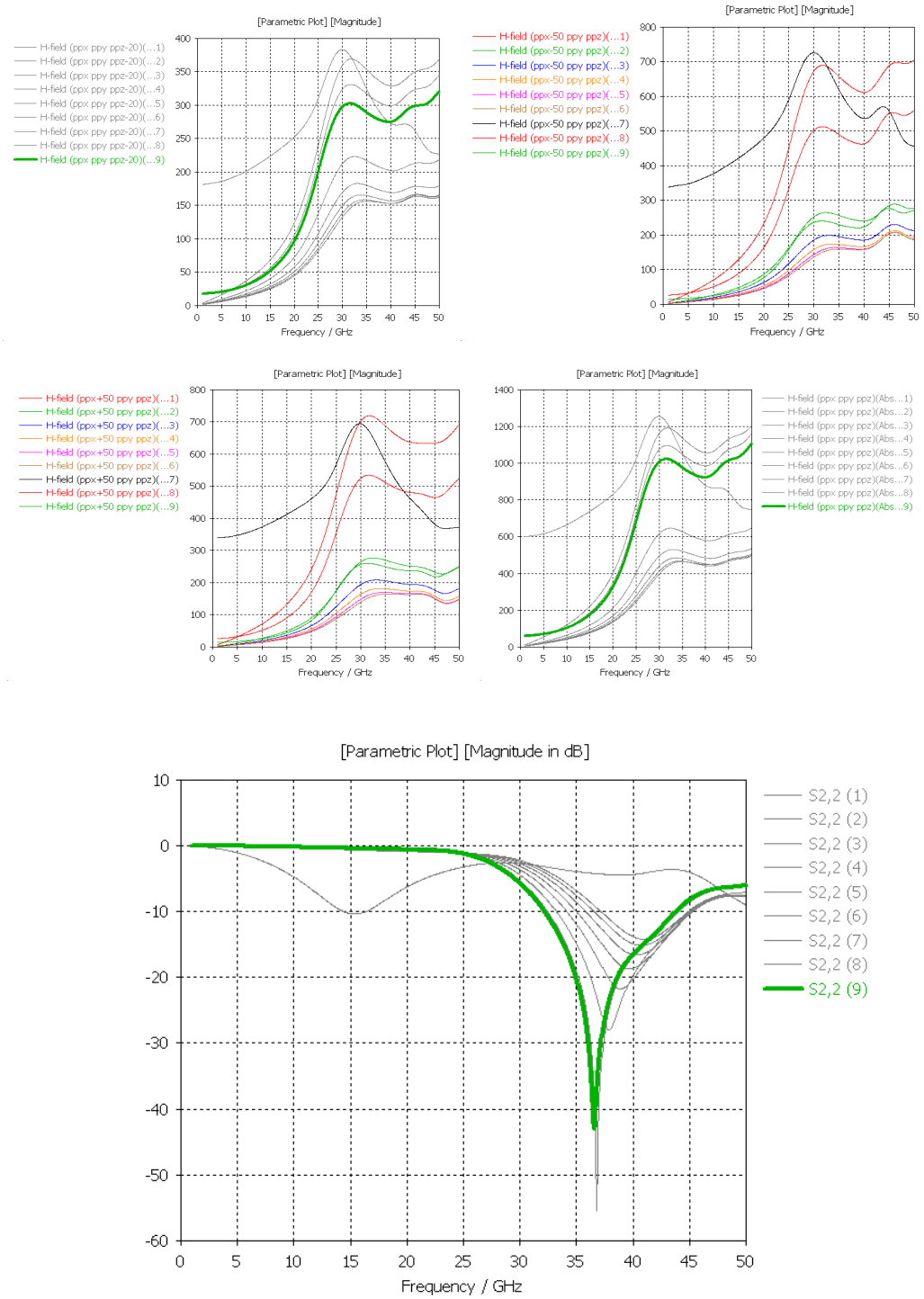

Figure 83 The S-parameters, and the H-field strength 20 nm away from the middle and side parts of the loop, 50 nm away from the middle part of the loop. 4 H field plots from each probe on the Figures 82-84 showing the difference in between them (the order of the lines is the same across the first 4 plots, thus it's easy to compare them with the winning one highlighted on the first plot, (which is for the Probe 1)). Then the S22 in dB shown for the Probe 1 position as well for clarification and for double-check. The sweeps of CPS width performed.

The last step in our design optimization study were the dimensions of the "bridge" at the end of our loop. Thus, we've run a few more simulations to distinguish the last parameters. Four probes were placed around the end of our feeding device to see the impact of the sweeps. The first probe was placed 20 nm away from the exact end of the feeding device as it shown on the Figure 67. This one is where the sample will be placed at for further investigations. The other probes were placed to show the decay of the field when going away from the conducting part as well as going away from the geometrical centre of the loop to prove that the field is well-concentrated exactly at the Probe 1 position area. The second probe was placed in the same plane as the Probe 1 but 50 nm away from the conducting loop (thus the distance is x2.5 bigger). The 3rd and the 4th Probes were placed on the same plane, which is parallel to the bridge, 20 nm away from it (same as the 1st one, all the probes are placed at the same height from the substrate). These two had the aim to prove the concentration of the field in the middle of the conducting loop compare to the corners of it. That's why there are 4 H field plots from each probe on the Figures 82-84 showing the difference in between them (the order of the lines is the same across the first 4 plots, thus it's easy to compare them with the winning one highlighted on the first plot, (which is for the Probe 1)). Then the S_{22} in dB shown for the Probe 1 position as well for clarification and for double-check. The results are presented on the Figures 82-84.

Thus, the optimum dimensions of the feeding structure were obtained, and we were ready for the fabrication. The H filed strength of 1600 A/m was achieved (2,01 mT, Figure 84). At the same time the field strength at the position of the probes on the side are more than 5 times smaller. That's why this sweep parameter was chosen as the winner apart from the point that the reflection coefficient for this frequency is not the best one (but still enough for good performance in terms of the dB value). At the same time the field strength decays with the same proportion as we are going away from the conducting part border (the last image). Thus, the final dimensions we've obtained from series of our parametric sweeps are shown on the Fig. 85.

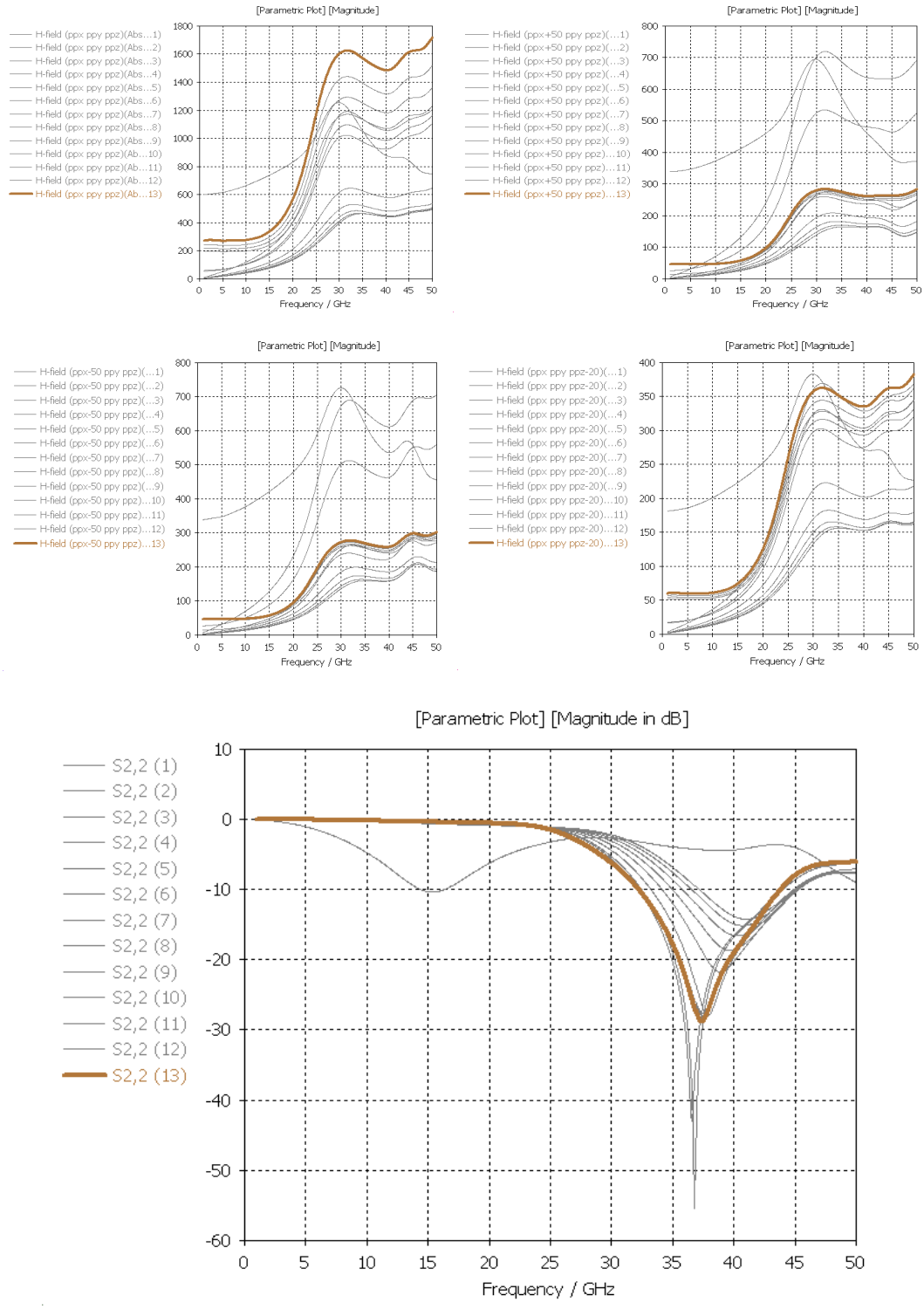

Figure 84 The S-parameters, and the H-field strength 20 nm away from the middle and side parts of the loop, 50 nm away from the middle part of the loop. 4 H field plots from each probe on the Figures 82-84 showing the difference in between them (the order of the lines is the same across the first 4 plots, thus it's easy to compare them with the winning one highlighted on the first plot, (which is for the Probe 1)). Then the S22 in dB shown for the Probe 1 position as well for clarification and for double-check. The sweeps of "bridge" size performed.

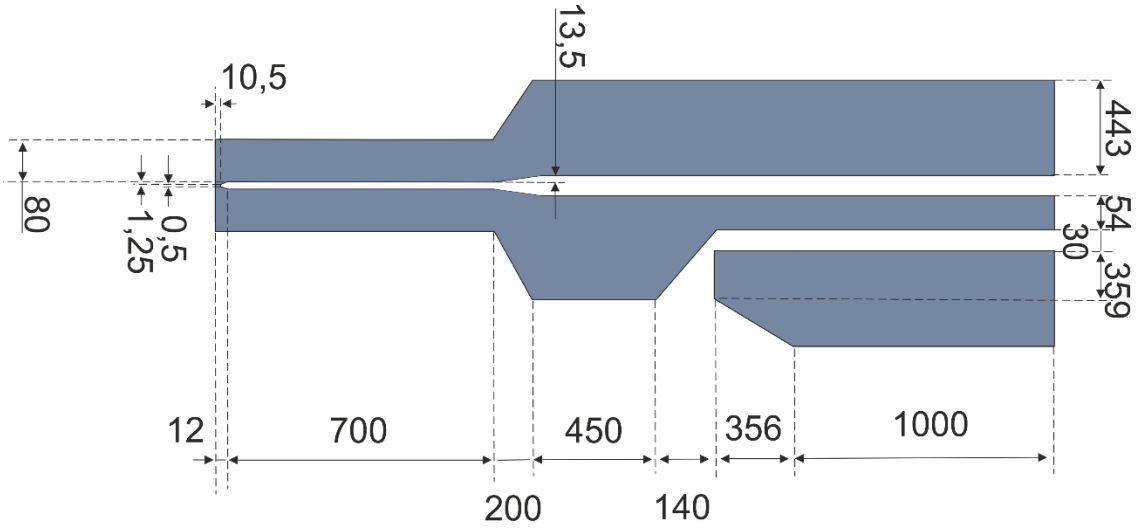

Figure 85 The final dimensions of the feeding device in microns obtained from the optimisation study and ready for the mask fabrication.

4.3 The Fabrication Preparation

The training was organized in Rome in a group of Professor Romolo Marcelli in accordance with an agreement made during the training courses in June 2016. The latter has shown that this research group has a huge experience in a field of microwave fabrication and measurements. They have a clean room with a photo- mask fabrication facilities as well as direct laser writing. They also doing fabrication of microwave structures on silicone substrates and has years of experience in measurements of transmission lines, switches, etc. That's why me and Alex Koelker from LCN have decided to plan a training here. We have a joint project about the EPR resonance and have decided to fabricate and measure our structure here in Rome.

The structure under study is a transmission line which has to bring the magnetic field to the hall-bar device perpendicular to its surface. The simulations for this problem were performed by me in CST Microwave Studio and by Dr. Abiola Oladipo in EM Pro. As a result of these simulations, we've got two designs of the transmission line configuration suitable for the purpose of the study with different frequency of operation, around 5 GHz and around 37 GHz. We've decided to check these designs by fabricating and measuring them in order to prove the difference in a frequency range. The design of the hall-bar was originally given by Hari Solanki from LCN and

changed by Abiola in order to have more space to put the feeding device. We've agreed to use the same read-out structure to feel the difference in a transmission line design. My design was based on the Balun connecting the CPW and tapered CPS lines in order to provide the correct connection of the balanced and unbalanced line types. The design made by Abiola was a simple CPW line connected to the tapered CPS line by two bonding wires. It originally came from the idea to fabricate the CPS part separately on chip with hall-bar device. This time we've decided to make them both on the same substrate (500 microns thick) and by the same metal (Au, since the Italian National Council of Research (CNR) group has an extensive experience with this metal) in order to simplify the fabrication and do it quicker.

The first step was absolutely technical. It was the implementation of the model from simulation tool for the mask fabrication software. It wasn't expected that the exported file from the simulation programming package will not always be correctly taken by AutoCAD. It came out to me that this "bridge" in between the simulation and fabrication is not so well performed by the soft companies because at the end the DXF format is not so unified and has a lot of individual special aspects. Finally, two groups of files were prepared.

First one was for photolithography. In order to satisfy the limits of the photomask and device fabrication I've made a few more simulations and found the optimum parameters. The aim was to fit the point that nothing should be smaller than 2 microns, so all the parameters were increased to be at least equal to this size for both of designs. Finally, the connecting part at the end of tapered CPS was chosen to be the same for both designs.

The second one was created with original parameters values and should be made by electron-beam lithography (EBL) technique. The "bridge" size at the ending part of CPS was in order of a few microns and the most important thing –the distance to the hall-bar device from the end of the line was 20 nm. This is the most critical parameter. According to the simulations, the field strength decays rapidly away from the transmission line. Therefore. the 2-micron distance is a big value in that case (first group).

So, the first mask (fabricated by photolithography) should prove the fact of the relations of the coupling power in between the transmission line and the read-out device with respect to the distance. It should perform very weak coupling.

Opposite to that the second mask design is for the case of a good coupling and the voltage measured in a hall bar induced by the magnetic field of a transmission line should be high.

The first design was tested also. The possibility to print the mask with 2 microns resolution was proved. The mask was fabricated (Fig. 87-90).

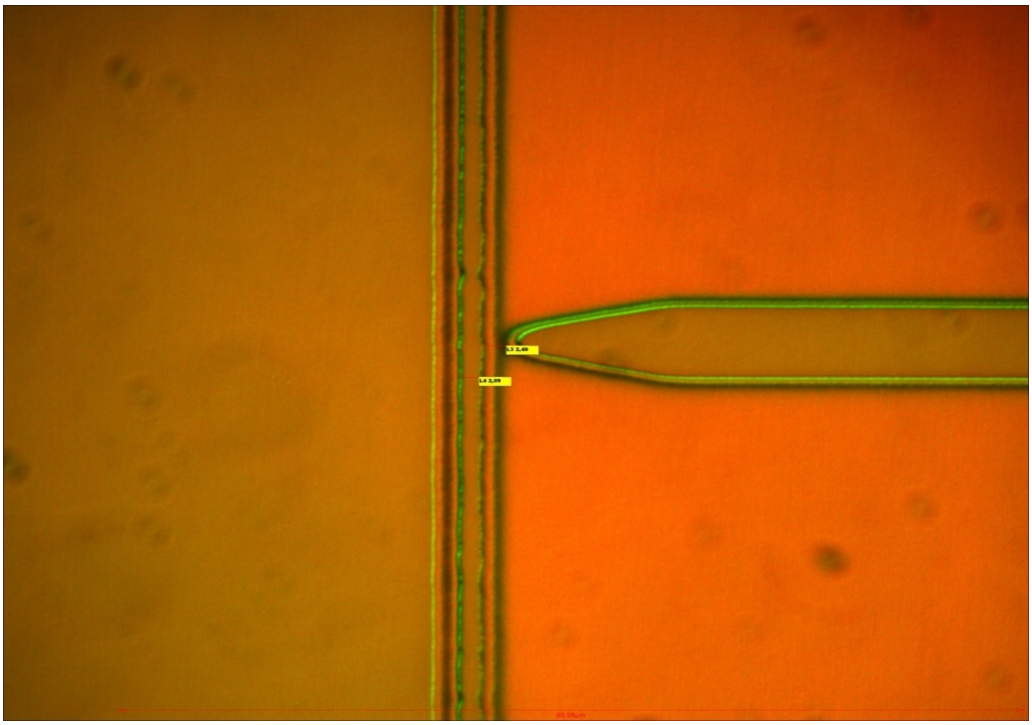

Figure 86 The ending part of CPS line mask fabrication test. The resolution of 2 micron is approved.

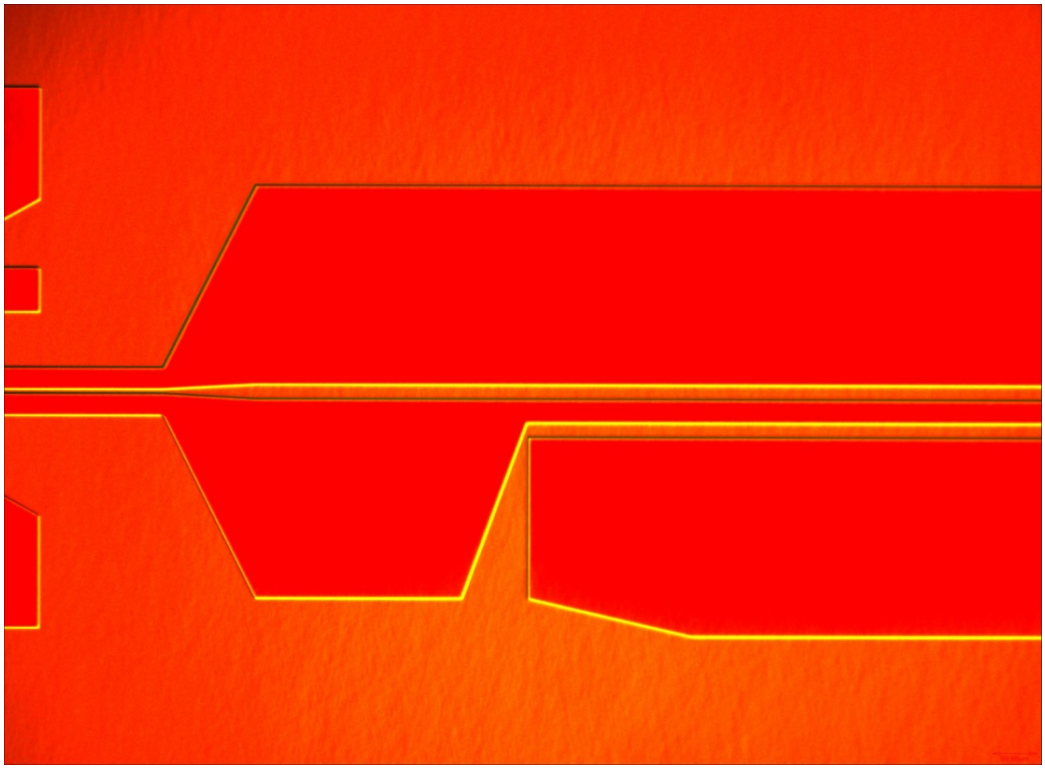

Figure 87 The CPW to CPS mask design with a Balun together with the hall-bar device. Balun part.

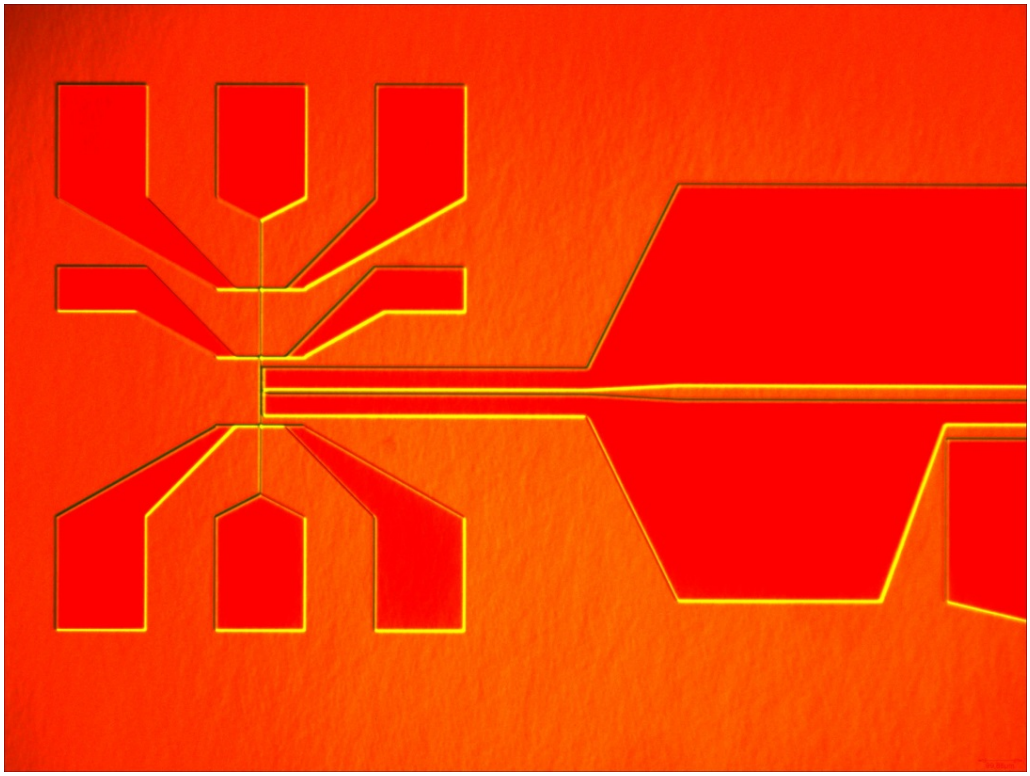

Figure 88 The CPW to CPS mask design with a Balun together with the hall-bar device.

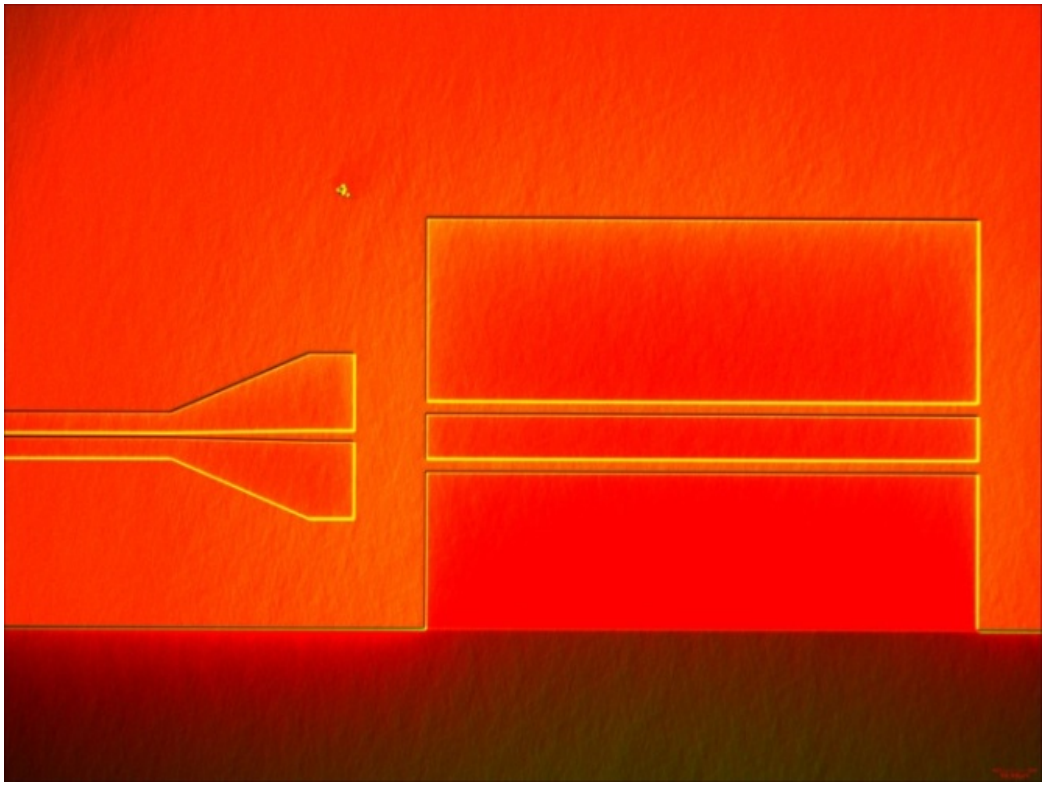

Figure 89 The CPS to CPW design with bonding wires connection instead of the balun together with the hall-bar device. Transmission part.

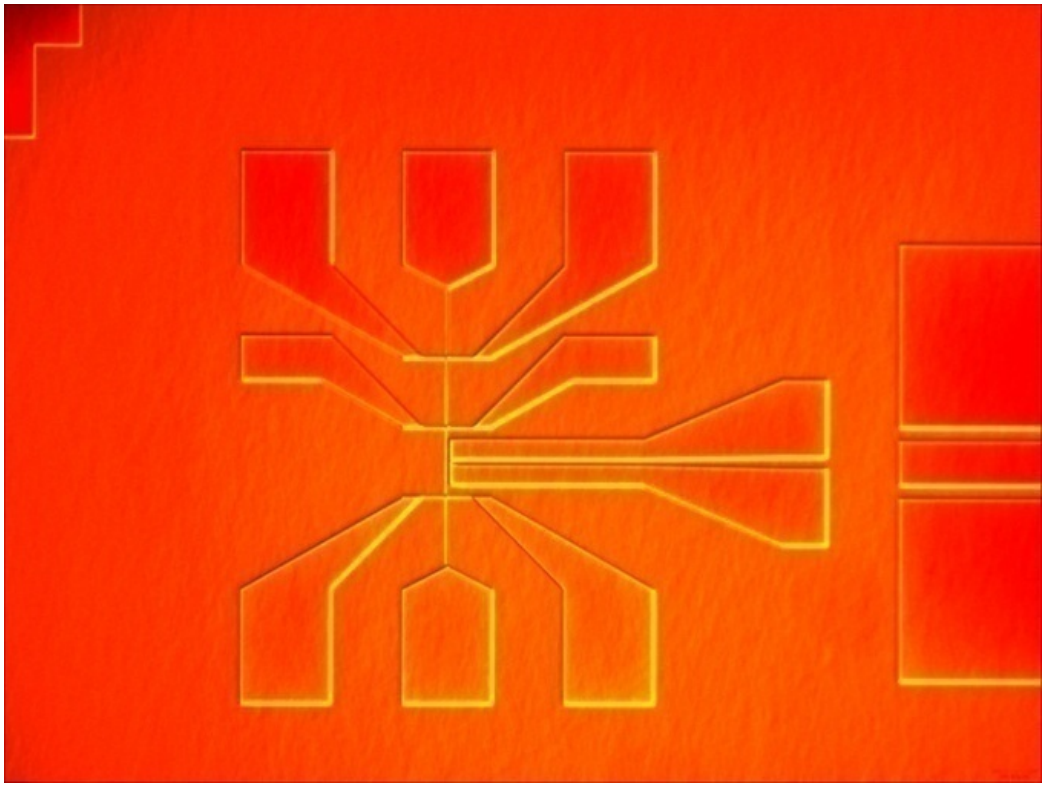

Figure 90 The CPS to CPW design with bonding wires instead of the balun connection together with the hall-bar device. Hall bar device part.

To sum up, all the preparations for the sample's fabrication and numerical tests of the designs were performed. The long story of numerical simulations for the design optimisation has ended here. The summary of the contributions as well as future plans are presented in the following Conclusions Chapter 5.

Chapter 5. Conclusions and future work

To sum up, it is needed to say that it was a very interesting journey to the spintronics world. The completely different areas of physics with their specific principles, properties and limitations united by the spintronics were investigated. Spintronics is a very interesting area which is situated on the edge of the microwave technologies known for quite a long period already but still very important and quantum mechanics which has started to be investigated deeper these days as the technologies took a giant step further and not only analytically.

In order to understand this area better quite a few techniques for material properties investigation were tested and investigated. Analytical, numerical and experimental sides of several aspects of the spintronics were tested and the results of those tests and investigations presented above.

Scanning Microwave Microscopy were studied analytically and experimentally in Chapter 3. The biological samples as well, some doped semiconductor samples, noble metals and Permalloy sample were investigated experimentally. Suitable images were obtained and used by my colleagues for their thesis works and publications later.

Electrostatic force microscopy was deeply studied theoretically, numerically and experimentally in Chapter 3 as well. The images of semiconductor and noble metals samples were obtained and investigated. It helped a lot to deep dive into the steps of experimental analysis as well as my colleagues to improve their skills and collect necessary information for their investigations.

Experimental and numerical studies led to the study of Classical Atomic Force Microscopy tip used in both SMM and EFM experimental setup. It was studied from the analytical and numerical point of view in order to present better and more precisely simulations at the high frequencies. The clear improvement of the simulation model was shown and stated. This contribution was the first one achieved in this investigation. The potential applications in a field of bacterial and living tissues stated.

Finally, the feeding device optimisation study was the second main contribution presented in Chapter 4. The final optimised parameters presented at the

Fig. 85. The H filed value reached for this design H=1600 A/m and it works at the Q frequency band. On the way to those results the study of microwave circuits as well as the understanding of the quantum mechanics or more precisely the Electron Paramagnetic Resonance (EPR) phenomena were performed. The device was prepared for fabrication as the mask model was created and fabricated for the original design and for one another in order to test them for comparison. Here is a need to say a few words about potential publications. The optimisation study of my design was made numerically and theoretically. Therefore, this is the first future potential publication. The second one is the comparison of my design and the second one which was chosen for comparison (with bonding wires instead of the balun) for which the mask was created. There is enough theoretical and numerical data. With additional funding and availability of my colleagues from CNR Rome the fabrication of the device based on our design could be finished. The second design data could be analysed, and the full comparison could be a source for the other publication.

Talking about the future plans, it is obvious from this investigation that the feeding device is nothing else but the “function” or even the “parameter” which acts on the magnetic field we’ve got from the source (this was clearly stated in Chapter 4 where the time evolution of the single electron wave function was presented). This “parametrised” magnetic field goes to the particle (electron) which perform the EPR and changes its spin towards the magnetic field applied. In other words, we may change the design or the kind of the feeding structure and control the resonance conditions in this way. The device could be simulated numerically. Thus, we may obtain the numerical simulation model (tool) for EPR control. It might be very time-consuming to write the code but it’s going to be very useful as the information processing and spintronic based devices are taking more and more attention these days.

References

[1] H. X. Tang, et al," Giant Planar Hall Effect in Epitaxial (Ga, Mn) As Devices" Phys. Rev. Let., Vol. 90, 10 (2003)

[2] Yuanbo Zhang et al, "Experimental observation of the quantum Hall effect and Berry's phase in graphene", Nature 438, 201-204, (2005)

[3] B. A. Bernevig, T. L. Hughes and Sh.-C. Zhang, "Quantum spin Hall effect and topological phase transition in HgTe quantum wells", Science, Vol. 314, Issue 5806, pp. 1757-1761 (2006)

[4] M. Abu-Teir, F. Sakran, M. Golosovsky, D. Davidov and A. Frenkel, "Local contactless measurement of the ordinary and extraordinary Hall-effect using near-field microwave microscopy", Appl. Phys. Lett. 80, 1776 (2002)

[5] D. Sullivan and D. S. Citrin, "Time-domain simulation of two electrons in a quantum dot" Journal of Applied Physics, Vol. 89, 3841 (2001)

[6] Marek Nowakowski, "The quantum mechanical current of the Pauli equation" Am. J. Phys., Vol. 67, 916 (1999)

[7] H. Bluhm, et.al, "Dephasing time of GaAs electron-spin qubits coupled to a nuclear bath exceeding 200 μs" Nature, Vol. 7, 109-113 (2011)

[8] L. DiCarlo, et. al, "Preparation and measurement of three-qubit entanglement in a superconducting circuit" Nature, Vol. 467, 574-578 (2010)

[9] M. Neeley et al," Generation of three-qubit entangled states using superconducting phase qubits", Nature, Vol. 467, 570-573 (2010)

[10] S. Amasha, et al, "Energy-Dependent Tunneling in a Quantum Dot" Proc. of SPIE, Vol. 6244, 624419 (2006)

[11] D. M. Sullivan and D. S. Citrin, "Time-Domain Simulation of Three-Dimensional Quantum Wires" Journal of Applied Physics, Vol. 96, 1540 (2004).

[12] R. Neumann and L. R. Schreiber, "Simulation of micro-magnet stray-field dynamics for spin qubit manipulation" Journal of Applied Physics 117, 193903 (2015)

[13] M. S. Blok et al, “Manipulating a qubit through the backaction of sequential partial measurements and real-time feedback” Nature Physics 10, 189–193 (2014)

[14] Gavin W. Morley et al,” Quantum control of hybrid nuclear–electronic qubits” Nature Materials 9, 725–729 (2010)

[15] Emily Mount et al, “Design, fabrication and experimental demonstration of junction surface ion traps” New Journal of Physics, Volume 15 (2013)

[16] S. Kalinin and A. Gruverman,” Scanning Probe Microscopy” Springer, New York, (2007)

[17] C. Simbrunner et al.,” On the effect of periodic Mg distribution in GaN: δ-Mg”, Appl. Phys. Lett. 90, 142108 (2007)

[18] S.G. Shengurov, V.N. Shabanov, “Growth of delta-doped silicon layers by molecular beam epitaxy with simultaneous low energy ion bombardment of the growth surface”, A.V. Tech. Phys. Lett. 23, 281 (1997)

[19] F.W. Ragay, M.R. Leys, J.H. Wolter, “Application of δ-doping in GaAs tunnel junctions”, Electronics Letters, Vol. 30, Issue 1, 86 – 87 (1994)

[20] P. Zeeman, “The Effect of Magnetization on the Nature of Light Emitted by a Substance”, Nature 55, 347 (1897).

[21] E. U. Condon, G. H. Shortley, “The Theory of Atomic Spectra”, Cambridge University Press, 379-396 (1935).

[22] L. C. Basset and D. D. Awschalom, “Quantum computation: Spinning towards scalable circuits”, Nature 489, 505–507 (2012)

[23] Y. Twig, E. Suhovoy and A. Blank, “Sensitive surface loop-gap micro resonators for electron spin resonance”, Rev. Sci. Instrum. 81, 104703 (2010)

[24] Dimitrios E. Anagnostou et al,” A 0–55-GHz Coplanar Waveguide to Coplanar Strip Transition”, IEEE Transactions on microwave theory and techniques, Vol. 56, No. 1, (2008)

[25] Shao-Gang Mao et al, IEEE Transactions on microwave theory and techniques, Vol. 48, No 1, (2000)

[26] J. P. Dehollain, J. J. Pla, E. Siew, K. Y. Tan, A. S. Dzurak and A. Morello, “Nanoscale broadband transmission lines for spin qubit control”, Nanotechnology, Vol. 24, Number 1 (2012)

[27] J. Baker-Jarvis and S. Kim, “The interaction of radio-frequency fields with dielectric materials at macroscopic to mesoscopic scales”, Journal of Research of the National Institute of Standards and Technology, Vol. 117 (2012)

[28] S. Drake, “Galileo at Work: His Scientific Biography.”, Dover Publications, New York, (1978)

[29] J. Kepler, “New Astronomy”, translated by William H. Donahue, Cambridge: Cambridge Univ. Pr., (1992)

[30] I. N. Veselovskiy, Yu. A. Beliy, “Nicolaus Copernicus”, Moscow, Science, pp. 304-318, (1974)

[31] D. Mendeleev, “Versuche eines Systems der Elemente nach ihren Atomgewichten und chemischen Functionen” [System of Elements according to their Atomic Weights and Chemical Functions], Journal für Praktische Chemie., pp. 106-251, (1869)

[32] W. Pauli, “Uber den Zusammenhang des Abschlusses der Elektronengruppen in Atom mit der Komplexstruktur der Spektren.”, Z. Phys., 31, 765—78, (1925), (translation into English) The Old Quantum Theory, ed. by D. ter Haar, Pergamon Press, 184, (1967)

[33] V.V. Zagorskiy, “Atom and Periodical Table for Phys-Math lyceums (in RU)”, Russian Chemical Journal, vol 38, 4, pp. 37-42, (1994)

[34] A.L. Buchachenko, “Chemical polarisation of electrons and nuclei” (in RU), Moscow, Science, p. 245, (1974).

[35] A.L. Buchachenko, "Magnetic effects in chemical reactions" (in RU) Chemistry Reports, vol. 45, pp. 761-793, (1976)

[36] A.L. Buchachenko, R.Z. Sagdeev, K.M. Salihov, “Magnetic and spin effects in chemical reactions” (in RU), Novosibirsk, Science, (1978)

[37] G. Davies, M.F. Hamer, "Optical Studies of the 1.945 eV Vibronic Band in Diamond", Proceedings of the Royal Society of London A., vol. 348 (1653), p. 285, (1976)

[38] Y. Mita, "Change of absorption spectra in type-Ib diamond with heavy neutron irradiation". Physical Review B, vol. 53 (17), pp. 11360–11364, (1996)

[39] K. Iakoubovskii, G.J. Adriaenssens, M. Nesladek, "Photochromism of vacancy-related centres in diamond", Journal of Physics: Condensed Matter, 12 (2), p. 189, (2000)

[40] J.H.N. Loubser, J.A. van Wyk, "Electron Spin Resonance in Annealed Type 1b Diamond", Diamond Research, vol. 11, pp.4–7, (1977)

[41] J.H.N. Loubser, J.A. van Wyk, "Electron spin resonance in the study of diamond", Reports on Progress in Physics, vol 41 (8), p. 1201, (1978)

[42] D. Redman, S. Brown, R. Sands, S. Rand, "Spin dynamics and electronic states of N-V centers in diamond by EPR and four-wave-mixing spectroscopy", Physical Review Letters, vol. 67 (24), pp. 3420–3423, (1991)

[43] G. D. Fuchs, V. V. Dobrovitski, R. Hanson, A. Batra, C. D. Weis, T. Schenkel, and D. D. Awschalom, “Excited-State Spectroscopy Using Single Spin Manipulation in Diamond”, Phys. Rev. Lett., vol 101, p. 117601, (2008)

[44] G.E. Uhlenbeck and S.A. Goudsmit, Die Naturwissenschaften, 13, 953-954, (1925)

[45] J.E. Wertz and J.R. Bolton, "Electron Spin Resonance. Elementary theory and practical applications", New York, (1972).

[46] P. A. Belov, Y. Hao and S. Sudhakaran, “Subwavelength microwave imaging using an array of parallel conducting wires as a lens”, Phys. Rev. B 73, 033108, (2006)

[47] J.W. Linnett, Wave Mechanics and Valency, Chap 3, Methuen and Co, London, (1960).

[48] R. Feynman, QED: The Strange Theory of Light and Matter, Penguin 1990 Edition, p. 84.

[49] Thomson, G. P., "Diffraction of Cathode Rays by a Thin Film", Nature. 119 (3007): 890–890, (1927)

[50] T. Okino, “Quantum Effect on Elementary Process of Diffusion and Collective Motion of Brown Particles”, Journal Modern Physics 9, pp. 1007-1028., (2018).

[51] Cole T., Pritchard H.O., Davidson N.R., McConnell H.M., “Molecular Physics”, vol. 1, p. 406, (1958)

[52] Alonso, Marcelo, Finn, Edward, “Physics”, Adison Wesley, (1992)

[53] E.K. Zavoyskiy, "Spin-magnetic resonance in paramagnetics", Fizicheskii Zhurnal (USSR), vol. 9,211, 245, (1945)

[54] P.A.M. Dirac, “Principles of quantum mechanics”, Oxford Press, (1930)

[55] Rabi I.I., Milliman S., Kusch P., Zacharias J.R., “The Molecular Beam Resonance Method for Measuring Nuclear Magnetic Moments. The Magnetic Moments of $_3Li^6$, $_3Li^7$ and $_9F^{19}$”, Physical Review, vol. 55, 526, (1939)

[56] Kellogg J.M., Rabi I.I., Ramsey N.F., Zacharias J.R., “An electrical quadrupole moment of the deuteron the radiofrequency spectra of HD and D_2 molecules in a magnetic field”, Physical Review, vol. 57, 677, (1940)

[57] Cargile B. J., Sevinsky J. R., Essader A. S., Eu J. P., Stephenson J. L., “Calculation of the isoelectric point of tryptic peptides in the pH 3.5-4.5 range based on adjacent amino acid effects”, Electrophoresis., vol. 29 (13), pp. 2768–2778, (2008)

[58] H. Kirchmayr, “Magnetic Anisotropy”, Encyclopedia of Materials: Science and Technology, pp. 4754-4757, (2001)

[59] P. A. Belov, R. Marques, S. I. Maslovski, I. S. Nefedov, M. Silveirinha, C. R. Simovski, and S. A. Tretyakov, “Strong spatial dispersion in wire media in the very large wavelength limit”, Phys. Rev. B 67, 113103 (2003)

[60] P. A. Belov and M. G. Silveirinha, “Resolution of sub-wavelength transmission devices formed by a wire medium”, Phys. Rev. E 73, 056607 (2006).

[61] A. E. Ageyskiy, S. Yu. Kosulnikov, S. I. Maslovski, Yu. S. Kivshar and P. A. Belov, “Quarter-wavelength nanorod lens based on internal imaging”, Physical Review B 85, 033105, (2012)

[62] J.C. Maxwell, “A dynamical theory of the electromagnetic field”, Philosophical Transactions of the Royal Society of London, 155, 459—512, (1865)

[63] P. A. Belov, Y. Zhao, S. Tse, P. Ikonen, M. G. Silveirinha, C. R. Simovski, S. Tretyakov, Y. Hao, and C. Parini, “Transmission of images with subwavelength resolution to distances of several wavelengths in the microwave range”, Phys. Rev. B 77, 193108 (2008).

[64] M. G. Silveirinha, P. Belov, and C. R. Simovskiy, “Ultimate limit of resolution of subwavelength imaging devices formed by metallic rods”, Opt. Lett. 33, 1726, (2008).

[65] P. Belov, G. Palikaras, Y. Zhao, A. Rahman, C. Simovski, Y. Hao, and C. Parini, “Experimental demonstration of multiwire endoscopes capable of manipulating near-fields with subwavelength resolution”, Appl. Phys. Lett. 97, 191905 (2010).

[66] H. Helmholtz, “On the sensations of tone”, Longmans, Green and Co, p.68, 579, (1875).

[67] T.L. Floyd, “Principles of electric circuits”, 5th edition, Prentice Hall, (1997)

[68] W. Thomson, “On the Electro-dynamic Qualities of Metals”, Proc. Royal Soc. London, 8, pp. 546–550, (1856)

[69] G. Giuliani, “A general law for electromagnetic induction”, EPS. 81 (6), p. 60002, (2008)

[70] L.W. Schubnikov, W.J. de Haas, “Magnetische Widerstands vergrösserung in Einkristallen von Wismutbeitiefen Temperaturen”, Proc. of the Royal Netherlands Academy of Arts and Science (in German), 33, pp. 363–378. (1930, Retrieved September 26, 2016.)

[71] H. Cao, et al.,” Topological insulator-based spin valve devices: evidence for spin polarized transport of spin momentum-locked topological surface states” Phys. Rev. Lett. 108, 216803, (2012)

[72] Harald Ibach, Hans Lüth, “Solid-State Physics: An Introduction to Principles of Materials Science”, pp. 479- 481, (2010)

[73] Mielke, C.H. et al.,” High magnetic field investigation of the Fermi surface of the pincainide compound”, Journal of Physics: Condensed Matter, 10, pp. 5289-5294. (1998).

[74] A.B. Pippard: Magnetoresistance in Metals, Cambridge University Press, (1989)

[75] T. McGuire, R. Potter, “Anisotropic Magnetoresistance in Ferromagnetic3d Alloys”, IEEE Transactions on Magnetics, 11 (4), 1018–1038, (1975)

[76] Wiśniewski, “Giant anisotropic magnetoresistance and magneto thermopower in cubic 3:4 uranium pnictides”, Applied Physics Letters, Vol. 90, Issue 19, 192106, (2007)

[77] G. Peach, “Theory of the pressure broadening and shift of spectral lines”, Advances in Physics. 30 (3), 367–474, (1981)

[78] J. Bass, W. P. Pratt, “Using domain walls to perform non-local measurements with high spin signal amplitudes”, JMMM. 200, 274–289, (1999)

[79] Z.Y. Leong, S.G. Tan, M.B.A. Jalil, S. Bala Kumar, G.C. Han, “Magnetoresistance modulation due to interfacial conductance of current perpendicular-to-plane spin valves”, Journal of Magnetism and Magnetic Materials, 310 (2), 635–637, (2007)

[80] D. Sun, et. al, “Spin Polarization at Organic-Ferromagnetic Interface: Effect of Contact Configuration”, Phys. Rev. Lett. 104 (23): 236602 (2010).

[81] Tz. Ma, A. B. Khanikaev, S. H. Mousavi, G. Shvets, “Topological terahertz circuits using semiconductors” arXiv:1401.1276

[82] A. B. Khanikaev, S. H. Mousavi, Wang-Kong Tse, M. Kargarian, A. H. MacDonald and G. Shvets, “Geometric phase and topology of elastic oscillations and vibrations in model systems: Harmonic oscillator and superlattice” Nature Materials, Vol. 12, 233-239 (2013)

[83] Jungpil Seo, Pedram Roushan, Haim Beidenkopf, Y. S. Hor, R. J. Cava and Ali Yazdani, “Transmission of topological surface states through surface barriers” Nature, Vol. 466, (2010)

[84] Pedram Roushan et al, “Spatial fluctuations of helical Dirac fermions on the surface of topological insulators” Nature, Vol. 460, (2009)

[85] Kai Sun, “Layered reduced graphene oxide with nanoscale interlayer gaps as a stable host for lithium metal anodes” Nature Materials, Vol. 14, March (2015)

[86] M. Hafezi et al, “Imaging topological edge states in silicon photonics” Nature Photon. 7, 1001–1005 (2013)

[87] N. Xu et al, “Direct observation of the spin texture in SmB6 as evidence of the topological Kondo insulator” Nature Com. 5, 4566 (2014)

[88] Yu. Shiomi et al,” Spin-Electricity Conversion Induced by Spin Injection into Topological Insulators” Phys. Rev. Lett. 113, 196601 (2014)

[89] X. Qian et al,” Quantum Spin Hall Effect and Topological Field Effect Transistor in Two-Dimensional Transition Metal Dichalcogenides” Science Vol. 346, Issue 6215, pp. 1344-1347 (2014)

[90] K. Yasuda et al,” Geometric Hall effects in topological insulator heterostructures” Nature Physics 12, 555–559 (2016)

[91] A. P. Slobozhanyuk et al, “Enhanced photonic spin Hall effect with subwavelength topological edge states” Laser & Photonics Reviews, 10: 656–664 (2016)

[92] Fabrice Lemoult, Nadege Kaina, Mathias Fink and Geoffroy Lerosey, “Wave propagation control at the deep subwavelength scale in metamaterials” Nature Physics, vol. 9, p. 55 (2013)

[93] F. Lemoult, M. Fink, and G. Lerosey, “Acoustic resonators for far-field control of sound on a subwavelength scale” Waves in Random and Complex Media, 4th edition, vol. 9, p. 591, (2011)

[94] Pavel A. Belov,” Single-mode subwavelength waveguides with wire metamaterials” Appl. Phys. Lett., vol. 103, p. 161103, (2013)

[95] C. Simovski et al, “Micro gap thermophotovoltaic systems with low emission temperature and high electric output” Phot. Nano. Fund. Appl., vol. 13, pp. 31–41, (2015)

[96] S. Kosulnikov et al, “Grating-based Dipole Antenna Configuration for High Gain Directional Radiation characteristics” EEE Trans. Antennas Propag., vol. 63, pp. 4848-4856, (2015)

[97] S. Kosulnikov et al, “Multi-mode broadband power transfer through a wire medium slab” IEEE Trans. Antennas Propag., vol. 99, (2016)

[98] I. Yagupov et al, “Anomalous polarization conversion in arrays of ultrathin ferromagnetic nanowires” Phys. Rev. B, vol. 92, pp. 041304(R), (2015)

[99] Yu. Tyshetskiy et al, “Guided modes in a spatially dispersive wire medium slab” J. Opt. Soc. Am. B, vol. 31, pp. 1753-1760, (2014)

[100] Wenhai Han, “Introduction to Scanning Microwave Microscopy”, Application note, Agilent Technologies, Inc., 5989-8881EN, (2008)

[101] B. T. Rosner and D. W. van der Weide, “High frequency dielectric properties distribution of BiFeO3BiFeO3 thin film using near-field microwave microscopy” Rev. Sci. Instrum. 73, 2505, (2002)

[102] V. V. Zavyalov, J. S. McMurray, and C. C. Williams," Scanning capacitance microscope methodology for quantitative analysis of p-np-n junctions" Rev. Sci. Instrum., vol. 70, p. 158, (1999)

[103] Agilent 5400 5500 Atomic Force Microscope (N9410S)

[104] Agilent Professional Network Analyzer (N5230A)

[105] Elmen, G.W.; H. D. Arnold," Permalloy, a new magnetic material of very high permeability" Bell System Technical Journal, pp. 101-111, (1923)

[106] David C. Jiles, Introduction to Magnetism and Magnetic Materials, Second Edition, CRC Press, (1998)

[107] G.W. Elmen," Magnetic Alloys of Iron, Nickel, and Cobalt", (1936)

[108] W. G Van der Wiel, S. De Franceschi, J. M Elzerman, T. Fujisawa, S. Tarucha, L. P Kouwenhoven," Electron transport through double quantum dots", Reviews of Modern Physics, vol. 75, 1, (2002)

[109] P. W. Chapman, O. N. Tufte, J. D. Zook, and D. Long," Electrical Properties and Resonance Scattering in Heavily Doped n-Type GaSb and Related Semiconductors" Journal of Applied Physics, Vol. 34, Issue 11, (2004)

[110] G Gramse et al," Quantitative sub-surface and non-contact imaging using scanning microwave microscopy" Nanotechnology, Vol. 26, 135701, (2015)

[111] E Brinciotti et al, Nanoscale," An Advanced Impedance Calibration Method for Nanoscale Measurements" Vol. 7, Issue 35,14715-14722 (2015)

[112] Eaton P et al., Atomic force microscopy. OUP, Oxford, (2010)

[113] Lin CW et al.," Nano-machining of gold and semiconductor surfaces", J Electrochem Soc, vol 134, pp. 1038-1039, (1987)

[114] Paul Girard, "Studies in Surface Science and Catalysis", Nanotechnology, Vol. 12, 485–490, (2001)

[115] A.S. Hou, F. Ho and D.-M. Bloom, "Ultrafast voltage-contrast scanning probe microscopy", Electron. Lett., vol. 28, 203, (1988)

[116] C. Bohm, F. Saurenbach, P. Taschner, C. Roths and E. Kubalek, “Electrostatic force microscopy: principles and some applications to semiconductors”, J. Phys. D: Appl. Phys., vol. 26, 842, (1996)

[117] C. Schonenberger, S.F. Alvarado, S.E. Lambert and I.L. Sanders, “Separation of magnetic and topographic effects in force microscopy”, J. Appl. Phys., vol. 67, 7278, (1990)

[118] R.M. Nyffenegger, R.M. Penner and R. Schierle, “Visualizing charge transport in silicon nanocrystals embedded in SiO2SiO2 films with electrostatic force microscopy”, Appl. Phys. Lett., vol. 71, 1878, (1997)

[119] Y. Shen, D.M. Barnett and P.M. Pinsky, “Finite-size effects and analytical modeling of electrostatic force microscopy applied to dielectric films”, Eng. Anal. Bound. Elem., vol. 32, 682, (2008)

[120] L. Fumagalli, G. Ferrari, M. Sampietro and G. Gomila, “Quantifying the dielectric constant of thick insulators”, Appl. Phys. Lett., vol. 91, 243110, (2007)

[121] L. Fumagalli et al, “Quantifying the dielectric constant of thick insulators by electrostatic force microscopy: effects of the microscopic parts of the probe”, Applied Physics Letters, vol. 96, 183107 (2010)

[122] Bi-Yi Wu, Xin-Qin Sheng, R. Fabregas and Y. Hao, “Full-wave modeling of broadband near field scanning microwave microscopy”, Scientific Reports 7, 16064, (2017)

[123] A. C. Torrezan, T. P. Mayer Alegre, and G. Medeiros-Ribeiro, “Microstrip resonators for electron paramagnetic resonance experiments”, Review of Scientific Instruments, vol. 80, 075111, (2009)

[124] Ygal Twig, Ekaterina Suhovoy, and Aharon Blank, “High-sensitivity Q-band electron spin resonance imaging system with submicron resolution”, Rev. Sci. Instrum. 81, 104703, (2010)

[125] R.J. Langley and A.J. Drinkwater, “Improved empirical model for the Jerusalem cross”, IEE Proc. H, Microw. Opt. Antennas, 129, (1), pp. 1–6, (1982)

[126] R.J. Langley and E.A. Parker, “Equivalent Circuit Model for Square Ring Slot Frequency Selective Surface”, Electron. Lett., vol 18, 7, pp. 294–296, (1982)

[127] S.B. Savia and E.A. Parker, “Equivalent circuit model for super dense linear dipole FSS”, IEE Proc. Microw. Antennas Propag., 150, (1), pp. 37–42, (2003)

[128] D.H. Johnson, “Origins of the equivalent circuit concept: The voltage-source equivalent”, Proceedings of the IEEE, vol. 91, (4), pp. 636–640, (2003)

[129] P.R. Gray et al,” Analysis and design of analog integrated circuits”, New York: Wiley, pp. §3.2, p. 172, (2001)